



HAL
open science

Theoretical and experimental determination of effective diffusion and thermodiffusion coefficients in porous media

Hossein Davarzani

► **To cite this version:**

Hossein Davarzani. Theoretical and experimental determination of effective diffusion and thermodiffusion coefficients in porous media. Other. Institut National Polytechnique de Toulouse - INPT, 2010. English. NNT : 2010INPT0003 . tel-04248716

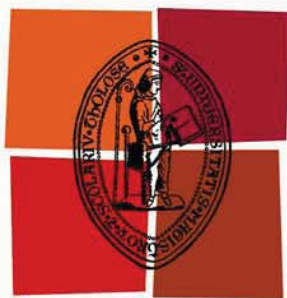
HAL Id: tel-04248716

<https://theses.hal.science/tel-04248716v1>

Submitted on 18 Oct 2023

HAL is a multi-disciplinary open access archive for the deposit and dissemination of scientific research documents, whether they are published or not. The documents may come from teaching and research institutions in France or abroad, or from public or private research centers.

L'archive ouverte pluridisciplinaire **HAL**, est destinée au dépôt et à la diffusion de documents scientifiques de niveau recherche, publiés ou non, émanant des établissements d'enseignement et de recherche français ou étrangers, des laboratoires publics ou privés.



Université
de Toulouse

THÈSE

**En vue de l'obtention du
DOCTORAT DE L'UNIVERSITÉ DE TOULOUSE**

Délivré par :

Institut National Polytechnique de Toulouse (INP Toulouse)

Discipline ou spécialité :

Sciences de la terre et des planètes solides (STP) transport en milieux poreux

Présentée et soutenue par :

Hossein DAVARZANI

le : vendredi 15 janvier 2010

Titre :

Déterminations Théorique et Expérimentale des
Coefficients de Diffusion et de Thermodiffusion
en Milieu Poreux

JURY

Abdelkader MOJTABI, Professeur à l'Université Paul Sabatier (UPS), Président du jury
Michel QUINTARD, Directeur de Recherche au CNRS, IMFT Directeur de thèse
Manuel MARCOUX, MCF à l'Université de Picardie Jules Verne, Membre
Pierre COSTESEQUE, MCF à l'Université Paul Sabatier, (UPS) Membre
Christelle LATRILLE, Ingénieur de Recherche au CEA de Paris, Membre

Ecole doctorale :

Sciences de l'Univers, de l'Environnement et de l'Espace (SDU2E)

Unité de recherche :

Institut de Mécanique des Fluides de Toulouse (IMFT)

Directeur(s) de Thèse :

Michel QUINTARD

Rapporteurs :

Azita AHMADI-SENICHAULT, Professeur à l'ENSAM de Bordeaux
Ziad SAGHIR, Professeur à l'Université de Ryerson Canada



Theoretical and Experimental Determination of Effective Diffusion and Thermal Diffusion Coefficients in Porous Media

Abstract

A multicomponent system, under nonisothermal condition, shows mass transfer with cross effects described by the thermodynamics of irreversible processes. The flow dynamics and convective patterns in mixtures are more complex than those of one-component fluids due to interplay between advection and mixing, solute diffusion, and thermal diffusion (or Soret effect). This can modify species concentrations of fluids crossing through a porous medium and leads to local accumulations. There are many important processes in nature and industry where thermal diffusion plays a crucial role. Thermal diffusion has various technical applications, such as isotope separation in liquid and gaseous mixtures, identification and separation of crude oil components, coating of metallic parts, etc. In porous media, the direct resolution of the convection-diffusion equations are practically impossible due to the complexity of the geometry; therefore the equations describing average concentrations, temperatures and velocities must be developed. They might be obtained using an up-scaling method, in which the complicated local situation (transport of energy by convection and diffusion at pore scale) is described at the macroscopic scale. At this level, heat and mass transfers can be characterized by effective tensors. The aim of this thesis is to study and understand the influence that can have a temperature gradient on the flow of a mixture. The main objective is to determine the effective coefficients modelling the heat and mass transfer in porous media, in particular the effective coefficient of thermal diffusion. To achieve this objective, we have used the volume averaging method to obtain the modelling equations that describes diffusion and thermal diffusion processes in a homogeneous porous medium. These results allow characterising the modifications induced by the thermal diffusion on mass transfer and the influence of the porous matrix properties on the thermal diffusion process. The obtained results show that the values of these coefficients in porous media are completely different from the one of the fluid mixture, and should be measured in realistic conditions, or evaluated with the theoretical technique developed in this study. Particularly, for low Péclet number (diffusive regime) the ratios of effective diffusion and thermal diffusion to their molecular coefficients are almost constant and equal to the inverse of the tortuosity coefficient of the porous matrix,

while the effective thermal conductivity is varying by changing the solid conductivity. In the opposite, for high Péclet numbers (convective regime), the above mentioned ratios increase following a power law trend, and the effective thermal diffusion coefficient decreases. In this case, changing the solid thermal conductivity also changes the value of the effective thermal diffusion and thermal conductivity coefficients. Theoretical results showed also that, for pure diffusion, even if the effective thermal conductivity depends on the particle-particle contact, the effective thermal diffusion coefficient is always constant and independent of the connectivity of the solid phase. In order to validate the theory developed by the up-scaling technique, we have compared the results obtained from the homogenised model with a direct numerical simulation at the microscopic scale. These two problems have been solved using COMSOL Multiphysics, a commercial finite elements code. The results of comparison for different parameters show an excellent agreement between theoretical and numerical models. In all cases, the structure of the porous medium and the dynamics of the fluid have to be taken into account for the characterization of the mass transfer due to thermal diffusion. This is of great importance in the concentration evaluation in the porous medium, like in oil reservoirs, problems of pollution storages and soil pollution transport. Then to consolidate these theoretical results, new experimental results have been obtained with a two-bulb apparatus are presented. The diffusion and thermal diffusion of a helium-nitrogen and helium-carbon dioxide systems through cylindrical samples filled with spheres of different diameters and thermal properties have been measured at the atmospheric pressure. The porosity of each medium has been determined by construction of a 3D image of the sample made with an X-ray tomograph device. Concentrations are determined by a continuous analysing the gas mixture composition in the bulbs with a katharometer device. A transient-state method for coupled evaluation of thermal diffusion and Fick coefficients in two bulbs system has been proposed. The determination of diffusion and thermal diffusion coefficients is done by comparing the temporal experimental results with an analytical solution modelling the mass transfer between two bulbs. The results are in good agreement with theoretical results and emphasize the porosity of the medium influence on both diffusion and thermal diffusion process. The results also showed that the effective thermal diffusion coefficients are independent from thermal conductivity ratio and particle-particle touching.

Déterminations Théorique et Expérimentale des Coefficients de Diffusion et de Thermodiffusion Effectifs en Milieu Poreux

Résumé en français

Les conséquences liées à la présence de gradients thermiques sur le transfert de matière en milieu poreux sont encore aujourd'hui mal appréhendées, essentiellement en raison de la complexité induite par la présence de phénomènes couplés (thermodiffusion ou effet Soret).

Le but de cette thèse est d'étudier et de comprendre l'influence que peut avoir un gradient thermique sur l'écoulement d'un mélange. L'objectif principal est de déterminer les coefficients effectifs modélisant les transferts de chaleur et de matière en milieux poreux, et en particulier le coefficient de thermodiffusion effectif. En utilisant la technique de changement d'échelle par prise de moyenne volumique nous avons développé un modèle macroscopique de dispersion incluant la thermodiffusion. Nous avons étudié en particulier l'influence du nombre de Péclet et de la conductivité thermique sur la thermodiffusion. Les résultats ont montré que pour de faibles nombres de Péclet, le nombre de Soret effectif en milieu poreux est le même que dans un milieu libre, et ne dépend pas du ratio de la conductivité thermique (solide/liquide). À l'inverse, en régime convectif, le nombre de Soret effectif diminue. Dans ce cas, un changement du ratio de conductivité changera le coefficient de thermodiffusion effectif. Les résultats théoriques ont montré également que, lors de la diffusion pure, même si la conductivité thermique effective dépend de la connectivité de la phase solide, le coefficient effectif de thermodiffusion est toujours constant et indépendant de la connectivité de la phase solide. Le modèle macroscopique obtenu par cette méthode est validé par comparaison avec des simulations numériques directes à l'échelle des pores. Un bon accord est observé entre les prédictions théoriques provenant de l'étude à l'échelle macroscopique et des simulations numériques au niveau de l'échelle de pores. Ceci démontre la validité du modèle théorique proposé. Pour vérifier et consolider ces résultats, un dispositif expérimental a été réalisé pour mesurer les coefficients de transfert en milieu libre et en milieu poreux. Dans cette partie, les nouveaux résultats expérimentaux sont obtenus avec un système du type « Two-Bulb apparatus ». La diffusion et la thermodiffusion des systèmes binaire hélium-azote et hélium-dioxyde de carbone, à travers des échantillons cylindriques remplis de billes de différents diamètres et

propriétés thermiques, sont ainsi mesurées à la pression atmosphérique. La porosité de chaque milieu a été déterminée par la construction d'une image 3D de l'échantillon par tomographie. Les concentrations sont déterminées par l'analyse en continu de la composition du mélange de gaz dans les ampoules à l'aide d'un catharomètre. La détermination des coefficients de diffusion et de thermodiffusion est réalisée par confrontation des relevés temporels des concentrations avec une solution analytique modélisant le transfert de matière entre deux ampoules.

Les résultats sont en accord avec les résultats théoriques. Cela permet de conforter l'influence de la porosité des milieux poreux sur les mécanismes de diffusion et de thermodiffusion. Ce travail ouvre ainsi la voie à une prise en compte de l'ensemble des mécanismes de diffusion dans l'établissement des modélisations numériques du transport en milieu poreux sous conditions non isothermes.



*Out beyond ideas of wrongdoing and rightdoing,
there is a field. I will meet you there.*

*When the soul lies down in that grass,
the world is too full to talk about
language, ideas,
even the phrase “each other”
doesn't make any sense.*

Rumi

*No amount of experimentation can ever prove me right;
a single experiment can prove me wrong.*

Einstein

*Ce n'est pas parce que les choses sont difficiles que nous n'osons pas,
c'est parce que nous n'osons pas qu'elles sont difficiles.*

Sénèque

Remerciements

Ma thèse, comme bien d'autres, a nécessité de nombreux efforts de motivation et de patience, et n'aurait pu aboutir sans la contribution et le soutien d'un grand nombre de personnes. Comment pourrais-je en effet remercier en seulement quelques mots les gens qui m'ont soutenu pendant ces trois années, tant leur aide et leur présence quotidienne ont été précieuses à mes yeux ?

Dans un premier temps, je tiens à remercier avec beaucoup de respect et de reconnaissance Michel Quintard, mon directeur de thèse et aussi le responsable du groupe GEMP qui m'a accueilli à l'IMFT de Toulouse. Je le remercie pour sa confiance en moi, ce qui m'a permis d'effectuer cette thèse et en même temps apprendre une langue et une culture très riche, que j'apprécie beaucoup. Sa rigueur, ainsi que ses qualités humaines tout au long de ces trois années auront très largement contribué à mener à bien ce travail. Je pense notamment aux nombreuses relectures de documents, mais également à l'aide très précieuse apportée lors des difficultés rencontrées durant cette période. Je souhaite ici dire particulièrement merci à Michel Quintard et à son épouse, Brigitte, pour m'avoir donné tellement d'amitié, en parallèle à un travail sérieux, d'avoir passé d'agréables moments, de bons repas français et pour le week-end spéléologique qui était un moment inoubliable. Rester dans la nature sauvage m'a permis de souffler et de me ressourcer afin de revenir à ma thèse avec le cerveau libéré et les idées plus claires.

Ensuite, je remercie très chaleureusement Manuel Marcoux, pour m'avoir encadré et guidé au quotidien avec une grande adresse. Je lui suis reconnaissant pour son esprit d'ouverture, son professionnalisme, sa pédagogie, sa disponibilité ainsi que ses qualités humaines. Ses yeux d'expert tant sur le plan théorique qu'expérimental ont apporté beaucoup à mes travaux de recherche. Merci Manuel pour les longues heures consacrées à vérifier et corriger ces nombreux articles, présentations, manuscrit de thèse, et pour ton aide et tes conseils en dehors du travail. Sincèrement, j'avais les meilleures encadrants qui peuvent exister !

Une partie de ma thèse a été financé par le projet ANR Fluxobat, je tiens donc à remercier une nouvelle fois Manuel Marcoux et Michel Quintard en tant que responsable scientifique de ce projet à l'IMFT et responsable du groupe GEMP, ainsi que Jacques Magnaudet, le directeur du laboratoire.

Je remercie l'attaché de coopération scientifique et technique de l'ambassade de France à Téhéran, Sixte Blanchy, pour m'avoir attribué une bourse du gouvernement français pendant un an. Je ne peux pas oublier de remercier chaleureusement Majid Kholghi mon professeur de Master pour son aide pendant la période des démarches administratives pendant l'inscription ; mais, malheureusement, les circonstances ne nous ont pas permis de travailler ensemble. Je voudrais remercier très chaleureusement le responsable des relations internationales de l'ENSEEIH, Majid Ahmadpanah, pour son

assistance précieuse. Je tiens à remercier Hadi Ghorbani, mon ancien collègue de l'université de Shahrood, qui m'a toujours supporté et encouragé.

Je remercie Azita Ahmadi qui m'a aidé et m'a supporté dans bien des situations difficiles, ainsi que pour le démarrage de la thèse.

J'adresse mes sincères remerciements à Ziad Saghir et Azita Ahmadi, qui ont accepté de rapporter sur ce travail. Je leur suis reconnaissant pour les remarques et commentaires éclairés qu'ils ont pu porter à la lecture de ce manuscrit.

Je remercie Kader Mojtabi qui m'a fait l'honneur de présider le jury de cette thèse. J'exprime mes profonds remerciements à Christelle Latrille et Piere Costesèque pour avoir accepté de juger ce travail. Je remercie tout particulièrement Kader Mojtabi et Piere Costesèque de l'IMFT pour les discussions constructives durant ma thèse sur le sujet de la thermodiffusion. Je remercie Helmut pour sa présence à ma soutenance qui m'a donné beaucoup d'énergie.

Je remercie Gérard Debenest, Rachid Ababou et Franck Plouraboué pour avoir suivi mon travail, leurs encouragements et leurs conseils constructifs.

J'ai aussi eu l'honneur de rencontrer Massoud Kaviany au cours d'une de ses visites à l'IMFT, je le remercie pour ses conseils généraux qui m'ont été utiles.

Merci à Juliette Chastanet, ancienne post-doc à l'IMFT, qui m'a beaucoup aidé à comprendre la théorie du changement d'échelle et qui a vérifié mes calculs numériques durant ma deuxième année de thèse.

Le travail rapporté dans ce manuscrit a été réalisé à l'Institut de Mécanique des Fluides de Toulouse, dans le Groupe d'Etude des Milieux Poreux. Je tiens donc à remercier la direction de l'IMFT, et Henri Boisson. Je remercie également tout le personnel de l'IMFT et en particulier Suzy Bernard, Yannick Exposito, Doris Barrau, Muriel Sabater, Sandrine Chupin, Hervé Ayroles. Je remercie Lionel Le Fur, le technicien du groupe pour son aide à la mise en place du dispositif expérimental.

Merci à David Bailly mon ami et collègue du bureau 210 pendant deux ans et quelques mois. Quand il n'y avait personne au laboratoire, bien tard, il y avait toujours David et ça m'a donné envie de rester et travailler. David, je n'oublierai jamais nos discussions sur différents sujets, durant les pauses. Les débats qui commencent par des sujets scientifiques et souvent se terminent par des sujets culturels, historiques ou *bien mystérieux*. Et je remercie sa « diptite » chérie, Emma Florens, futur docteur de l'IMFT, qui passait souvent pour nous voir.

Je remercie aussi mon amie et ma collègue de bureau, Marion Musielak, ancienne stagiaire et nouvelle doctorante très sérieuse. Je la remercie pour ses encouragements, son aide pour corriger mes lettres en français et pour sa gentillesse. Je lui souhaite bon courage pour sa thèse qui vient de démarrer.

Je remercie mes anciens collègues de bureau pendant presque un an: Laurent Risser, Pauline Assemat, Romain Guibert au bout du couloir, bureau 110, où j'ai commencé ma thèse.

Toute mon amitié à Yohan Davit (le grand chef), Stephanie Veran (Mme Tissoires spécialiste des mots fléchés), Alexandre (le Grand) Lapène, Florent Henon (avec ou sans sabre chinois), Vincent Sarrot (champion des chiffres et des lettres), Yunli Wang (championne de rallye), Clément Louriou (dominateur d'informatique et d'acquisition des données), les inséparables : Fabien Chauvet + Ian Billanou, Dominique Courret (passionné de poissons), Bilal Elhajar (champion de tennis), Arnaud Pujol (fameux ciné-man du groupe), Faiza Hidri, Solenn Cotel, Haishan Luo, Hassane Fatmi, Karine Spielmann (championne de ping pong), Mehdi Rebai, Damien Chenu. Je les remercie pour leur amitié et pour leur soutien moral, avec eux j'ai vécu des moments inoubliables plein d'amitié avec ambiance et humour à coté du travail. Je remercie aussi tous les responsables et les membres de la fameuse pause café du groupe. Merci à tous, sans eux cette aventure aurait sûrement été moins plaisante.

Souvent, parler dans sa langue maternelle ça aide à oublier la nostalgie du pays ; je remercie donc Hossein Fadaei et sa femme qui ont organisé quelques randonnées durant ces années.

Je suis très fier d'avoir appris la langue française, je remercie beaucoup mes professeurs de l'Alliance Française de Toulouse en particulier Sébastien Palusci et Lucie Pépin. Grâce à Lucie j'ai beaucoup avancé en communication orale, je l'en remercie beaucoup. Pendant cette période, à l'Alliance Française de Toulouse, j'ai trouvé des amis de tous les coins du monde. Ils sont très nombreux et gentils. Je remercie particulièrement Luciano Xavier, Isaac Suarez, Pavel Dub, Laia Moret Gabarro, Zaira Arellano, Fernando Maestre, Paula Margaretic, Azucena Castinera, Alan Llamas qui sont restés fidèles.

Au cours de l'été 2009 j'ai participé à une école d'été sur la modélisation des réservoirs pétroliers à l'université technique du Danemark (DTU) de Lyngby ; c'était un grand honneur pour moi de rencontrer Alexander Shapiro et ses collègues du département de génie chimique et biochimique. Je remercie également Osvaldo Chiavone, Negar Sadegh et Yok Pongthunya pour leur amitié pendant cette période.

Je remercie mes anciens amis et mes anciens collègues de l'université de Shahrood, je voulais leur dire que même si la distance nous sépare physiquement, l'esprit d'amitié est toujours resté entre nous et je ne vous oublierai jamais.

Enfin, je tiens à remercier du fond du coeur mes parents et ma famille pour les encouragements et le soutien qu'ils m'ont apporté tout au long du parcours qui m'a mené jusqu'ici.

« Be paian amad in daftar hekaiat hamchenan baghist !»

(Ce cahier se termine, mais l'histoire continue !)



Table of Contents

1. General Introduction	2
1.1 Industrial interest of Soret effect	4
1.2 Theoretical Direct numerical solution (DNS)	6
1.3 Theoretical upscaling methods	6
1.3.1 Multi-scale, hierarchical system	6
1.3.2 Upscaling tools for porous media	9
1.4 Experimental methods	10
1.4.1 Two-bulb method.....	10
1.4.2 The Thermogravitational Column.....	12
1.4.3 Thermal Field-Flow Fractionation (ThFFF)	13
1.4.4 Forced Rayleigh-Scattering Technique.....	13
1.4.5 The single-beam Z-scan or thermal lens technique	14
1.5 Concentration measurement	14
1.5.1 From the variation of thermal conductivity	15
1.5.2 From the variation of viscosity	16
1.5.3 Gas Chromatography (GC).....	16
1.5.4 Analysis by mass spectrometer.....	18
1.6 Conclusion	19
2. Theoretical predictions of the effective diffusion and thermal diffusion coefficients in porous media	21
2.1 Introduction.....	25
2.2 Governing microscopic equation.....	27
2.3 Volume averaging method.....	29
2.4 Darcy's law	31
2.4.1 Brinkman term	31
2.4.2 No-linear case	32
2.4.3 Low permeability correction.....	33

2.5	Transient conduction and convection heat transport	34
2.5.1	One equation local thermal equilibrium	36
2.5.2	Two equation model.....	48
2.5.3	Non-equilibrium one-equation model.....	49
2.6	Transient diffusion and convection mass transport.....	51
2.6.1	Local closure problem.....	53
2.6.2	Closed form.....	56
2.6.3	Non thermal equilibrium model.....	57
2.7	Results.....	59
2.7.1	Non-conductive solid-phase ($k_\sigma \approx 0$)	60
2.7.2	Conductive solid-phase ($k_\sigma \neq 0$).....	67
2.7.3	Solid-solid contact effect	71
2.8	Conclusion	76
3.	Microscopic simulation and validation.....	78
3.1	Microscopic geometry and boundary conditions	79
3.2	Non-conductive solid-phase ($k_\sigma \approx 0$).....	80
3.2.1	Pure diffusion ($Pe \approx 0, k_\sigma \approx 0$).....	80
3.2.2	Diffusion and convection ($Pe \neq 0, k_\sigma \approx 0$)	83
3.3	Conductive solid-phase ($k_\sigma \neq 0$)	85
3.3.1	Pure diffusion ($Pe \approx 0, k_\sigma \neq 0$)	85
3.3.2	Diffusion and convection ($Pe \neq 0, k_\sigma \neq 0$)	92
3.4	Conclusion	97
4.	A new experimental setup to determine the effective coefficients	99
4.1	Introduction.....	102
4.2	Experimental setup	103
4.2.1	Diffusion in a two-bulb cell	106
4.2.2	Two-bulb apparatus end correction	109

4.2.3	Thermal diffusion in a two-bulb cell	110
4.2.4	A transient-state method for thermal diffusion processes	111
4.3	Experimental setup for porous media.....	113
4.4	Results.....	113
4.4.1	Katharometer calibration.....	113
4.4.2	Diffusion coefficient	115
4.4.3	Effective diffusion coefficient in porous media.....	117
4.4.4	Free fluid and effective thermal diffusion coefficient	121
4.4.5	Effect of solid thermal conductivity on thermal diffusion.....	127
4.4.6	Effect of solid thermal connectivity on thermal diffusion.....	130
4.4.7	Effect of tortuosity on diffusion and thermal diffusion coefficients ...	132
4.5	Discussion and comparison with theory	134
4.6	Conclusion	137
5.	General conclusions and perspectives.....	139

List of tables

Table 1-1. Flux-force coupling between heat and mass	5
Table 2-1. Objectives of each order of momentum analysis	49
Table 4-1. Thermal conductivity and corresponding katharometer reading for some gases at atmospheric pressure and $T=300^{\circ}\text{K}$	105
Table 4-2. The properties of CO_2 , N_2 and He required to calculate k_{mix} ($T=300^{\circ}\text{C}$, $P=1$ atm.).....	115
Table 4-3. Molecular weight and Lennard-Jones parameters necessary to estimate diffusion coefficient	117
Table 4-4. Estimation of diffusion coefficients for binary gas mixtures He-CO_2 and He-N_2 at temperatures 300, 350 and $\bar{T} = 323.7^{\circ}\text{K}$, pressure 1 bar.....	117
Table 4-5. Measured diffusion coefficient for He-N_2 and different media	120
Table 4-6. Measured diffusion coefficient for He-CO_2 and different medium	121
Table 4-7. Measured thermal diffusion and diffusion coefficient for He-N_2 and for different media	124
Table 4-8. Measured diffusion coefficient and thermal diffusion coefficient for He-CO_2 and for different media	125
Table 4-9. Measured diffusion coefficient and thermal diffusion coefficient for He-N_2 and different media.....	127
Table 4-10. The solid (spheres) and fluid mixture physical properties ($T=300\text{ K}$)	128
Table 4-11. The solid (spheres) and fluid mixture physical properties ($T=300\text{ K}$)	131
Table 4-12. Porous medium tortuosity coefficients	133

List of figures

Fig. 1-1 Example of a multi-scale system	7
Fig. 1-2. A schematic diagram of the two-bulb apparatus used to determine the thermal diffusion factors for binary gas mixtures	11
Fig. 1-3. Principle of Thermogravitational Cell with a horizontal temperature gradient...	12
Fig. 1-4. Principle of Thermal Field-Flow Fractionation (ThFFF)	13
Fig. 1-5. Principle of forced Rayleigh scattering	14
Fig. 1-6. Diagram showing vertical section of the katharometer	15
Fig. 1-7. Schematics of a Gas Chromatograph Flame Ionization Detector (GC-FID).....	17
Fig. 1-8. Schematics of a Gas Chromatograph Electron Capture Detector (GC-ECD) ...	17
Fig. 1-9. Schematics of a simple mass spectrometer	18
Fig. 2-1. Problem configuration	28
Fig. 2-2. Normalized temperature versus position, for three different times (triangle, Direct Numerical Simulation= $\frac{\langle T_\beta \rangle^\beta - T_c}{T_H - T_c}$); circles, Direct Numerical Simulation = $\frac{\langle T_\sigma \rangle^\sigma - T_c}{T_H - T_c}$; solid line, Local-equilibrium model= $\frac{\langle T \rangle - T_c}{T_H - T_c}$)	44
Fig. 2-3. Normalized temperature versus position, for three different times (triangle, Direct Numerical Simulation= $\frac{\langle T_\beta \rangle^\beta - T_c}{T_H - T_c}$); circles, Direct Numerical Simulation = $\frac{\langle T_\sigma \rangle^\sigma - T_c}{T_H - T_c}$; solid line, Local-equilibrium model= $\frac{\langle T \rangle - T_c}{T_H - T_c}$)	46
Fig. 2-4. Chang's unit cell	55
Fig. 2-5. Spatially periodic arrangement of the phases	59
Fig. 2-6. Representative unit cell ($\varepsilon_\beta=0.8$)	60
Fig. 2-7. Effective diffusion, thermal diffusion and thermal conductivity coefficients at $Pe=0$	62
Fig. 2-8. Effective, longitudinal coefficients as a function of Péclet number ($k_\sigma \approx 0$ and $\varepsilon_\beta = 0.8$): (a) mass dispersion, (b) thermal dispersion, (c) thermal diffusion and (d) Soret number	65
Fig. 2-9. Comparison of closure variables $b_{s\beta} _x$ and $b_{T\beta} _x$ for $\varepsilon_\beta=0.8$	66
Fig. 2-10. The influence of conductivity ratio (κ) on (a) effective, longitudinal thermal conductivity and (b) effective thermal diffusion coefficients ($\varepsilon_\beta=0.8$)	68

Fig. 2-11. Comparison of closure variables fields $b_{T\beta}$ and $b_{S\beta}$ for different thermal conductivity ratio (κ) at pure diffusion ($Pe=0$ & $\varepsilon_\beta=0.8$)	69
Fig. 2-12. Comparison of closure variables fields $b_{T\beta} _x$ and $b_{S\beta} _x$ for different thermal conductivity ratio (κ) at convective regime ($Pe=14$ & $\varepsilon_\beta=0.8$)	70
Fig. 2-13. The influence of conductivity ratio (κ) on the effective coefficients by resolution of the closure problem in a Chang's unit cell ($\varepsilon_\beta=0.8$, $Pe=0$).....	71
Fig. 2-14. Spatially periodic model for solid-solid contact	72
Fig. 2-15. Effective thermal conductivity for (a) non-touching particles, $a/d=0$ (b) touching particles, $a/d=0.002$, ($\varepsilon_\beta=0.36$, $Pe=0$)	72
Fig. 2-16. Spatially periodic unit cell to solve the thermal diffusion closure problem with solid-solid connections $a/d=0.002$, ($\varepsilon_\beta=0.36$, $Pe=0$).....	73
Fig. 2-17. Effective thermal conductivity and thermal diffusion coefficient for touching particles, $a/d=0.002$, $\varepsilon_\beta=0.36$, $Pe=0$	74
Fig. 2-18. Comparison of closure variables fields $b_{T\beta}$ and $b_{S\beta}$ when the solid phase is continue, for different thermal conductivity ratio (κ) at pure diffusion.....	75
Fig. 2-19. Effective thermal conductivity and thermal diffusion coefficient for touching particles, $a/d=0.002$, $\varepsilon_\beta=0.36$	76
Fig. 3-1. Schematic of a spatially periodic porous medium (T_H : Hot Temperature and T_C : Cold Temperature).....	79
Fig. 3-2. Comparison between theoretical and numerical results at diffusive regime and $\kappa=0$, (a) time evolution of the concentration at $x = 15$ and (b and c) instantaneous temperature and concentration field	82
Fig. 3-3. Comparison between theoretical and numerical results, $\kappa=0$ and $Pe=1$, (a and b) instantaneous temperature and concentration field, (c) time evolution of the concentration at $x = 0.5, 7.5$ and 13.5	84
Fig. 3-4. Influence of the thermal conductivity ratio on the temperature and concentration fields	86
Fig. 3-5. (a) Temperature and (b) concentration profiles for different conductivity ratio	87
Fig. 3-6. Temporal evolution of the separation profiles for different thermal conductivity ratio.....	88
Fig. 3-7. Comparison between theoretical and numerical results at diffusive regime and $\kappa=10$, temporal evolution of (a) temperature and (b) concentration profiles	89

Fig. 3-8. Effect of thermal conductivity ratio at diffusive regime on (a and b) instantaneous temperature and concentration field at $t=10$ and (b) time evolution of the concentration at $x = 15$	91
Fig. 3-9. Comparison between theoretical and numerical results, $\kappa=10$ and $Pe=1$, (a) time evolution of the concentration at $x = 0.5, 7.5$ and 13.5 (b and c) instantaneous temperature and concentration field	93
Fig. 3-10. Influence of Péclet number on steady-state (a) temperature and (b) concentration profiles ($\kappa=10$)	94
Fig. 3-11. Influence of Péclet number on steady-state concentration at the exit ($\kappa=10$)....	95
Fig. 3-12. Influence of (a) separation factor and (b) conductivity ratio on pick point of the concentration profile.....	96
Fig. 4-1. Sketch of the two-bulb experimental set-up used for the diffusion and thermal diffusion tests.....	104
Fig. 4-2. Dimensions of the designed two-bulb apparatus used in this study	104
Fig. 4-3. Katharometer used in this study (CATARC MP – R)	105
Fig. 4-4. A schematic of katharometer connection to the bulb.....	106
Fig. 4-5. Two-bulb apparatus	106
Fig. 4-6. Katharometer calibration curve with related estimation of thermal conductivity values for the system $He-CO_2$	114
Fig. 4-7. Solute transport process in porous media	115
Fig. 4-8. Cylindrical samples filled with glass sphere.....	118
Fig. 4-9. X-ray tomography device (Skyscan 1174 type) used in this study.....	119
Fig. 4-10. Section images of the tube (inner diameter $d = 0.795$ cm) filled by different materials obtained by an X-ray tomography device (Skyscan 1174 type).....	119
Fig. 4-11. Composition-time history in two-bulb diffusion cell for $He-N_2$ system for different medium. ($T_c = 300K$ and $c_{ib}^0 = 100\%$).....	120
Fig. 4-12. Composition-time history in two-bulb diffusion cell for $He-CO_2$ system for different medium ($T = 300K$ and $c_{ib}^0 = 100\%$).....	121
Fig. 4-13. Schematic diagram of two bulb a) diffusion and b) thermal diffusion processes	122
Fig. 4-14. Composition-time history in two-bulb thermal diffusion cell for $He-N_2$ binary mixture for different media ($\Delta T = 50K$, $\bar{T} = 323.7K$ and $c_{ib}^0 = 50\%$)	124

Fig. 4-15. Composition-time history in two-bulb thermal diffusion cell for <i>He-CO₂</i> binary mixture for different media .($\Delta T = 50K$, $\bar{T} = 323.7K$ and $c_{1b}^0 = 50\%$)	125
Fig. 4-16. New experimental thermal diffusion setup without the valve between the two bulbs	126
Fig. 4-17. Composition-time history in two-bulb thermal diffusion cell for <i>He-N₂</i> binary mixture for different media ($\Delta T = 50K$, $\bar{T} = 323.7K$ and $c_{1b}^0 = 61.25\%$)	127
Fig. 4-18. Cylindrical samples filled with different materials (H: stainless steal, G: glass spheres and $\varepsilon=42.5$)	128
Fig. 4-19. Katharometer reading time history in two-bulb thermal diffusion cell for <i>He-CO₂</i> binary mixture for porous media having different thermal conductivity (3 samples of stainless steal and 3 samples of glass spheres) ($\Delta T = 50K$, $\bar{T} = 323.7K$ and $c_{1b}^0 = 50\%$).....	129
Fig. 4-20. Cylindrical samples filled with different materials (A: glass spheres, B: aluminium spheres and $\varepsilon=0.56$).....	130
Fig. 4-21. Katharometer time history in two-bulb thermal diffusion cell for <i>He-CO₂</i> binary mixture for porous media made of different thermal conductivity (aluminum and glass spheres) ($\Delta T = 50K$, $\bar{T} = 323.7K$ and $c_{1b}^0 = 50\%$)	131
Fig. 4-22. Definition of tortuosity coefficient in porous media, $L=$ straight line and $L'=$ real path length	132
Fig. 4-23. Cylindrical samples filled with different materials producing different tortuosity but the same porosity $\varepsilon=66\%$ (E: cylindrical material and F: glass wool).....	133
Fig. 4-24. Composition time history in two-bulb thermal diffusion cell for <i>He-CO₂</i> binary mixture in porous media made of the same porosity ($\varepsilon=66\%$) but different tortuosity (cylindrical materials and glass wool) ($\Delta T = 50K$, $\bar{T} = 323.7K$ and $c_{1b}^0 = 50\%$)	134
Fig. 4-25. Comparison of experimental effective diffusion coefficient data with the theoretical one obtained from volume averaging technique for different porosity and a specific unit cell.....	135
Fig. 4-26. Comparison of experimental effective thermal diffusion coefficient data with theoretical one obtained from volume averaging technique for different porosity and a specific unit cell.....	136
Fig. 4-27. Comparison of the experimental thermal diffusion ratio data with theoretical one obtained from volume averaging technique for different porosity and a specific unit cell	136

Fig. 5-1. 3D geometry of the closure problem with particle-particle touching made with COMSOL Multiphysics.....	141
Fig. 5-2. Discrepancy between numerical results and experimental measurements in a packed thermo- gravitational cell	142
Fig. 5-3. Proposition of experimental setup for convective regime	143

Chapter 1

General Introduction

1. General Introduction

The Ludwig-Soret effect, also known as thermal diffusion (or thermal diffusion and also thermo-migration), is a classic example of coupled heat and mass transport in which the motion of the particles in a fluid mixture is driven by a heat flux coming from a thermal gradient. Generally, heaviest particle moves from hot to cold, but the reverse is also seen under some conditions. The Soret effect has been studied for about 150 years with more active periods following economic interests (separation of isotopes in the 30s, petroleum engineering in the 90s ...). Many researchers have developed different techniques to measure this effect and deduced theories to explain it. However, because of the complexity of this coupled phenomenon, only recently, there has been an agreement on the values of the thermal diffusion coefficients measured by different techniques. Theoretically, there exists a rigorous approach based on the kinetic gas theory which explains the thermal diffusion effect for binary and multi-component ideal gas mixtures. For liquids, the theories developed are not enough accurate and there is still a lack of understanding on the basis of the effect for these mixtures. The situation becomes even more complicated when considering porous media. Fluid and flow problems in porous media have attracted the attention of industrialists, engineers and scientists from varying disciplines, such as chemical, environmental, and mechanical engineering, geothermal physics and food science. The main goal of the present thesis is to understand this complexity in porous media when there is a coupling between heat and mass transfer. The main objective is to study if the effective thermal diffusion depends on the following

- the void fraction of the phases and the structure of the solid matrix, i.e., the extent of the continuity of the solid phase,
- the thermal conductivity of each phase, i.e., the relative magnitude of thermal conductivity ratio,
- the contact between the no-consolidated particles, i.e., the solid surface coatings,
- the fluid velocity, i.e., dispersion and free convection in pore spaces.

The background and main goal of this thesis is presented in this chapter.

In chapter 2 we present a theoretical approach based on the volume averaging method to determine the effective transport coefficients in porous media. In this part, we are

interested in the upscaling of mass and energy coupled conservation equations of each component of the mixture.

Chapter 3 presents a validation of the proposed theory by comparing the predicted behavior to results obtained from a direct pore-scale simulation.

In chapter 4, coefficients of diffusion and thermal diffusion are measured directly using specially designed two-bulb method, and different synthetic porous media with different properties.

Finally, in chapter 5, conclusions and suggestions for future work are presented.

Introduction générale en français

L'effet de Ludwig-Soret, également connu sous le nom de thermal diffusion (ou thermomigration), est un exemple classique de phénomène couplé de transport de chaleur et matière dans lequel le mouvement molécules (ou des particules) dans un mélange fluide est produit par un flux de chaleur dérivant d'un gradient thermique. En général, la particule la plus lourde se dirige vers la région plus froide, mais l'inverse est également possible sous certaines conditions. L'effet Soret est étudié depuis près de 150 ans avec des périodes plus actives suivant les intérêts économiques (séparations d'isotopes dans les années 30, génie pétrolier dans les années 90 ...). Différentes techniques ont été mises aux points pour mesurer cet effet et développer les théories pour l'expliquer. Toutefois, en raison de la complexité de ce phénomène couplé, ce n'est que récemment qu'il y a eu un accord sur les valeurs des coefficients de thermal diffusion mesurées par des techniques différentes. Théoriquement, il existe une approche rigoureuse basée sur la théorie cinétique des gaz qui explique l'effet de thermal diffusion pour les mélanges binaires et multi-composants de gaz parfaits. Pour les liquides, les théories développées ne sont pas assez précises et il y a toujours un manque de compréhension sur les fondements de cet effet. La situation devient encore plus compliquée lorsque l'on considère cet effet en milieux poreux. Les problèmes d'écoulement de fluides multiconstituants en milieu poreux en présence de gradients thermiques ont attiré l'attention des industriels, des ingénieurs et des scientifiques de différentes disciplines, telles que la chimie, l'environnement, le génie mécanique, la physique géothermique et science des aliments. L'objectif principal de cette thèse est de comprendre cette complexité dans les milieux poreux lorsqu'il existe un couplage entre les

transferts de chaleur et de matière. L'objectif est d'étudier si la thermal diffusion effective dépend de :

- la fraction de vide dans le milieu (porosité) et la structure de la matrice solide, par exemple la continuité de la phase solide,
- la conductivité thermique de chaque phase, et en particulier la valeur du rapport des conductivités thermiques,
- le contact entre les particules non-consolidées, et la forme générale de la surface d'échange de la matrice solide,
- la vitesse du fluide, c'est à dire la dispersion et la convection naturelle dans les espaces du pore.

Le contexte et l'objectif principal de cette thèse sont présentés dans le chapitre 1.

En chapitre 2, nous présentons une approche théorique basée sur la méthode de prise de moyenne volumique afin de déterminer les coefficients de transport effectifs dans un milieu poreux. Dans cette partie, nous appliquons les techniques de changement d'échelle des équations couplées de conservations de la matière et de l'énergie.

Le chapitre 3 présente une validation de la théorie proposée en comparant les résultats théoriques avec les résultats obtenus par simulation directe d'échelle du pore.

En chapitre 4, les coefficients de diffusion et de thermal diffusion sont mesurés directement en utilisant un dispositif expérimental à deux bulbes, développé spécifiquement pour ce travail, et appliqué à différents milieux poreux modèles réalisés dans différentes gammes de propriétés thermo-physique.

Enfin, en chapitre 5, les conclusions et suggestions pour les travaux futurs sont présentées.

1.1 Industrial interest of Soret effect

In order to optimize production costs when extracting fluid field by producers, it is important to know precisely the distribution of different species in the field. This distribution has generally been generated over long formation period and separation has been mainly influenced by the gravity and the distribution of pressure in the reservoir. Considerable methods have been implemented in order to obtain reliable thermodynamic models, allow obtaining correctly the distribution of species in the reservoir. Since it is not

possible to ignore the important vertical extension of a given field, it is very possibly that this distribution is influenced by thermal diffusion and convection (gravity is one of the first components included in the models), but also by the geothermal gradient (natural temperature gradient of the earth).

This gradient could be the cause of migration of species in a phenomenon known as the Soret effect or thermal diffusion (more generally, the name thermal diffusion is used to describe this effect in a gas mixture; whereas Soret effect or Ludwig effect will be used in liquids). This is the creation of a concentration gradient of the chemical species by the presence of a thermal gradient, i.e., the existence of a thermal gradient is causing migration of species. This effect, discovered by C. Ludwig in 1856 [55] (and better exploited by C. Soret in 1880 [98]) is a particular phenomenon since it is associated to *coupled thermodynamic phenomena*, i.e. a flux created by a force of different nature (here a concentration gradient is induced by the presence of a thermal gradient), Table 1-1 summarizes the flux-force coupling effects between heat and mass transfer.

Table 1-1. Flux-force coupling between heat and mass

Flux\Force	∇T	∇c
Heat	Fourier's law of conduction	Dufour effect
Mass	Soret effect	Fick's law of diffusion

The study of these relations between flux and forces of this type is called Thermodynamics of Linear Irreversible Processes [38]. The main characteristic quantity for thermal diffusion is a coefficient called Soret coefficient (S_T). Many works have been undertaken to determine this quantity with different approaches: experimental approaches (Soret Coefficients in Crude Oil under microgravity condition [35, 100], thermo-gravitational column) or theoretical approaches (molecular dynamics simulations [89, 34], multi-component numerical models [91]). Most of these research concluded that values obtained experimentally are different from the theoretical one. These differences are mainly explained by the fact that the measurements are technically simpler in a free medium (without the porous matrix), and the effects due to pore-scale velocity fluctuations or to differences in thermal conductivity between rock and liquid are then not taken into account. Failures in the thermo-gravitational model based on the free fluid equations is a

good example of the need to determine a new model for the phenomena of diffusion and thermal diffusion in porous media. There are several theoretical and experimental methods available to determine the transport properties in porous media

1.2 Theoretical Direct numerical solution (DNS)

The direct numerical simulation of flows through porous formations is difficult due to the medium fine scale heterogeneity and also the complexity of dynamic systems. An accurate well-resolved computation often requires great amount of computer memory and CPU time, which can easily exceed the limit of today's computer resources.

Despite of this difficulty, the direct resolution of microscopic equation in porous media can be interesting for reasons of fundamental research, e.g., validation of macroscopic models (see for example [80] and [19]) as we have done in this study (Chapter 3). There are also many problems for which the upscaling processes are not possible or they are very difficult to achieve; therefore DNS can be used to resolve the problem in a simpler geometry problem on a volume containing a small number of pores.

In practice, it is often sufficient to predict the large scale solutions to certain accuracy. Therefore, alternative theoretical approaches have been developed.

1.3 Theoretical upscaling methods

The understanding and prediction of the behavior of the flow of multiphase or multicomponent fluids through porous media are often strongly influenced by heterogeneities, either large-scale lithological discontinuities or quite localized phenomena [29]. Considerable information can be gained about the physics of multiphase flow of fluids through porous media via laboratory experiments and pore-scale models; however, the length scales of these data are quite different from those required from field-scale simulations. The presence of heterogeneities in the medium also greatly complicates the flow. Therefore, we must understand the effects of heterogeneities and coefficients on different length scales.

1.3.1 Multi-scale, hierarchical system

Observation and modelling scales (Fig. 1-1) can be classified as

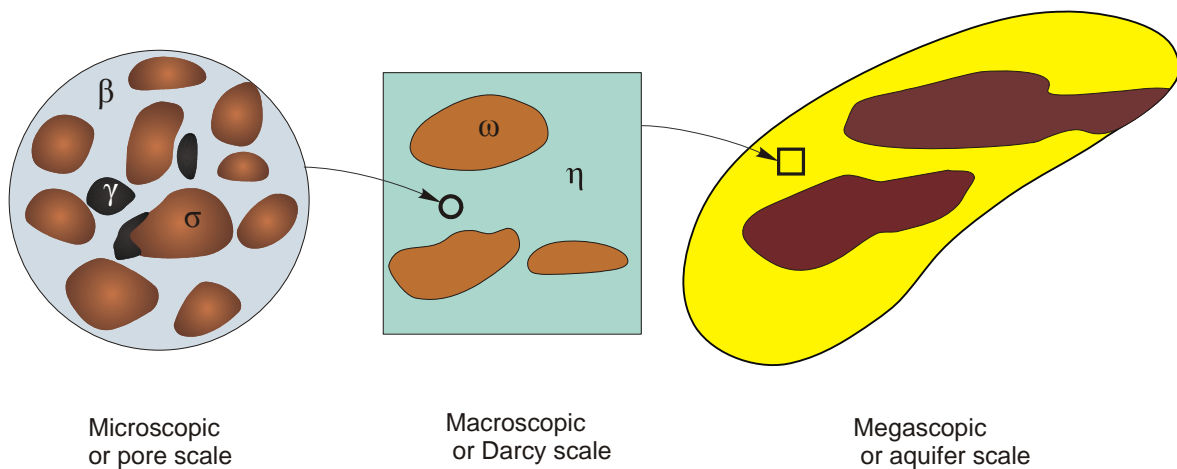
- microscopic scale or pore scale,
- macroscopic or Darcy scale, usually a few characteristic dimensions of the pore,

- mesoscopic or macroscopic scale heterogeneities of the porous medium, which correspond to variations in facies,
- megascopic scale or scale of the aquifer, reservoir, etc.

The physical description of the first two scales has been the subject of many studies. Taking into account the effect of heterogeneity, poses many problems often unresolved when level description in the model used is too large (e.g. a mesh numerical model too large compared to heterogeneities).

In a porous medium, the equations of continuum mechanics permit to describe the transport processes within the pores. For a large number of pores, the detailed description of microscopic processes is generally impractical. It is therefore necessary to move from a microscopic description at the pore scale to a macroscopic description throughout a certain volume of porous medium including a large number of pores.

In this section we describe briefly these different scales and their influences on the transport equations.



Microscopic scale: β =water phase, σ =solid phase, γ =organic phase.

Macroscopic scale: η and ω are porous media of different characteristics.

Megascopic scale: here the aquifer contains two mesoscopic heterogeneities.

Fig. 1-1 Example of a multi-scale system

I. Microscopic scale

The microscopic description focuses on the behavior of a large number of molecules of the present phases (e.g., organic phase and water phase shown in Fig. 1-1). The equations describing their transport are those of the continuum mechanics. The flow is well described by the following equations

- Mass balance equations for all components in the considered phase. In these equations may appear, in addition to the accumulation, convection and diffusion terms, chemical reaction terms known as homogeneous chemical reaction as they take place within this phase
- The Navier-Stokes equations describing the momentum balance
- The equation of heat transfer if there are temperature gradients in the system
- Boundary conditions on interfaces with other phases which depend upon the physics of the problem.

II. Macroscopic scale

The direct resolution of microscopic equations on a volume containing a small numbers of pores is usually possible and interesting for reasons of fundamental research (e.g. validation of macroscopic models). However, it is usually impossible to solve these microscopic equations on a large volume. In practice, it must be obtained a macroscopic description representing the effective behavior of the porous medium for a representative elementary volume (REV) containing many pores. Many techniques have been used to move from the pore scale to the REV scale [23]. Integration on the REV (called volume averaging technique) of the microscopic conservation equations allow obtaining macroscopic equations which are valid for average variables called macroscopic variables [7, 91].

In the case of a homogeneous porous medium, the REV size can be characterized by a sphere whose diameter is about 30 times the average grain diameter [7]. The problems associated with upscaling from the microscopic scale to the macroscopic scale will be treated in the next chapter.

At the macroscopic scale, the description of the flow of phases introduces new equations which are the transposition of the mass balance, momentum and energy microscopic equations. For example, the equation of Darcy is the momentum balance at the

macroscopic scale. In these macroscopic equations appear effective properties, as the permeability in Darcy's law, the relative permeabilities and capillary pressure in the multiphase case, etc. These effective properties can be theoretically deduced from microscopic properties by using upscaling techniques. They are most often estimated from measurements on a macroscopic scale. The direct measurement of these properties is not simple, because of heterogeneities of the medium.

III. Mesoscopic and Megascopic scale

The macroscopic properties are rarely the same at every point of the aquifer. Natural medium are in fact generally heterogeneous. It is sometimes possible to take into account the effect of these heterogeneities by solving the equations with a macroscopic mesh size smaller than the characteristic size of the heterogeneities. If this is not possible, the situation is similar to that already encountered in the transition between microscopic and macroscopic scales: it must be established a valid description at the mesoscopic or megascopic.

1.3.2 Upscaling tools for porous media

In the macroscopic description of mass and heat transfer in porous media, the convection-diffusion phenomena (or dispersion) are generally analyzed using an up-scaling method, in which the complicated local situation (transport by convection and diffusion at the pore scale) is finally described at the macroscopic scale by effective tensors [65]. To model transport phenomena in porous media, several methods exist. These tools are listed below

- integral transform methods,
- fractional approaches,
- homogenization,
- volume averaging technique
- central limit approaches,
- Taylor–Aris–Brenner (TAB) moment methods,
- spectral integral approaches,
- Fast Fourier transform (FFT) and Greens functions methods,
- mixture and hybrid averaging/mixture approaches,

- projection operator methods,
- stationary stochastic convective type approaches,
- and nonstationary stochastic convective type methods.

The reader can look at [23] for a brief description of different types of hierarchies and recommended tools which may be applied.

Among others, the method of moments [11], the volume averaging method [14] and the homogenization method [61] are the most used techniques. In this study, we shall use the volume averaging method to obtain the macro-scale equations that describe thermal diffusion in a homogeneous porous medium [23]. It has been extensively used to predict the effective transport properties for many processes including transport in heterogeneous porous media [83], two-phase flow [79], two-Phase inertial flow [53], reactive media [111, 1], solute transport with adsorption [2] multi-component mixtures [80].

1.4 Experimental methods

In this section, we present a review of different methods used for measuring the diffusion and thermal diffusion effect in gas. There is more than 150 years that the thermal diffusion effect was firstly observed by Ludwig. Along these years, researchers have designed a wide variety of setup for measuring this effect. Measuring thermal diffusion compared to diffusion and dispersion is not an easy task because this effect is usually very small and slow.

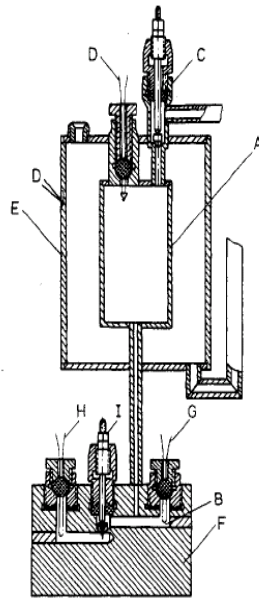
In this section, the goal is not to explain all existing methods, but to describe briefly the methods most commonly used.

1.4.1 Two-bulb method

The two-bulb technique is the most widely used method for determining the diffusion coefficients [114] and thermal diffusion [37] coefficients of gases. The basic arrangement for a two-bulb cell consists of two chambers of relatively large volume joined by a small-volume diffusion tube. Initially, the two chambers are filled with fluid mixtures of different composition at the same pressure which are allowed to approach a uniform composition by means of diffusion through the tube.

Experimental investigations of thermal diffusion have usually been based on the determination of the difference in composition of two parts of a fluid mixture which are at

different temperatures. A temperature gradient is set up in the tube by bringing the bulbs to different temperatures, uniform over each bulb. Provided the ratio of the bulbs volume is known, the separation can be found from the change in composition which occurs in one bulb only. A two-bulb apparatus used to determine the thermal diffusion coefficients is illustrated in Fig. 1-2. In this type of the two-bulb apparatus due to the large ratio in the volume of the two bulbs, almost all change in the gas mixture composition occurs in the lower bulb. In the literature, numerous measurements were made in free medium in 50s and 60s (see for instance some *series* of measurements which were done by Ibbs, 1921; Heath, 1941; van Itterbeek, 1947; Mason, 1962; Saxena, 1966; Humphreys, 1970; Grew, 1977; Shashkov, 1979 and Zhdanov, 1980).



A: top bulb; B: bottom bulb; C: gas inlet valve; D: thermocouple; E: metal jacket; F: metal block; G and H: thermistor elements and I: isolation valve

Fig. 1-2. A schematic diagram of the two-bulb apparatus used to determine the thermal diffusion factors for binary gas mixtures [95]

1.4.2 The Thermogravitational Column

Another method for measuring thermal diffusion coefficients is the thermogravitational column which consists of two vertical plates separated by a narrow space under a horizontal [54] or vertical [30] thermal gradient. The principle is to use a thermal gradient to simultaneously produce a mass flux by thermal diffusion and a convection flux. Starting from a mixture of homogeneous composition, the coupling of the two transport mechanisms leads to a separation of the components. In most experimental devices, the applied thermal gradient is horizontal and the final composition gradient is globally vertical. The separation rate in this system defined as the concentration difference between the top and the bottom cell. Thermogravitational column was devised by Clusius and Dickel (1938). The phenomenology of thermogravitational transport was exposed by Furry et al. (1939), and was validated by many experiments. The optimal coupling between thermal diffusion and convection ratio (maximum separation) correspond to an optimal thickness of the cell in free fluid (less than one millimetre for usual liquids) and an optimal permeability in porous medium [56, 57]. The so called packed thermal diffusion cell (PTC) was described and intensively used to perform experiments on varieties of ionic and organic mixtures [54, 21, 66]. The separation in a thermogravitational column can be substantially increased by inclining the column [72]. Recently, Mojtabi et al., 2003, showed that the vibrations can lead whether to increase or to decrease heat and mass transfers or delay or accelerate the onset of convection [18].

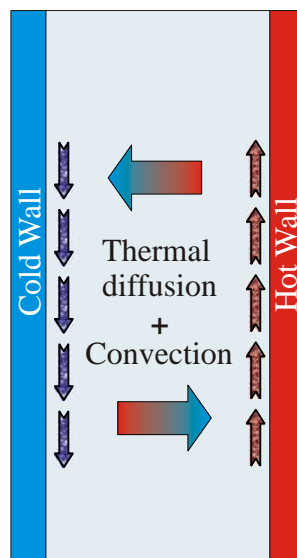


Fig. 1-3. Principle of Thermogravitational Cell with a horizontal temperature gradient

1.4.3 Thermal Field-Flow Fractionation (ThFFF)

Thermal field-flow fractionation (ThFFF) is a sub-technique of the FFF family that relies on a temperature gradient (create a thermal diffusion force) to characterize and separate polymers and particles. A schematic of the TFFF system is shown in Fig. 1-4. Separation of suspended particles is typically performed in a solvent carrier. Higher molecular weight particles react more to the thermal gradient and compact more tightly against the cold. Because of the parabolic velocity profile of the carrier, lower molecular weight will have a higher average velocity. The difference in average velocity results in the spatial and temporal separation along the ThFFF channel. The TFFF system possesses unique characteristics making it more suitable for some separations than conventional system [13]. Thermal Field-Flow Fractionation (Thermal FFF) is an excellent technique for measuring Soret coefficients particularly for dissolved polymers and suspended particles [96].

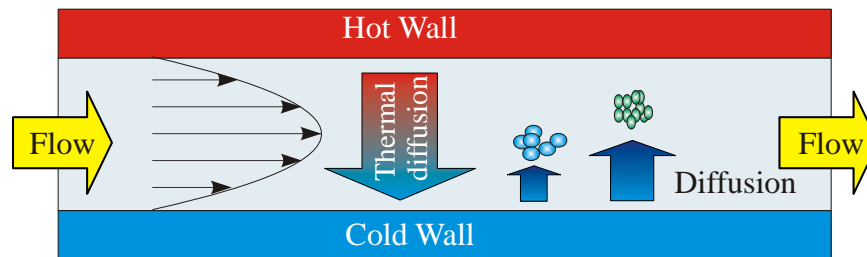


Fig. 1-4. Principle of Thermal Field-Flow Fractionation (ThFFF)

1.4.4 Forced Rayleigh-Scattering Technique

The principle of the forced Rayleigh scattering method is illustrated in Fig. 1-5. Two pulsed, high-power laser beams of equal wavelength and equal intensity intersect in an absorbing sample. They generate an optical interference fringe pattern whose intensity distribution is spatially sinusoidal. Following partial absorption of the laser light, this interference pattern induces a corresponding temperature grating, which in turn causes a concentration grating by the effect of thermal diffusion. Both gratings contribute to a combined refractive index grating that is read out by diffraction of a third laser beam. Analyzing the time dependent diffraction efficiency, three transport coefficients can be obtained (the thermal diffusivity, the translation diffusion coefficient D , and the thermal diffusion coefficient D_T). The ratio of the thermal diffusion coefficient and the translation diffusion coefficient allows the determination of the Soret coefficient S_T [113].

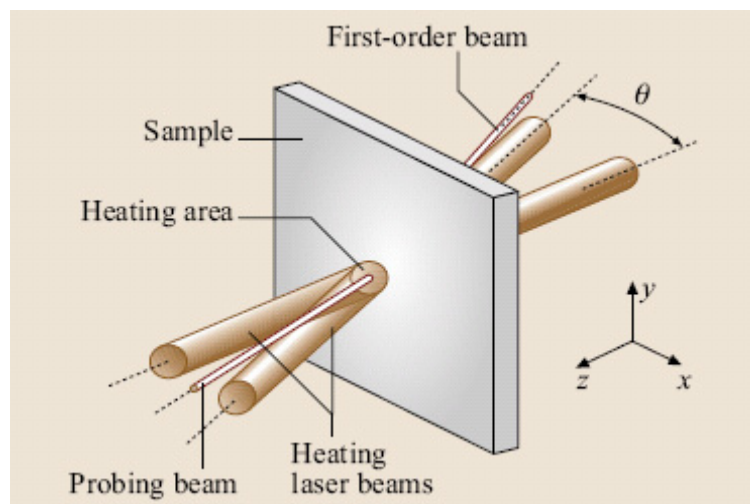


Fig. 1-5. Principle of forced Rayleigh scattering [99]

1.4.5 The single-beam Z-scan or thermal lens technique

The z-scan is a simple technique for determining the absorptive and refractive nonlinear optical properties of matter. In this type of technique a single laser beam is used for both heating and detecting. Any effect that creates variation of the refractive index can be studied with this setup. Giglio and Vendramini, 1974 [36] noticed that, when an intense narrow laser beam is reflected in a liquid, beside the thermal expansion, the Soret effect appears. This work showed the effect of the laser beam in binary mixtures compared to pure liquids. This technique for determination of the Soret coefficient is based on analysing the optical nonlinearities of the laser light.

1.5 Concentration measurement

A number of methods have been used for measuring the change in composition resulting from thermal diffusion or diffusion. In some early investigations the gas was analysed by chemical methods, but for many mixtures there are more rapid and convenient methods depending on the variation with composition of properties such as thermal conductivity, viscosity and optical refractivity. The development in recent years of *Gas Chromatography-Mass Spectrometry (GC-MS)* has enabled some progress to be made. In this section, we describe briefly these methods of measurement.

1.5.1 From the variation of thermal conductivity

An instrument was originally devised by Shakespear in 1915 (see [27]) and as the instrument was primarily intended to measure the *purity of the air*, the name "katharometer" was given to it. Katharometer [sometimes spelled "catherometer" and often referred to as the *thermal conductivity detector* (TCD) or the *hot-wire detector* (HWD)] was applied by Ibbs (1921) in his first experiments on thermal diffusion.

As we can see in Fig. 1-6, a typical kind of katharometer consists of a metal block in which one chamber is filled or purged with the gas mixture of unknown concentration and another one with a reference gas. Each chamber contains a platinum filament forming a branch of a Wheatstone bridge circuit and heated by the bridge current. The block serves as a heat sink at constant temperature. The katharometer concentration calibration is limited to a binary mixture. Therefore, this method is not appropriate in the case of more than two components.

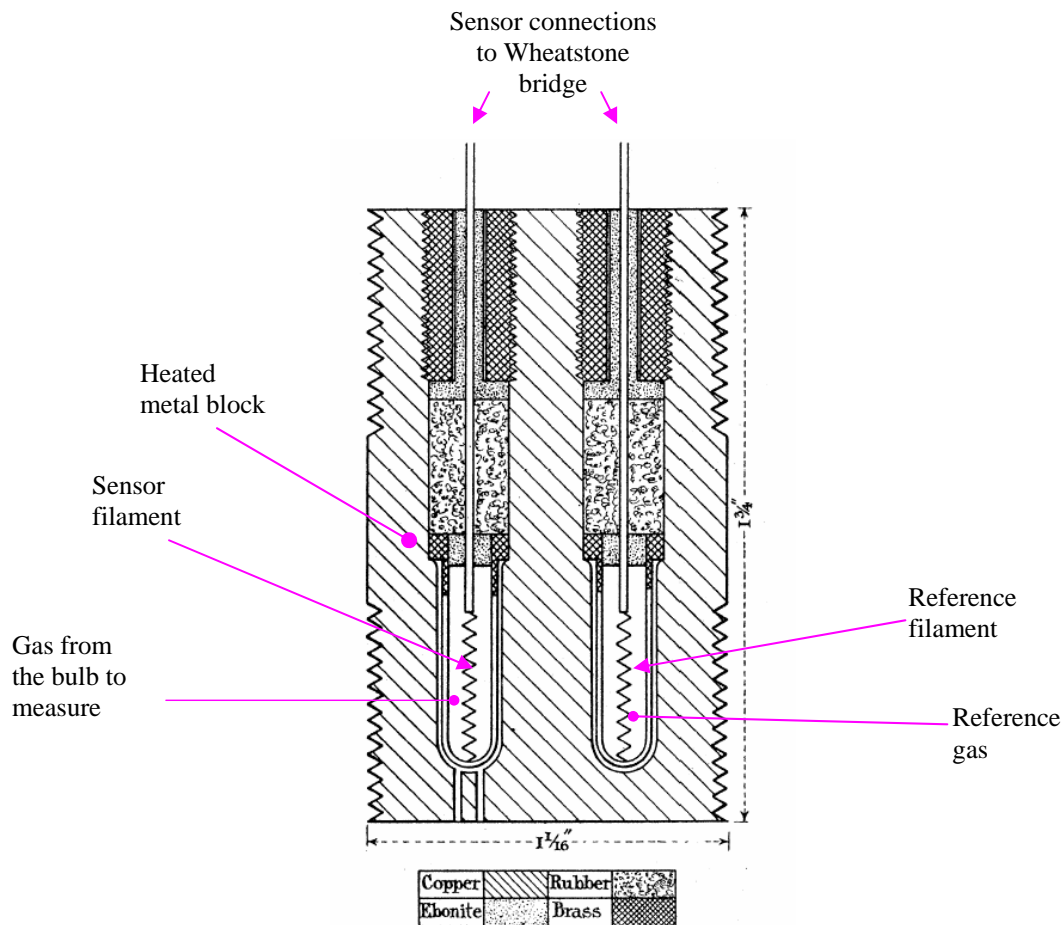


Fig. 1-6. Diagram showing vertical section of the katharometer [27]

Heat loss by radiation, convection, and leak through the supports is minimised in order to let the conduction through the gas be the dominant transfer mechanism of heat from the filament to the surroundings. Changes in gas composition in a chamber lead to temperature changes of the filament and thus to accompanying changes in resistance which are measured with the completed Wheatstone bridge. The heat lost from the filament will depend on both the thermal conductivity of the gas and its specific heat. Both these parameters will change in the presence of a different gas or solute vapor and as a result the temperature of the filament changes, causing a change in potential across the filament. This potential change is amplified and either fed to a suitable recorder or passed to an appropriate data acquisition system. As the detector filament is in thermal equilibrium with its surroundings and the device actually responds to the heat lost from the filament, the detector is extremely flow and pressure sensitive. Consequently, all katharometer detectors must be carefully thermostated and must be fitted with reference cells to help compensate for changes in pressure or flow rate. Usually, one of the spirals of the katharometer is sealed permanently in air and the resistance readings are the *reference readings*. Other filament is connected with the gas as *analyze reading*. The katharometer has the advantage that its open cell can form part of the diffusion cell, and so it can indicate continuously the changes in composition as diffusion and thermal diffusion proceeds without sampling.

1.5.2 From the variation of viscosity

Van Itterbeek and van Paemel (1938, 1940) ([101, 102], see also [50]) have developed a method of measurement based on the damping of an oscillating-disk viscometers. The oscillating disk itself is a part of the top bulb of the thermal diffusion cells. The change in the composition of the upper part due to thermal diffusion, changes the viscosity of the mixture and then corresponding change in composition is found from calibration curve. This method has a precision of the same as the conductivity detector.

1.5.3 Gas Chromatography (GC)

In a Gas Chromatograph the sample is injected into a heated inlet where it is vaporized, and then transferred into a chromatographic column. Different compounds are separated in the column, primarily through their physical interaction with the walls of the column. Once

separated, the compounds are fed into a detector. There are two types of the detector: Flame Ionization Detector (FID) and Electron Capture Detector (ECD). Schematic of a gas chromatograph flame ionization detector is illustrated in Fig. 1-7. As we can see in this figure, GC-FID uses a flame ionization detector for identification of compounds. The flame ionization detector responds to compounds that create ions when combusted in a hydrogen-air flame. These ions pass into a detector and are converted to an electrical signal. This method of analysis can be used for the detection of compounds such as ethanol, acetaldehyde, ethyl acetate, and higher alcohols.

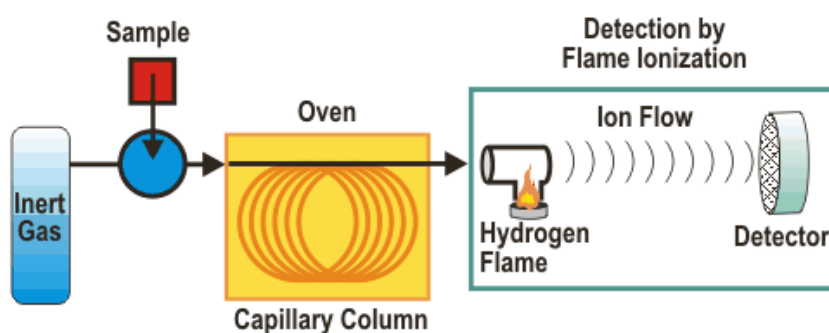


Fig. 1-7. Schematics of a Gas Chromatograph Flame Ionization Detector (GC-FID)

The ECD or electron capture detector (Fig. 1-8) measures electron capturing compounds (usually halogenated) by creating an electrical field in which molecules exiting a GC column can be detected by the drop in current in the field.

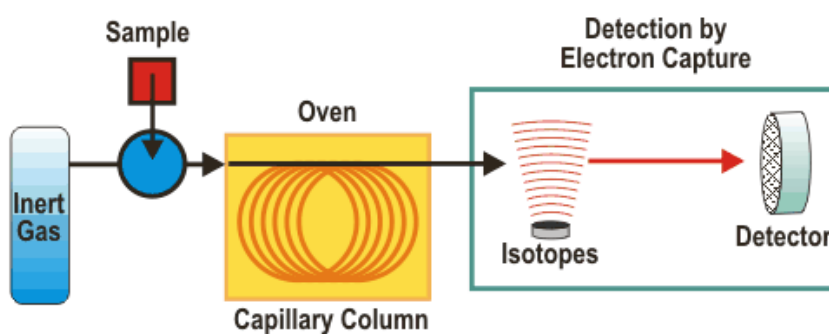


Fig. 1-8. Schematics of a Gas Chromatograph Electron Capture Detector (GC-ECD)

The ECD works by directing the gas phase output from the column across an electrical field applied across two electrodes, either using a constant DC potential or a pulsed potential. The electrical field is produced using a thermally stable ^{63}Ni source that ionizes

some of the carrier gas or auxiliary detector gas (usually nitrogen or a mixture of argon 95%, methane 5%) and produces a current between a biased pair of electrodes. The ECD is one of the most sensitive gas chromatography detectors available. The sensitivity of the ECD enables it to provide unmatched performance for extremely tough applications. It is the first choice for certain environmental chromatography applications due to its extreme sensitivity to halogenated compounds like PCBs (Polychlorinated biphenyls), organochlorine pesticides, herbicides, and halogenated hydrocarbons. The ECD is 10-1000 time more sensitive than the FID (Flame Ionization Detector), but has a limited dynamic range and finds its greatest application in analysis of halogenated compounds.

1.5.4 Analysis by mass spectrometer

Mass spectrometers are sensitive detectors of isotopes based on their masses. For the study of thermal diffusion in isotopic mixtures, a mass spectrometer is necessary. In the mass spectrometer the mixture is first ionized by passage through an electron beam as shown in Fig. 1-9; the ions are accelerated by an electric field and then passed through a slit system into a magnetic field by which they are deflected through an angle which depends on the mass and velocity. The final element of the mass spectrometer is the detector. The detector records either the charge induced or the current produced when an ion passes by or hits a surface. The combination of a mass spectrometer and a gas chromatograph makes a powerful tool for the detection of trace quantities of contaminants or toxins.

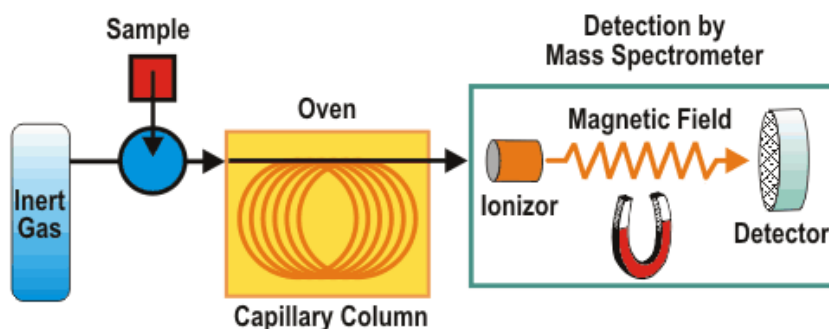


Fig. 1-9. Schematics of a simple mass spectrometer

1.6 Conclusion

From the discussion in section 1.3, it is clear that models of transport in porous media are related to scale description. The prediction and modelling of fluid flow processes in the subsurface is necessary e.g. for groundwater remediation or oil recovery. In most applications the fluid flow is determined by, in general, highly heterogeneous distribution of the soil properties. The conclusion of the detailed knowledge of the heterogeneous parameter distribution into a flow model is computationally not feasible. It is therefore an important task to develop upscaling methods to simplify the small-scale flow model while still including the impact of the heterogeneities as far as possible. In this study we have used the volume averaging technique to obtain the macro-scale properties of the porous media because this method has been proved to be suitable tool for modelling transport phenomena in heterogeneous porous media.

Different experimental techniques, which permit to measure the separation and therefore calculate the thermal diffusion coefficients, have been presented. It follows that, two-bulb method, among other methods, is a suitable method for this study since we can measure the both diffusion and thermal diffusion coefficients. It is easily adoptable to apply for a porous medium case. In this method thermal diffusion process does not disturb by the free convection which is negligible in this system.

Katharometer, despite its limitation to binary mixtures, is still most commonly used detector in many industries. Katharometer is simple in design and requires minimal electronic support and, as a consequence, is also relatively inexpensive compared with other detectors. Its open cell can form part of the diffusion cell, and so it can indicate continuously the changes in composition without sampling. This is why that in this study, we have used a conductivity detector method with katharometer to analyze the separation process in a two-bulb method.

Chapter 2

Theoretical Predictions of the Effective Diffusion and Thermal diffusion Coefficients in Porous Media

2. Theoretical predictions of the effective diffusion and thermal diffusion coefficients in porous media

This chapter presents the theoretical determination of the effective Darcy-scale coefficients for heat and mass transfer in porous media, including the thermal diffusion effect, using a volume averaging technique. The closure problems related to the pore-scale physics are solved over periodic unit cells representative of the porous structure.

Nomenclature of Chapter 2

a_v	$A_{\beta\sigma}/\mathcal{V}$, interfacial area per unit volume, m^{-1}	p_β	Pressure in the β -phase, Pa
A_0	Specific surface area, m^{-1}	$\langle p_\beta \rangle^\beta$	Intrinsic average pressure in the β -phase, Pa
$\mathcal{A}_{\beta\sigma}$	Area of the β - σ interface contained within the macroscopic region, m^2	\mathbf{r}	Position vector, m
$\mathcal{A}_{\beta e}$	Area of the entrances and exits of the β - σ phase associated with the macroscopic system, m^2	r_β	Scalar field that maps $(\langle T_\beta \rangle^\beta - \langle T_\sigma \rangle^\sigma)$ onto \tilde{c}_β
$A_{\beta\sigma}$	Area of the β - σ interface within the averaging volume, m^2	Sc	Schmidt number
b_i	Gas slip factor	S_T	Soret number, 1/K
$\mathbf{b}_{C\beta}$	Mapping vector field for \tilde{c}_β , m	s_β	Scalar field that maps $(\langle T_\beta \rangle^\beta - \langle T_\sigma \rangle^\sigma)$ onto \tilde{T}_β
$\mathbf{b}_{S\beta}$	Mapping vector field for \tilde{c}_β , m	s_σ	Scalar field that maps $(\langle T_\beta \rangle^\beta - \langle T_\sigma \rangle^\sigma)$ onto \tilde{T}_σ
$\mathbf{b}_{S\beta} _x$	x -coordinate coefficient of $\mathbf{b}_{S\beta}$	\mathbf{S}_T^*	Effective Soret number, 1/K
$\mathbf{b}_{S\beta\beta}$	Vector field that maps $\nabla \langle T_\beta \rangle^\beta$ onto \tilde{c}_β , m	$\mathbf{S}_T^* _{xx}$	Longitudinal Soret number, 1/K
$\mathbf{b}_{S\beta\sigma}$	Vector field that maps $\nabla \langle T_\sigma \rangle^\sigma$ onto \tilde{c}_β , m	t	Time, s
$\mathbf{b}_{T\beta}$	Mapping vector field for \tilde{T}_β , m	t^*	Characteristic process time, s
$\mathbf{b}_{T\beta} _x$	x -coordinate coefficient of $\mathbf{b}_{T\beta}$	T_β	Temperature of the β -phase, K

$\mathbf{b}_{T\beta\beta}$	Vector field that maps $\nabla\langle T_\beta \rangle^\beta$ onto \tilde{T}_β, m	$\langle T_\beta \rangle^\beta$	Intrinsic average temperature in the β -phase, K
$\mathbf{b}_{T\beta\sigma}$	Vector field that maps $\nabla\langle T_\sigma \rangle^\sigma$ onto \tilde{T}_β, m	\tilde{T}_β	Spatial deviation temperature, K
$\mathbf{b}_{T\sigma\beta}$	Vector field that maps $\nabla\langle T_\beta \rangle^\beta$ onto \tilde{T}_σ, m	$\mathbf{u}_{c\beta}$	One-equation model mass transport coefficient associated with $\nabla(\langle T_\beta \rangle^\beta - \langle T_\sigma \rangle^\sigma)$ in the β -phase equation
$\mathbf{b}_{T\sigma\sigma}$	Vector field that maps $\nabla\langle T_\sigma \rangle^\sigma$ onto \tilde{T}_σ, m	$\mathbf{u}_{\beta\beta}$	Two-equation model heat transport coefficient associated with $\nabla\langle T_\beta \rangle^\beta$ in the β -phase equation
c_p	Constant pressure heat capacity, J.kg/K	$\mathbf{u}_{\beta\sigma}$	Two-equation model heat transport coefficient associated with $\nabla\langle T_\sigma \rangle^\sigma$ in the β -phase equation
c_β	Total mass fraction in the β -phase	$\mathbf{u}_{\sigma\beta}$	Two-equation model heat transport coefficient associated with $\nabla\langle T_\beta \rangle^\beta$ in the σ -phase equation
$\langle c_\beta \rangle^\beta$	Intrinsic average mass fraction in the β -phase	$\mathbf{u}_{\sigma\sigma}$	Two-equation model heat transport coefficient associated with $\nabla\langle T_\sigma \rangle^\sigma$ in the σ -phase equation
\tilde{c}_β	Spatial deviation mass fraction in the β -phase	\bar{p}	Mean pressure, Pa
D_β	Binary diffusion coefficient, m^2/s	$p_{c\beta}$	Capillary pressure, Pa
$D_{T\beta}$	Thermal diffusion coefficient, $m^2/s.K$	Pe	Cell Péclet number
$\mathbf{D}_{T\beta}^*$	Total thermal diffusion tensor, $m^2/s.K$	Pr	Prandtl number
$D_{T\beta}^* _{xx}$	Longitudinal thermal diffusion coefficient, $m^2/s.K$	r_0	Radius of the averaging volume, m
$\mathbf{D}_{T\beta\beta}^*$	Effective thermal diffusion tensor associated with $\nabla\langle T_\beta \rangle^\beta$ in the β -phase	\mathbf{v}_β	Mass average velocity in the β -phase, m/s
$\mathbf{D}_{T\beta\sigma}^*$	Effective thermal diffusion tensor associated with $\nabla\langle T_\sigma \rangle^\sigma$ in the β -phase	$\langle \mathbf{v}_\beta \rangle^\beta$	Intrinsic average mass average velocity in the β -phase, m/s
\mathbf{D}_β^*	Total dispersion tensor, m^2/s	$\tilde{\mathbf{v}}_\beta$	Spatial deviation mass average velocity, m/s
$D_\beta^* _{xx}$	Longitudinal dispersion coefficient, m^2/s	V_β	Volume of the β -phase contained within the averaging volume, m^3
\mathbf{F}	Forchheimer correction tensor	\mathcal{V}	Local averaging volume, m^3

g	Gravitational acceleration, m ² /s	x, y	Cartesian coordinates, m
h	Film heat transfer coefficient, $J/m.s.K$	z	Elevation in the gravitational field, m
I	Unit tensor	<i>Greek symbols</i>	
k_a	Apparent gas permeability, m ²	β_F	A factor experimentally deduced
$k_{r\beta}$	Relative permeability	ε_β	Volume fraction of the β -phase or porosity
k_β	Thermal conductivity of the fluid phase, W/m.K	κ	k_σ/k_β , conductivity ratio
k_σ	Thermal conductivity of the solid phase, W/m.K	λ	Mean free path of gas, μm
K_{β}	Permeability tensor, m ²	μ_β	Dynamic viscosity for the β -phase, Pa.s
k_{$\beta\beta$}	Two-equation model effective thermal conductivity tensor associated with $\nabla\langle T_\beta \rangle^\beta$ in the β -phase equation	$\tilde{\mu}_\beta$	Effective viscosity, Pas.s
k_{$\beta\sigma$}	Two-equation model effective thermal conductivity tensor associated with $\nabla\langle T_\sigma \rangle^\sigma$ in the σ -phase equation	ν_β	Kinematic viscosity for the β -phase, m ² /s
k_{$\sigma\beta$}	Two-equation model effective thermal conductivity tensor associated with $\nabla\langle T_\beta \rangle^\beta$ in the σ -phase equation	ρ_β	Total mass density in the β -phase, kg/m ³
k_{$\sigma\sigma$}	Two-equation model effective thermal conductivity tensor associated with $\nabla\langle T_\sigma \rangle^\sigma$ in the σ -phase equation	τ	Scalar tortuosity factor
k_{β} [*] , k [*]	Total thermal conductivity tensors for no-conductive and conductive solid phase, W/m.K	φ	Arbitrary function
k_{β} [*] _{$_{xx}$}	Longitudinal thermal dispersion coefficient, W/m.K	ψ	Separation factor or dimensionless Soret number
k_∞	Klinkenberg permeability, W/m.K	<i>Subscripts, superscripts and other symbols</i>	
k_∞^*	Asymptotic thermal dispersion coefficient, W/m.K	<i>ref</i>	Refers to the reference gas
ℓ	Characteristic length associated with the microscopic scale, m	β	Fluid-phase
ℓ_{UC}	Characteristic length scale associated with a unit cell, m	σ	Solid-phase
ℓ_β	Characteristic length for the β -phase, m	$\beta\sigma$	β - σ interphase
L	Characteristic length for macroscopic quantities, m	βe	Fluid-phase entrances and exits
L_ε	Characteristic length for $\nabla\varepsilon$, m	*	Effective quantity

M	Gas molecular weight, g/mol	$\langle \rangle$	Spatial average
$\mathbf{n}_{\beta\sigma}$	Unit normal vector directed from the β -phase toward the σ -phase	$\langle \rangle^\beta$	Intrinsic β -phase average

2.1 Introduction

It is well established, see for instance [39], that a multicomponent system under nonisothermal condition is subject to mass transfer related to coupled-transport phenomena. This has strong practical importance in many situations since the flow dynamics and convective patterns in mixtures are more complex than those of one-component fluids due to the interplay between advection and mixing, solute diffusion, and the Soret effect (or thermal diffusion) [112]. The Soret coefficient may be positive or negative depending on the direction of migration of the reference component (to the cold or to the hot region).

There are many important processes in nature and technology where thermal diffusion plays a crucial role. Thermal diffusion has various technical applications, such as isotope separation in liquid and gaseous mixtures [86, 87], polymer solutions and colloidal dispersions [112], study of compositional variation in hydrocarbon reservoirs [32], coating of metallic items, etc. It also affects component separation in oil wells, solidifying metallic alloys, volcanic lava, and in the Earth Mantle [45].

Platten and Costesèque (2004) searched the response to the basic question: "is the Soret coefficient the same in a free fluid and in a porous medium?" They measured separately four coefficients: isothermal diffusion and thermal diffusion coefficients, both in free fluid and porous media. They measured the diffusion coefficient in free fluid by the open-ended-capillary (OEC) technique, and then they generalized the same OEC technique to porous media. The thermal diffusion coefficient in the free system has also been measured by the thermogravitational column technique [73]. The thermal diffusion coefficient of the same mixture was determined in a porous medium by the same technique, except that they filled the gap between two concentric cylinders with zirconia spheres. In spite of the small errors that they had on the Soret coefficient due to measuring independently diffusion and thermal diffusion coefficient they announced that the Soret coefficient is the same in a free fluid and in porous medium [74]. The experimental study of Costesèque et al. (2004) for a horizontal Soret-type thermal diffusion cell, filled first with the free liquid and next with a porous medium showed also that the results are not significantly different [20].

Saghir et al. (2005) have reviewed some aspects of thermal diffusion in porous media; including the theory and the numerical procedure which have been developed to simulate these phenomena [91]. In many other works on thermal diffusion in a square porous cavity,

the thermal diffusion coefficient in free fluid almost has been used instead of an effective coefficient containing the tortuosity and dispersion effect. Therefore, there are many discrepancies between the predictions and measurements separation.

The effect of dispersion on effective diffusion is now well established (see for example Saffman (1959), Bear (1972), ...) but this effect on thermal diffusion has received limited attention. Fargue et al. (1998) searched the dependence of the effective thermal diffusion coefficient on flow velocity in a porous packed thermogravitational column. They showed that the effective thermal diffusion coefficient in thermogravitational column filled with porous media includes a dependency upon the fluid velocity. Their results showed that the behaviour of the effective thermal diffusion coefficient looks very similar to the effective diffusion coefficient in porous media [31].

The numerical model of Nasrabadi and Firoozabadi (2006) in a packed thermogravitational column was not able to reveal a dispersion effect on the thermal diffusion process, perhaps mainly due to low velocities [66].

In this chapter, we have used the volume averaging method which has been extensively used to predict the effective isothermal transport properties in porous media. The considered media can also be subjected to thermal gradients coming from natural origin (geothermal gradients, intrusions,...) or from anthropic anomalies (waste storages,...). Thermal diffusion has rarely been taken completely under consideration, in most description, coupled effects being generally forgotten or neglected. However, the presence of temperature gradient in the medium can generate a mass flux.

For modelling mass transfer by thermal diffusion, the effective thermal conductivity must be first determined. Different models have been investigated for two-phase heat transfer systems depending on the validity of the local thermal equilibrium assumption. When one accepts this assumption, macroscopic heat transfer can be described correctly by a classical one-equation model [47, 82, 79, 84]. The reader can look at [3] for the possible impact of non-equilibrium on various flow conditions. For many initial boundary-value problems, the two-equation model shows an asymptotic behaviour that can be modelled with a “non equilibrium” one-equation model [115, 116]. The resulting thermal dispersion tensor is greater than the one-equation local-equilibrium dispersion tensor. It can also be obtained through a special closure problem as shown in [64]. These models can also be extended to more complex situations like two-phase flow [65], reactive transport [77, 85, 93].

However, for all these models many coupling phenomena have been discarded in the upscaling analysis. This is particularly the case for the possible coupling with the transport of constituents in the case of mixtures.

A model for Soret effect in porous media has been determined by Lacabanne et al (2002), they presented a homogenization technique for determining the macroscopic Soret number in porous media. They assumed a periodic porous medium with the periodical repetition of an elementary cell. In this model, the effective thermal diffusion and isothermal diffusion coefficient are calculated by only one closure problem while, in this study, two closure problems have to be solved separately to obtain effective isothermal and thermal diffusion coefficients. They have also studied the local coupling between velocity and Soret effect in a tube with a thermal gradient. The results of this model showed that when convection is coupled with Soret effect, diffusion removes the negative part of the separation profile [51]. However, they calculated the effective coefficients for a purely diffusive regime for which one cannot observe the effect of force convection and conductivity ratio as explained later in this study. In addition, these results have not been validated with experimental results or a direct pore-scale numerical approach.

In this chapter, effective properties will be calculated for a simple unit-cell but for various physical parameters, in particular the Péclet number and the thermal conductivity ratio.

2.2 Governing microscopic equation

We consider in this study a binary mixture fluid flowing through a porous medium subjected to a thermal gradient. This system is illustrated in Fig. 2-1, the fluid phase is identified as the β -phase while the rigid and impermeable solid is represented by the σ -phase.

From the thermodynamics of irreversible processes as originally formulated by Onsager (1931) the diagonal effects that describe heat and mass transfer are Fourier's law which relates heat flow to the temperature gradient and Fick's law which relates mass flow to the concentration gradient. There are also cross effects or coupled-processes: the Dufour effect quantifies the heat flux caused by the concentration gradient and the Soret effect, the mass flux caused by the temperature gradient.

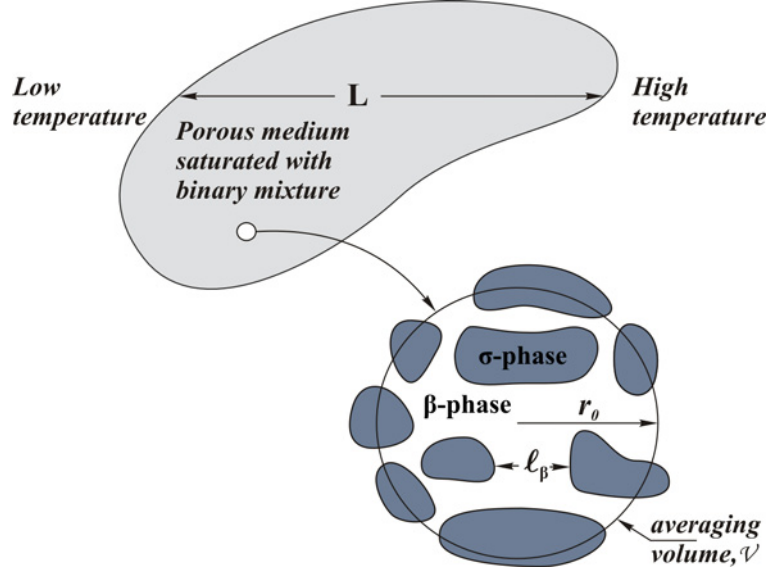


Fig. 2-1. Problem configuration

In this study, we neglect the Dufour effect, which is justified in liquids [75] but in gaseous mixtures the Dufour coupling may become more and more important and can change the stability behaviour of the mixture in a Rayleigh-Bénard problem in comparison to liquid mixtures [43].

Therefore, the transport of energy at the pore level is described by the following equations and boundary conditions for the fluid (β -phase) and solid (σ -phase)

$$(\rho c_p)_\beta \frac{\partial T_\beta}{\partial t} + (\rho c_p)_\beta \nabla \cdot (T_\beta \mathbf{v}_\beta) = \nabla \cdot (k_\beta \nabla T_\beta), \text{ in the } \beta\text{-phase} \quad (2-1)$$

$$\text{BC1: } T_\beta = T_\sigma, \text{ at } \mathcal{A}_{\beta\sigma} \quad (2-2)$$

$$\text{BC2: } \mathbf{n}_{\beta\sigma} \cdot (k_\beta \nabla T_\beta) = \mathbf{n}_{\beta\sigma} \cdot (k_\sigma \nabla T_\sigma), \text{ at } \mathcal{A}_{\beta\sigma} \quad (2-3)$$

$$(\rho c_p)_\sigma \frac{\partial T_\sigma}{\partial t} = \nabla \cdot (k_\sigma \nabla T_\sigma), \text{ in the } \sigma\text{-phase} \quad (2-4)$$

where $\mathcal{A}_{\beta\sigma}$ is the area of the β - σ interface contained within the macroscopic region.

We assume in this work that the physical properties of the fluid and solid are constant. Then the component pore-scale mass conservation is described by the following equation and boundary conditions for the fluid phase [9]

$$\frac{\partial c_\beta}{\partial t} + \nabla \cdot (c_\beta \mathbf{v}_\beta) = \nabla \cdot (D_\beta \nabla c_\beta + D_{T\beta} \nabla T_\beta), \text{ in the } \beta\text{-phase} \quad (2-5)$$

At the fluid-solid interfaces there is no transport of solute so that the mass flux (the sum of diffusion and thermal diffusion flux) is zero

$$\text{BC1: } \mathbf{n}_{\beta\sigma} \cdot (D_{\beta} \nabla c_{\beta} + D_{T\beta} \nabla T_{\beta}) = 0, \text{ at } \mathcal{A}_{\beta\sigma} \quad (2-6)$$

where c_{β} is the mass fraction of one component in the β -phase, D_{β} and $D_{T\beta}$ are the molecular isothermal diffusion coefficient and thermal diffusion coefficient. $\mathbf{n}_{\beta\sigma}$ is unit normal from the liquid to the solid phase. We neglect any accumulation and reaction of solute at the fluid-solid interface as well as the phenomenon of surface diffusion.

To describe completely the problem, the equations of continuity and motion have to be introduced for the fluid phase. We use Stokes equation for the flow motion at the pore-scale, assuming classically negligible inertia effects, also named creeping flow. This is a type of fluid flow where advective inertial forces are small compared to viscous forces (the Reynolds number is low, i.e. $Re \ll 1$). This is a typical situation in flows where the fluid velocities are very slow, the viscosities are very large, or the length-scales of the flow are very small. The Stokes equation, the continuity equation, and the no-slip boundary condition are then written as

$$\nabla \cdot \mathbf{v}_{\beta} = 0, \text{ in the } \beta\text{-phase} \quad (2-7)$$

$$0 = -\nabla p + \mu_{\beta} \nabla \cdot (\nabla \mathbf{v}_{\beta}) + \rho_{\beta} \mathbf{g}, \text{ in the } \beta\text{-phase} \quad (2-8)$$

$$\text{BC1: } \mathbf{n}_{\beta\sigma} \cdot \mathbf{v}_{\beta} = 0, \text{ at } \mathcal{A}_{\beta\sigma} \quad (2-9)$$

In this problem, we also consider the flow of the β -phase to be steady, incompressible, and laminar. It is assumed that the solid phase is rigid and impervious to solute diffusion and the thermal and solutal expansions have been neglected.

2.3 Volume averaging method

Because the direct solution of the convection-diffusion equation is in general impossible due to the complex geometry of the porous medium, equations describing average concentrations and velocities must be developed [109]. The associated averaging volume, \mathcal{V} is shown in Fig. 2-1. The development of local volume averaged equations requires that we define two types of averages in terms of the averaging volume [111]. For any quantity ψ_{β} associated with the β -phase, the superficial average is defined according to

$$\langle \varphi_\beta \rangle = \frac{1}{\mathcal{V}} \int_{V_\beta} \varphi_\beta dV \quad (2-10)$$

while the second average is the intrinsic average defined by

$$\langle \varphi_\beta \rangle^\beta = \frac{1}{V_\beta} \int_{V_\beta} \varphi_\beta dV \quad (2-11)$$

Here we have used V_β to represent the volume of the β -phase contained within the averaging volume. These two averages are related by

$$\langle \varphi_\beta \rangle = \varepsilon_\beta \langle \varphi_\beta \rangle^\beta \quad (2-12)$$

in which ε_β is the volume fraction of the β -phase or porosity in the one phase flow case.

The phase or superficial averages are volume fraction dependent. From the diagram in Fig. 2-1 we can see that the sum of volume fractions of the two phases satisfies

$$\varepsilon_\beta + \varepsilon_\sigma = 1 \quad (2-13)$$

In order to carry out the necessary averaging procedures to derive governing differential equations for the intrinsic average fields, we need to make use of the spatial averaging theorem, written here for any general scalar quantity φ_β associated with the β -phase

$$\langle \nabla \varphi_\beta \rangle = \nabla \langle \varphi_\beta \rangle + \frac{1}{\mathcal{V}} \int_{A_{\beta\sigma}} \mathbf{n}_{\beta\sigma} \varphi_\beta dA \quad (2-14)$$

A similar equation may be written for any fluid property associated with the β -phase. Note that the area integral in equation (2-14) involves unit normal from the β -phase to the σ - phase. In writing corresponding equation for the σ -phase, we realize that $\mathbf{n}_{\beta\sigma} = -\mathbf{n}_{\sigma\beta}$ according to the definitions of the unit normal. Following classical ideas [111] we will try to solve approximately the problems in terms of averaged values and deviations.

The pore-scale fields deviation in the β -phase and σ -phase are respectively defined by

$$\varphi_\beta = \langle \varphi_\beta \rangle^\beta + \tilde{\varphi}_\beta \quad \text{and} \quad \varphi_\sigma = \langle \varphi_\sigma \rangle^\sigma + \tilde{\varphi}_\sigma \quad (2-15)$$

The classical length-scale constraints (Fig. 2-1) have been imposed by assuming

$$\ell_\beta \ll r_0 \ll L \quad (2-16)$$

After performing the volume averaging on the original boundary value problem and solving the associated closure problems, the final form of the transport equations contains local averages, rather than micro-scale point values. Thus, the microscopic equations that hold for a point in space are developed into the appropriate macroscopic equations, which hold at a given point for some volume in space of the porous medium.

2.4 Darcy's law

If we assume that density and viscosity are constants, the flow problem can be solved independently from the heat and constituent transport equations, and the change of scale for Stokes flow equation and continuity has already been investigated and this leads to Darcy's law and the volume averaged continuity equation [94, 110] written as

$$\langle \mathbf{v}_\beta \rangle = -\frac{\mathbf{K}_\beta}{\mu_\beta} \cdot \left(\nabla \langle p_\beta \rangle^\beta - \rho_\beta \mathbf{g} \right), \text{ in the porous medium} \quad (2-17)$$

$$\nabla \cdot \langle \mathbf{v}_\beta \rangle = 0, \text{ in the porous medium} \quad (2-18)$$

where \mathbf{K}_β is the permeability tensor.

Note that the Darcy velocity, $\langle \mathbf{v}_\beta \rangle$, is a superficial velocity based on the entire volume, not just the fluid volume. One can also related the Darcy velocity to the average intrinsic velocity, $\langle \mathbf{v}_\beta \rangle^\beta$ as

$$\langle \mathbf{v}_\beta \rangle = \varepsilon_\beta \langle \mathbf{v}_\beta \rangle^\beta \quad (2-19)$$

Values of the liquid-phase permeability vary widely, from 10^{-7} to $10^{-9} m^2$ for clean gravel down to 10^{-18} to $10^{-20} m^2$ for granite (Bear, 1979 [7]). A Darcy (or Darcy unit) and millidarcies (mD) are units of permeability, named after Henry Darcy. These units are widely used in petroleum engineering and geology. The unit Darcy is equal to $0.987 \times 10^{-12} m^2$ but most of the times it is simply assumed $1D = 10^{-12} m^2$.

Darcy's law is applicable to low velocity flow, which is generally the case in porous media flow, and to regions without boundary shear flow, such as away from walls. When wall shear is important, the Brinkman extension can be used as discussed below. A Forchheimer equation is appropriate when the inertial effect is important. In some situations (e.g., Vafai and Tien, 1981), the Brinkman and Forchheimer equations are both employed. One must use an effective correlation of apparent gas permeability in tight porous media because of Knudsen effect.

2.4.1 Brinkman term

The Brinkman extension to Darcy's law equation (introduced by Brinkman in 1947) includes the effect of wall or boundary shear on the flow velocity, or

$$0 = -\nabla \langle p_\beta \rangle^\beta + \rho_\beta \mathbf{g} - \frac{\mu_\beta}{\mathbf{K}_\beta} \langle \mathbf{v}_\beta \rangle + \tilde{\mu}_\beta \nabla^2 \langle \mathbf{v}_\beta \rangle \quad (2-20)$$

the third term on the RHS is a shear stress term such as would be required by no-slip condition. The coefficient $\tilde{\mu}_\beta$ is an effective viscosity, which in general is not equal to the fluid viscosity, μ_β , as discussed by Nield and Bejan (1999) [70]. For many situations, the use of the boundary shear term is not necessary. Without discussing the validity of Brinkman's equation near a wall or in areas of rapid porosity variations, the effect is only significant in a region close to the boundary whose thickness is of order of the square root of the gas permeability, $\mathbf{K}_\beta^{0.5}$, (assuming $\tilde{\mu}_\beta = \mu_\beta$), so for most applications and also in this study the effect can be ignored.

The Brinkman equation is also often employed at the interface between a porous medium and a free fluid (fluid with no porous medium), in order to obtain continuity of shear stress (more detail in [70] and [47])

2.4.2 No-linear case

At low pore velocities, Darcy's law works quite well. However, as the pore velocities increase, the inertial effect becomes very important, the flow resistance becomes non-linear, and the Forchheimer equation is more appropriate as

$$0 = -\nabla \langle p_\beta \rangle^\beta + \rho_\beta \mathbf{g} - \frac{\mu_\beta}{\mathbf{K}_\beta} \langle \mathbf{v}_\beta \rangle - \rho_\beta \beta_F \|\langle \mathbf{v}_\beta \rangle\| \langle \mathbf{v}_\beta \rangle \quad (2-21)$$

The third term on the RHS is a nonlinear flow resistance term. According to Nield and Bejan (1999), the above equation is based on the work of Dupuit (1863) and Forchheimer (1901) as modified by Ward (1964). β_F is a factor to be experimentally deduced.

Whitaker, (1996) derived Darcy's law with the Forchheimer correction for homogeneous porous media using the method of volume averaging. Beginning with the Navier-Stokes equations, they found that the volume averaged momentum equation to be given by

$$\langle \mathbf{v}_\beta \rangle = -\frac{\mathbf{K}_\beta}{\mu_\beta} \cdot \left(\nabla \langle p_\beta \rangle^\beta - \rho_\beta \mathbf{g} \right) - \mathbf{F} \cdot \langle \mathbf{v}_\beta \rangle \quad (2-22)$$

where \mathbf{F} is the Forchheimer correction tensor. In this equation, \mathbf{K}_β and \mathbf{F} are determined by closure problems that must be solved using a spatially periodic model of a porous medium [110].

2.4.3 Low permeability correction

Based on Darcy's law, the mass flux for a given pressure drop should decrease as the average pressure is reduced due to the change in gas density. However, Knudsen found that at low pressures, the mass flux reaches a minimum value and then increases with decreasing pressure, which is due to slip, or the fact that the fluid velocity at the wall is not zero due to free-molecule flow. As the capillary tubes get smaller and smaller, the gas molecular mean free path becomes of the same order, and free molecule, or Knudsen, diffusion becomes important.

Assuming gas flow in an idealized porous medium, using Poiseuille's law or Darcy's law, a correlation between the apparent and "true" permeability of a porous medium was derived as (Klinkenberg, 1941)

$$\mathbf{k}_a = k_\infty \left(1 + \frac{b_i}{\bar{P}} \right) \mathbf{I} \quad (2-23)$$

Eq. (2-23) is also referred to as the Klinkenberg correlation, where \bar{P} is the mean pressure, \mathbf{k}_a is the apparent gas permeability observed at the mean pressure, and k_∞ is called "true" permeability or Klinkenberg permeability. For a large average pressure, the correction factor in parentheses goes to zero, and the apparent and true permeabilities tend to become equal. As the average pressure decreases, the two permeabilities can deviate significantly from each other. This behavior is confirmed by data presented by Klinkenberg (1941) for glass filters and core samples and by Reda (1987) for tuff.

The gas slip factor b_i is a coefficient that depends on the mean free path of a particular gas and the average pore radius of the porous medium b_i can be calculated by

$$b_i = \frac{4f\lambda\bar{P}}{\ell_\beta} \quad (2-24)$$

where, ℓ_β is the radius of a capillary or a pore, λ is the mean free path of the gas molecules, and f is proportionality factor. The Klinkenberg coefficient for air can be estimated as

$$b_{air} = 0.11k_\ell^{-0.39}, \text{ with } 10^{-14} > k_\ell > 10^{-19} \quad \text{Heid et al. (1950)} \quad (2-25)$$

$$b_{air} = 0.86k_\ell^{-0.33}, \text{ whit } 10^{-14} > k_\ell > 10^{-17} \quad \text{Jones and Owens (1980)} \quad (2-26)$$

the Klinkenberg coefficient for a given porous medium is different for each gas and is dependent on the local temperature. The Klinkenberg factor can be corrected for different conditions as follows [41]

$$k_g = k_\ell \left(1 + \frac{b_i}{P}\right) b_i = b_{ref} \left(\frac{\mu_i}{\mu_{air} T_{ref}}\right) \left(\frac{M_{ref}}{M_i}\right)^{1/2} \left(\frac{T_i}{T_{ref}}\right)^{1/2} \quad (2-27)$$

where subscript *ref* refers to the reference gas, which is usually air, and *M* is the molecular weight. The temperature *T* is in absolute units.

Another transport mechanism, configurational diffusion, occurred in very low permeability of approximately $10^{-21} m^2$, where the gas molecule size is comparable to the pore diameter. The gas-phase permeability may be different than the liquid-phase permeability due to this effect.

2.5 Transient conduction and convection heat transport

The process of volume averaging begins by forming the superficial average of Eqs. (2-1) to (2-4), in the case of a homogeneous medium for the β -phase

$$\left\langle (\rho c_p)_\beta \frac{\partial T_\beta}{\partial t} \right\rangle + \left\langle (\rho c_p)_\beta \nabla \cdot (T_\beta \mathbf{v}_\beta) \right\rangle = \left\langle \nabla \cdot (k_\beta \nabla T_\beta) \right\rangle, \text{ in the } \beta\text{-phase} \quad (2-28)$$

$$\begin{aligned} (\rho c_p)_\beta \frac{\partial}{\partial t} \langle T_\beta \rangle + (\rho c_p)_\beta \nabla \cdot \langle \mathbf{v}_\beta T_\beta \rangle + \frac{1}{\mathcal{V}} \int_{A_{\beta\sigma}} \mathbf{n}_{\beta\sigma} \cdot \mathbf{v}_\beta T_\beta dA &= \nabla \cdot \langle k_\beta \nabla T_\beta \rangle \\ + \frac{1}{\mathcal{V}} \int_{A_{\beta\sigma}} \mathbf{n}_{\beta\sigma} \cdot k_\beta \nabla T_\beta dA & \end{aligned} \quad (2-29)$$

And, with the spatial decomposition of the temperature and velocity for the β -phase

$$\tilde{T}_\beta = T_\beta - \langle T_\beta \rangle^\beta, \quad \tilde{\mathbf{v}}_\beta = \mathbf{v}_\beta - \langle \mathbf{v}_\beta \rangle^\beta, \quad \langle \tilde{\mathbf{v}}_\beta \rangle = 0, \quad \langle \tilde{T}_\beta \rangle = 0 \quad (2-30)$$

we have

$$\varepsilon_\beta (\rho c_p)_\beta \frac{\partial}{\partial t} \langle T_\beta \rangle^\beta + (\rho c_p)_\beta \nabla \cdot \left\langle \varepsilon_\beta \langle T_\beta \rangle^\beta \langle \mathbf{v}_\beta \rangle^\beta + \langle \tilde{T}_\beta \tilde{\mathbf{v}}_\beta \rangle \right\rangle \quad (2-31)$$

$$= \nabla \cdot \left(k_\beta \left(\nabla \langle T_\beta \rangle + \frac{1}{\mathcal{V}} \int_{A_{\beta\sigma}} \mathbf{n}_{\beta\sigma} T_\beta dA \right) \right) + \frac{1}{\mathcal{V}} \int_{A_{\beta\sigma}} \mathbf{n}_{\beta\sigma} \cdot k_\beta \nabla T_\beta dA$$

$$\varepsilon_\beta (\rho c_p)_\beta \frac{\partial}{\partial t} \langle T_\beta \rangle^\beta + (\rho c_p)_\beta \nabla \cdot \left\langle \varepsilon_\beta \langle T_\beta \rangle^\beta \langle \mathbf{v}_\beta \rangle^\beta + \langle \tilde{T}_\beta \tilde{\mathbf{v}}_\beta \rangle \right\rangle \quad (2-32)$$

$$= \nabla \cdot \left(k_\beta \left(\varepsilon_\beta \nabla \langle T_\beta \rangle^\beta + \frac{1}{\mathcal{V}} \int_{A_{\beta\sigma}} \mathbf{n}_{\beta\sigma} (\tilde{T}_\beta + \langle T_\beta \rangle^\beta) dA \right) \right) + \frac{1}{\mathcal{V}} \int_{A_{\beta\sigma}} \mathbf{n}_{\beta\sigma} \cdot k_\beta \nabla T_\beta dA$$

Imposing the length-scale constraint to obtain the intrinsic form

$$\varepsilon_\beta (\rho c_p)_\beta \frac{\partial}{\partial t} \langle T_\beta \rangle^\beta + \varepsilon_\beta (\rho c_p)_\beta \langle \mathbf{v}_\beta \rangle^\beta \cdot \nabla \langle T_\beta \rangle^\beta + (\rho c_p)_\beta \nabla \cdot \langle \tilde{T}_\beta \tilde{\mathbf{v}}_\beta \rangle \quad (2-33)$$

$$= \nabla \cdot \left(k_\beta \left(\varepsilon_\beta \nabla \langle T_\beta \rangle^\beta + \frac{1}{\mathcal{V}} \int_{A_{\beta\sigma}} \mathbf{n}_{\beta\sigma} \tilde{T}_\beta dA \right) \right) + \frac{1}{\mathcal{V}} \int_{A_{\beta\sigma}} \mathbf{n}_{\beta\sigma} \cdot k_\beta \nabla T_\beta dA$$

In differential equations like equation (2-33) we can clearly identify different terms as

- The terms involving area integrals of the unit normal multiplied by the spatial deviations reflect the tortuosity of the porous medium, since they are highly dependent on the geometry of the interfacial region.
- The volume integrals of the velocity deviations multiplied by the temperature deviations are responsible for what is commonly known as hydrodynamic dispersion.
- The area integrals of the unit normal multiplied by the diffusive fluxes are the contributions from interfacial mass transport.

The σ -phase transport equation is analogous to Eq. (2-33) without the convection term and we list the result as

$$\varepsilon_\sigma (\rho c_p)_\sigma \frac{\partial}{\partial t} \langle T_\sigma \rangle^\sigma = \nabla \cdot \left(k_\sigma \left(\varepsilon_\sigma \nabla \langle T_\sigma \rangle^\sigma + \frac{1}{\mathcal{V}} \int_{A_{\sigma\beta}} \mathbf{n}_{\sigma\beta} \tilde{T}_\sigma dA \right) \right) \quad (2-34)$$

$$+ \frac{1}{\mathcal{V}} \int_{A_{\beta\sigma}} \mathbf{n}_{\sigma\beta} \cdot k_\sigma \nabla T_\sigma dA$$

2.5.1 One equation local thermal equilibrium

Since we have neglected Dufour effect, the heat transfer problem may be solved independently from Eqs. (2-5) and (2-6). This question has received a lot of attention in the literature. The one-equation equilibrium model consists of a single transport equation for both the σ and β -regions. When the two temperatures in the two regions are close enough, the transport equations that represent the two-equation model can be added to produce this model. We mean that the principle of local-scale heat equilibrium is valid. The conditions for the validity of a one-equation conduction model have been investigated by Quintard et al. (1993). They have examined the process of transient heat conduction for a two-phase system in terms of the method of volume averaging. Using two equation models, they have explored the principle of local thermal equilibrium as a function of various parameters, in particular the conductivity ratio, micro-scale and macro-scale dimensionless times and topology [79]. The one-equation equilibrium model is obtained directly from the two-equation model by imposing the constraints associated with local mass equilibrium.

The local equilibrium model obtained when there is a fast exchange between the different regions, is characterized by

$$\langle T \rangle = \langle T_\beta \rangle^\beta = \langle T_\sigma \rangle^\sigma \quad (2-35)$$

If we accept this idea, Eq. (2-33) and Eq. (2-34) can be added to obtain:

$$\begin{aligned} & \left(\varepsilon_\beta (\rho_p)_\beta + \varepsilon_\sigma (\rho_p)_\sigma \right) \frac{\partial}{\partial t} \langle T \rangle + \varepsilon_\beta (\rho_p)_\beta \langle \mathbf{v}_\beta \rangle^\beta \cdot \nabla \langle T \rangle \\ & = \nabla \cdot (\varepsilon_\beta k_\beta + \varepsilon_\sigma k_\sigma) \nabla \langle T \rangle + \nabla \cdot \left(\frac{k_\beta}{\mathcal{V}} \int_{A_{\beta\sigma}} \mathbf{n}_{\beta\sigma} \tilde{T}_\beta dA \right) + \nabla \cdot \left(\frac{k_\sigma}{\mathcal{V}} \int_{A_{\beta\sigma}} \mathbf{n}_{\sigma\beta} \tilde{T}_\sigma dA \right) \\ & - (\rho_p)_\beta \nabla \cdot \langle \tilde{T}_\beta \tilde{\mathbf{v}}_\beta \rangle \end{aligned} \quad (2-36)$$

Equation (2-33) is not too useful in its current form because of the terms containing the spatial deviations \tilde{T}_β . Therefore, one seeks to relate this spatial deviation to the averaged

temperature $\langle T_\beta \rangle^\beta$ and their gradient. This will help us to obtain a closure of the problem,

i.e., to have enough equations to allow a solution for the averaged temperature.

In order to develop this closure scheme, we derive governing differential equations for the spatial deviation by subtracting the average equation (2-33) from the point equation (2-1).

We then make a determination of the most important terms in the governing equations for \tilde{T}_β by using estimates of the order of magnitude of all the terms.

Finally, we postulate the functional dependence of \tilde{T}_β on $\langle T_\beta \rangle^\beta$ by analyzing the form of the differential equation and boundary conditions. The resulting constitutive equations will have functions that need to be evaluated in order to allow calculations of the important transport coefficients.

In order to develop the governing differential equation for \tilde{T}_β we divide Eq. (2-33) by ε_β and the result can be expressed as

$$\begin{aligned}
& (\rho c_p)_\beta \frac{\partial}{\partial t} \langle T_\beta \rangle^\beta + (\rho c_p)_\beta \langle \mathbf{v}_\beta \rangle^\beta \cdot \nabla \langle T_\beta \rangle^\beta \\
& = \nabla \cdot \left(k_\beta \left(\nabla \cdot \langle T_\beta \rangle^\beta \right) + \varepsilon_\beta^{-1} \nabla \varepsilon_\beta \nabla \langle T_\beta \rangle^\beta + \left(\frac{\varepsilon_\beta^{-1}}{\mathcal{V}} \int_{A_{\beta\sigma}} \mathbf{n}_{\beta\sigma} \tilde{T}_\beta dA \right) \right) \\
& + \frac{\varepsilon_\beta^{-1}}{\mathcal{V}} \int_{A_{\beta\sigma}} \mathbf{n}_{\beta\sigma} \cdot k_\beta \nabla T_\beta dA - (\rho c_p)_\beta \varepsilon_\beta^{-1} \nabla \cdot \langle \tilde{T}_\beta \tilde{\mathbf{v}}_\beta \rangle
\end{aligned} \tag{2-37}$$

If we subtract Eq. (2-37) from Eq. (2-1), we obtain the following governing differential equation for the spatial deviation temperature, \tilde{T}_β in β -phase

$$\begin{aligned}
& (\rho c_p)_\beta \frac{\partial \tilde{T}_\beta}{\partial t} + (\rho c_p)_\beta \mathbf{v}_\beta \cdot \nabla T_\beta - (\rho c_p)_\beta \langle \mathbf{v}_\beta \rangle^\beta \cdot \nabla \langle T_\beta \rangle^\beta = \nabla \cdot (k_\beta \nabla \tilde{T}_\beta) \\
& - \varepsilon_\beta^{-1} \nabla \varepsilon_\beta \cdot k_\beta \nabla \langle T_\beta \rangle^\beta - \varepsilon_\beta^{-1} \nabla \cdot \left(\frac{k_\beta}{\mathcal{V}} \int_{A_{\beta\sigma}} \mathbf{n}_{\beta\sigma} \tilde{T}_\beta dA \right) \\
& - \frac{\varepsilon_\beta^{-1}}{\mathcal{V}} \int_{A_{\beta\sigma}} \mathbf{n}_{\beta\sigma} \cdot k_\beta \nabla T_\beta dA - (\rho c_p)_\beta \varepsilon_\beta^{-1} \nabla \cdot \langle \tilde{T}_\beta \tilde{\mathbf{v}}_\beta \rangle
\end{aligned} \tag{2-38}$$

One can express the interfacial flux as

$$\frac{1}{\mathcal{V}} \int_{A_{\beta\sigma}} \mathbf{n}_{\beta\sigma} \cdot k_\beta \nabla T_\beta dA = -(\nabla \varepsilon_\beta) k_\beta \nabla \langle T_\beta \rangle^\beta + \frac{1}{\mathcal{V}} \int_{A_{\beta\sigma}} \mathbf{n}_{\beta\sigma} \cdot k_\beta \nabla \tilde{T}_\beta dA \tag{2-39}$$

In this equation we have made use of a theorem developed by Gray (1975), relating area integrals of the unit normal to gradients in volume fraction, for this case

$$\frac{1}{\mathcal{V}} \int_{A_{\beta\sigma}} \mathbf{n}_{\beta\sigma} dA = -\nabla \varepsilon_\beta \tag{2-40}$$

Since the volume fraction of the β -phase have been taken as constant, this integral sum to zero.

The point temperature field T_β will vary microscopically within each phase over distances on the order of the characteristic length ℓ_β indicated in Fig. 2-1. This is also the characteristic length associated with large variations in the spatial deviation field \tilde{T}_β . However, the average field $\langle T_\beta \rangle^\beta$ is treated as being constant within the averaging volume, \mathcal{V} . It undergoes significant variations only over distances L which is much greater than the characteristic length ℓ_β . These two widely different length scales in the problem helps us to simplify the transport equations for the spatial deviations by making order of magnitude estimates of the terms in equation (2-38) and the equation for \tilde{T}_β .

The order of magnitude of the non-local convective transport term can be expressed as

$$\nabla \cdot \langle \tilde{T}_\beta \tilde{\mathbf{v}}_\beta \rangle = \mathbf{O} \left(\frac{\langle \mathbf{v}_\beta \rangle^\beta \tilde{T}_\beta}{L} \right) \quad (2-41)$$

and the order of magnitude of the local convective transport is

$$\mathbf{v}_\beta \cdot \nabla \tilde{T}_\beta = \mathbf{O} \left(\frac{\langle \mathbf{v}_\beta \rangle^\beta \tilde{T}_\beta}{\ell_\beta} \right) \quad (2-42)$$

This indicates that the non-local convective transport can be neglected when-ever

$$\ell_\beta \ll L \quad (2-43)$$

Similarly, we can estimate the diffusive terms as follows

$$\nabla \cdot \left(\frac{k_\beta}{(\rho c_p)_\beta} \nabla \tilde{T}_\beta \right) = \mathbf{O} \left(\frac{k_\beta \tilde{T}_\beta}{(\rho c_p)_\beta \ell_\beta^2} \right) \quad (2-44)$$

and for the local diffusive transport term

$$\nabla \cdot \left(\frac{k_\beta}{(\rho c_p)_\beta} \int_{A_{\beta\sigma}} \mathbf{n}_{\beta\sigma} \tilde{T}_\beta dA \right) = \mathbf{O} \left(\frac{k_\beta \tilde{T}_\beta}{(\rho c_p)_\beta \ell_\beta L} \right) \quad (2-45)$$

In Eq. (2-44) we have used the characteristic length ℓ_β to estimate the second derivative of \tilde{T}_β . In Eq. (2-45) we have noted that area $A_{\beta\sigma}$ divided by the volume \mathcal{V} will have a magnitude of order ℓ_β . However, the term in parenthesis is an averaged quantity, and thus will vary significantly over distances of order L . Again, if the criterion of equation (2-43) is satisfied, we can simplify the transport equation by making the approximation

$$\nabla \cdot \left(\frac{k_\beta}{(\rho c_p)_\beta} \int_{A_{\beta\sigma}} \mathbf{n}_{\beta\sigma} \tilde{T}_\beta dA \right) \ll \nabla \cdot \left(\frac{k_\beta}{(\rho c_p)_\beta} \nabla \tilde{T}_\beta \right) \quad (2-46)$$

and by substitution $T_\beta = \tilde{T}_\beta + \langle T_\beta \rangle^\beta$ in second term finally we will obtain our transport

equation for \tilde{T}_β

$$\begin{aligned} (\rho c_p)_\beta \frac{\partial \tilde{T}_\beta}{\partial t} + (\rho c_p)_\beta \mathbf{v}_\beta \cdot \nabla \tilde{T}_\beta + (\rho c_p)_\beta \tilde{\mathbf{v}}_\beta \cdot \nabla \langle T_\beta \rangle^\beta &= \nabla \cdot (k_\beta \nabla \tilde{T}_\beta) \\ - \frac{\varepsilon_\beta^{-1}}{\mathcal{V}} \int_{A_{\beta\sigma}} \mathbf{n}_{\beta\sigma} \cdot k_\beta \nabla \tilde{T}_\beta dA - (\rho c_p)_\beta \varepsilon_\beta^{-1} \nabla \cdot \langle \tilde{T}_\beta \tilde{\mathbf{v}}_\beta \rangle & \end{aligned} \quad (2-47)$$

Finally, there is a time constraint involved here which can be readily derived if we write the order of magnitude of the time derivative in equation (2-38) as

$$\frac{\partial \tilde{T}_\beta}{\partial t} = \mathbf{O} \left(\frac{\tilde{T}_\beta}{t^*} \right) \quad (2-48)$$

where t^* is the characteristic time required for the temperature to change through a fixed point in space. This time would be on the order of L divided by the pulse velocity in the β -phase, say $\langle v_\beta \rangle^\beta$

$$t^* = \mathbf{O} \left(\frac{L}{\langle v_\beta \rangle^\beta} \right) \quad (2-49)$$

If we compare the order of magnitude of the time derivative in equation (2-48) with that of the diffusive term in equation (2-44) we see that the spatial deviation field can be treated as being quasi-steady if

$$\frac{t^* k_\beta}{(\rho c_p)_\beta \ell_\beta^2} = \left(\frac{L}{\ell_\beta} \right) \frac{k_\beta}{(\rho c_p)_\beta \langle v_\beta \rangle^\beta \ell_\beta} \gg 1 \quad (2-50)$$

Under this conditions the quasi-steady approximation can be made in equation (2-47)

$$\frac{\partial \tilde{T}_\beta}{\partial t} \ll \frac{k_\beta}{(\rho c_p)_\beta} \nabla^2 \tilde{T}_\beta \quad (2-51)$$

This allows us to consider the closure problems as quasi-steady

$$(\rho c_p)_\beta \mathbf{v}_\beta \cdot \nabla \tilde{T}_\beta + (\rho c_p)_\beta \tilde{\mathbf{v}}_\beta \cdot \nabla \langle T_\beta \rangle^\beta = \nabla \cdot (k_\beta \nabla \tilde{T}_\beta) - \frac{\varepsilon_\beta^{-1}}{\mathcal{V}} \int_{A_{\beta\sigma}} \mathbf{n}_{\beta\sigma} \cdot k_\beta \tilde{T}_\beta dA \quad (2-52)$$

$$\text{BC1: } \tilde{T}_\beta = \tilde{T}_\sigma \quad , \text{ at } \mathcal{A}_{\beta\sigma} \quad (2-53)$$

$$\text{BC2: } -\mathbf{n}_{\beta\sigma} \cdot k_{\beta} \nabla \tilde{T}_{\beta} = -\mathbf{n}_{\beta\sigma} \cdot k_{\sigma} \nabla \tilde{T}_{\sigma} + \mathbf{n}_{\beta\sigma} \cdot (k_{\beta} - k_{\sigma}) \nabla \langle T_{\beta} \rangle^{\beta}, \text{ at } \mathcal{A}_{\beta\sigma} \quad (2-54)$$

$$\text{BC3: } \tilde{T}_{\beta} = f(\mathbf{r}, t), \text{ at } \mathcal{A}_{\beta e} \text{ \& } \tilde{T}_{\sigma} = g(\mathbf{r}, t) \quad (2-55)$$

$$0 = \nabla \cdot (k_{\beta} \nabla \tilde{T}_{\beta}) - \frac{\varepsilon_{\beta}^{-1}}{\nu} \int_{\mathcal{A}_{\beta\sigma}} \mathbf{n}_{\beta\sigma} \cdot k_{\beta} \tilde{T}_{\beta} dA \quad (2-56)$$

I. Closure variable

In order to obtain a closure, we need to relate the spatial deviations \tilde{T}_{β} , \tilde{T}_{σ} to the average temperature $\langle T \rangle$. The transport equations for spatial deviation fields are linear in the averaged terms. We are thus encouraged to look for linear relations between the spatial deviations and average concentrations of the type [14]

$$\tilde{T}_{\beta} = \mathbf{b}_{T\beta} \cdot \nabla \langle T \rangle \quad (2-57)$$

$$\tilde{T}_{\sigma} = \mathbf{b}_{T\sigma} \cdot \nabla \langle T \rangle \quad (2-58)$$

in which $\mathbf{b}_{T\beta}$ and $\mathbf{b}_{T\sigma}$ are referred to as the closure variables for solid and liquid respectively. These vectors are functions of position only, since the time dependence of the \tilde{T}_{β} and \tilde{T}_{σ} comes only from the time dependence of the average temperature appearing in the equations and boundary conditions for the spatial deviation. If we substitute equations (2-57) and (2-58) into equation (2-52) to (2-56), we can derive transport equations for the closure functions for each phases. In doing this we can neglect higher derivatives of the average fields in the expressions for the gradients. This approximation is consistent with the constraint $\ell_{\beta} \ll L$ described previously. If we treat the representative region as a unit cell in a spatially periodic porous medium, we can replace the boundary condition imposed in equation (2-55) with a spatially periodic condition [111]. The closed equations are listed below, together with their boundary conditions at the fluid-solid interfaces [79, 111]

Problem I:

$$\left(\rho c_p\right)_{\beta} \mathbf{v}_{\beta} \cdot \nabla \mathbf{b}_{T\beta} + \left(\rho c_p\right)_{\beta} \tilde{\mathbf{v}}_{\beta} + \frac{\varepsilon_{\beta}^{-1}}{\nu} \int_{\mathcal{A}_{\beta\sigma}} \mathbf{n}_{\beta\sigma} \cdot k_{\beta} \nabla \mathbf{b}_{T\beta} dA = k_{\beta} \nabla^2 \mathbf{b}_{T\beta} \quad (2-59)$$

$$\text{BC1: } \mathbf{b}_{T\beta} = \mathbf{b}_{T\sigma}, \text{ at } \mathcal{A}_{\beta\sigma} \quad (2-60)$$

$$\text{BC2: } -\mathbf{n}_{\beta\sigma} \cdot k_{\beta} \nabla \mathbf{b}_{T\beta} = -\mathbf{n}_{\beta\sigma} \cdot k_{\sigma} \nabla \mathbf{b}_{T\sigma} + \mathbf{n}_{\beta\sigma} \cdot (k_{\beta} - k_{\sigma}), \text{ at } \mathcal{A}_{\beta\sigma} \quad (2-61)$$

$$\frac{-\varepsilon_\sigma^{-1}}{\mathcal{V}} \int_{A_{\beta\sigma}} \mathbf{n}_{\beta\sigma} k_\beta \nabla \mathbf{b}_{T\beta} dA = k_\sigma \nabla^2 \mathbf{b}_{T\sigma} \quad (2-62)$$

$$\text{Periodicity: } \mathbf{b}_{T\beta}(\mathbf{r} + \ell_i) = \mathbf{b}_{T\beta}(\mathbf{r}) \ \& \ \mathbf{b}_{T\sigma}(\mathbf{r} + \ell_i) = \mathbf{b}_{T\sigma}(\mathbf{r}), \ i=1,2,3 \quad (2-63)$$

$$\text{Averages: } \langle \mathbf{b}_{T\beta} \rangle^\beta = 0, \ \langle \mathbf{b}_{T\sigma} \rangle^\sigma = 0 \quad (2-64)$$

This way of writing the problem, i.e., under an integro-differential form, is reminiscent of the fact that this must be compatible with the full two-equation model as described, for instance, in [82]. However, following the mathematical treatment described also in this paper (using the decomposition described by Eqs. 20 in ref [82]), this problem reduces to (the proof involves the use of periodicity conditions) the following problem.

Problem I:

$$(\rho c_p)_\beta \mathbf{v}_\beta \cdot \nabla \mathbf{b}_{T\beta} + (\rho c_p)_\beta \tilde{\mathbf{v}}_\beta = k_\beta \nabla^2 \mathbf{b}_{T\beta} \quad (2-65)$$

$$\text{BC1: } \mathbf{b}_{T\beta} = \mathbf{b}_{T\sigma}, \ \text{at } A_{\beta\sigma} \quad (2-66)$$

$$\text{BC2: } -\mathbf{n}_{\beta\sigma} \cdot k_\beta \nabla \mathbf{b}_{T\beta} = -\mathbf{n}_{\beta\sigma} \cdot k_\sigma \nabla \mathbf{b}_{T\sigma} + \mathbf{n}_{\beta\sigma} \cdot (k_\beta - k_\sigma), \ \text{at } A_{\beta\sigma} \quad (2-67)$$

$$0 = k_\sigma \nabla^2 \mathbf{b}_{T\sigma} \quad (2-68)$$

$$\text{Periodicity: } \mathbf{b}_{T\beta}(\mathbf{r} + \ell_i) = \mathbf{b}_{T\beta}(\mathbf{r}) \ \& \ \mathbf{b}_{T\sigma}(\mathbf{r} + \ell_i) = \mathbf{b}_{T\sigma}(\mathbf{r}), \ i=1,2,3 \quad (2-69)$$

$$\text{Averages: } \langle \mathbf{b}_T \rangle = \varepsilon_\beta \langle \mathbf{b}_{T\beta} \rangle^\beta + \varepsilon_\sigma \langle \mathbf{b}_{T\sigma} \rangle^\sigma = 0 \quad (2-70)$$

In fact, the resulting field is also compatible with Eqs. (2-64), which is consistent with the local-equilibrium closure being compatible with the one from the two-equation model, as a limit case.

II. Transport equation for averaged temperature

In order to obtain the closed form of the macroscopic equation, we recall Eq. (2-36)

$$\begin{aligned} & \left(\varepsilon_\beta (\rho c_p)_\beta + \varepsilon_\sigma (\rho c_p)_\sigma \right) \frac{\partial}{\partial t} \langle T \rangle + \varepsilon_\beta (\rho c_p)_\beta \langle \mathbf{v}_\beta \rangle^\beta \cdot \nabla \langle T \rangle \\ & = \nabla \cdot (\varepsilon_\beta k_\beta + \varepsilon_\sigma k_\sigma) \nabla \langle T \rangle + \nabla \cdot \left(\frac{k_\beta}{\mathcal{V}} \int_{A_{\beta\sigma}} \mathbf{n}_{\beta\sigma} \tilde{T}_\beta dA \right) + \nabla \cdot \left(\frac{k_\sigma}{\mathcal{V}} \int_{A_{\beta\sigma}} \mathbf{n}_{\sigma\beta} \tilde{T}_\sigma dA \right) \\ & - (\rho c_p)_\beta \nabla \cdot \langle \tilde{T}_\beta \tilde{\mathbf{v}}_\beta \rangle \end{aligned} \quad (2-71)$$

In order to obtain a transport equation for the averaged temperature $\langle T \rangle$, we substitute the representations for \tilde{T}_β and \tilde{T}_σ (equations (2-57) and (2-58)) into the spatially averaged convective diffusion equation for two phases, equation (2-36) or (2-71). Note that, in this case, one cannot neglect terms involving second derivatives of the average concentration. It is a mistake to neglect these terms in the transport equations since they are of the same order as the tortuosity or dispersion tensors. As was done in the development of the equations for the average temperature, we treat all averaged quantities as constants within the averaging volume. Therefore, the transport equation obtained has the form

$$\begin{aligned} & \left(\varepsilon_\beta (\rho c_p)_\beta + \varepsilon_\sigma (\rho c_p)_\sigma \right) \frac{\partial}{\partial t} \langle T \rangle + (\rho c_p)_\beta \nabla \cdot \left(\varepsilon_\beta \langle \mathbf{v}_\beta \rangle^\beta \langle T \rangle \right) \\ & = \nabla \cdot \left(\left((\varepsilon_\beta \lambda_\beta + \varepsilon_\sigma \lambda_\sigma) \mathbf{I} + \frac{k_\beta - k_\sigma}{\nu} \int_{A_{\beta\sigma}} \mathbf{n}_{\beta\sigma} \mathbf{b}_{T\beta} dA \right) \nabla \langle T \rangle \right) \\ & - (\rho c_p)_\beta \nabla \cdot \left(\langle \tilde{\mathbf{v}}_\beta \mathbf{b}_{T\beta} \rangle \nabla \langle T \rangle \right) \end{aligned} \quad (2-72)$$

A product (of two vectors) such as $\mathbf{n}_{\beta\sigma} \mathbf{b}_{T\beta}$ is called a dyad product and is a special form of the second-order tensors. Each tensor is decomposed as

$$\mathbf{n}_{\beta\sigma} = n_{\beta\sigma 1} \mathbf{s}_1 + n_{\beta\sigma 2} \mathbf{s}_2 + n_{\beta\sigma 3} \mathbf{s}_3 \quad (2-73)$$

where \mathbf{s}_i is the unit vector in the i -direction. Then the dyad product is given by

$$\mathbf{n}_{\beta\sigma} \mathbf{b}_{T\beta} = \begin{bmatrix} n_{\beta\sigma 1} \mathbf{b}_{T\beta 1} & n_{\beta\sigma 1} \mathbf{b}_{T\beta 2} & n_{\beta\sigma 1} \mathbf{b}_{T\beta 3} \\ n_{\beta\sigma 2} \mathbf{b}_{T\beta 1} & n_{\beta\sigma 2} \mathbf{b}_{T\beta 2} & n_{\beta\sigma 2} \mathbf{b}_{T\beta 3} \\ n_{\beta\sigma 3} \mathbf{b}_{T\beta 1} & n_{\beta\sigma 3} \mathbf{b}_{T\beta 2} & n_{\beta\sigma 3} \mathbf{b}_{T\beta 3} \end{bmatrix} \quad (2-74)$$

Also, the unit tensor used in Eq. (2-77) is

$$\mathbf{I} = \begin{bmatrix} 1 & 0 & 0 \\ 0 & 1 & 0 \\ 0 & 0 & 1 \end{bmatrix} \quad (2-75)$$

in Cartesian coordinates.

Then the closed form of the convective-dispersion governing equation for $\langle T \rangle$ can be written

$$\left(\varepsilon_\beta (\rho c_p)_\beta + \varepsilon_\sigma (\rho c_p)_\sigma \right) \frac{\partial}{\partial t} \langle T \rangle + (\rho c_p)_\beta \nabla \cdot \left(\varepsilon_\beta \langle \mathbf{v}_\beta \rangle^\beta \langle T \rangle \right) = \nabla \cdot (\mathbf{k}^* \nabla \langle T \rangle) \quad (2-76)$$

where \mathbf{k}^* is the thermal dispersion tensor given by

$$\mathbf{k}^* = (\varepsilon_\beta k_\beta + \varepsilon_\sigma k_\sigma) \mathbf{I} + \frac{(k_\beta - k_\sigma)}{\mathcal{V}} \int_{A_{\beta\sigma}} \mathbf{n}_{\beta\sigma} \mathbf{b}_{T\beta} dA - (\rho c_p)_\beta \langle \tilde{\mathbf{v}}_\beta \mathbf{b}_{T\beta} \rangle \quad (2-77)$$

As an illustration of such a local-equilibrium situation, we will compare a direct simulation of the pore-scale equations with a macro-scale prediction. The geometry is an array of N_{UC} of the periodic Unit Cell (UC) shown in Fig. 2-6 . The initial temperature in the domain is a constant, T_C . The fluid is injected at $x=0$ at temperature T_H . The temperature is imposed at the exit boundary and is equal to T_C . This latter boundary condition has been taken for a practical reason: we have ongoing experiments using the two-bulb method, which is closely described by this kind of boundary-value problem. In addition, this particular problem will help us to illustrate some theoretical considerations given below. The parameters describing the case were:

$$\begin{aligned} N_{UC} &= 120 ; \ell_{UC} = 2 \times 10^{-3} \text{ m} ; k_\beta = 1 \text{ W/m.K} ; k_\sigma = 4 \text{ W/m.K} ; \varepsilon_\beta = 0.615 \\ (\rho c_p)_\beta &= 4.18 \times 10^6 \text{ J/m}^3 \text{ K} ; (\rho c_p)_\sigma = 4 \times 10^6 \text{ J/m}^3 \text{ K} ; \langle v_\beta \rangle^\beta = 1.4 \times 10^{-4} \text{ m/s} \\ k^* &= 1.607 \text{ W/m.K} \end{aligned} \quad (2-78)$$

An example of comparison between the averaged temperatures obtained from the direct simulation and theoretical predictions is given Fig. 2-2. We considered three stages:

- a short time after injection, which is often the source of a discrepancy between actual fields and macro-scale predicted ones, because of the vicinity of the boundary,
- an intermediate time, i.e., a field less impacted by boundary conditions,
- a long time typical of the steady-state condition associated to the initial boundary-value problem under consideration.

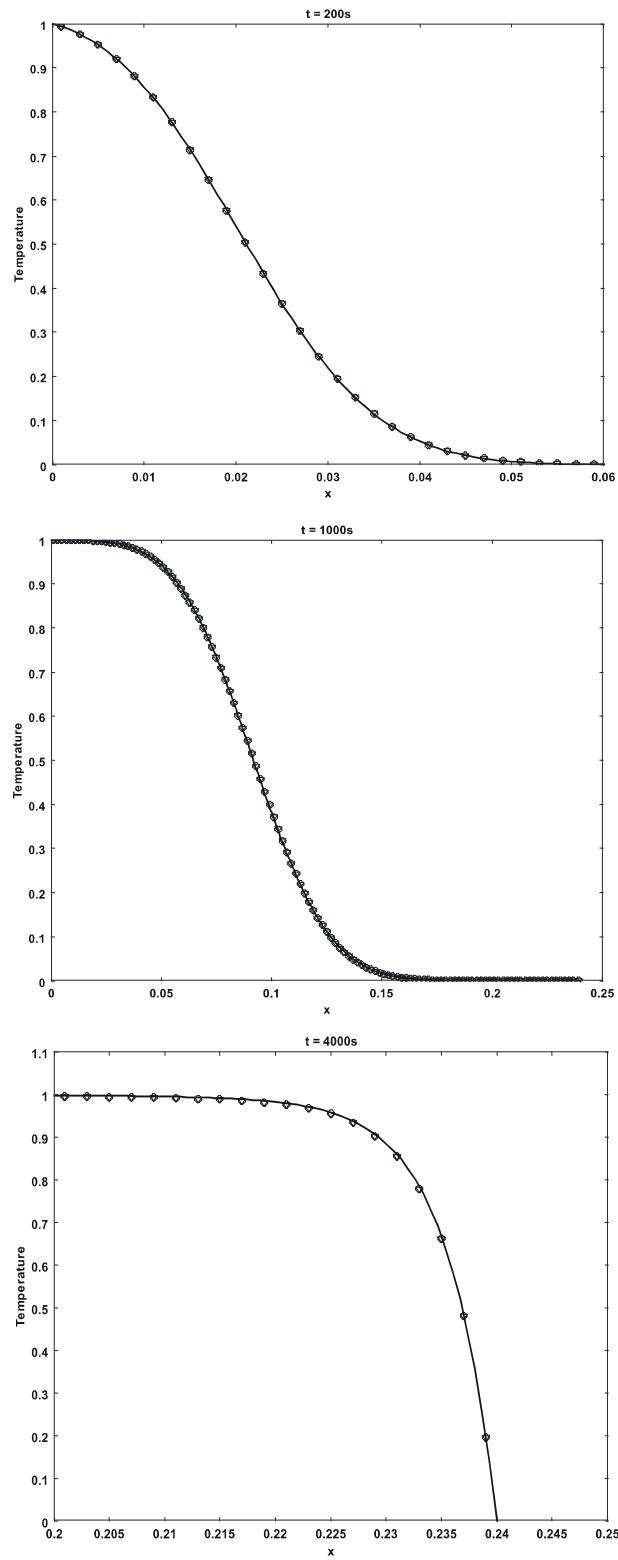


Fig. 2-2. Normalized temperature versus position, for three different times (triangle, Direct Numerical Simulation= $\frac{\langle T_\beta \rangle^\beta - T_c}{T_H - T_c}$; circles, Direct Numerical Simulation= $\frac{\langle T_\sigma \rangle^\sigma - T_c}{T_H - T_c}$; solid line, Local-equilibrium model= $\frac{\langle T \rangle - T_c}{T_H - T_c}$)

We see on these figures a very good agreement between the direct simulations and the predictions with the local equilibrium model. This illustrates the fact that the local-equilibrium model does allow to represent correctly the system behaviour for moderate contrasts of the pore-scale physical properties. What happens when this contrast becomes dramatic, i.e., when the pore-scale characteristic times are very different? To illustrate the problem, we designed such a case by taking the following parameters:

$$\begin{aligned}
 N_{UC} &= 480 ; \ell_{UC} = 2 \times 10^{-3} \text{ m} ; k_{\beta} = 1 \text{ W/mK} ; k_{\sigma} = 0.01 \text{ W/mK} ; \varepsilon_{\beta} = 0.615 \\
 (\rho c_p)_{\beta} &= 4 \times 10^6 \text{ J/m}^3 \text{ K} ; (\rho c_p)_{\sigma} = 4 \times 10^6 \text{ J/m}^3 \text{ K} ; \langle v_{\beta} \rangle^{\beta} = 6.95 \times 10^{-5} \text{ m/s} \\
 k^* &= 0.455 \text{ W/m.K}
 \end{aligned} \tag{2-79}$$

The comparison between the averaged temperatures obtained from direct numerical simulations and the theoretical predictions of the local-equilibrium model are presented in Fig. 2-3 for three different times. At early stages, we see a clear difference between the averaged temperatures of the two phases, and also a clear difference with the local-equilibrium predictions. This difference is also visible for intermediate times, and one sees that the local-equilibrium model has an effective conductivity which is too small. However, at steady-state, it is remarkable to see that the temperature fields revert to the local-equilibrium conditions and that, despite the steep gradient near the boundary, the local-equilibrium models offers a very good prediction. It must be pointed out that this possibility has not been documented in the literature, and this may explain certain confusion in the discussion about the various macro-scale models. Without going into many details, we may summarize the discussion as follows:

- for moderate thermal properties contrasts, the local-equilibrium predictions are very good, and not very sensitive to boundary conditions or initial conditions,
- the situation is much more complex for higher contrasts, which lead to non-equilibrium conditions.

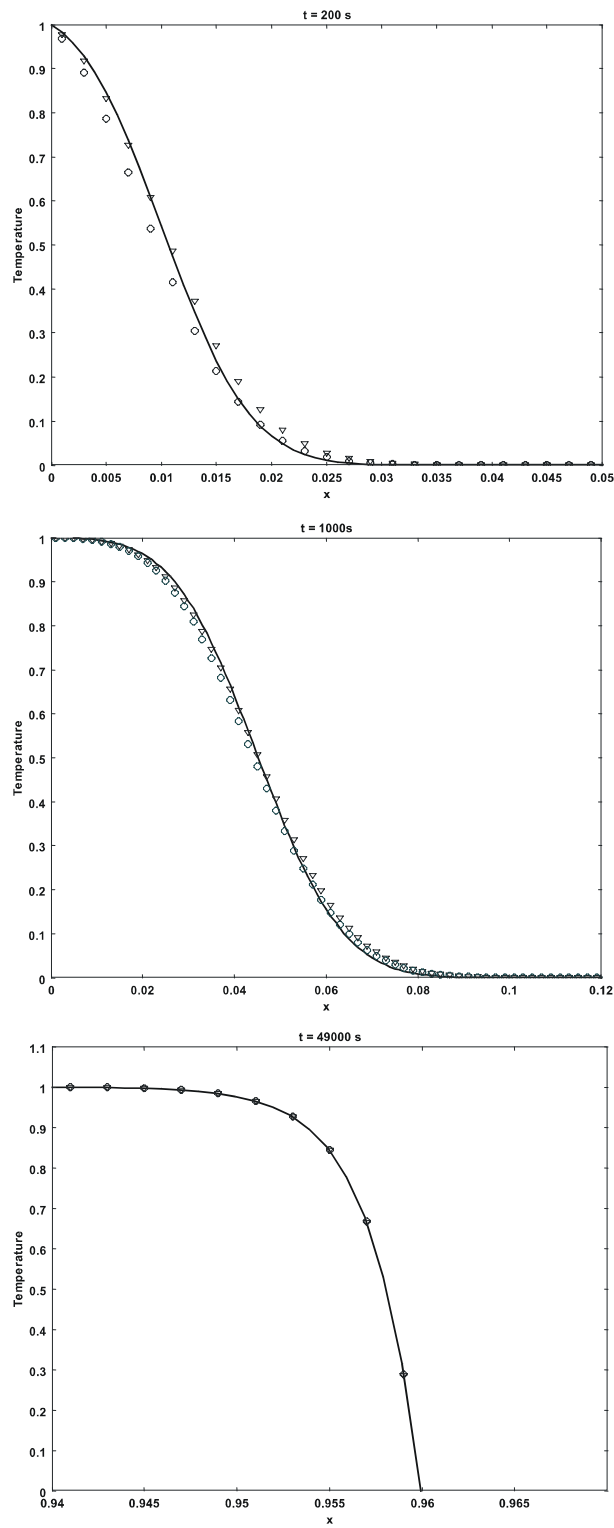


Fig. 2-3. Normalized temperature versus position, for three different times (triangle, Direct Numerical Simulation= $\frac{\langle T_\beta \rangle^\beta - T_C}{T_H - T_C}$); circles, Direct Numerical Simulation= $\frac{\langle T_\sigma \rangle^\sigma - T_C}{T_H - T_C}$); solid line, Local-equilibrium model= $\frac{\langle T \rangle - T_C}{T_H - T_C}$)

If the local equilibrium assumption does not hold, the different stages for the typical problem considered here are as following:

- early stages: initial conditions with sharp gradients and the vicinity of boundaries create non-equilibrium situations that are difficult to homogenize. They may be modelled through modified boundary conditions ([71], [16]), mixed models (i.e., a small domain keeping pore-scale description such as in [6]).
- two-equation behaviour: in general, the initial sharp gradients are smoothed after some time and more homogenizable conditions are found. Different models may be used: mixed models, different types of two-equation models (see a review and discussion in [83]), or more sophisticated equations in [105]. Two-equation models may be more or less sophisticated, for instance, two-equation models with first order exchange terms [11, 82, 79, 115, 116] or two-equation models with more elaborate exchange terms like convolution terms that would model non local and memory effects [64]. This is beyond the scope of this paper to develop such a theory for our double-diffusion problem.
- asymptotic behaviour: if the medium has an infinite extent (this can also be mimicked by convective conditions at the exit for a sufficiently large domain), cross diffusion may lead to a so-called asymptotic behaviour which may be described by a one-equation model with a different effective thermal conductivity, larger than the local-equilibrium value. This asymptotic behaviour for dispersion problems has been investigated by several authors and the link between the one-equation model obtained and the properties of the two-equation model well documented ([116], [2], [81]). The one-equation non-equilibrium model may be derived directly by a proper choice of the averaged concentration/temperature and deviations as in [81] and [65].
- Complex history: It must be emphasized that non-equilibrium models corresponding to the asymptotic behaviour require special situations to be valid. If events along the flow path change due to forcing terms like source terms, heterogeneities, boundaries, the conditions leading to the asymptotic behaviour are disturbed and a different history develops. This is what happened in our test case. The boundary effects dampened the asymptotic behaviour that has probably taken place in our system (in the absence of an interpretation with two-equation models or one-equation asymptotic models, we cannot distinguish between the two

possibilities, while the large extent of the domain has probably favoured an asymptotic behaviour) and this led to a steady-state situation well described by the local-equilibrium model. This possibility has not been seen by many investigators. However, it must be taken into account for practical applications. Hence, for our test case, it would be better to use a two-equation model, which truly embeds the one-equation local-equilibrium model, than the asymptotic model that would fail to catch the whole history.

Now we have at our disposal a mapping vector that gives the local temperature field in terms of the averaged value. It is important to remark that the upscaling of the heat equation problem has been solved independently from the solute transport problem. This feature is a key approximation that will simplify the treatment of the solute transport equation as explained in section 2.6.

2.5.2 Two equation model

In this case the time and length scales are such that a unique macroscopic or effective medium cannot represent the macroscopic behavior of the two phases. The two-equation model consists of separate heat transport equations for both the σ and β -phases. The dominant coupling between the two equations is represented by an inter-phase flux that depends, in the simpler version, on an exchange coefficient and the difference between the temperatures of the two phases. The spatial deviation temperatures in terms of the macroscopic source terms is often represented as

$$\tilde{T}_\beta = \mathbf{b}_{T\beta\beta} \cdot \nabla \langle T_\beta \rangle^\beta + \mathbf{b}_{T\beta\sigma} \cdot \nabla \langle T_\sigma \rangle^\sigma - s_\beta \left(\langle T_\beta \rangle^\beta - \langle T_\sigma \rangle^\sigma \right) \quad (2-80)$$

$$\tilde{T}_\sigma = \mathbf{b}_{T\sigma\beta} \cdot \nabla \langle T_\beta \rangle^\beta + \mathbf{b}_{T\sigma\sigma} \cdot \nabla \langle T_\sigma \rangle^\sigma - s_\sigma \left(\langle T_\beta \rangle^\beta - \langle T_\sigma \rangle^\sigma \right) \quad (2-81)$$

Here the mapping vectors and the scalars are obtained from the solution of steady, pore scale closure problems (see Quintard et al. 1997). Then, the macroscopic equation for the β -phase, is expressed as [82]

$$\begin{aligned} & \varepsilon_\beta (\rho c_p)_\beta \frac{\partial}{\partial t} \langle T_\beta \rangle^\beta + (\rho c_p)_\beta \nabla \cdot \left(\varepsilon_\beta \langle \mathbf{v}_\beta \rangle^\beta \langle T_\beta \rangle^\beta \right) - \mathbf{u}_{\beta\beta} \cdot \nabla \langle T_\beta \rangle^\beta - \mathbf{u}_{\beta\sigma} \cdot \nabla \langle T_\sigma \rangle^\sigma \\ & = \nabla \cdot \left(\mathbf{k}_{\beta\beta} \cdot \nabla \langle T_\beta \rangle^\beta + \mathbf{k}_{\beta\sigma} \cdot \nabla \langle T_\sigma \rangle^\sigma \right) - a_v h \left(\langle T_\beta \rangle^\beta - \langle T_\sigma \rangle^\sigma \right) \end{aligned} \quad (2-82)$$

In this equation, the effective properties such as $\mathbf{k}_{\beta\beta}$, $\mathbf{k}_{\beta\sigma}$, $\mathbf{u}_{\beta\beta}$, $\mathbf{u}_{\beta\sigma}$ and the volumetric heat exchange coefficient $a_v h$, are obtained explicitly from the mapping vectors, and

representation of these coefficients are given in [82]. An equation analogous to equation (2-82) describes the intrinsic average temperature for the σ -phase, and this equation is given by

$$\begin{aligned} & \varepsilon_{\sigma} (\rho c_p)_{\sigma} \frac{\partial}{\partial t} \langle T_{\sigma} \rangle^{\sigma} - \mathbf{u}_{\sigma\beta} \cdot \nabla \langle T_{\beta} \rangle^{\beta} - \mathbf{u}_{\sigma\sigma} \cdot \nabla \langle T_{\sigma} \rangle^{\sigma} \\ & = \nabla \cdot (\mathbf{k}_{\sigma\beta} \cdot \nabla \langle T_{\beta} \rangle^{\beta} + \mathbf{k}_{\sigma\sigma} \cdot \nabla \langle T_{\sigma} \rangle^{\sigma}) + a_v h (\langle T_{\beta} \rangle^{\beta} - \langle T_{\sigma} \rangle^{\sigma}) \end{aligned} \quad (2-83)$$

This two-equations model is fully compatible with the one-equation model with the effective thermal dispersion tensor of equation (2-76) given by [82]

$$\mathbf{k}^* = \mathbf{k}_{\beta\beta} + \mathbf{k}_{\beta\sigma} + \mathbf{k}_{\sigma\beta} + \mathbf{k}_{\sigma\sigma} \quad (2-84)$$

2.5.3 Non-equilibrium one-equation model

If the local equilibrium assumption is not made, it is possible to obtain a one-equation non-equilibrium model which consists of a single transport equation for both the σ and β -regions. Similarly, it can be shown that, the two equation model described in the last section reduces to a single dispersion equation for sufficiently long time. It can be obtained by defining an enthalpy averaged temperature and working with the upscaling process by defining deviations with respect to this temperature [65]. One can begin with the two-equation model, determine the sum of the spatial moments of the two equations, and construct a one-equation model that matches the sum of the first three spatial moments in the long-time limit. The second analysis yields exactly the same equation as the first as explained in Quintard et al. (2001) for the case of dispersion in heterogeneous systems [81]. A complete three-dimensional moment's analysis associated with a two-equation model has been proposed in reference [115]. It is shown that a model with two equations converges asymptotically to a model with one equation, and it is possible to obtain an expression for the asymptotic global dispersion coefficient. A similar analysis was presented in the case of miscible transport in a stratified structure [2]; in this case some coefficients are zero.

The processes of a spatial moment analysis are listed in Table 2-1.

Table 2-1. Objectives of each order of momentum analysis

Order of moment	Definition
Zeroth	The total amount of field present in each phase

First	The average position
Second	Measure of the spread of the pulse relative to its average position

Consider a pulse introduced into spatially infinite system at time $t=0$. As the pulse transported, the temperature in each phase will change with position and time according to Eqs. (2-82) and (2-83).

From zeroth spatial moment, we can see that a quasi-equilibrium condition is reached when

$$t \gg \frac{\varepsilon_{\beta}(\rho c_p)_{\beta} \varepsilon_{\sigma}(\rho c_p)_{\sigma}}{a_v h (\varepsilon_{\beta}(\rho c_p)_{\beta} + \varepsilon_{\sigma}(\rho c_p)_{\sigma})} \quad (2-85)$$

The first order moment provides that the difference between the two mean pulse positions is a constant and, as a result, both pulses will move at the same velocity. Given this result, one tries to obtain the rate of spread of the pulses in each phase relative to their mean position by second moment analysis which shows that the difference in the pulse spreads is constant. Then, considering a flow parallel to the x -axis, the one-equation model can be written as

$$\left(\varepsilon_{\beta}(\rho c_p)_{\beta} + \varepsilon_{\sigma}(\rho c_p)_{\sigma} \right) \frac{\partial \langle T \rangle_{\infty}}{\partial t} + (\rho c_p)_{\beta} \frac{\partial \left(\varepsilon_{\beta} \langle v_{\beta} \rangle^{\beta} \langle T \rangle_{\infty} \right)}{\partial x} = k_{\infty}^* \frac{\partial^2 \left(\varepsilon_{\beta} \langle T \rangle_{\infty} \right)}{\partial x^2} \quad (2-86)$$

The asymptotic thermal dispersion coefficient k_{∞}^* is given by [115, 2]

$$k_{\infty}^* = k_{\beta\beta} + k_{\beta\sigma} + k_{\sigma\beta} + k_{\sigma\sigma} + \frac{\left(\varepsilon_{\beta}(\rho c_p)_{\beta} \langle v_{\beta} \rangle^{\beta} \right)^2}{a_v h \left(\varepsilon_{\beta}(\rho c_p)_{\beta} + \varepsilon_{\sigma}(\rho c_p)_{\sigma} \right)^2} \quad (2-87)$$

k_{∞}^* can be much greater than k^* as it is illustrated by numerical examples obtained for the case of a stratified system in Ahmadi et al. (1998). We note that, in this case there is no reason for equality between the regional averages; however, the difference between the two regional temperatures will generally be constrained by [81]

$$\langle T_{\beta} \rangle^{\beta} - \langle T_{\sigma} \rangle^{\sigma} \ll \langle T_{\beta} \rangle^{\beta} \quad \text{or} \quad \langle T_{\sigma} \rangle^{\sigma} \quad (2-88)$$

2.6 Transient diffusion and convection mass transport

In this section we have applied the volume averaging method to solute transport with Soret effect in the case of a homogeneous medium in the β -phase. We now take the spatial average of (2-5), using the spatial averaging theorem [111] on the convective and diffusive terms. We begin our analysis with the definition of two spatial decompositions for local concentration and velocity

$$\left\langle \frac{\partial c_\beta}{\partial t} \right\rangle + \left\langle \nabla \cdot (c_\beta \mathbf{v}_\beta) \right\rangle = \left\langle \nabla \cdot (D_\beta \nabla c_\beta + D_{T\beta} \nabla T_\beta) \right\rangle \quad (2-89)$$

$$\begin{aligned} \frac{\partial \langle c_\beta \rangle}{\partial t} + \nabla \cdot \langle c_\beta \mathbf{v}_\beta \rangle + \int_{A_{\beta\sigma}} \mathbf{n}_{\beta\sigma} c_\beta \mathbf{v}_\beta dA = \\ \nabla \cdot \langle D_\beta \nabla c_\beta + D_{T\beta} \nabla T_\beta \rangle + \int_{A_{\beta\sigma}} \mathbf{n}_{\beta\sigma} (D_\beta \nabla c_\beta + D_{T\beta} \nabla T_\beta)_\beta dA \end{aligned} \quad (2-90)$$

$$\frac{\partial \langle c_\beta \rangle}{\partial t} + \nabla \cdot \langle c_\beta \mathbf{v}_\beta \rangle = \nabla \cdot \langle D_\beta \nabla c_\beta + D_{T\beta} \nabla T_\beta \rangle \quad (2-91)$$

In this equation we have considered the fluid flow to be incompressible, and have made use of no-slip boundary condition and equation (2-6) at the fluid-solid interface

$$\begin{aligned} \frac{\partial \left(\varepsilon_\beta \langle c_\beta \rangle^\beta \right)}{\partial t} + \nabla \cdot \varepsilon_\beta \langle c_\beta \mathbf{v}_\beta \rangle^\beta = \nabla \cdot \langle D_\beta \nabla c_\beta + D_{T\beta} \nabla T_\beta \rangle \\ = \nabla \cdot \left(D_\beta \nabla \left(\varepsilon_\beta \langle c_\beta \rangle^\beta \right) + \frac{D_\beta}{\mathcal{V}} \int_{A_{\beta\sigma}} \mathbf{n}_{\beta\sigma} c_\beta dA + D_{T\beta} \nabla \left(\varepsilon_\beta \langle T_\beta \rangle^\beta \right) \right. \\ \left. + \frac{D_{T\beta}}{\mathcal{V}} \int_{A_{\beta\sigma}} \mathbf{n}_{\beta\sigma} T_\beta dA \right) \end{aligned} \quad (2-92)$$

We define the spatial deviations of the point concentrations and velocities from the intrinsic phase average values by the relations

$$\begin{aligned} c_\beta &= \langle c_\beta \rangle^\beta + \tilde{c}_\beta, \text{ in } V_\beta \\ \mathbf{v}_\beta &= \langle \mathbf{v}_\beta \rangle^\beta + \tilde{\mathbf{v}}_\beta, \text{ in } V_\beta \end{aligned} \quad (2-93)$$

The averaged quantities and their gradients are taken to be constants within the averaging volume \mathcal{V} , and this makes equation (2-92) to the form

$$\begin{aligned}
\frac{\partial \langle c_\beta \rangle^\beta}{\partial t} + \langle \mathbf{v}_\beta \rangle^\beta \cdot \nabla \langle c_\beta \rangle^\beta &= \nabla \cdot \left(D_\beta \nabla \langle c_\beta \rangle^\beta \right) + \varepsilon_\beta^{-1} \nabla \cdot \left(\frac{D_\beta}{\mathcal{V}} \int_{A_{\beta\sigma}} \mathbf{n}_{\beta\sigma} \tilde{c}_\beta dA \right) \\
+ \varepsilon_\beta^{-1} \nabla \varepsilon_\beta \cdot \left(D_\beta \nabla \langle c_\beta \rangle^\beta \right) + \nabla \cdot \left(D_{T\beta} \nabla \langle T_\beta \rangle^\beta \right) + \varepsilon_\beta^{-1} \nabla \cdot \left(\frac{D_{T\beta}}{\mathcal{V}} \int_{A_{\beta\sigma}} \mathbf{n}_{\beta\sigma} \tilde{T}_\beta dA \right) \\
+ \varepsilon_\beta^{-1} \nabla \varepsilon_\beta \cdot \left(D_{T\beta} \nabla \langle T_\beta \rangle^\beta \right) - \varepsilon_\beta^{-1} \nabla \cdot \langle \tilde{c}_\beta \tilde{\mathbf{v}}_\beta \rangle
\end{aligned} \tag{2-94}$$

Here, we have assumed that, as a first approximation, $\langle \tilde{\mathbf{v}}_\beta \rangle = 0$ and $\langle \tilde{c}_\beta \rangle = 0$. Therefore, the volume averaged convective transport has been simplified to

$$\langle c_\beta \mathbf{v}_\beta \rangle = \varepsilon_\beta \langle \mathbf{v}_\beta \rangle^\beta \langle c_\beta \rangle^\beta + \langle \tilde{c}_\beta \tilde{\mathbf{v}}_\beta \rangle \tag{2-95}$$

Subtracting Eq. (2-94) from Eq. (2-5) yields the governing equation for \tilde{c}_β

$$\begin{aligned}
\frac{\partial \tilde{c}_\beta}{\partial t} + \mathbf{v}_\beta \cdot \nabla \tilde{c}_\beta + \tilde{\mathbf{v}}_\beta \cdot \nabla \langle c_\beta \rangle^\beta &= \nabla \cdot \left(D_\beta \nabla \tilde{c}_\beta \right) + \nabla \cdot \left(D_{T\beta} \nabla \tilde{T}_\beta \right) \\
+ \varepsilon_\beta^{-1} \nabla \cdot \left(\frac{D_\beta}{\mathcal{V}} \int_{A_{\beta\sigma}} \mathbf{n}_{\beta\sigma} \tilde{c}_\beta dA \right) + \varepsilon_\beta^{-1} \nabla \varepsilon_\beta \cdot \left(D_\beta \nabla \langle c_\beta \rangle^\beta \right) + \varepsilon_\beta^{-1} \nabla \cdot \left(\frac{D_{T\beta}}{\mathcal{V}} \int_{A_{\beta\sigma}} \mathbf{n}_{\beta\sigma} \tilde{T}_\beta dA \right) \\
+ \varepsilon_\beta^{-1} \nabla \varepsilon_\beta \cdot \left(D_{T\beta} \nabla \langle T_\beta \rangle^\beta \right) - \varepsilon_\beta^{-1} \nabla \cdot \langle \tilde{c}_\beta \tilde{\mathbf{v}}_\beta \rangle
\end{aligned} \tag{2-96}$$

One can also use the definitions of the spatial deviations to obtain boundary conditions for \tilde{c}_β from the boundary condition in Eq. (2-6). At the σ - β interface, we find that \tilde{c}_β satisfies the relations

$$\text{BC1: } -\mathbf{n}_{\beta\sigma} \cdot \left(D_\beta \nabla \tilde{c}_\beta + D_{T\beta} \nabla \tilde{T}_\beta \right) = \mathbf{n}_{\beta\sigma} \cdot \left(D_\beta \nabla \langle c_\beta \rangle^\beta + D_{T\beta} \nabla \langle T_\beta \rangle^\beta \right), \text{ at } \mathcal{A}_{\beta\sigma} \tag{2-97}$$

and at the entrance and exit surface

$$\text{BC2: } \tilde{c}_\beta = f(\mathbf{r}, t), \text{ at } \mathcal{A}_{\beta e} \tag{2-98}$$

The spatial deviations must satisfy the additional constraint that their average values be zero, in accordance with their definition in Eq. (2-93).

$$\langle \tilde{c}_\beta \rangle^\beta = 0 \tag{2-99}$$

The spatial deviation field is subject to simplifications allowed the development of a relatively simple closure scheme to relate spatial deviations to average concentration.

The non-local diffusion and thermal diffusion terms can be discarded on the basis of

$$\varepsilon_\beta^{-1} \nabla \cdot \left(\frac{D_\beta}{\mathcal{V}} \int_{A_{\beta\sigma}} \mathbf{n}_{\beta\sigma} \tilde{c}_\beta dA \right) \ll \nabla \cdot (D_\beta \nabla \tilde{c}_\beta) \quad (2-100)$$

$$\varepsilon_\beta^{-1} \nabla \cdot \left(\frac{D_{T\beta}}{\mathcal{V}} \int_{A_{\beta\sigma}} \mathbf{n}_{\beta\sigma} \tilde{T}_\beta dA \right) \ll \nabla \cdot (D_{T\beta} \nabla \tilde{T}_\beta) \quad (2-101)$$

The fourth and the sixth terms in the right hand side of Eq. (2-96) are diffusion and thermal diffusion sources. On the basis of the length-scale constraint given by $\ell_\beta \ll L_\varepsilon$ we can discard these two terms. This constraint is automatically satisfied in homogeneous porous media for which L_ε is infinite [111].

The last term in the right hand side of this equation is the non-local convective transport and can be neglected whenever $\ell_\beta \ll L$.

The closure problem for \tilde{c}_β will be quasi-steady whenever the constraint

$$\frac{\ell_\beta^2}{D_\beta t^*} \ll 1 \quad (2-102)$$

is satisfied. Therefore, the quasi-steady closure problem for the spatial deviation concentration takes the form

$$\mathbf{v}_\beta \cdot \nabla \tilde{c}_\beta + \tilde{\mathbf{v}}_\beta \cdot \nabla \langle c_\beta \rangle^\beta = \nabla \cdot (D_\beta \nabla \tilde{c}_\beta) + \nabla \cdot (D_{T\beta} \nabla \tilde{T}_\beta) \quad (2-103)$$

and the associated boundary conditions are

$$\text{BC1: } -\mathbf{n}_{\beta\sigma} \cdot (D_\beta \nabla \tilde{c}_\beta + D_{T\beta} \nabla \tilde{T}_\beta) = \mathbf{n}_{\beta\sigma} \cdot (D_\beta \nabla \langle c_\beta \rangle^\beta + D_{T\beta} \nabla \langle T_\beta \rangle^\beta), \text{ at } \mathcal{A}_{\beta\sigma} \quad (2-104)$$

$$\text{BC2: } \tilde{c}_\beta = f(\mathbf{r}, t), \text{ at } \mathcal{A}_{\beta e} \quad (2-105)$$

2.6.1 Local closure problem

We wish to solve the closure problem in some representative region. So, we must discard the boundary condition given by equation (2-104) and replace it with some local condition associated with the representative region. This naturally leads us to treat the representative region as a unit cell in a spatially periodic model of a porous medium [111]. Therefore, the boundary condition given by Eq. (2-105) takes the form

$$\text{Periodicity: } \tilde{c}_\beta(\mathbf{r} + \ell_i) = \tilde{c}_\beta(\mathbf{r}), \quad i=1,2,3 \quad (2-106)$$

Here the single non-homogeneous term in the local closure problem is proportional to

$\nabla \langle c \rangle_x$ and $\nabla \langle T \rangle_x$ so we can express \tilde{c}_β as

$$\tilde{c}_\beta = \mathbf{b}_{C\beta} \cdot \nabla \langle c_\beta \rangle^\beta + \mathbf{b}_{S\beta} \cdot \nabla \langle T \rangle \quad (2-107)$$

in which $\mathbf{b}_{C\beta}$ and $\mathbf{b}_{S\beta}$ are referred to as the closure variables which are specified by the following boundary value problems. In developing these equations, we have collected all terms proportional to $\nabla \langle c_\beta \rangle^\beta$ and $\nabla \langle T \rangle$, and written equation and the boundary conditions in the form

$$a \nabla \langle c_\beta \rangle^\beta + b \nabla \langle T \rangle = 0 \quad (2-108)$$

where a and b are expressions containing the vector functions in the constitutive equation. In order to satisfy Eq. (2-108), we set each of the terms a and b , individually equal to zero, and this gives rise to the following equations. The solution of these problems is all subject to the constraint of equation (2-99). This means that the volume integrals of the vector fields must be zero.

Problem IIa

$$\mathbf{v}_\beta \cdot \nabla \mathbf{b}_{C\beta} + \tilde{\mathbf{v}}_\beta = D_\beta \nabla^2 \mathbf{b}_{C\beta} \quad (2-109)$$

$$\text{BC: } -\mathbf{n}_{\beta\sigma} \cdot D_\beta \nabla \mathbf{b}_{C\beta} = \mathbf{n}_{\beta\sigma} \cdot D_\beta, \text{ at } A_{\beta\sigma} \quad (2-110)$$

$$\text{Periodicity: } \mathbf{b}_{C\beta}(\mathbf{r} + \ell_i) = \mathbf{b}_{C\beta}(\mathbf{r}), i=1,2,3 \quad (2-111)$$

$$\text{Averages: } \langle \mathbf{b}_{C\beta} \rangle^\beta = 0 \quad (2-112)$$

Problem IIb

$$\mathbf{v}_\beta \cdot \nabla \mathbf{b}_{S\beta} = D_\beta \nabla^2 \mathbf{b}_{S\beta} + D_{T\beta} \nabla^2 \mathbf{b}_{T\beta} \quad (2-113)$$

$$\text{BC: } -\mathbf{n}_{\beta\sigma} \cdot (D_\beta \nabla \mathbf{b}_{S\beta} + D_{T\beta} \nabla \mathbf{b}_{T\beta}) = \mathbf{n}_{\beta\sigma} \cdot D_{T\beta}, \text{ at } A_{\beta\sigma} \quad (2-114)$$

$$\text{Periodicity: } \mathbf{b}_{S\beta}(\mathbf{r} + \ell_i) = \mathbf{b}_{S\beta}(\mathbf{r}), i=1,2,3 \quad (2-115)$$

$$\text{Averages: } \langle \mathbf{b}_{S\beta} \rangle^\beta = 0 \quad (2-116)$$

The closure problem can be solved also in a Chang's unit cell shown in Fig. 2-4, in this case, we can replace the periodic boundary conditions for $\mathbf{b}_{S\beta}$ and $\mathbf{b}_{C\beta}$ by a Dirichlet boundary condition. Therefore, the closure problem for pure diffusion and for Chang's unit cell becomes

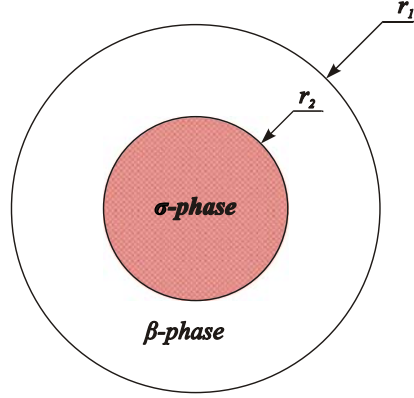


Fig. 2-4. Chang's unit cell

Problem I for Chang's unit cell

$$\nabla^2 \mathbf{b}_{T\beta} = 0 \quad (2-117)$$

$$\text{BC1: } \mathbf{b}_{T\beta} = \mathbf{b}_{T\sigma}, \text{ at } A_{\beta\sigma} \quad (2-118)$$

$$\text{BC2: } -\mathbf{n}_{\beta\sigma} \cdot k_{\beta} \nabla \mathbf{b}_{T\beta} = -\mathbf{n}_{\beta\sigma} \cdot k_{\sigma} \nabla \mathbf{b}_{T\sigma} + \mathbf{n}_{\beta\sigma} \cdot (k_{\beta} - k_{\sigma}), \text{ at } A_{\beta\sigma} \quad (2-119)$$

$$0 = k_{\sigma} \nabla^2 \mathbf{b}_{T\sigma} \quad (2-120)$$

$$\text{BC3: } \mathbf{b}_{T\beta} = 0, \text{ at } r = r_2 \quad (2-121)$$

Problem IIa for Chang's unit cell

$$\nabla^2 \mathbf{b}_{C\beta} = 0 \quad (2-122)$$

$$\text{BC1: } -\mathbf{n}_{\beta\sigma} \cdot D_{\beta} \nabla \mathbf{b}_{C\beta} = \mathbf{n}_{\beta\sigma} \cdot D_{\beta}, \text{ at } A_{\beta\sigma} \quad (2-123)$$

$$\text{BC1: } \mathbf{b}_{C\beta} = 0, \text{ at } r = r_2 \quad (2-124)$$

Problem IIb for Chang's unit cell

$$0 = D_{\beta} \nabla^2 \mathbf{b}_{S\beta} + D_{T\beta} \nabla^2 \mathbf{b}_{T\beta} \quad (2-125)$$

$$\text{BC1: } -\mathbf{n}_{\beta\sigma} \cdot (D_{\beta} \nabla \mathbf{b}_{S\beta} + D_{T\beta} \nabla \mathbf{b}_{T\beta}) = \mathbf{n}_{\beta\sigma} \cdot D_{T\beta}, \text{ at } A_{\beta\sigma} \quad (2-126)$$

$$\text{BC2: } \mathbf{b}_{S\beta} = 0, \text{ at } r = r_2 \quad (2-127)$$

2.6.2 Closed form

By substituting \tilde{c}_β and \tilde{T}_β from decomposition equations into Eq. (2-94) and imposing the local equilibrium condition, Eq. (2-35), the closed form of the convection-double diffusion equation can be expressed by

$$\frac{\partial \langle \varepsilon_\beta c_\beta \rangle^\beta}{\partial t} + \nabla \cdot \left(\varepsilon_\beta \langle \mathbf{v}_\beta \rangle^\beta \langle c_\beta \rangle^\beta \right) = \nabla \cdot \left(\varepsilon_\beta \mathbf{D}_\beta^* \cdot \nabla \langle c_\beta \rangle^\beta + \varepsilon_\beta \mathbf{D}_{T\beta}^* \cdot \nabla \langle T \rangle \right) \quad (2-128)$$

where the total dispersion and total thermal-dispersion tensors are defined by

$$\mathbf{D}_\beta^* = D_\beta \left(\mathbf{I} + \frac{1}{V_\beta} \int_{A_{\beta\sigma}} \mathbf{n}_{\beta\sigma} \mathbf{b}_{C\beta} dA \right) - \langle \tilde{\mathbf{v}}_\beta \mathbf{b}_{C\beta} \rangle^\beta \quad (2-129)$$

$$\mathbf{D}_{T\beta}^* = D_\beta \left(\frac{1}{V_\beta} \int_{A_{\beta\sigma}} \mathbf{n}_{\beta\sigma} \mathbf{b}_{S\beta} dA \right) + D_{T\beta} \left(\mathbf{I} + \frac{1}{V_\beta} \int_{A_{\beta\sigma}} \mathbf{n}_{\beta\sigma} \mathbf{b}_{T\beta} dA \right) - \langle \tilde{\mathbf{v}}_\beta \mathbf{b}_{S\beta} \rangle^\beta \quad (2-130)$$

The area integral of the functions in this equations multiplied by the unit normal from one phase to another have been defined as tortuosity, which can be written for isotropic media

$$\frac{\mathbf{I}}{\tau} = \mathbf{I} + \frac{1}{V_\beta} \int_{A_{\beta\sigma}} \mathbf{n}_{\beta\sigma} \mathbf{b}_{C\beta} dA \quad (2-131)$$

We can define an effective diffusion tensor, in the isotropic case, according to

$$\mathbf{D}_{eff} = \frac{D_\beta \mathbf{I}}{\tau} \quad (2-132)$$

The influence of hydrodynamic dispersion appears in the volume integral of the function multiplied by the spatial deviation in the velocity

$$\mathbf{D}_{Hyd.} = - \langle \tilde{\mathbf{v}}_\beta \mathbf{b}_{S\beta} \rangle^\beta \quad (2-133)$$

Therefore, the total dispersion tensor appearing in Eq. (2-128) is the sum of the effective diffusion coefficient and the dispersion tensor as

$$\mathbf{D}_\beta^* = \mathbf{D}_{eff} + \mathbf{D}_{Hyd.} \quad (2-134)$$

For a diffusive regime, the hydrodynamic tensor will be zero. If we look at the effective diffusion and thermal diffusion coefficients in equations (2-129) and (2-130), we can conclude that the only condition that will produce the same tortuosity effect for diffusion and thermal diffusion mechanism is

$$\frac{1}{V_\beta} \int_{A_{\beta\sigma}} \mathbf{n}_{\beta\sigma} \mathbf{b}_{S\beta} dA = 0 \quad (2-135)$$

The numerical results in the next chapter will solve this problem.

2.6.3 Non thermal equilibrium model

When the thermal equilibrium is not valid, the temperature deviations are written in terms of the gradient of the average temperature in two phases and we can write the concentration deviation as

$$\tilde{c}_\beta = \mathbf{b}_{C\beta} \cdot \nabla \langle c_\beta \rangle^\beta + \mathbf{b}_{S\beta\beta} \cdot \nabla \langle T_\beta \rangle^\beta + \mathbf{b}_{S\beta\sigma} \cdot \nabla \langle T_\sigma \rangle^\sigma - r_\beta \left(\langle T_\beta \rangle^\beta - \langle T_\sigma \rangle^\sigma \right) \quad (2-136)$$

By substitution of this new concentration deviation and temperature deviation from equation (2-80) in β -phase into our quasi-steady closure problem for the spatial deviation concentration, equations (2-103)-(2-106), we obtain following boundary value problems for diffusion and thermal diffusion closure variables.

We note that the problem for $\mathbf{b}_{C\beta}$ is the same as problem IIa for thermal equilibrium-one equation model. Here are all the closure problem to determine the closure variable $\mathbf{b}_{C\beta}$, $\mathbf{b}_{S\beta\beta}$, $\mathbf{b}_{S\beta\sigma}$ and r_β to model a macroscopic scale coupled heat and mass transfer in porous media

Problem IIIa

$$\mathbf{v}_\beta \cdot \nabla \mathbf{b}_{C\beta} + \tilde{\mathbf{v}}_\beta = D_\beta \nabla^2 \mathbf{b}_{C\beta} \quad (2-137)$$

$$\text{BC: } -\mathbf{n}_{\beta\sigma} \cdot D_\beta \nabla \mathbf{b}_{C\beta} = \mathbf{n}_{\beta\sigma} D_\beta, \text{ at } A_{\beta\sigma} \quad (2-138)$$

$$\text{Periodicity: } \mathbf{b}_{C\beta}(\mathbf{r} + \ell_i) = \mathbf{b}_{C\beta}(\mathbf{r}), i=1,2,3 \quad (2-139)$$

$$\text{Averages: } \langle \mathbf{b}_{C\beta} \rangle^\beta = 0 \quad (2-140)$$

Problem IIIb

$$\mathbf{v}_\beta \cdot \nabla \mathbf{b}_{S\beta\beta} = D_\beta \nabla^2 \mathbf{b}_{S\beta\beta} + D_{T\beta} \nabla^2 \mathbf{b}_{T\beta\beta} \quad (2-141)$$

$$\text{BC: } -\mathbf{n}_{\beta\sigma} \cdot (D_\beta \nabla \mathbf{b}_{S\beta\beta} + D_{T\beta} \nabla \mathbf{b}_{T\beta\beta}) = \mathbf{n}_{\beta\sigma} \cdot D_{T\beta}, \text{ at } A_{\beta\sigma} \quad (2-142)$$

$$\text{Periodicity: } \mathbf{b}_{S\beta\beta}(\mathbf{r} + \ell_i) = \mathbf{b}_{S\beta\beta}(\mathbf{r}), i=1,2,3 \quad (2-143)$$

$$\text{Averages: } \langle \mathbf{b}_{S\beta\beta} \rangle^\beta = 0 \quad (2-144)$$

Problem IIIc

$$\mathbf{v}_\beta \cdot \nabla \mathbf{b}_{S\beta\sigma} = D_\beta \nabla^2 \mathbf{b}_{S\beta\sigma} + D_{T\beta} \nabla^2 \mathbf{b}_{T\beta\sigma} \quad (2-145)$$

$$\text{BC: } -\mathbf{n}_{\beta\sigma} \cdot (D_\beta \nabla \mathbf{b}_{S\beta\sigma} + D_{T\beta} \nabla \mathbf{b}_{T\beta\sigma}) = 0, \text{ at } A_{\beta\sigma} \quad (2-146)$$

$$\text{Periodicity: } \mathbf{b}_{S\beta\sigma}(\mathbf{r} + \ell_i) = \mathbf{b}_{S\beta\sigma}(\mathbf{r}), \text{ } i=1,2,3 \quad (2-147)$$

$$\text{Averages: } \langle \mathbf{b}_{S\beta\sigma} \rangle^\beta = 0 \quad (2-148)$$

Problem IIId

$$\mathbf{v}_\beta \cdot \nabla r_\beta = D_\beta \nabla^2 r_\beta + D_{T\beta} \nabla^2 s_\beta \quad (2-149)$$

$$\text{BC: } -\mathbf{n}_{\beta\sigma} \cdot (D_\beta \nabla r_\beta + D_{T\beta} \nabla s_\beta) = 0, \text{ at } A_{\beta\sigma} \quad (2-150)$$

$$\text{Periodicity: } r_\beta(\mathbf{r} + \ell_i) = r_\beta(\mathbf{r}), \text{ } i=1,2,3 \quad (2-151)$$

$$\text{Averages: } \langle r_\beta \rangle^\beta = 0 \quad (2-152)$$

By substituting \tilde{c}_β and \tilde{T}_β from the decomposition given by equations (2-80) and (2-136) into Eq. (2-94), the closed form of the convection-double diffusion equation for the non-equilibrium two-equation temperature model case can be expressed by

$$\begin{aligned} & \frac{\partial \langle \varepsilon_\beta c_\beta \rangle^\beta}{\partial t} + \nabla \cdot (\varepsilon_\beta \langle \mathbf{v}_\beta \rangle^\beta \langle c_\beta \rangle^\beta) - \nabla \cdot (\mathbf{u}_{C\beta} \cdot (\langle T_\beta \rangle^\beta - \langle T_\sigma \rangle^\sigma)) = \\ & \nabla \cdot \varepsilon_\beta (\mathbf{D}_\beta^* \cdot \nabla \langle c_\beta \rangle^\beta + \mathbf{D}_{T\beta\beta}^* \cdot \nabla \langle T_\beta \rangle^\beta + \mathbf{D}_{T\beta\sigma}^* \cdot \nabla \langle T_\sigma \rangle^\sigma) \end{aligned} \quad (2-153)$$

where the effective tensors are defined by

$$\mathbf{D}_\beta^* = D_\beta \left(\mathbf{I} + \frac{1}{V_\beta} \int_{A_{\beta\sigma}} \mathbf{n}_{\beta\sigma} \mathbf{b}_{C\beta} dA \right) - \langle \tilde{\mathbf{v}}_\beta \mathbf{b}_{C\beta} \rangle^\beta \quad (2-154)$$

$$\mathbf{D}_{T\beta\beta}^* = D_\beta \left(\frac{1}{V_\beta} \int_{A_{\beta\sigma}} \mathbf{n}_{\beta\sigma} \mathbf{b}_{S\beta\beta} dA \right) + D_{T\beta} \left(\mathbf{I} + \frac{1}{V_\beta} \int_{A_{\beta\sigma}} \mathbf{n}_{\beta\sigma} \mathbf{b}_{T\beta\beta} dA \right) - \langle \tilde{\mathbf{v}}_\beta \mathbf{b}_{S\beta\beta} \rangle^\beta \quad (2-155)$$

$$\mathbf{D}_{T\beta\sigma}^* = D_\beta \left(\frac{1}{V_\beta} \int_{A_{\beta\sigma}} \mathbf{n}_{\beta\sigma} \mathbf{b}_{S\beta\sigma} dA \right) + D_{T\beta} \left(\mathbf{I} + \frac{1}{V_\beta} \int_{A_{\beta\sigma}} \mathbf{n}_{\beta\sigma} \mathbf{b}_{T\beta\sigma} dA \right) - \langle \tilde{\mathbf{v}}_\beta \mathbf{b}_{S\beta\sigma} \rangle^\beta \quad (2-156)$$

$$\mathbf{u}_{C\beta} = -D_\beta \left(\frac{1}{V_\beta} \int_{A_{\beta\sigma}} \mathbf{n}_{\beta\sigma} r_\beta dA \right) - D_{T\beta} \left(\frac{1}{V_\beta} \int_{A_{\beta\sigma}} \mathbf{n}_{\beta\sigma} s_\beta dA \right) + \langle \tilde{\mathbf{v}}_\beta r_\beta \rangle^\beta \quad (2-157)$$

2.7 Results

In order to illustrate the main features of the proposed multiple scale analysis, we have solved the dimensionless form of the closure problems, for thermal equilibrium case (I, IIa, IIb), on a simple unit cell, to determine the effective properties. We note here that the resolution of all models described in the last section and comparison between different models are not the objective of this study.

If we treat the representative region as a unit cell in a spatially periodic porous medium, we can replace the boundary condition imposed at $\mathcal{A}_{\beta e}$ with a spatially periodic condition [111]. One such periodic porous media used in this study is shown in Fig. 2-5. The entire phase system can be generated by translating the unit cell distances corresponding to the lattice base vectors ℓ_i , ($i=1,2,3$). The entire set of equations can then be solved within a single unit cell. The spatial periodicity boundary conditions are used in this study at the edges of the unit cell, as shown in Fig. 2-6.

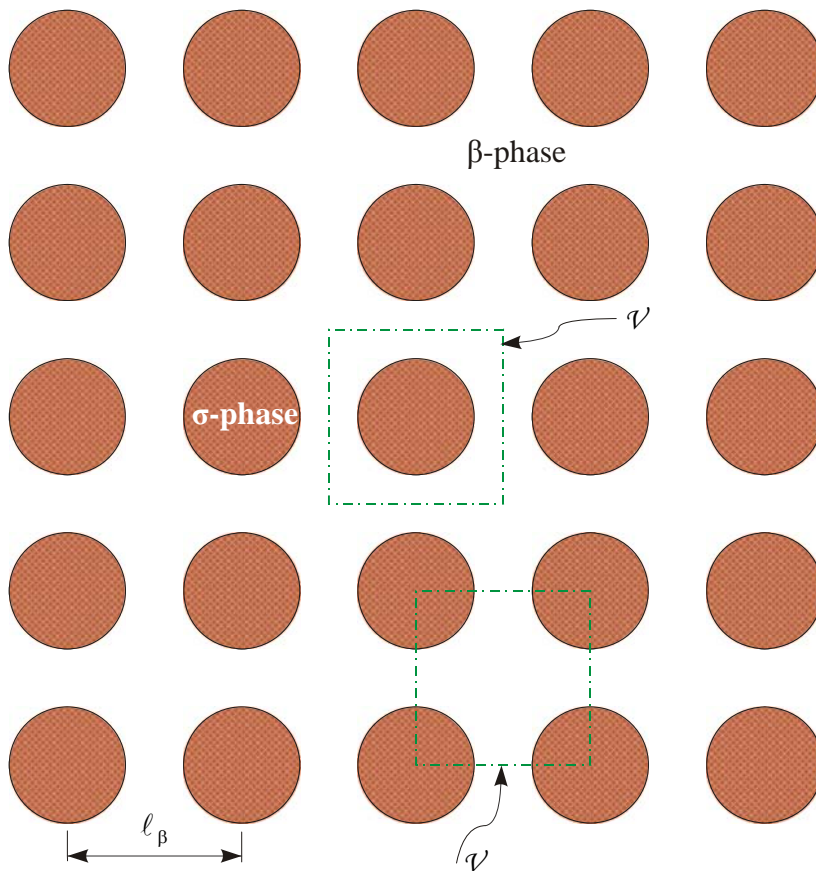


Fig. 2-5. Spatially periodic arrangement of the phases

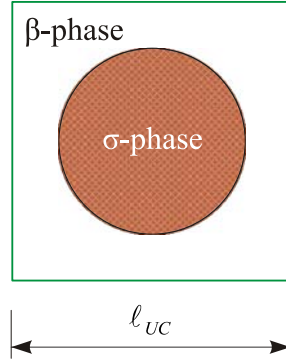


Fig. 2-6. Representative unit cell ($\varepsilon_\beta=0.8$)

This unit cell which will be used to compute the effective coefficients is a symmetrical cell Fig. 2-6, for an ordered porous media (in line arrangement of circular cylinders). This type of geometry has already been used for many similar problems [80, 111]. Then, the macro-scale effective properties are determined by equations (2-77), (2-129) and (2-130). For this illustration we have fixed the fluid mixture properties at $(\rho c_p)_\sigma / (\rho c_p)_\beta = 1$. The numerical simulations have been done using the COMSOLTM Multiphysics finite elements code. In this study, we have calculated the longitudinal coefficients which will be needed to simulate a test case for the macroscopic, one-dimensional equation.

2.7.1 Non-conductive solid-phase ($k_\sigma \approx 0$)

In this section, the solid thermal conductivity is assumed to be very small and will be neglected in the equations. The corresponding closure problems and effective coefficients in this case ($k_\sigma \approx 0$) are listed as below

Problem I ($k_\sigma \approx 0$): closure problem for effective thermal conductivity coefficient

$$(\rho c_p)_\beta \mathbf{v}_\beta \cdot \nabla \mathbf{b}_{T\beta} + (\rho c_p)_\beta \tilde{\mathbf{v}}_\beta = k_\beta \nabla^2 \mathbf{b}_{T\beta} \quad (2-158)$$

$$\text{BC1: } -\mathbf{n}_{\beta\sigma} \cdot \nabla \mathbf{b}_{T\beta} = \mathbf{n}_{\beta\sigma}, \text{ at } A_{\beta\sigma} \quad (2-159)$$

$$\text{Periodicity: } \mathbf{b}_{T\beta}(\mathbf{r} + \ell_i) = \mathbf{b}_{T\beta}(\mathbf{r}), \text{ } i=1,2,3 \quad (2-160)$$

$$\text{Averages: } \langle \mathbf{b}_{T\beta} \rangle^\beta = 0 \quad (2-161)$$

Problem IIa ($k_\sigma \approx 0$): closure problem for the effective diffusion coefficient

$$\mathbf{v}_\beta \cdot \nabla \mathbf{b}_{c\beta} + \tilde{\mathbf{v}}_\beta = D_\beta \nabla^2 \mathbf{b}_{c\beta} \quad (2-162)$$

$$\text{BC: } -\mathbf{n}_{\beta\sigma} \cdot D_\beta \nabla \mathbf{b}_{c\beta} = \mathbf{n}_{\beta\sigma} D_\beta, \text{ at } A_{\beta\sigma} \quad (2-163)$$

$$\text{Periodicity: } \mathbf{b}_{c\beta}(\mathbf{r} + \ell_i) = \mathbf{b}_{c\beta}(\mathbf{r}), i=1,2,3 \quad (2-164)$$

$$\text{Averages: } \langle \mathbf{b}_{c\beta} \rangle^\beta = 0 \quad (2-165)$$

Problem IIb ($k_\sigma \approx 0$): the closure problem for the effective thermal diffusion coefficient

$$\mathbf{v}_\beta \cdot \nabla \mathbf{b}_{s\beta} = D_\beta \nabla^2 \mathbf{b}_{s\beta} + D_{T\beta} \nabla^2 \mathbf{b}_{T\beta} \quad (2-166)$$

$$\text{BC: } -\mathbf{n}_{\beta\sigma} \cdot (D_\beta \nabla \mathbf{b}_{s\beta} + D_{T\beta} \nabla \mathbf{b}_{T\beta}) = \mathbf{n}_{\beta\sigma} \cdot D_{T\beta}, \text{ at } A_{\beta\sigma} \quad (2-167)$$

$$\text{Periodicity: } \mathbf{b}_{s\beta}(\mathbf{r} + \ell_i) = \mathbf{b}_{s\beta}(\mathbf{r}), i=1,2,3 \quad (2-168)$$

$$\text{Averages: } \langle \mathbf{b}_{s\beta} \rangle^\beta = 0 \quad (2-169)$$

and the effective coefficients are calculated with

$$\mathbf{k}_\beta^* = k_\beta \left(\varepsilon_\beta \mathbf{I} + \frac{1}{V} \int_{A_{\beta\sigma}} \mathbf{n}_{\beta\sigma} \mathbf{b}_{T\beta} dA \right) - (\rho c_p)_\beta \langle \tilde{\mathbf{v}}_\beta \mathbf{b}_{T\beta} \rangle \quad (2-170)$$

$$\mathbf{D}_\beta^* = D_\beta \left(\mathbf{I} + \frac{1}{V_\beta} \int_{A_{\beta\sigma}} \mathbf{n}_{\beta\sigma} \mathbf{b}_{c\beta} dA \right) - \langle \tilde{\mathbf{v}}_\beta \mathbf{b}_{c\beta} \rangle^\beta \quad (2-171)$$

$$\mathbf{D}_{T\beta}^* = D_\beta \left(\frac{1}{V_\beta} \int_{A_{\beta\sigma}} \mathbf{n}_{\beta\sigma} \mathbf{b}_{s\beta} dA \right) + D_{T\beta} \left(\mathbf{I} + \frac{1}{V_\beta} \int_{A_{\beta\sigma}} \mathbf{n}_{\beta\sigma} \mathbf{b}_{T\beta} dA \right) - \langle \tilde{\mathbf{v}}_\beta \mathbf{b}_{s\beta} \rangle^\beta \quad (2-172)$$

The macroscopic equations for $\langle T_\beta \rangle^\beta$ and $\langle c_\beta \rangle^\beta$ become

$$(\rho c_p)_\beta \frac{\partial \langle \varepsilon_\beta T_\beta \rangle^\beta}{\partial t} + (\rho c_p)_\beta \nabla \cdot \left(\varepsilon_\beta \langle \mathbf{v}_\beta \rangle^\beta \langle T_\beta \rangle^\beta \right) = \nabla \cdot \left(\varepsilon_\beta \mathbf{k}^* \cdot \nabla \langle T_\beta \rangle^\beta \right) \quad (2-173)$$

$$\frac{\partial \langle \varepsilon_\beta c_\beta \rangle^\beta}{\partial t} + \nabla \cdot \left(\varepsilon_\beta \langle \mathbf{v}_\beta \rangle^\beta \langle c_\beta \rangle^\beta \right) = \nabla \cdot \left(\varepsilon_\beta \mathbf{D}_\beta^* \cdot \nabla \langle c_\beta \rangle^\beta + \varepsilon_\beta \mathbf{D}_{T\beta}^* \cdot \nabla \langle T_\beta \rangle^\beta \right) \quad (2-174)$$

One can find in the literature several expressions for the effective diffusion coefficient base on the porosity, such as Wakao and Smith (1962) $D_\beta^* = \varepsilon_\beta D_\beta$, Weissberg (1963)

$$D_{\beta}^* = \frac{D_{\beta}}{1 - \frac{1}{2} \ln \varepsilon_{\beta}}, \text{ Maxwell (1881)} \quad D_{\beta}^* = \frac{2D_{\beta}}{3 - \varepsilon_{\beta}} \text{ (see Quintard (1993)).}$$

For isotropic systems one may write $\mathbf{D}_{\beta}^*/D_{\beta}$ as \mathbf{I}/τ , where τ is the scalar tortuosity of the porous matrix. The arbitrary, two dimensional effective tensor Φ_{β}^* is defined as

$$\Phi_{\beta}^* = \begin{bmatrix} \varphi_{\beta}^*|_{xx} & \varphi_{\beta}^*|_{xy} \\ \varphi_{\beta}^*|_{yx} & \varphi_{\beta}^*|_{yy} \end{bmatrix}$$

For the symmetric geometry shown in Fig. 2-6, when the Péclet number is zero, the effective coefficients are also symmetric; therefore, we can write $\varphi_{\beta}^* = \varphi_{\beta}^*|_{xx} = \varphi_{\beta}^*|_{yy}$ and $\varphi_{\beta}^*|_{xy} = \varphi_{\beta}^*|_{yx} = 0$. For a dispersive regime generated by a pressure gradient in the x -direction, the longitudinal dispersion coefficient $\varphi_{\beta}^*|_{xx}$ is obviously more important than the transversal dispersion coefficient $\varphi_{\beta}^*|_{yy}$. In this study, as it is mentioned in the previous section, we have just calculated the longitudinal coefficients which will be needed to simulate a test case for the macroscopic, one-dimensional equation.

Fig. 2-7 shows our results of the closure problem resolution (A.I, A.IIa and A.IIb) in the case of pure diffusion ($Pe = 0$).

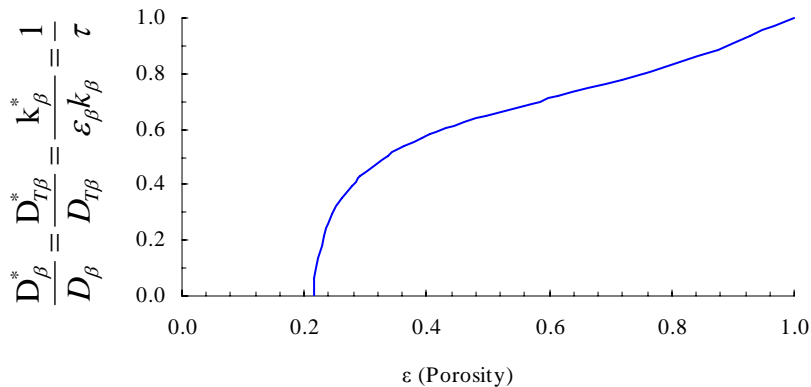


Fig. 2-7. Effective diffusion, thermal diffusion and thermal conductivity coefficients at $Pe=0$

We have therefore found that the effective thermal diffusion coefficient can also be estimated with this single tortuosity coefficient.

$$\frac{\mathbf{D}_\beta^*}{D_\beta} = \frac{\mathbf{D}_{T\beta}^*}{D_{T\beta}} = \frac{\mathbf{k}_\beta^*}{\varepsilon_\beta k_\beta} = \frac{\mathbf{I}}{\tau} \quad (2-175)$$

Here, the starred parameters are the effective coefficients and the others are the coefficient in the free fluid.

This relationship is similar to the one obtained for the effective diffusion and thermal conductivity in the literature [80, 111]. Therefore, we can say that the tortuosity factor acts in the same way on Fick diffusion coefficient and on thermal diffusion coefficient. In this case, the tortuosity is defined as

$$\frac{\mathbf{I}}{\tau} = \mathbf{I} + \frac{1}{V_\beta} \int_{A_{\beta\sigma}} \mathbf{n}_{\beta\sigma} \mathbf{b}_{T\beta} dA = \mathbf{I} + \frac{1}{V_\beta} \int_{A_{\beta\sigma}} \mathbf{n}_{\beta\sigma} \mathbf{b}_{C\beta} dA \quad (2-176)$$

This integral called tortuosity since, in the absence of fluid flow, it modifies the diffusive properties of the system for the solute and heat transport.

The results with convection ($Pe \neq 0$), are illustrated in Fig. 2-8. One can see that, for low Péclet number (diffusive regime), the ratio of effective diffusion coefficient to molecular diffusion coefficient in the porous medium is almost constant and equal to the inverse of the tortuosity of the porous matrix, which is consistent with previously published results. On the opposite, for high Péclet numbers, the above mentioned ratio changes following a power-law trend after a transitional regime. The curves of longitudinal mass dispersion (Fig. 2-8a) and thermal dispersion (Fig. 2-8b) have the classical form of dispersion curves [111]. In our case, the longitudinal mass and heat dispersion coefficients can be represented by

$$\frac{\mathbf{D}_\beta^*|_{xx}}{D_\beta} = \frac{\mathbf{k}_\beta^*|_{xx}}{\varepsilon_\beta k_\beta} = \frac{1}{1.20} + 0.0234 Pe^{1.70} \quad (2-177)$$

where the dimensionless Péclet number is defined as

$$Pe = \frac{\langle \mathbf{v}_\beta \rangle^\beta \ell_{UC}}{D_\beta} \quad (2-178)$$

The dispersive part of the effective longitudinal thermal diffusion coefficient decreases with the Péclet number (Fig. 2-8c) and for high Péclet number it becomes negative. As we can see in Fig. 2-8c, there is a change of sign of the effective thermal diffusion coefficient.

This phenomenon may be explained by the fact that, by increasing the fluid velocity, the gradient of $b_{T\beta}|_x$ (x -coordinate of $\mathbf{b}_{T\beta}$) changes gradually its direction to the perpendicular flow path which could lead to a reversal the $b_{S\beta}|_x$ (x -coordinate of $\mathbf{b}_{S\beta}$) distribution and as a result, a change of the $D_{T\beta}^*|_{xx}$ sign (see Fig. 2-9).

This curve can be fitted with a correlation as

$$\frac{D_{T\beta}^*|_{xx}}{D_{T\beta}} = \frac{1}{1.20} + 0.0052Pe^{2.00} \quad (2-179)$$

The results in terms of Soret number, which is the ratio of isothermal diffusion coefficient on thermal diffusion coefficient, are original. Fig. 2-8d shows the ratio of effective Soret number to the Soret number in free fluid as a function of the Péclet number. The results show that, for a diffusive regime, one can use the same Soret number in porous media as the one in the free fluid ($S_T^*|_{xx}/S_T = 1$). This result agrees with the experimental results of Platten and Costesèque (2004) and Costesèque et al. (2004) but, for convective regimes, the effective Soret number is not equal with the one in the free fluid. For this regime, the Soret ratio decreases with increasing the Péclet number, and for high Péclet number it becomes negative.

To test the accuracy of the numerical solution, we have solved the steady-state vectorial closures A.I, A.IIa and A.IIb analytically for a plane Poiseuille flow between two horizontal walls separated by a gap H .

For this case, we found the following relation between the effective longitudinal thermal diffusion and the thermal diffusion in the free fluid ($\varepsilon_\beta = 1$)

$$\frac{D_{T\beta}^*|_{xx}}{D_{T\beta}} = 1 - \frac{Pr}{Sc} \times \frac{Pe^2}{210} \quad (2-180)$$

and the longitudinal dispersion is given (Wooding, 1960) by

$$\frac{D_\beta^*|_{xx}}{D_\beta} = 1 + \frac{Pe^2}{210} \quad (2-181)$$

Here, Pe is defined as $Pe = \frac{\langle v_{z\beta} \rangle^\beta H}{D_\beta}$ where $\langle v_{z\beta} \rangle^\beta$ is the z -component of the intrinsic average velocity of the fluid. The predicted values agree with the analytical results.

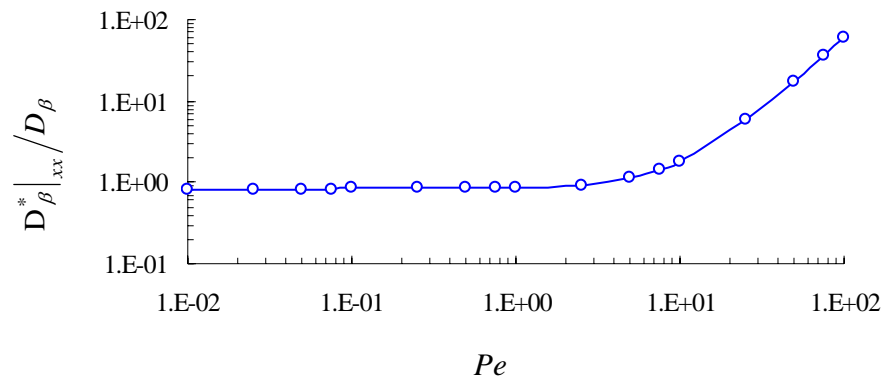
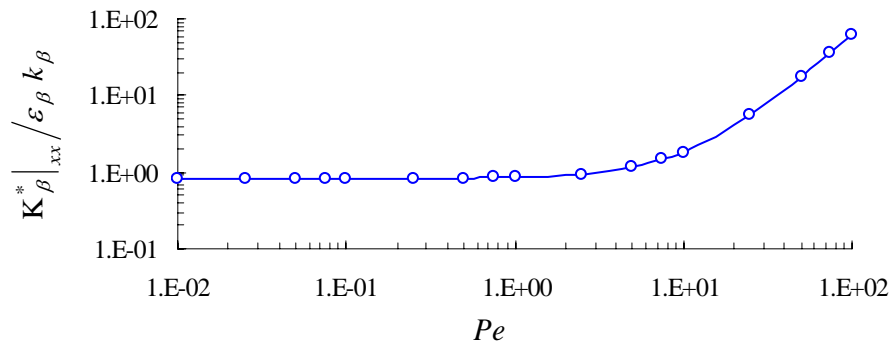
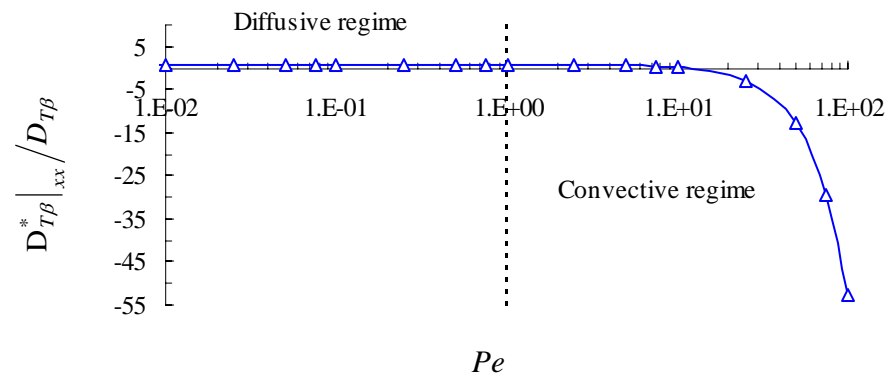
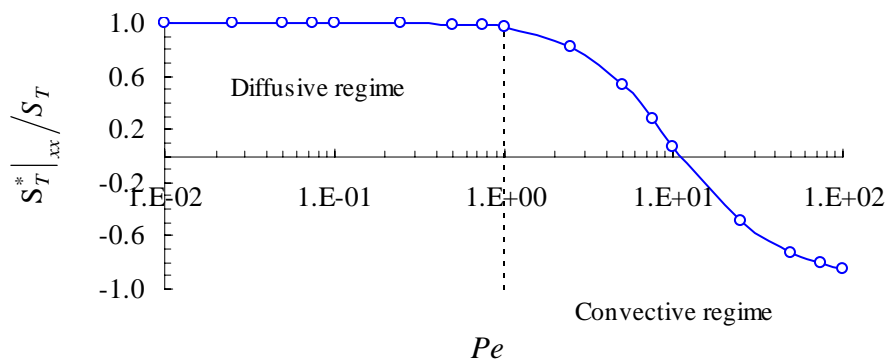
a**b****c****d**

Fig. 2-8. Effective, longitudinal coefficients as a function of Péclet number ($k_{\sigma} \approx 0$ and $\varepsilon_{\beta} = 0.8$): (a) mass dispersion, (b) thermal dispersion, (c) thermal diffusion and (d) Soret number

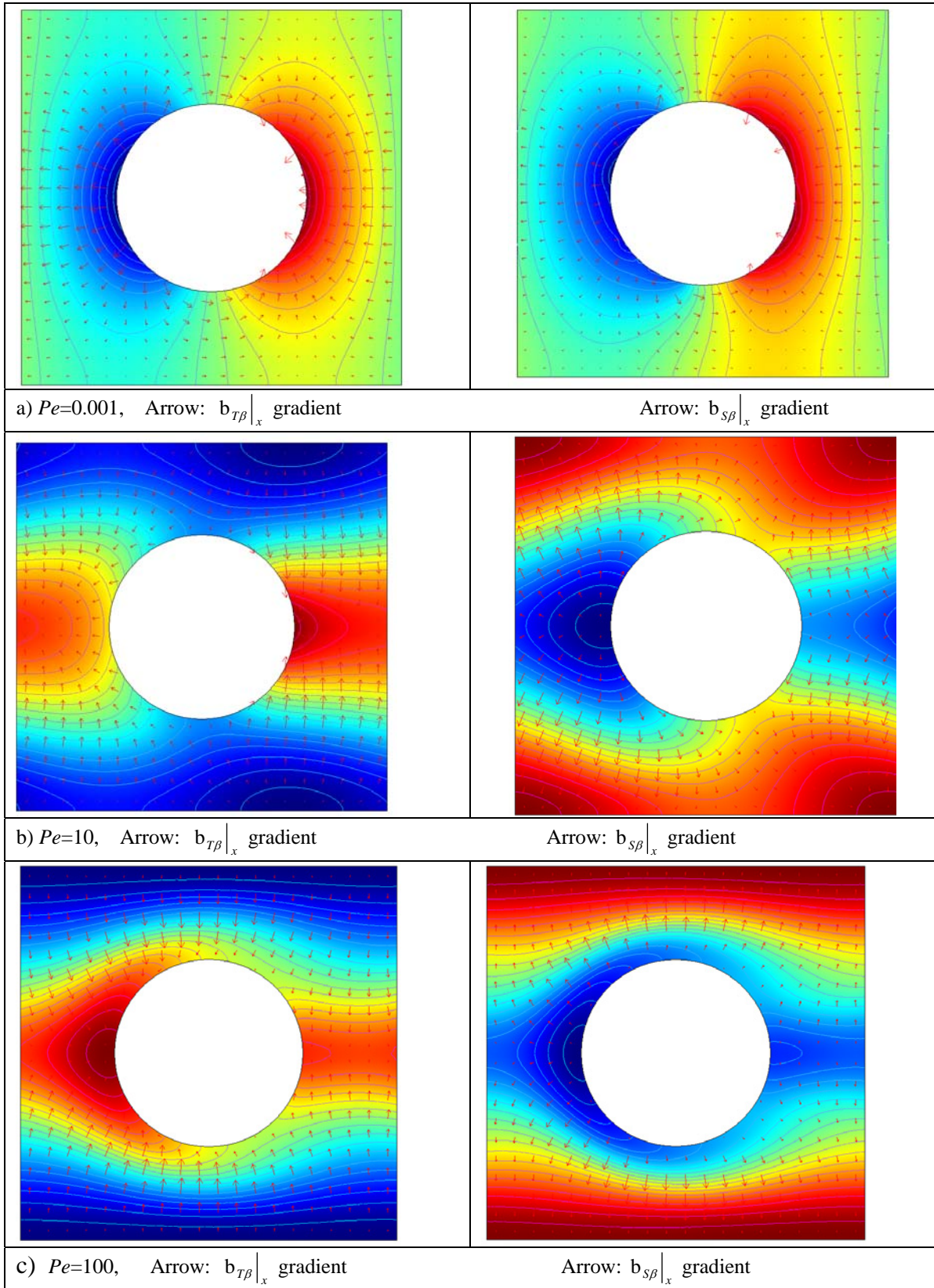


Fig. 2-9. Comparison of closure variables $b_{S\beta}|_x$ and $b_{T\beta}|_x$ for $\epsilon_\beta=0.8$

2.7.2 Conductive solid-phase ($k_\sigma \neq 0$)

In the previous section, we made the assumption $k_\sigma = 0$ only for simplification whereas, for example, the soil thermal conductivity is about 0.52 W/m.K, and it depends greatly on the solid thermal conductivity (in the order of 1 W/m.K) and varies with the soil texture. The thermal conductivity of most common non-metallic solid materials is about 0.05-20 W/m.K, and this value is very large for metallic solids [47]. Values of k_β for most common organic liquids range between 0.10 and 0.17 W/m.K at temperatures below the normal boiling point, but water, ammonia, and other highly polar molecules have values several times as large [76].

The increase of the effective thermal conductivity when increasing the phase conductivity ratio, κ , is well established from experimental measurements and theoretical approaches ([47, 111]) but the influence of this ratio on thermal diffusion is yet unknown. In this section, we study the influence of the conductivity ratio on the effective thermal diffusion coefficient. To achieve that, we solved numerically the closure problems with different conductivity ratios. Fig. 2-10 shows the dependence of the effective tensors with the conductivity ratio, for different Péclet numbers. As shown in Fig. 2-10a the effective conductivity initially increases with an increase in κ and then reaches an asymptote. As the Péclet number increases, convection dominates and the effect of κ on $k^*/\varepsilon_\beta k_\beta$ is noticeably different. The transition between the high and low Péclet number regimes occurs around $Pe = 10$ (see also [47]). For higher Péclet numbers ($Pe > 10$), $k^*/\varepsilon_\beta k_\beta$ is enhanced by lowering κ , as shown in Fig. 2-10 a for $Pe = 14$. Our results for $D_{T\beta}^*/D_{T\beta}$ have a similar behaviour as $k^*/\varepsilon_\beta k_\beta$. Fig. 2-10 b shows the influence of the conductivity ratio on the effective thermal diffusion coefficients for different Péclet numbers. One can see that increasing the solid thermal conductivity increases the value of the effective thermal diffusion coefficient for low Péclet numbers.

On the contrary, for high Péclet numbers ($Pe > 10$) increasing the thermal conductivity ratio decreases the absolute value of the effective thermal diffusion coefficient. As shown in Fig. 2-10b, the thermal conductivity ratio has no influence on the thermal diffusion coefficients for the pure diffusion case ($Pe = 0$). As we can see also in Fig. 2-11, both

closure variables fields $b_{s\beta}$ and $b_{T\beta}$ change with the thermal conductivity ratio but coupling results defined by Eq. (2-172), when velocity field is zero, are constant.

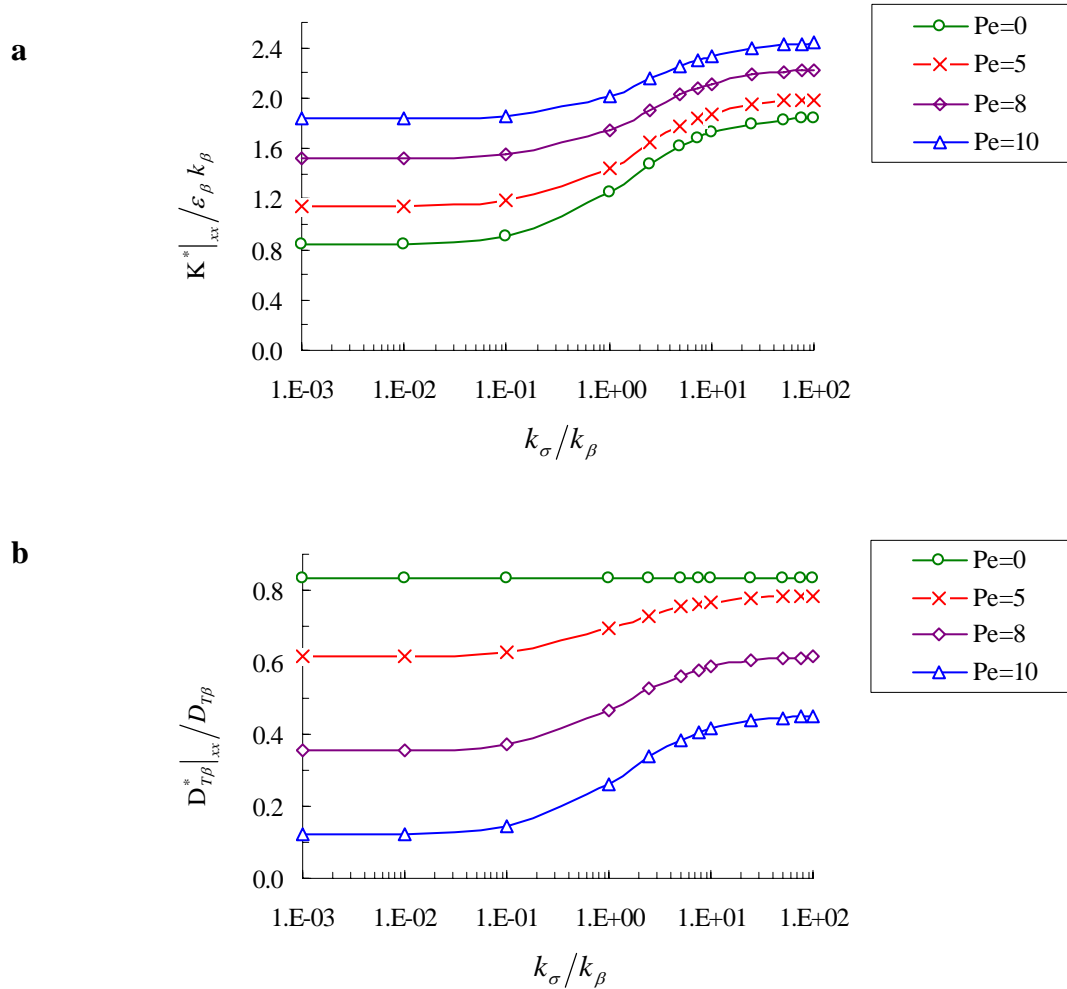


Fig. 2-10. The influence of conductivity ratio (κ) on (a) effective, longitudinal thermal conductivity and (b) effective thermal diffusion coefficients ($\varepsilon_\beta=0.8$)

Fig. 2-12 shows the closure variables fields $b_{T\beta}|_x$ and $b_{s\beta}|_x$ for a Péclet number equal to 14, we can see also that both closure variables change with the thermal conductivity ratio. We can also solve the closure problem in a Chang's unit cell (Fig. 2-4). In the closure problem we have a Dirichlet boundary condition in place of a periodic boundary. We have solved the closure problems given by Eqs. (2-117)-(2-121) for the thermal conductivity coefficients and Eqs. (2-125)-(2-127) for the thermal diffusion coefficient for pure

diffusion. Fig. 2-13 shows the effective thermal diffusion and thermal conductivity versus the thermal conductivity ratio. One can see here also that, for pure diffusion, changing the conductivity ratio does not change the effective values.

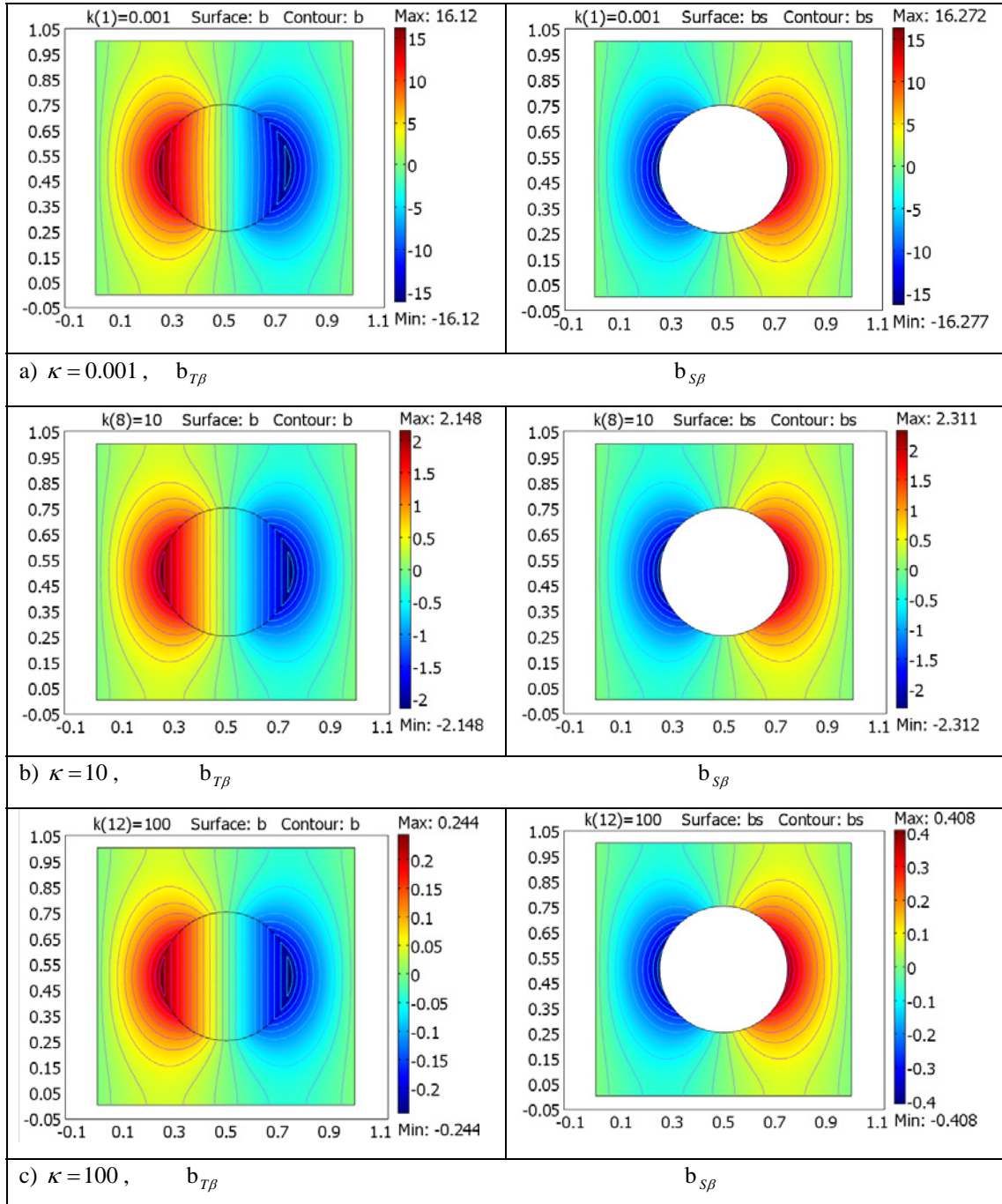


Fig. 2-11. Comparison of closure variables fields $b_{T\beta}$ and $b_{S\beta}$ for different thermal conductivity ratio (κ) at pure diffusion ($Pe = 0$ & $\varepsilon_\beta = 0.8$)

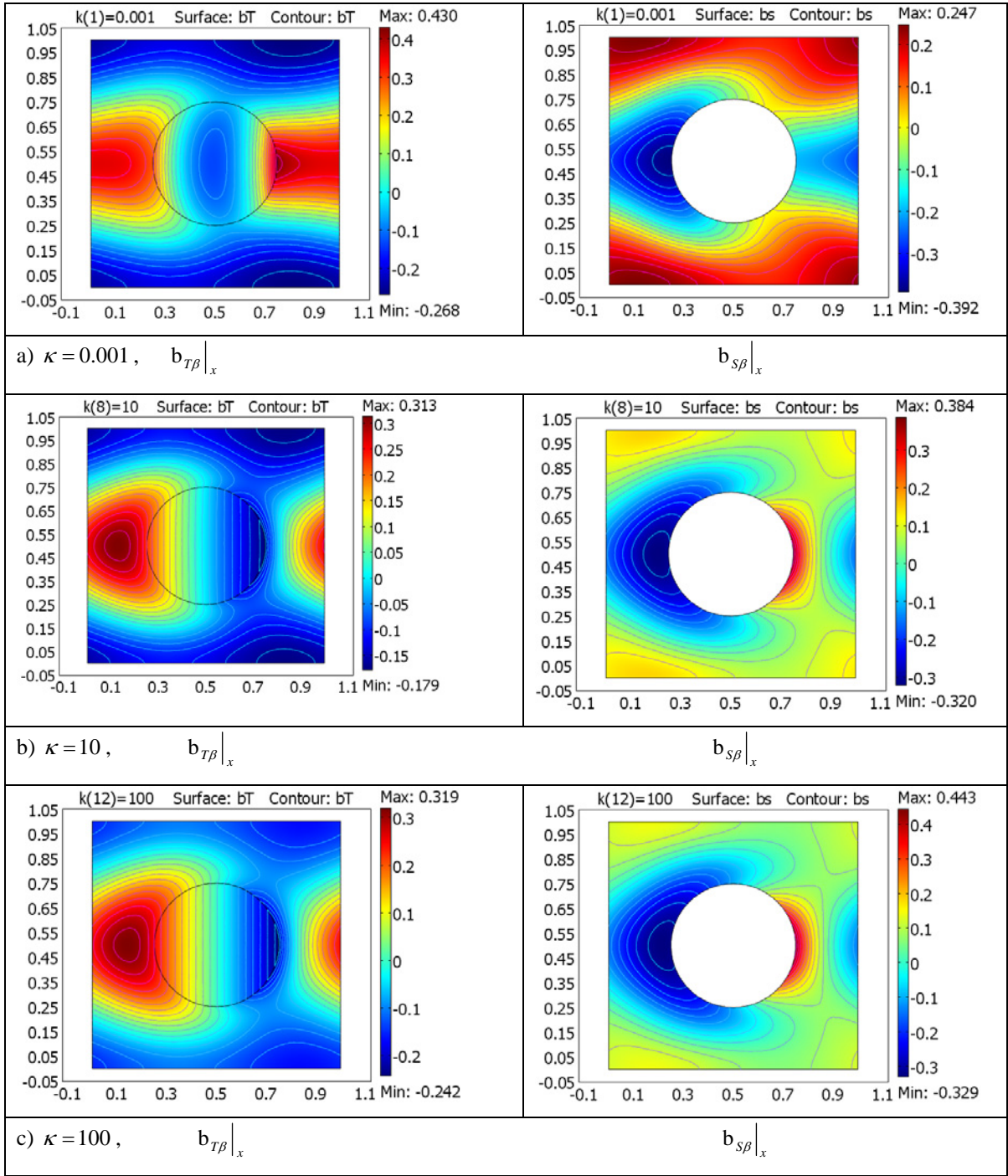


Fig. 2-12. Comparison of closure variables fields $b_{T\beta}|_x$ and $b_{S\beta}|_x$ for different thermal conductivity ratio (κ) at convective regime ($Pe = 14$ & $\varepsilon_\beta = 0.8$)

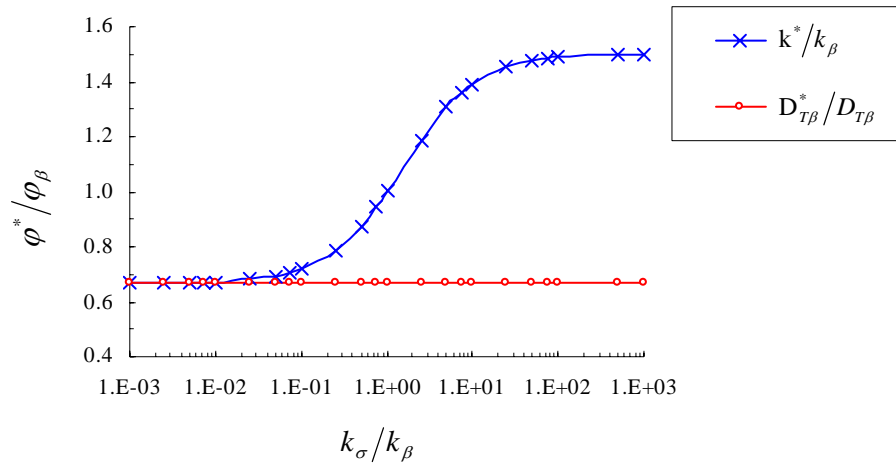


Fig. 2-13. The influence of conductivity ratio (κ) on the effective coefficients by resolution of the closure problem in a Chang's unit cell ($\varepsilon_\beta=0.8$, $Pe=0$)

2.7.3 Solid-solid contact effect

It has been emphasized in the literature that the “solid-solid contact effect” has a great consequence on the effective thermal conductivity [79, 92], it can also change the effective thermal diffusion coefficient.

In order to model the effect of particle-particle contact we used the model illustrated in Fig. 2-14, in which the particle-particle contact area is determined by the adjustable parameter a/d (the fraction of particle-particle contact area).

When $a/d=0$ then the β -phase is continuous and the ratio k^*/k_β becomes constant for large values of κ . When a/d is not zero, at large values of κ , the solution predicts a linear dependence of k^*/k_β on the ratio κ . The calculated results for both the continuous β -phase (non-touching particles) and the continuous σ -phase (touching particles) are shown in Fig. 2-15. The comparison presented by Nozad et al. (1985) showed a very good agreement between theory and experiment. Sahraoui and Kaviany (1993) repeated the computation of Nozad et al. and find that the selection of $a/d=0.002$ gives closest agreement with experiments.

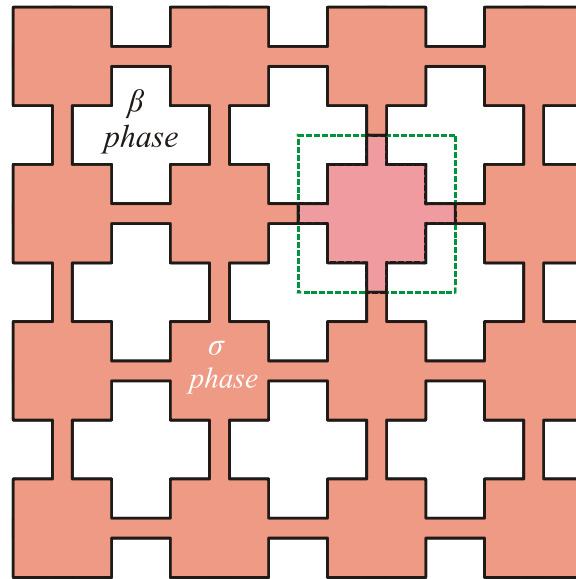


Fig. 2-14. Spatially periodic model for solid-solid contact

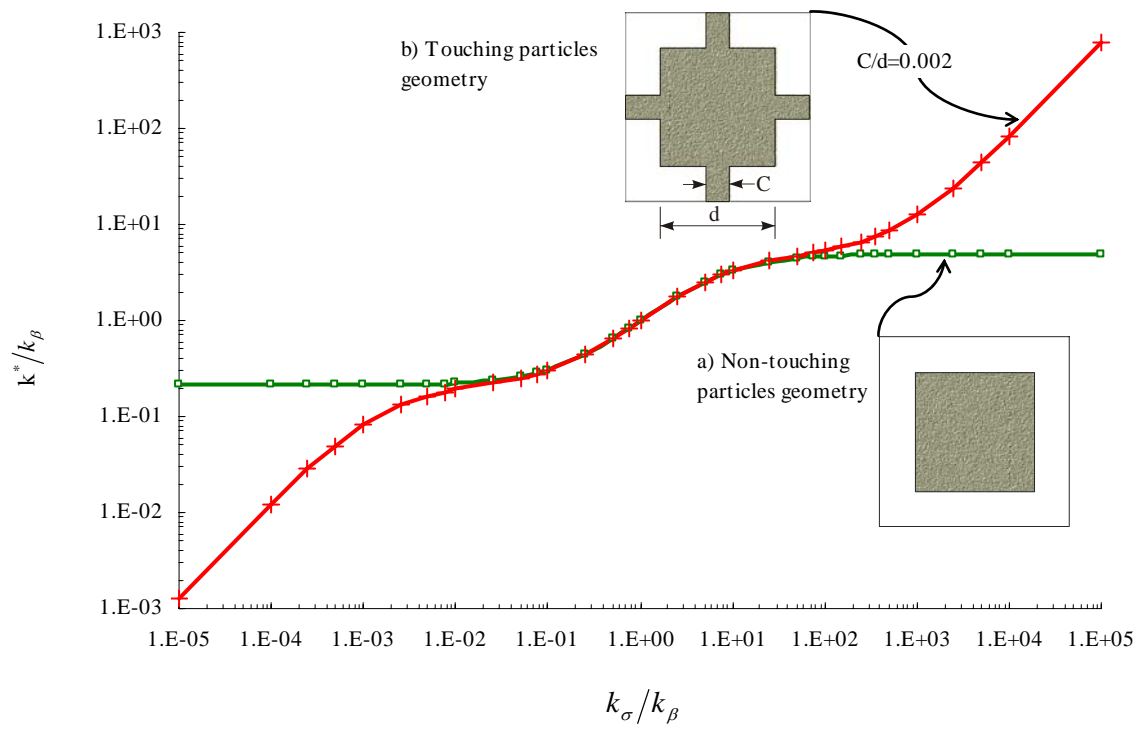


Fig. 2-15. Effective thermal conductivity for (a) non-touching particles, $a/d=0$ (b) touching particles, $a/d=0.002$, ($\varepsilon_\beta=0.36$, $Pe=0$)

Unfortunately we cannot use this type of geometry to study the effect of solid-solid connection on effective thermal diffusion coefficient because the fluid phase is not continuous. We have used therefore a geometry which has only particle connection in the x -direction as shown in Fig. 2-16.

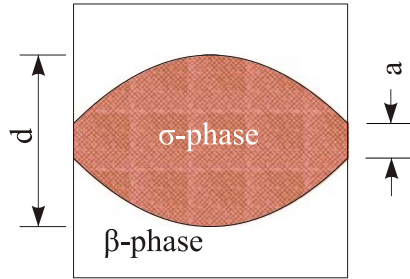


Fig. 2-16. Spatially periodic unit cell to solve the thermal diffusion closure problem with solid-solid connections $a/d=0.002$, ($\epsilon_\beta=0.36$, $Pe=0$)

Fig. 2-17 shows the results for the effective coefficient obtained from the resolution of the closure problem for pure diffusion on the unit cell shown in Fig. 2-16. The a/d ratio has been selected to be 0.002. It is clear from Fig. 2-17 that, while the particle connectivity changes greatly the effective values, the effective thermal diffusion coefficients is independent of the solid connectivity.

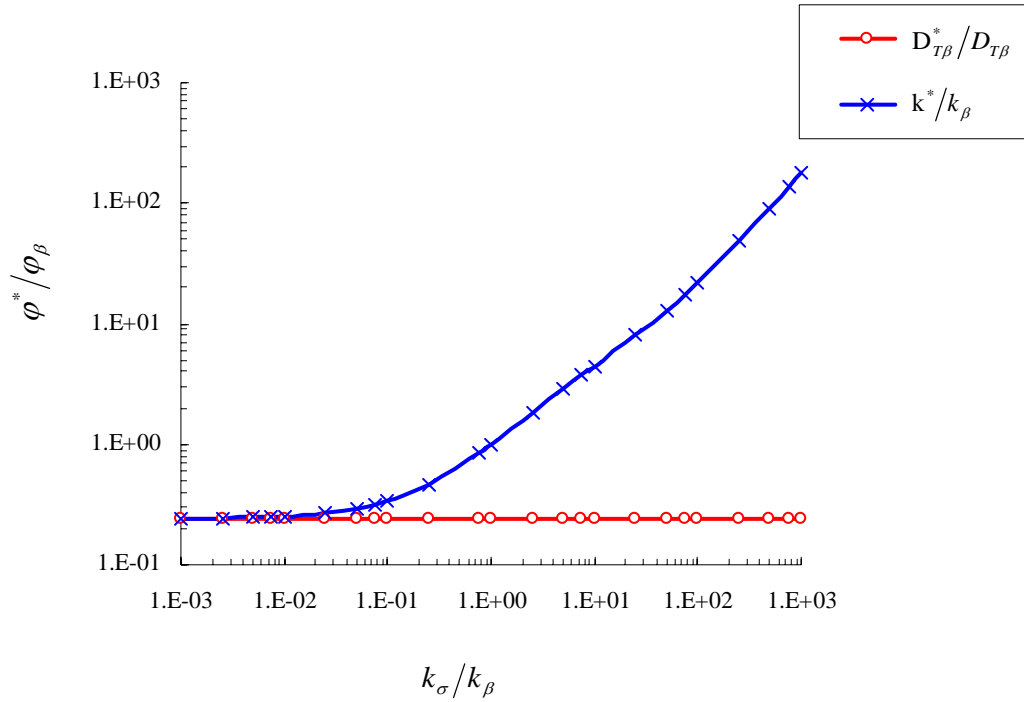


Fig. 2-17. Effective thermal conductivity and thermal diffusion coefficient for touching particles, $a/d=0.002$, $\varepsilon_\beta=0.36$, $Pe=0$

The same problems have been solved on the geometry shown in Fig. 2-14 but without y-connection parts.

Comparison of closure variables fields $b_{T\beta}$ and $b_{S\beta}$ when the solid phase is continuous, for different thermal conductivity ratios (κ) and pure diffusion are shown in Fig. 2-18. As we can see the closure variable for concentration $b_{S\beta}$ also change with conductivity ratio.

The effective thermal conductivity and thermal diffusion coefficients for this closure problem are plotted in Fig. 2-19, despite the results illustrated in Fig. 2-15, the ratio k^*/k_β becomes constant for small values of κ because in y-direction there is not any particle-particle resistance. At large values of κ the solution predicts a linear dependence of k^*/k_β , on the ratio κ . However, the ratio $D_{T\beta}^*/D_{T\beta}$ remains constant with the thermal conductivity ratio κ .

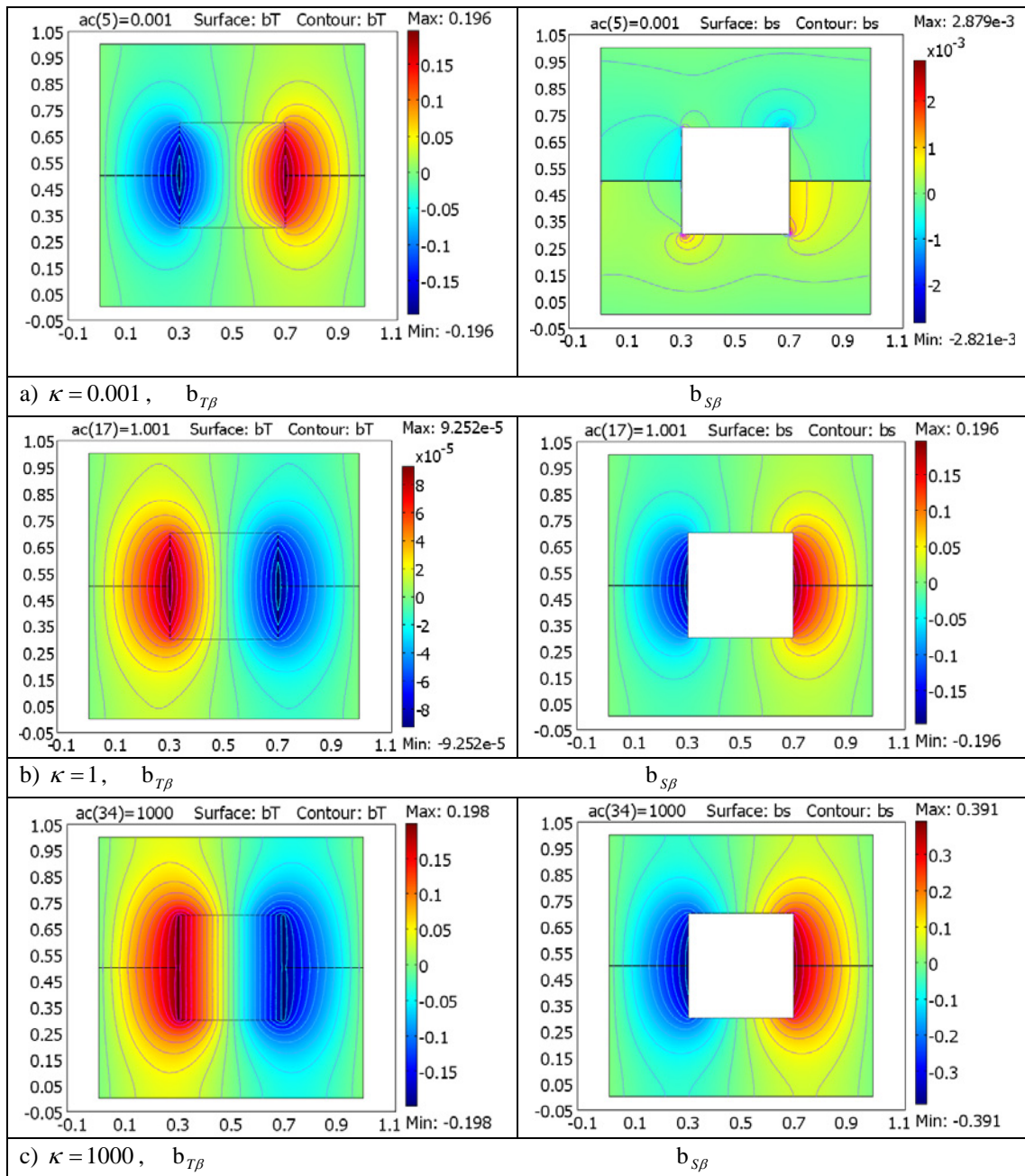


Fig. 2-18. Comparison of closure variables fields $b_{T\beta}$ and $b_{S\beta}$ when the solid phase is continue, for different thermal conductivity ratio (κ) at pure diffusion

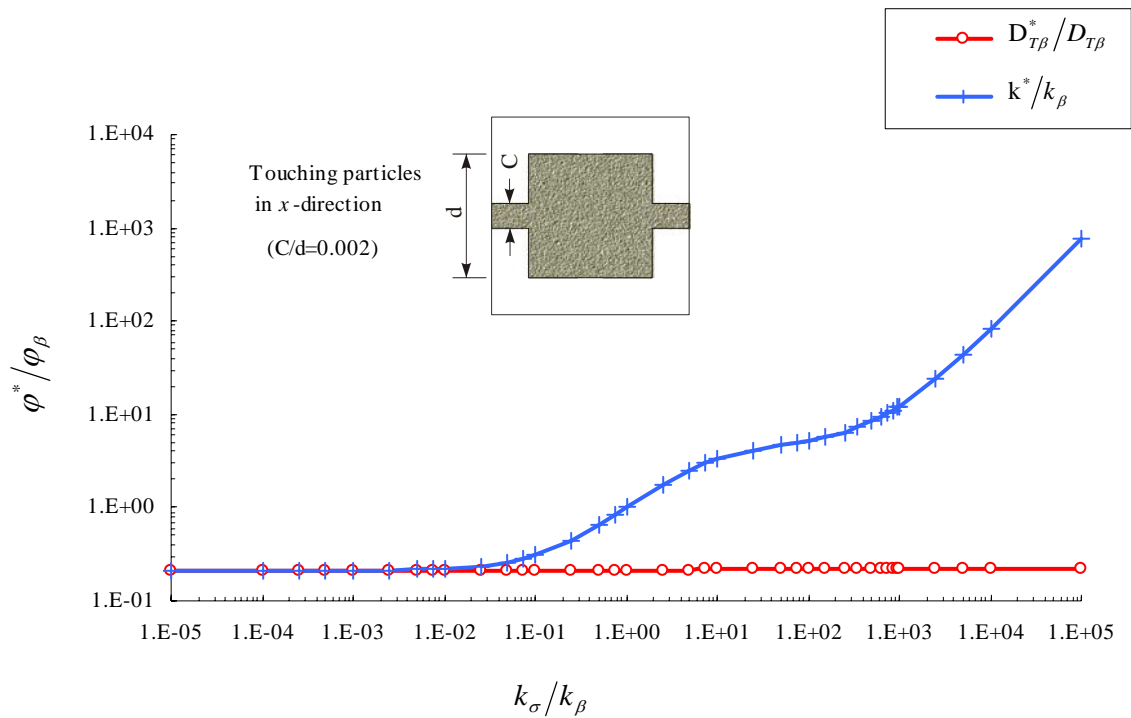


Fig. 2-19. Effective thermal conductivity and thermal diffusion coefficient for touching particles, $a/d=0.002$, $\varepsilon_\beta=0.36$

2.8 Conclusion

To summarize our findings, in this chapter we determined the effective Darcy-scale coefficients for heat and mass transfer in porous media using a volume averaging technique including thermal diffusion effects. We showed that the effective Soret number may depart from the micro-scale value because of advection effects. The results show that, for low Péclet numbers, the effective thermal diffusion coefficient is the same as the effective diffusion coefficient and that it does not depend on the conductivity ratio. However, in this regime, the effective thermal conductivity changes with the conductivity ratio. On the opposite, for high Péclet numbers, both the effective diffusion and thermal conductivity increase following a power-law trend, while the effective thermal diffusion coefficient decreases. In this regime, a change of the conductivity ratio will change the effective thermal diffusion coefficient as well as the effective thermal conductivity coefficient. At pure diffusion, even if the effective thermal conductivity depends on the particle-particle contact, the effective thermal diffusion coefficient is always constant and independent on the connectivity of the solid phase.

Chapter 3

Microscopic simulation and validation

3. Microscopic simulation and validation

In this chapter, the macroscopic model obtained by the theoretical method is validated by comparison with direct numerical simulations at the pore-scale. Then, coupling between forced convection and Soret effect for different cases is investigated.

Nomenclature of Chapter 3

$A_{\beta\sigma}$	Area of the β - σ interface contained within the macroscopic region, m ²	$\langle T_\beta \rangle^\beta$	Intrinsic average temperature in the β -phase, K
A_S	segregation area, m ²	T_H, T_C	Hot and cold temperature
c_p	Constant pressure heat capacity, J.kg/K	\mathbf{v}_β	Mass average velocity in the β -phase, m/s
c_β	Total mass fraction in the β -phase	x, y	Cartesian coordinates, m
$\langle c_\beta \rangle^\beta$	Intrinsic average mass fraction in the β -phase	<i>Greek symbols</i>	
c_0	Initial concentration	ε_β	Volume fraction of the β -phase or porosity
Da	Darcy number	κ	k_σ/k_β , conductivity ratio
D_β	Binary diffusion coefficient, m ² /s	μ_β	Dynamic viscosity for the β -phase, Pa.s
$D_{T\beta}$	Thermal diffusion coefficient, m ² /s.K	ρ_β	Total mass density in the β -phase, kg/m ³
$\mathbf{D}_{T\beta}^*$	Total thermal diffusion tensor, m ² /s.K	τ	Scalar tortuosity factor
\mathbf{D}_β^*	Total dispersion tensor, m ² /s	ψ	Separation factor or dimensionless Soret number
k_β	Thermal conductivity of the fluid phase, W/m.K	<i>Subscripts, superscripts and other symbols</i>	
k_σ	Thermal conductivity of the solid phase, W/m.K	β	Fluid-phase
\mathbf{K}_β	Permeability tensor, m ²	σ	Solid-phase
$\mathbf{k}_\beta^*, \mathbf{k}^*$	Total thermal conductivity tensors for no-conductive and conductive solid phase, W/m.K	$\beta\sigma$	β - σ interphase
$\mathbf{n}_{\beta\sigma}$	Unit normal vector directed from the β -phase toward the σ -phase	*	Effective quantity
Pe	Cell Péclet number	$\langle \rangle$	Spatial average
S_T	Soret number	$\langle \rangle^\beta$	Intrinsic β -phase average
\mathbf{S}_T^*	Effective Soret number		
t	Time, s		
T_β	Temperature of the β -phase, K		

3.1 Microscopic geometry and boundary conditions

In order to validate the theory developed by the up-scaling technique in the previous chapter, we have compared the results obtained by the macro-scale equations with direct, pore scale, simulations. The porous medium is made of an array of the unit cell described in Fig. 2-6. The array is chosen with 15 unit cells, as illustrated in Fig. 3-1.

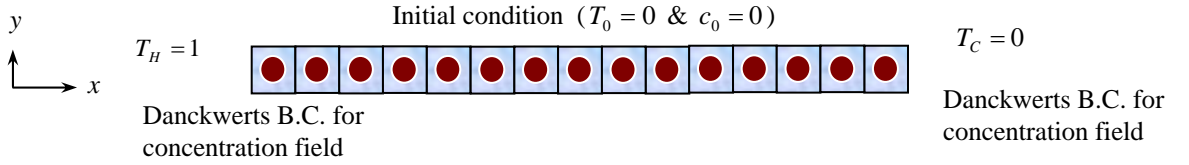


Fig. 3-1. Schematic of a spatially periodic porous medium (T_H : Hot Temperature and T_C : Cold Temperature)

In the macro-scale problem, the effective coefficients are obtained from the previous solution of the closure problem. The macroscopic, effective coefficients are the axial diagonal terms of the tensor. Given the boundary and initial conditions, the resulting macro-scale problem is one-dimensional.

Calculations have been carried out in the case of a binary fluid mixture with simple

properties such that, $\psi = \Delta T \times \frac{D_{T\beta}}{D_\beta} = 1$ and $(\rho c_p)_\sigma = (\rho c_p)_\beta$.

Microscopic scale simulations, as well as the resolution for the macroscopic problem, have been performed using COMSOL MultiphysicsTM.

The 2D pore-scale dimensionless equations and boundary conditions to be solved are Eqs. (2-1)-(2-9). Velocity was taken to be equal to zero (no-slip) on every surface except at the entrance and exit boundaries. Danckwerts condition (Danckwerts, 1953) was imposed for the concentration at the entrance and exit (Fig. 3-1). In this dimensionless system, we have imposed a thermal gradient equal to one.

$$\text{BC1: } x = 0 \quad \mathbf{n}_{\beta e} \cdot (\nabla c_\beta + \psi \nabla T_\beta) = 0 \quad \text{and } T = T_H = 1 \quad (3-1)$$

$$\text{BC2: } x = 15 \quad \mathbf{n}_{\beta e} \cdot (\nabla c_\beta + \psi \nabla T_\beta) = 0 \quad \text{and } T = T_C = 0 \quad (3-2)$$

$$\text{IC: } t = 0 \quad c = c_0 = 0 \quad \text{and } T = T_0 = 0 \quad (3-3)$$

Mass fluxes are taken equal to zero on other outside boundaries and on all fluid-solid boundary surfaces. Zero heat flux was used on the outside boundary except at the entrance and exit boundaries where we have imposed a thermal gradient. In the case of conductive solid-phase, the continuity boundary condition has been imposed for heat flux on the fluid-solid boundary surface while these surfaces will be adiabatic for a no-conductive solid-phase case.

Macroscopic fields are also obtained using the dimensionless form of equations (2-17), (2-18) (2-76) and (2-128). We obtained, from a method for predicting the permeability tensor [78], a Darcy number equal to $Da = K_\beta / \ell_{UC}^2 = 0.25$, for the symmetric cell shown in Fig. 2-6.

The boundary condition at the exit and entrance of the macro-scale domain were taken similar to the pore scale expressions but in terms of the averaged variables. Depending on the pressure boundary condition and therefore the Péclet numbers, we can have different flow regimes. First, we assume that the solid phase is not conductive (Section 3.2) and we compare the results of the theory with the direct simulation. Then, the comparison will be done for a conductive solid-phase (Section 3.3) and different Péclet numbers. In all cases, the micro-scale values are cell averages obtained from the micro-scale fields.

3.2 Non-conductive solid-phase ($k_\sigma \approx 0$)

In this section, the solid thermal conductivity is assumed to be very small and will be neglected in the equations and the solid-phase energy equation is not solved. Therefore we can express the equation of heat transfer Eq. (2-1) to Eq. (2-4) as

$$\left(\rho c_p\right)_\beta \frac{\partial T_\beta}{\partial t} + \left(\rho c_p\right)_\beta \nabla \cdot (T_\beta \mathbf{v}_\beta) = \nabla \cdot (k_\beta \nabla T_\beta), \text{ in the } \beta\text{-phase} \quad (3-4)$$

$$\text{BC1: } \mathbf{n}_{\beta\sigma} \cdot (k_\beta \nabla T_\beta) = 0, \text{ at } \mathcal{A}_{\beta\sigma} \quad (3-5)$$

The various contributions of the fluid flow including pure diffusion and dispersion can be expressed as presented in the followings.

3.2.1 Pure diffusion ($Pe \approx 0, k_\sigma \approx 0$)

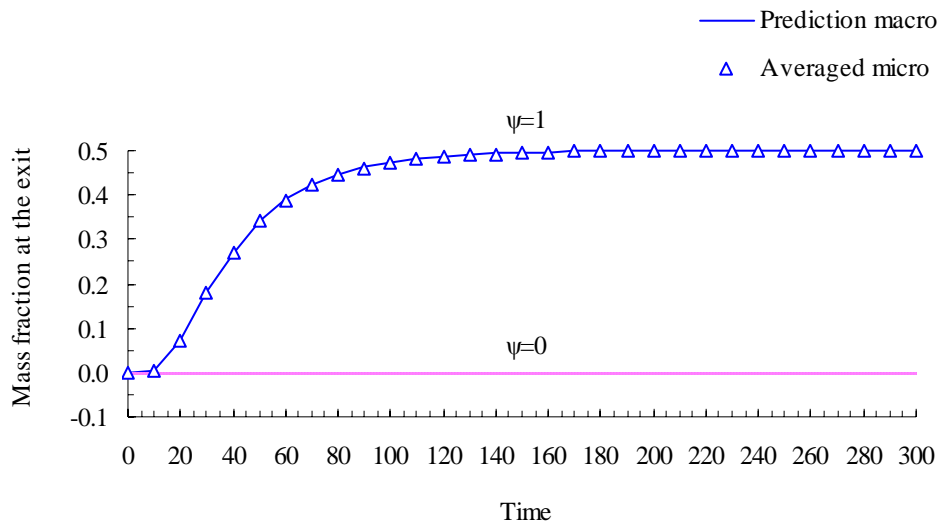
We have first investigated the Soret effect on mass transfer in the case of a static homogeneous mixture. In this case, we have imposed a temperature gradient equal to one,

in the dimensionless system, for the microscopic and macroscopic models, and we have imposed a Danckwerts boundary condition for concentration at the medium entrance and exit. The porosity ε_β of the unit cell is equal to 0.8 and, therefore, in the case of pure diffusion, the effective coefficients (diffusion, thermal conductivity and thermal diffusion) have been calculated with a single tortuosity coefficient equal to 1.20 as obtained from the solution of the closure problem shown in Fig. 2-7.

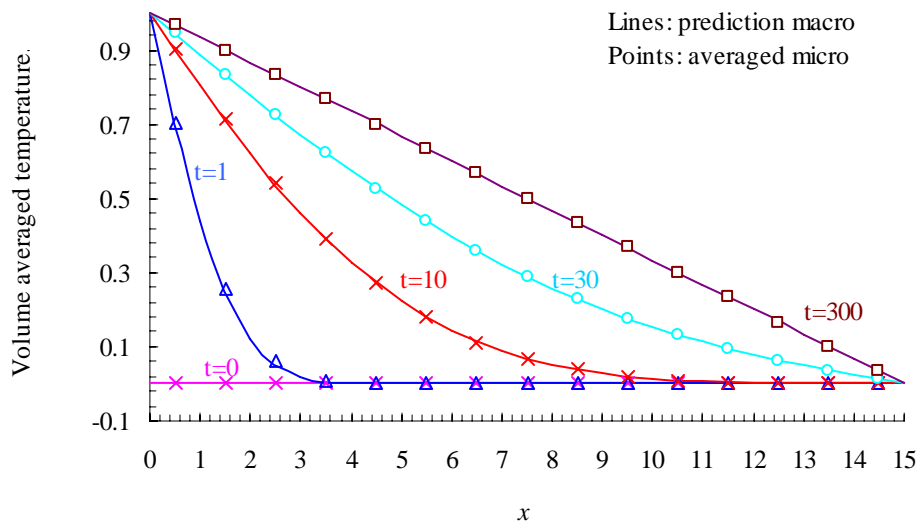
Fig. 3-2a shows the temporal evolution of the concentration at the exit for the two models, microscopic and macroscopic, with ($\psi = 1$) and without ($\psi = 0$) thermal diffusion.

One can see that thermal diffusion modifies the local concentration and we cannot ignore this effect. The maximum modification at steady-state is equal to ψ . We also see that the theoretical results are here in excellent agreement with the direct simulation numerical results.

a



b



c

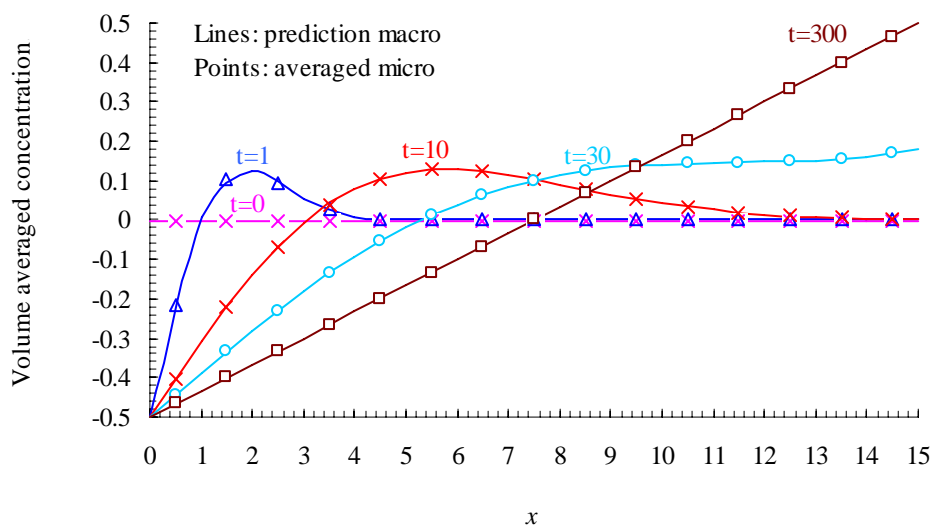


Fig. 3-2. Comparison between theoretical and numerical results at diffusive regime and $\kappa=0$, (a) time evolution of the concentration at $x = 15$ and (b and c) instantaneous temperature and concentration field

Fig. 3-2b and Fig. 3-2c show the distribution of temperature and concentration in the medium at given times. Here also, one can observe the change of the concentration profile generated by the Soret effect compared with the isothermal case ($c=0$), and the microscopic model also perfectly fits the macroscopic results. These modifications are well matched with temperature profiles for each given time.

3.2.2 Diffusion and convection ($Pe \neq 0, k_\sigma \approx 0$)

Next, we have imposed different pressure gradients on the system shown in Fig. 3-3. The temperature and concentration profiles at $Pe = 1$ for different times are shown in Fig. 3-3a and Fig. 3-3b, respectively.

The results show a significant change in the concentration profile because of species separation when imposing a thermal gradient. Here, also, the theoretical predictions are in very good agreement with the direct simulation of the micro-scale problem.

Comparison of the concentration elution curves at $x=0.5, 7.5$ and 13.5 in Fig. 3-3c between the two regimes (with and without thermal diffusion) also shows that the elution curve for no-thermal diffusion is different from the one with thermal diffusion. The shape of these curves is very different from the pure diffusion case (Fig. 3-2a) because, in this case, the thermal diffusion process is changed by forced convection. One also observes a very good agreement between the micro-scale simulations and the macro-scale predictions.

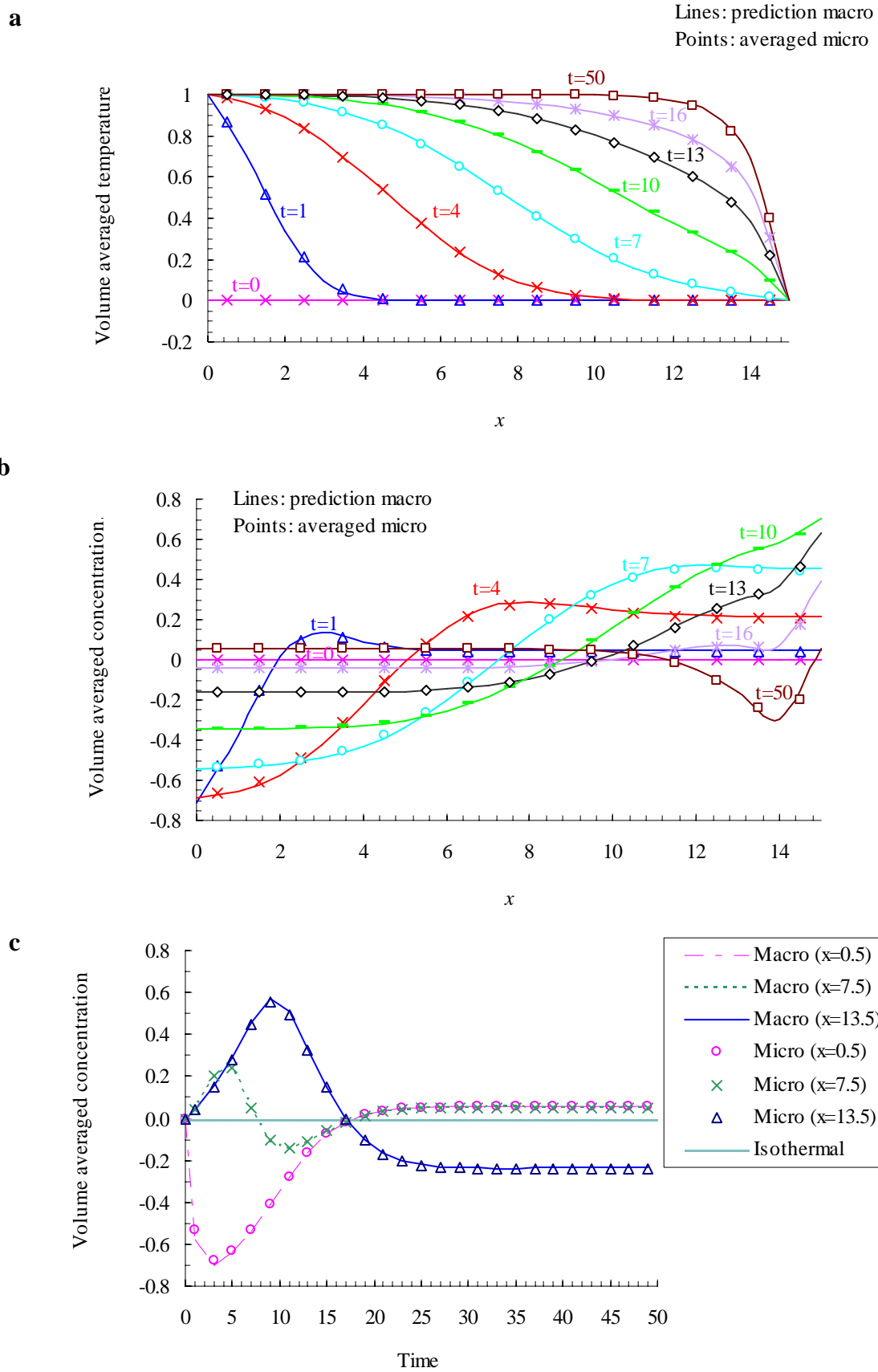


Fig. 3-3. Comparison between theoretical and numerical results, $\kappa=0$ and $Pe=1$, (a and b) instantaneous temperature and concentration field, (c) time evolution of the concentration at $x = 0.5, 7.5$ and 13.5

3.3 Conductive solid-phase ($k_\sigma \neq 0$)

Thermal properties of the solid matrix have also to be taken into account in the thermal diffusion process. In this section, the heat diffusion through the solid-phase is considered. Therefore, the comparison has been done for the same micro-scale model but with a conductive solid-phase. First, we compare the results for a pure diffusion system and then we will describe the local dispersion coupling with Soret effect.

3.3.1 Pure diffusion ($Pe \approx 0, k_\sigma \neq 0$)

Before we start to compare the theoretical results with the numerical one for the case of a conductive solid-phase, in order to see clearly the influence of the thermal conductivity ratio on the separation process, we have solved the microscopic coupled heat and mass transport equations (Eqs. (2-1)-(2-6)) in a simple geometry containing two unit cells. In the dimensionless system shown in Fig. 3-4.

Danckwerts conditions were imposed for the concentration at the entrance and exit (Fig. 3-1). In this dimensionless system, we have imposed a horizontal thermal gradient equal to one.

$$\text{BC1: } x = 0 \quad \mathbf{n}_{\beta e} \cdot (\nabla c_\beta + \psi \nabla T_\beta) = 0 \quad \text{and } T = T_H = 1 \quad (3-6)$$

$$\text{BC2: } x = 2 \quad \mathbf{n}_{\beta e} \cdot (\nabla c_\beta + \psi \nabla T_\beta) = 0 \quad \text{and } T = T_C = 0 \quad (3-7)$$

$$\text{IC: } t = 0 \quad c = c_0 = 0 \quad \text{and } T = T_0 = 0 \quad (3-8)$$

Mass fluxes are taken equal to zero on other outside boundaries and on all fluid-solid boundary surfaces. The continuity boundary condition has been imposed for heat flux on the fluid-solid boundary surface. Steady-state concentration and temperature fields for different thermal conductivity ratio are represented in Fig. 3-4. As we can see, the concentration distribution (or separation) depends on the temperature distribution in the medium. When the temperature distribution changes with the thermal conductivity, it will also change the concentration distribution.

Fig. 3-5 shows the steady-state concentration and temperature profiles at $y=0.5$ (a section situated in the middle of the medium). We can see clearly that the thermal conductivity ratio changes the final temperature and concentration profiles. However, the final separations are constant. That means, although the thermal conductivity ratio change

locally the concentration distribution in the medium, it has no influence on the final separation. We discuss this point in more details below.

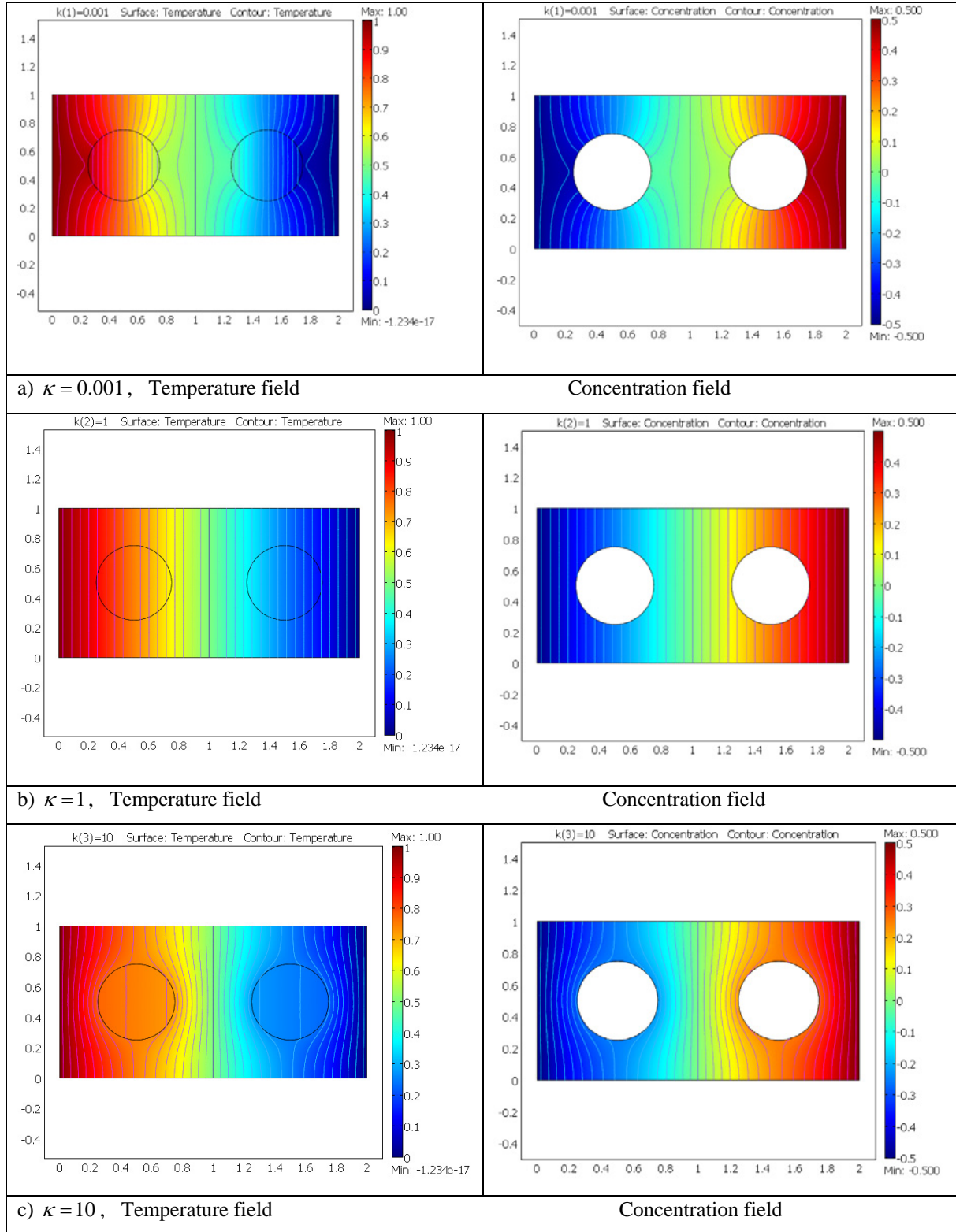


Fig. 3-4. Influence of the thermal conductivity ratio on the temperature and concentration fields

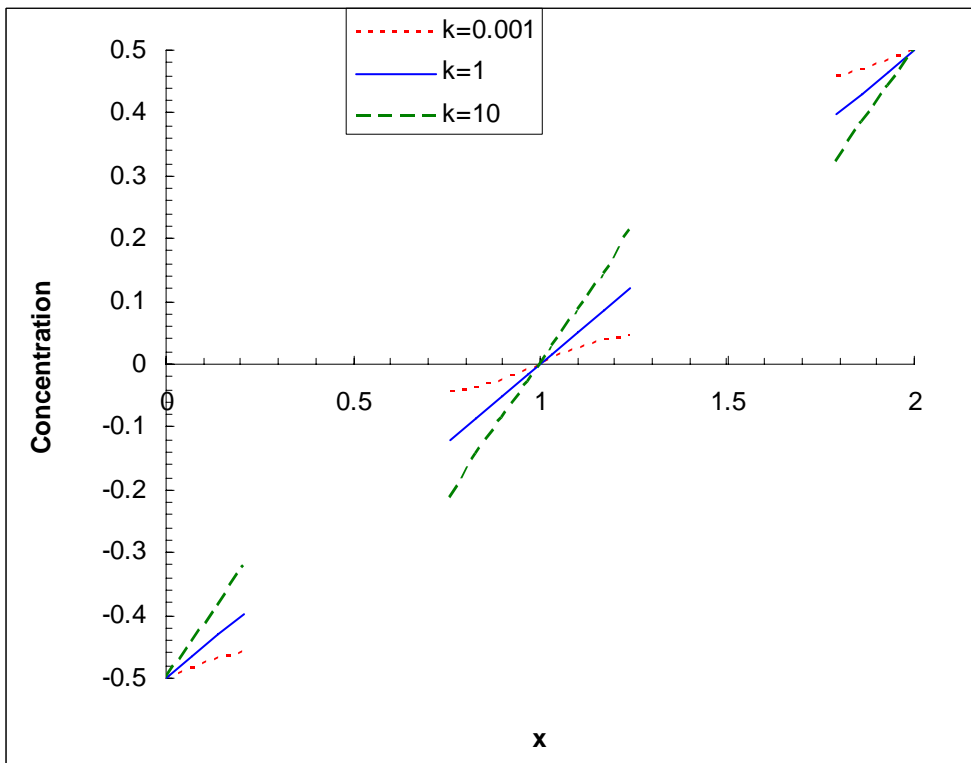
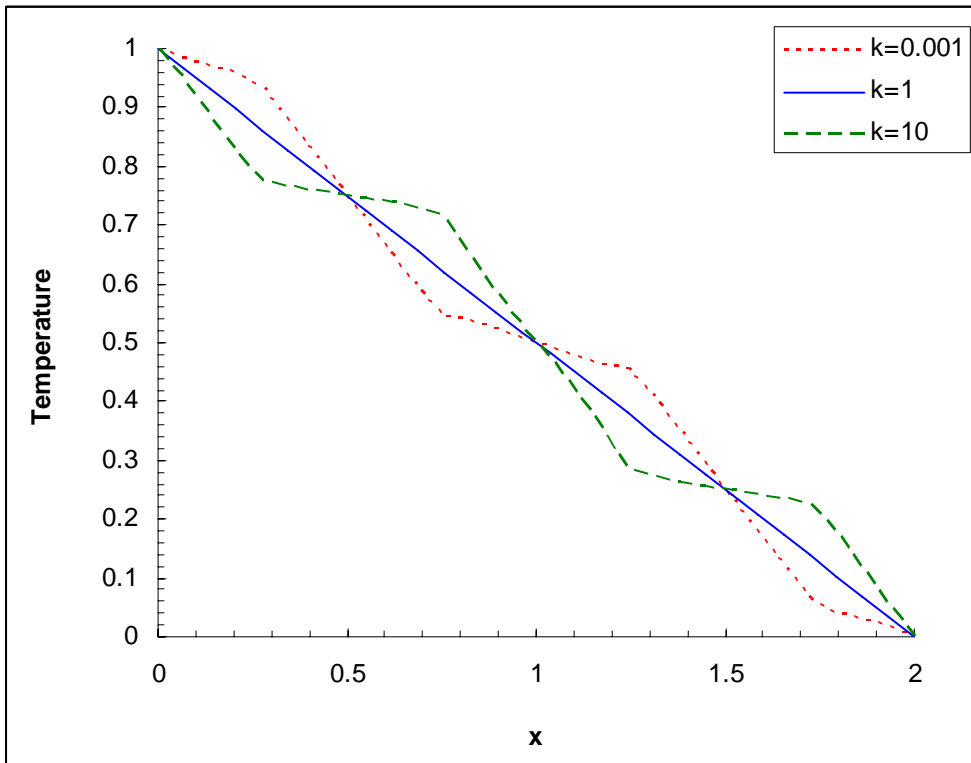


Fig. 3-5. (a) Temperature and (b) concentration profiles for different conductivity ratio

The influence of the thermal conductivity on the transient separation process is presented in Fig. 3-6 for different time steps.

As we can see, the thermal conductivity of the solid phase locally changes the concentration profile. We must note here that one cannot judge from these results whether the thermal conductivity ratio has an influence on the effective thermal diffusion coefficient or not. Actually, we must compare the average of the fields with the theoretical results as we will show in the following example.

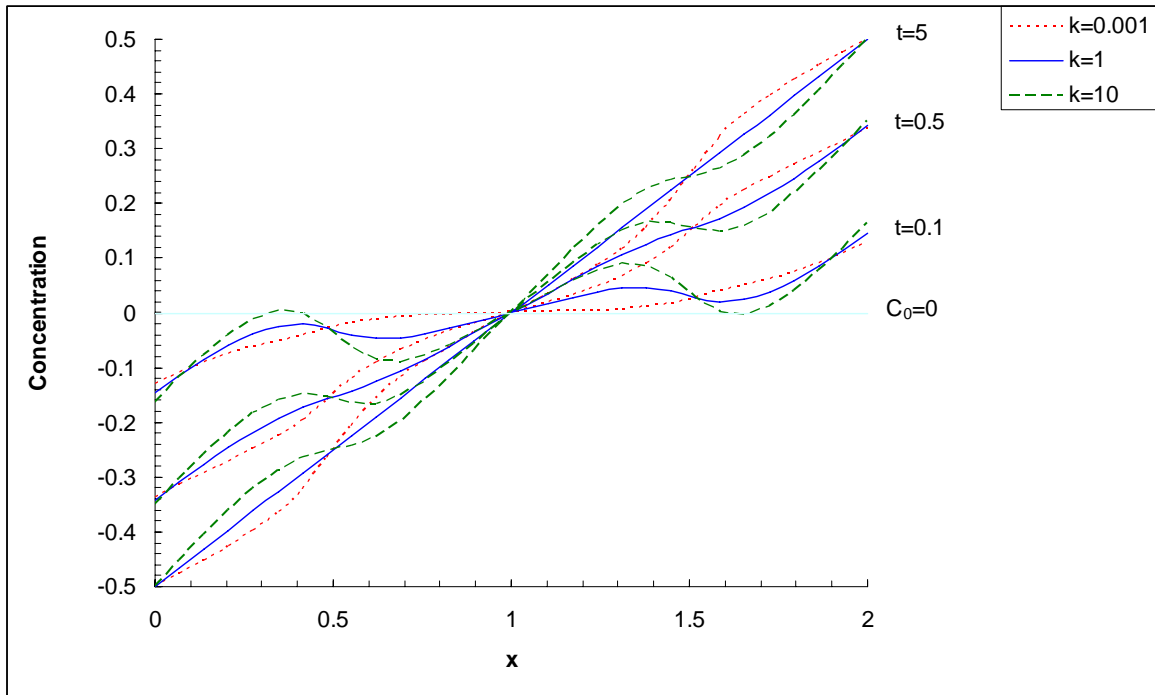
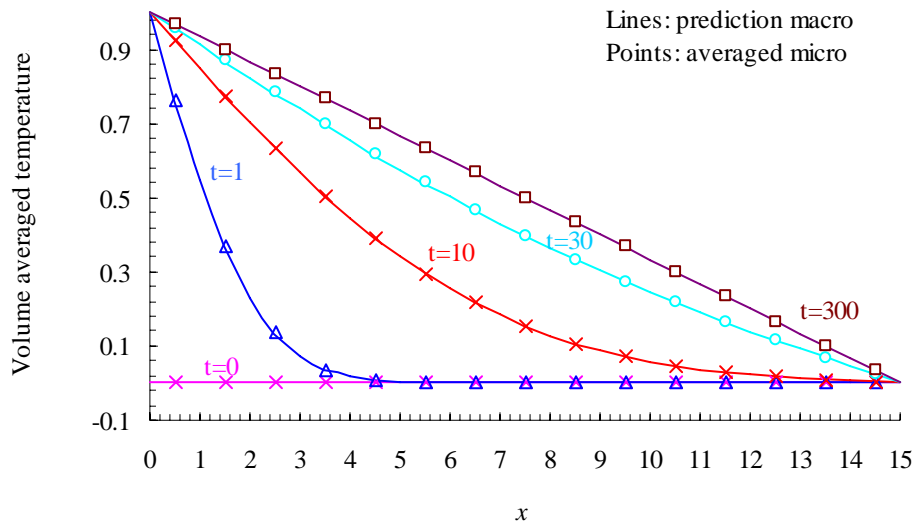


Fig. 3-6. Temporal evolution of the separation profiles for different thermal conductivity ratio

In this example, the pure diffusion ($Pe = 0$) problem has been solved for a ratio of conductivity equal to 10 ($\kappa = 10$). In this condition, the local thermal equilibrium is valid as shown in Quintard et al. (1993). Then, we can compare the results of the micro-scale model and the macro-scale model using only one effective thermal conductivity (local thermal equilibrium). We have shown in Section 3.3 that the thermal conductivity ratio has no influence on the effective thermal diffusion coefficient for diffusive regimes. Therefore, we can use the same tortuosity factor for the effective diffusion and the thermal diffusion coefficient that the one used in the previous section ($D_{\beta}^* = 0.83D_{\beta}$ and $D_{T\beta}^* = 0.83D_{T\beta}$). Whereas, we know that for pure diffusion, increasing the conductivity ratio increases the effective thermal conductivity. According to Fig. 2-10a for $Pe = 0$ and $\kappa = 10$, we obtain

$k^* = 1.72\varepsilon_\beta k_\beta$. Fig. 3-7a and Fig. 3-7b show the temporal change in temperature and concentration profile for both models.

a



b

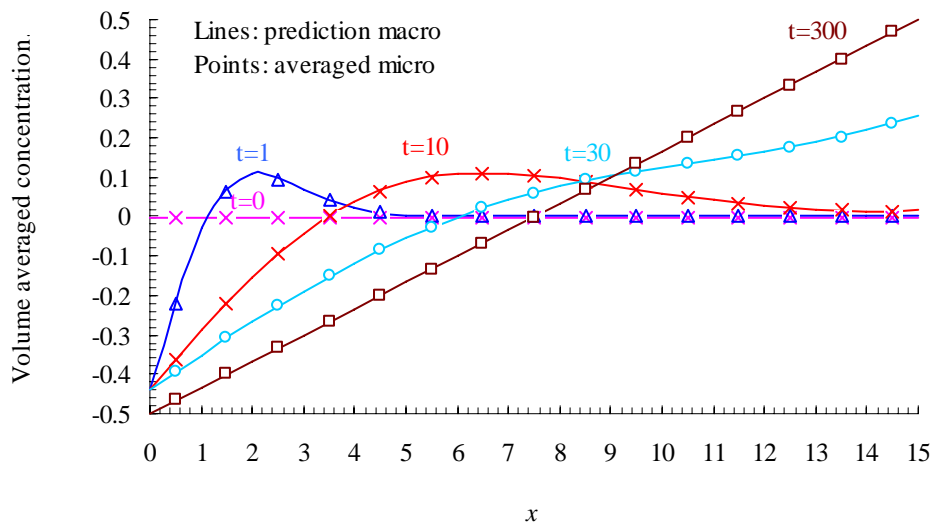


Fig. 3-7. Comparison between theoretical and numerical results at diffusive regime and $\kappa=10$, temporal evolution of (a) temperature and (b) concentration profiles

The symbols represent the direct numerical results (averages over each cell) and the lines are the results of the one-dimensional macro-scale model. One sees that, for a conductive solid-phase, our macro-scale predictions for concentration and temperature profiles are in excellent agreement with the micro-scale simulations.

In order to well understand the effect of the thermal conductivity ratio on the thermal diffusion process, we have plotted in Fig. 3-8 the temperature and concentration profiles for different thermal conductivity ratios, at a given time solution ($t=10$). As shown in this figure, a change in thermal conductivity changes the temperature profiles (Fig. 3-8a) and, consequently, the concentration profiles (Fig. 3-8b). Since we showed that the thermal diffusion coefficient is constant at pure diffusion, we conclude that modifications in concentration because of different thermal conductivity ratio come from changing the temperature profiles. These modifications can be well distinguishable in Fig. 3-8c which shows the time evolution of the concentration at $x = 15$ for different thermal conductivity ratio.

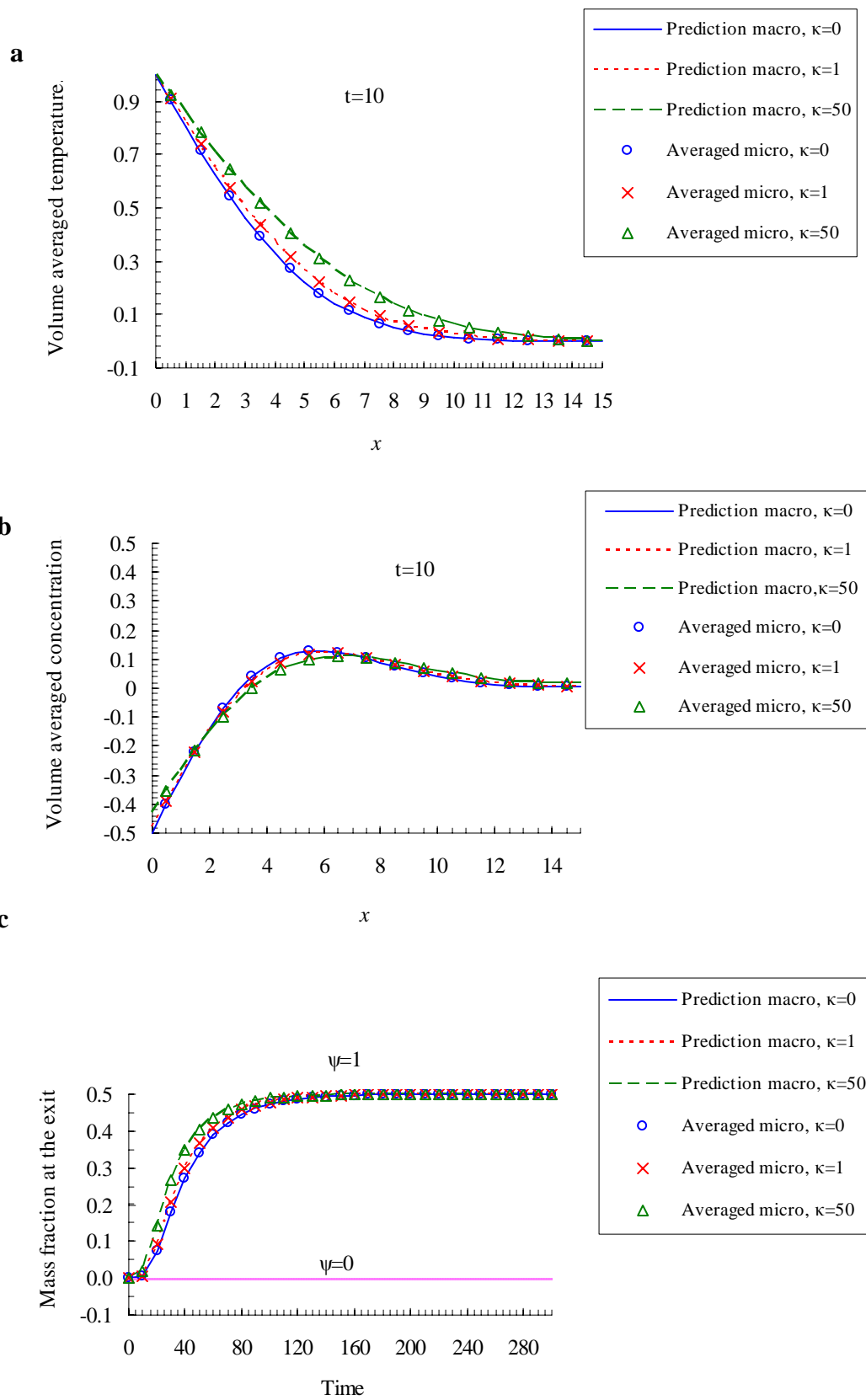


Fig. 3-8. Effect of thermal conductivity ratio at diffusive regime on (a and b) instantaneous temperature and concentration field at $t=10$ and (b) time evolution of the concentration at $x = 15$

3.3.2 Diffusion and convection ($Pe \neq 0, k_\sigma \neq 0$)

A comparison has been made for $Pe=1$ and a thermal conductivity equal to 10. The temperature and concentration profiles for different times are shown in Fig. 3-9a and Fig. 3-9b, respectively. Here, also, the theoretical predictions are in very good agreement with the direct simulation of the micro-scale problem.

Fig. 3-10a shows the effect of the Péclet number on the axial temperature distribution in the medium. At small Pe , the temperature distribution is linear, but as the pressure gradient (or Pe) becomes large, convection dominates the axial heat flow.

In Fig. 3-10b the steady-state distribution of the concentration is plotted for different Péclet numbers. One can see clearly that the concentration profile changes with the Péclet number. For example, for $Pe = 2$, because the medium has been homogenized thermally by advection in most of the porous domain, the concentration profile is almost the same as in the isothermal case (without thermal diffusion). Near the exit boundary, there is a temperature gradient which generates a considerable change in the concentration profile with an optimum point. This peak is a dynamic one resulting from coupling between convection and Soret effect.

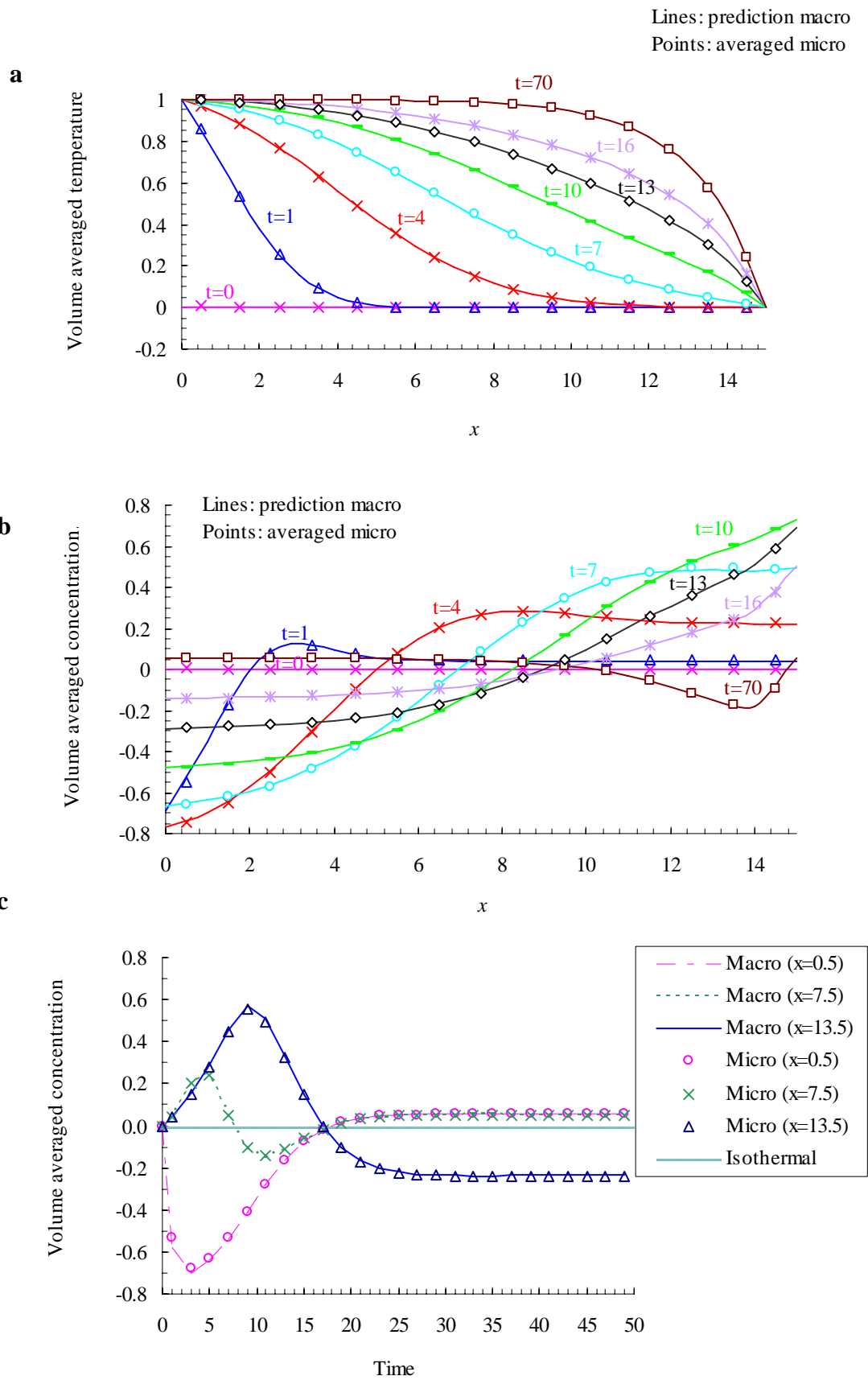


Fig. 3-9. Comparison between theoretical and numerical results, $\kappa=10$ and $Pe=1$, (a) time evolution of the concentration at $x = 0.5, 7.5$ and 13.5 (b and c) instantaneous temperature and concentration field

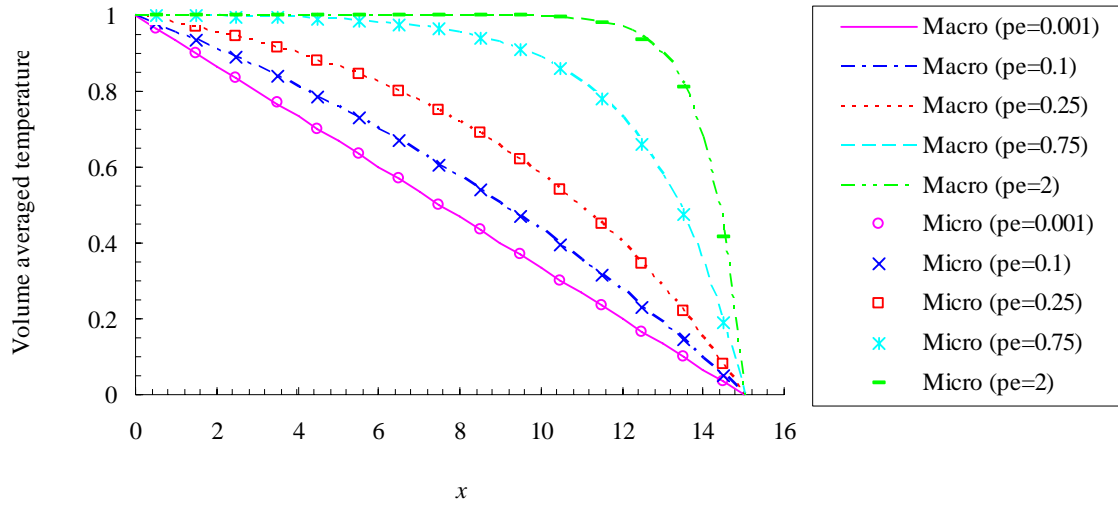
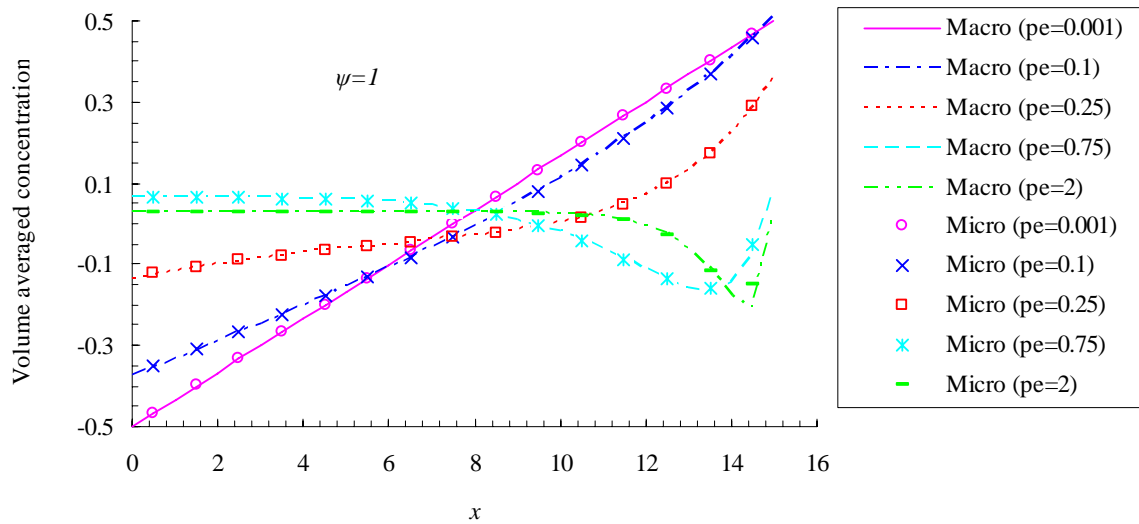
a**b**

Fig. 3-10. Influence of Péclet number on steady-state (a) temperature and (b) concentration profiles ($\kappa=10$)

If we define a new parameter, A_s , named segregation rate defined as the surface between isothermal and thermal diffusion case concentration profiles, we can see that increasing the Péclet number decreases the segregation rate. The obtained puff concentration at the exit ($x=15$) and for different Péclet numbers is illustrated in Fig. 3-11. The results show that the maximum separation passing through the exit point increases with increasing the Péclet number while occurring in shorter period.

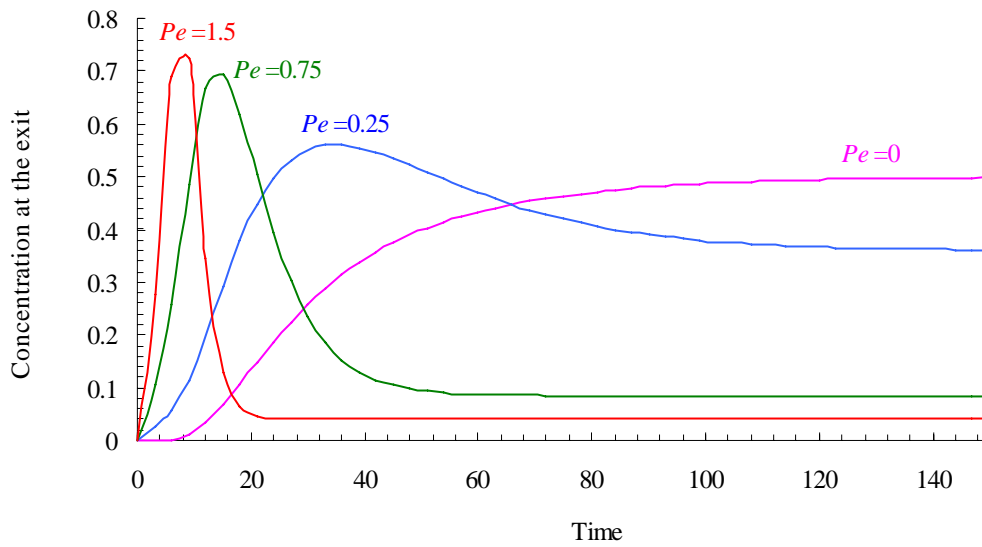


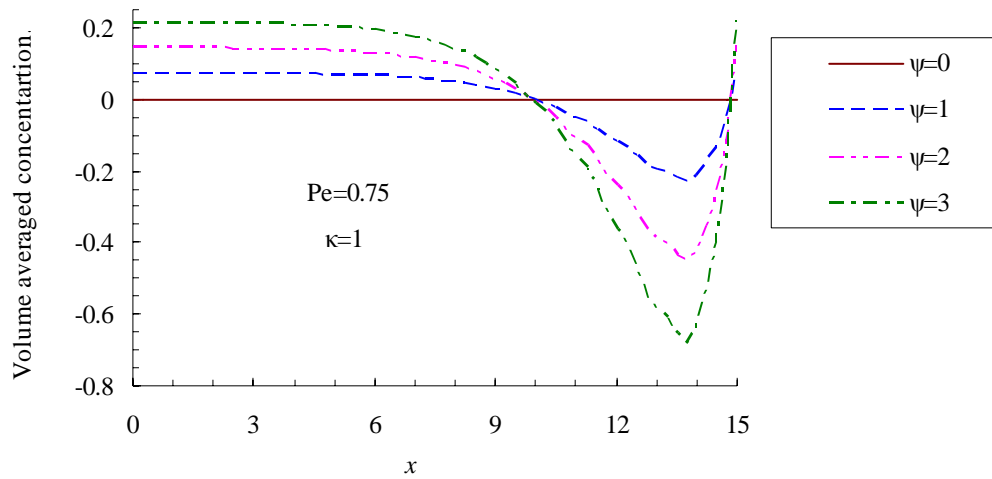
Fig. 3-11. Influence of Péclet number on steady-state concentration at the exit ($\kappa=10$)

As shown in Fig. 3-12 the concentration profile, and consequently the peak point, not only depends on the Péclet number, but also it is changed by the conductivity ratio, κ and separation factor, ψ .

The concentration profile in the case of $Pe = 0.75$ and $\kappa = 1$ for different separation factors, ψ , has been plotted in Fig. 3-12a. One can see that increasing the separation factor increases the local segregation area of species. Fig. 3-12b shows the influence of the conductivity ratio for a fixed Péclet number and separation factor ($Pe = 2$ and $\psi = 1$) on the concentration profile near the exit boundary (x between 10 and 15). The results show that a high conductivity ratio leads to smaller optimum point but higher segregation area than the ideal non-conductive solid-phase case. This means that the segregation area will be a function of $\frac{\psi\kappa}{Pe}$. This specific result should be of importance in the analysis of

species separation and especially in thermogravitational column, filled with a porous medium.

a



b

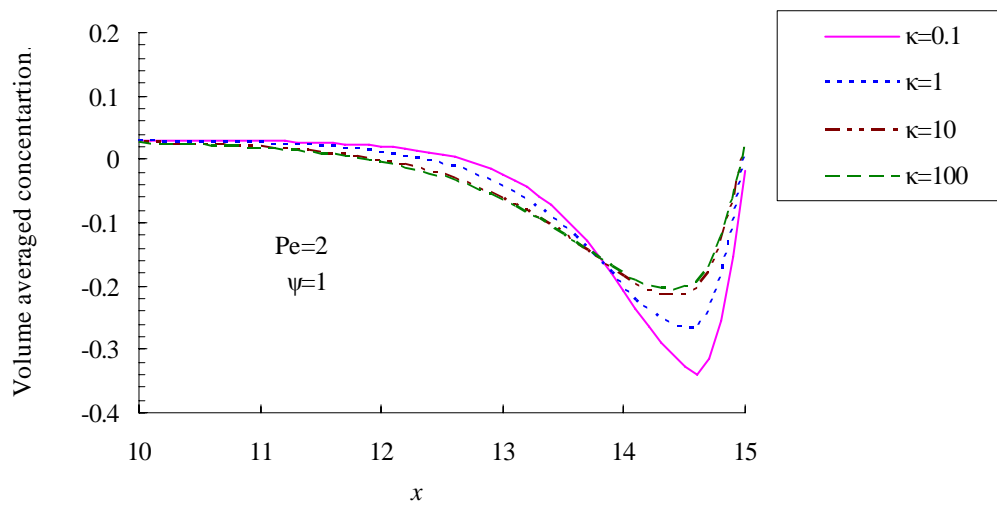


Fig. 3-12. Influence of (a) separation factor and (b) conductivity ratio on pick point of the concentration profile

3.4 Conclusion

In order to validate the theory developed by the up-scaling technique in the previous chapter, we have compared the results obtained by the macro-scale equations with direct pore-scale simulations. The porous medium is made of an array of unit cells. A good agreement has been found between macro-scale resolutions and micro-scale, direct simulations, which validates the proposed theoretical model. We have presented a situation illustrating how variations of Péclet number, conductivity ratio and separation factor coupled with Soret effect can change locally the segregation of species in a binary mixture. This may be of a great importance when evaluating the concentration in applications like reservoir engineering, waste storage, and soil contamination.

Chapter 4

**A new experimental setup to determine
the effective coefficients**

4. A new experimental setup to determine the effective coefficients

The theoretical model developed in chapter 2 concerning the effective thermal diffusion coefficient at pure diffusion regime confirmed that the tortuosity factor acts in the same way on both isothermal Fick diffusion coefficient and on thermal diffusion coefficient. We have shown also that the effective thermal diffusion coefficient does not depend on the solid to fluid conductivity ratio.

In this study, a new experimental setup has been designed and fabricated to determine directly the effective diffusion and thermal diffusion coefficients for binary mixture. New experimental results obtained with a two-bulb apparatus are presented. The diffusion and thermal diffusion of helium-nitrogen and helium-carbon dioxide system through cylindrical samples filled with glass spheres of different diameters and thermal conductivities are measured at the atmospheric pressure. Concentrations are determined by analysing the gas mixture composition in the bulbs with a katharometer device. A transient-state method for coupled evaluation of thermal diffusion and Fick coefficient in two bulbs system is proposed.

Nomenclature of Chapter 4

A	Cross-sectional area of the connecting tube, m^2	S_T	Soret number, 1/K
A_{12}^* , B_{12}^* , C_{12}^*	Ratios of collision integrals for calculating the transport coefficients of mixtures for the Lennard-Jones (6-12) potential	S_T^*	Effective Soret number, 1/K
c_1^0, c_2^0	Initial mass fraction of the heavier and lighter component	T	Temperature of the colder bulb, K
c_{ib}	Mass fraction of component i in the b bulb	T_0	Initial temperature, K
c_{it}	Mass fraction of component i in the t bulb	T'	Temperature of the hotter bulb, K
c_i^∞	Mass fraction of component i at equilibrium	T^*	Dimensionless temperature
c^o	Mass fraction at time $t = 0$	\bar{T}	Averaged temperature, K
D_{12}	Diffusion coefficient, m^2/s	t	Time, s
d	Diameter of the connecting tube, m	t^*	Diffusion relaxation time, s
D^*	Effective diffusion coefficient, m^2/s	V	Volume of the bulb, m^3
D^T	Thermal diffusion coefficient, m^2/s	V_b	Volume of the bottom bulb, m^3
D_T^*	Effective thermal diffusion coefficient, m^2/s	V_t	Volume of the top bulb, m^3
J_i	Mass diffusion flux, $kg/m^2.s$	x_α	Mole fraction of species α
k_B	Boltzmann constant, 1.38048 J/K	x_β	Mole fraction of species β
k_{mix}	Thermal conductivity of the gas mixture, W.m/K		
k_T	Thermal diffusion ratio	<i>Greek symbols</i>	
k_T^*	Effective thermal diffusion ratio	α_T	Thermal diffusion factor
k_α	Thermal conductivity of the pure chemical species α , W.m/K	β	Characteristic constant of the two-bulb diffusion cell defined in Eq. (4-10), m^{-2}
ℓ	Length of the connecting tube, m	Δc_1	Change in the concentration of heavier component at the steady state in the lower bulb
M_i	Molar mass of component i , g/mol	ε_{12}	Characteristic Lennard-Jones energy parameter (maximum attractive energy between two molecules), $kg.m^2/s^2$
m	Particle shape factor	ε	Fractional void space (porosity)

N	The number of chemical species in the mixture	μ_α	Dynamic viscosity of pure species α , g/cm.s
N_i	Mass flux of component i, kg/m ² .s	σ_{12}	Characteristic Lennard-Jones length (collision diameter), Å
n	Number density of molecules	τ	Tortuosity
p	Pressure, bar	τ_i	Thermal diffusion relaxation time, s
R_K	Katharometer reading, mV	$\Phi_{\alpha\beta}$	The interaction parameter for gas-mixture viscosity
S	Separation rate	Ω_D	Collision integral for diffusion
S, Q	Quantities in the expression for α_T	$\Omega^{(l,s)*}$	Collision integral
S_g	Partial gas saturation		

4.1 Introduction

In the previous chapters we developed a theoretical model to predict effective thermal diffusion coefficients from micro-scale parameters (thermal diffusion coefficient, pore-scale geometry, thermal conductivity ratio and Péclet numbers). The results confirm that for a pure diffusion regime, the effective Soret number in porous media is the same as the one in the free fluid [24, 25]. This means that the tortuosity factor acts in the same way on the Fick diffusion coefficient and on the thermal diffusion coefficient. In the present work, the influences of pore-scale geometry on effective thermal diffusion coefficients in gas mixtures have been measured experimentally. Related to coupled-transport phenomena, the classical diffusion equation is completed with the additional thermal diffusion term. The mass flux, considering a mono-dimensional problem of diffusion, in the x -direction for a binary system, not subjected to external forces, and in which the pressure, but not the temperature, is uniform, can be written

$$J_1 = -\rho_\beta \left[D_{12} \frac{\partial c_1}{\partial x} + D_T \frac{\partial T}{\partial x} \right] \quad (4-1)$$

where D_{12} is the ordinary diffusion coefficient and D_T the thermal diffusion coefficient. Defining thermal diffusion ratio $k_T = TD_T/D_{12}$, we can write (as in [52])

$$J_1 = -\rho_\beta D_{12} \left[\frac{\partial c_1}{\partial x} + \frac{k_T}{T} \frac{\partial T}{\partial x} \right] \quad (4-2)$$

Other quantities encountered are the thermal diffusion factor, α_T , (for gases) and the Soret coefficient, S_T , defined in literatures by $\alpha_T = k_T/c_1^0 c_2^0$ and $S_T = k_T/T$ respectively.

When k_T in equation (4-2) is positive, heaviest species (1) moves toward the colder region, and when it is negative, this species moves toward the warmer region. In some cases, there is a change in sign of the thermal diffusion ratio as the temperature is lowered (See [17] and [13]).

By now, data for gas thermal diffusion in porous medium are not available and there is some uncertainty for the question concerning the relationship between the effective liquid thermal diffusion coefficient and the micro-scale parameters (such as pore-scale geometry) [20, 74].

In this study, using a gaseous mixture has the advantage that the relaxation time is much smaller compared to the one of liquid mixture.

The main purpose of this part is to measure directly the binary diffusion and thermal diffusion coefficients in porous media for the systems $He-N_2$ and $He-CO_2$, using a two-bulb cell close to the design of Ney and Armistead [67]. This method has been used already in many works to determine transport properties in binary and ternary gases as well as liquids, with accurate results.

4.2 Experimental setup

In this study we have designed and fabricated a new experimental setup that has been proven suitable results for the study of diffusion and thermal diffusion in free fluid. It is an all-glass two-bulb apparatus, containing two double-spherical layers 1 (top) and 2 (bottom) as shown in Fig. 4-1. In fact, the particular difference between this system and the earliest two-bulb systems is that each bulb contains an interior glass sphere to serve as reservoir bulb and another exterior glass spheres in which, in the space between two glass layers there may be a water circulation to regulate the reservoir temperature. As shown in Fig. 4-2, the reservoir bulbs with equal and constant volume $V_t = V_b = 1000 \text{ cm}^3$, joined by an insulated rigid glass tube of inner diameter $d = 0.795 \text{ cm}$ and length 8 cm containing a valve also made especially of 0.795 cm bore, and 5.87 cm long. Therefore, the total length of the tube in which the diffusion processes occur is about $\ell = 13.87 \text{ cm}$. To avoid convection, the apparatus was mounted vertically, with the hotter bulb uppermost.

The concentration is determined by analysing the gas mixture composition in each bulb with a katharometer. As we described in Section 1.5.1, katharometer, or thermal conductivity detector (Daynes 1933 [26], Jessop 1966 [46]), has already been used to measure the concentration of binary gas mixtures. The method is based on the ability of gases to conduct heat and the property that the thermal conductivity of a gas mixture is a function of the concentration of its components. The thermal conductivity of a gas is inversely related to its molecular weight. Hydrogen has approximately six times the conductivity of nitrogen for example. The thermal conductivity of some gases with corresponding katharometer reading at atmospheric pressure is listed in Table 4-1.

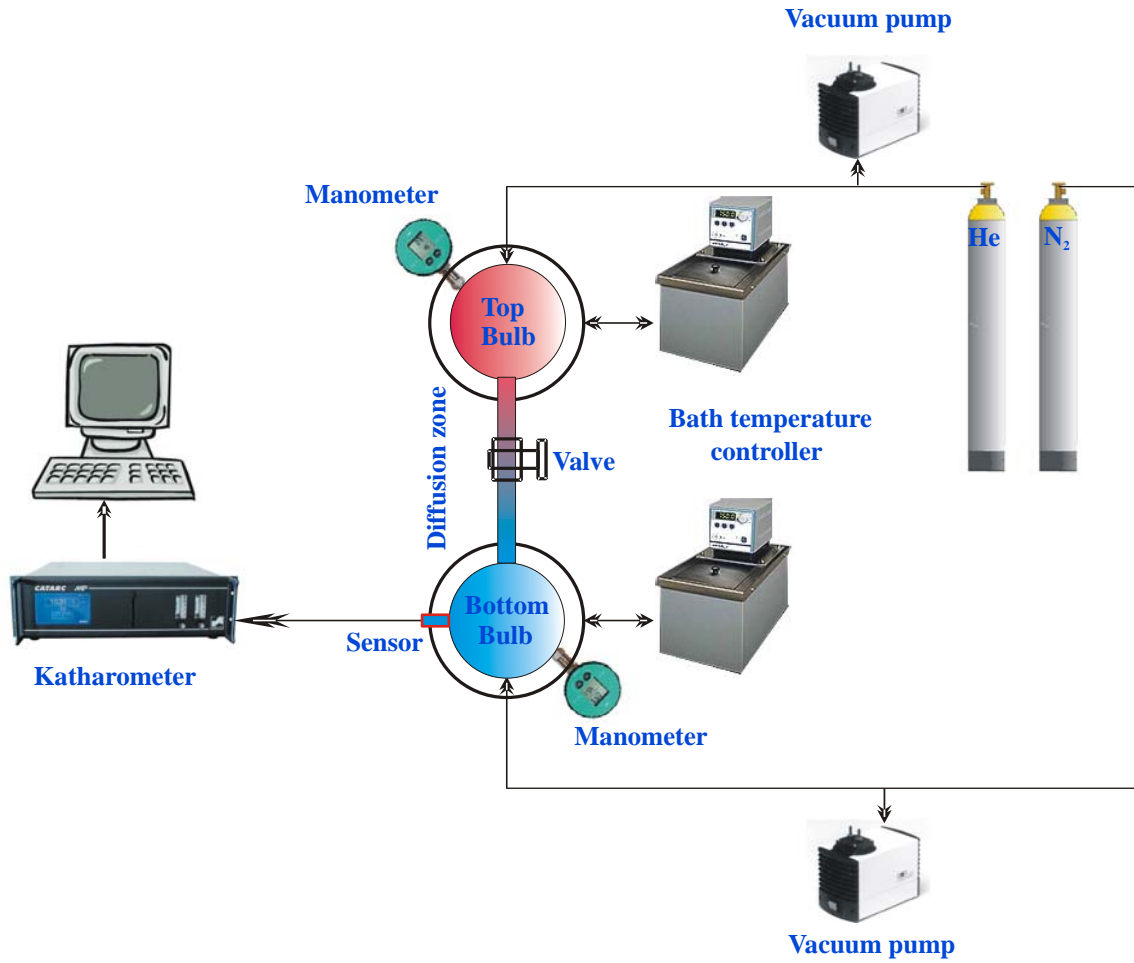


Fig. 4-1. Sketch of the two-bulb experimental set-up used for the diffusion and thermal diffusion tests

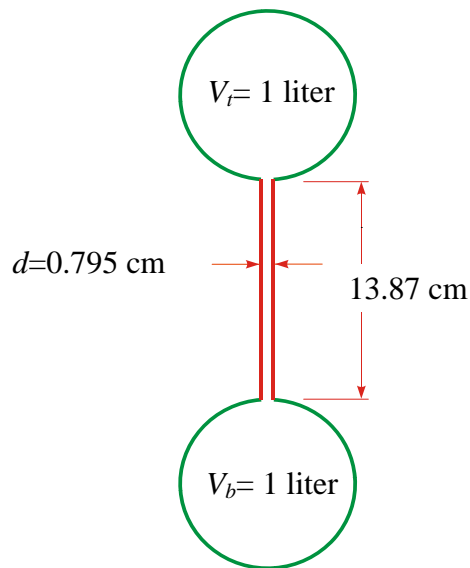


Fig. 4-2. Dimensions of the designed two-bulb apparatus used in this study

Table 4-1. Thermal conductivity and corresponding katharometer reading for some gases at atmospheric pressure and $T=300^{\circ}\text{K}$

Gas	<i>Air</i>	N_2	CO_2	<i>He</i>
$k(W/m.K)$	0.0267	0.0260	0.0166	0.150
$R_K(mV)$	1122	1117	976	2345

In this study, we have used the analyzer ARELCO-CATARC MP-R model (Fig. 4-3) with a sensor operating on the principle of thermal conductivity detection. The electronics high-performance microprocessor of this device allows analysing the binary gas mixtures with $\pm 0.5\%$ repeatability. The touch screen display allows also seeing and verifying all essential parameters e.g. scale analog output, temperature control, and access menus. This type of Katharometer works with a circulation of the analyzed and reference gases into the sensors. The first series of the experiment showed that the sampling with circulation cannot be applied in the two-bulb method because gas circulation can perturb the establishment of the temperature gradient in the system. Small changes in the pressure in one bulb may produce forced convection in the system and cause a great error in the concentration evaluation. Therefore, in this study we have eliminated the pump system between the bulbs and katharometer sensors. Instead we connected the katharometer analyser sensor directly to the bulbs as shown in Fig. 4-4. Therefore, the open cell of the katharometer form a part of the diffusion cell, and so it can indicate continuously and without sampling the changes in composition as diffusion and thermal diffusion processes. The other sensor of the katharometer has been sealed permanently in air and the readings are the reference readings.



Fig. 4-3. Katharometer used in this study (CATARC MP – R)

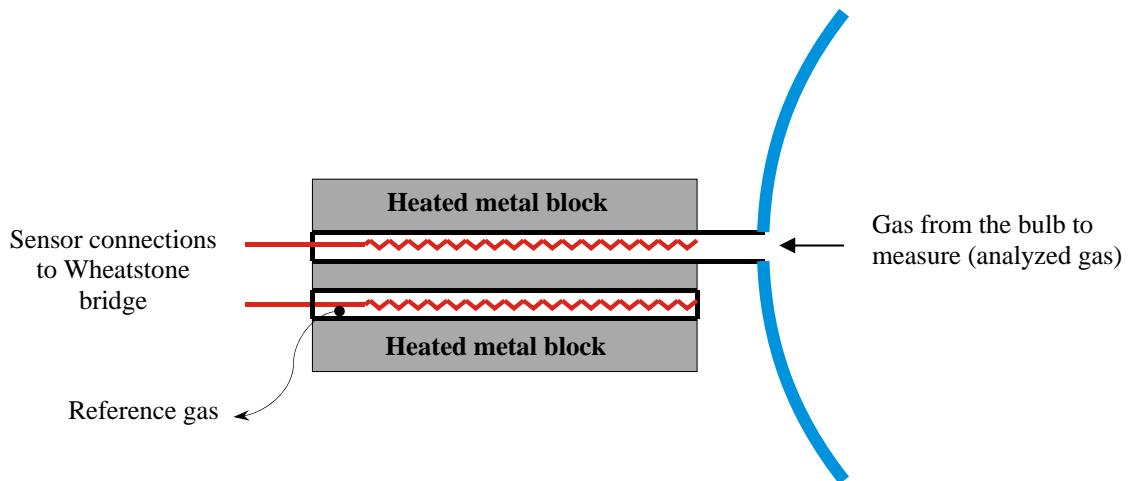


Fig. 4-4. A schematic of katharometer connection to the bulb

For gases, the diffusion coefficient is inversely proportional to the absolute pressure and directly proportional to the absolute temperature to the 1.75 power as given by the Fuller et al. [33] correlation discussed in Reid et al. (1987).

Pressure and temperature measurements are made with two manometers and thermometers. The temperature of each bulb is kept at a constant value by circulating water from a bath temperature controller. In this study, for all diffusion measurements, the temperature of two bulbs system is fixed to 300 °K. The gas purities are: He : 100%, N_2 : 100% and CO_2 : 100%.

4.2.1 Diffusion in a two-bulb cell

The two-bulb diffusion cell is a simple device that can be used to measure diffusion coefficients in binary gas mixtures. Fig. 4-5 shows a schematic of the two-bulb apparatus.

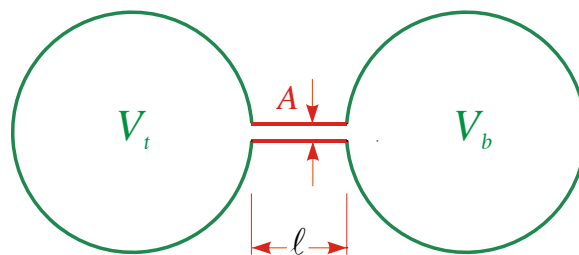


Fig. 4-5. Two-bulb apparatus

Two vessels containing gases with different compositions are connected by a capillary tube. The katharometer cell itself is connected with the bulb and its volume is negligible compared to the volume of the bulbs. The katharometer cell and the two bulbs were kept at a constant temperature of about 300 °C.

The vacuum pumps are used at the beginning of the experiment to eliminate the gas phase initially in the diffusion cell and in the gas flow lines.

At the start of the experiment (at $t = 0$), the valve is opened and the gases in the two bulbs can diffuse along the capillary tube. An analysis of binary diffusion in the two-bulb diffusion apparatus has been presented by Ney and Armistead (1947) [67] (see, also, Geankoplis, 1972). It is assumed that each bulb is at a uniform composition (the composition of each bulb is, of course, different until equilibrium is reached). It is further assumed that the volume of the capillary tube connecting the bulbs is negligible in comparison to the volume of the bulbs themselves. This allows expressing the component material balances for each bulb as follows

$$\rho_{\beta} V_b \frac{dc_{ib}}{dt} = -\rho_{\beta} V_t \frac{dc_{it}}{dt} = -N_i A \quad (4-3)$$

where A is the cross-sectional area of the capillary tube, c_{it} is the mass fraction of component i in the top bulb, and c_{ib} is the mass fraction of that component in the bottom bulb. The mass flux of species i through the capillary tube N_i is considered to be positive if moving from top bulb to bottom bulb.

The density can be computed from the ideal gas law at the average temperature \bar{T}

$$\rho_{\beta} = \frac{P}{R\bar{T}} \quad (4-4)$$

at constant temperature and pressure the density of an ideal gas is a constant; thus, there is no volume change on mixing and in the closed system the total flux N_t must be zero.

The composition in each bulb at any time is related to the composition at equilibrium c_i^{∞} by

$$(V_t + V_b)c_i^{\infty} = V_t c_{it} + V_b c_{ib} \quad (4-5)$$

The compositions at the start of the experiment are, therefore, related by

$$(V_t + V_b)c_i^{\infty} = V_t c_{it}^0 + V_b c_{ib}^0 \quad (4-6)$$

where c^0 is the mass fraction at time $t = 0$.

In the analysis of Ney and Armistead it is assumed that, for $i=1$ at any instant, the flux N_1 is given by its one dimensional, steady-state diffusion flux as

$$J_1 = \frac{\rho_\beta D_{12}}{\ell} (c_{1b} - c_{1t}) \quad (4-7)$$

Thus ($J_1 = N_1$),

$$\rho_\beta V_b \frac{dc_{1b}}{dt} = -\rho_\beta \frac{D_{12}}{\ell} A (c_{1b} - c_{1t}) \quad (4-8)$$

To eliminate c_{1t} from Eq.(4-8) one makes use of the component material balance for both bulbs, Eqs. (4-6) and (4-7).

$$\frac{dc_{1b}}{dt} = -\beta D_{12} (c_{1b} - c_1^\infty) \quad (4-9)$$

where β is a cell constant defined by

$$\beta = \frac{(V_t + V_b)A}{\ell V_t V_b} \quad (4-10)$$

A similar equation for the mass fraction of component 2 in bulb t may also be derived.

Equation (4-9) is easily integrated, starting from the initial condition that at $t = 0$, $c_{1b} = c_{1b}^0$, to give

$$c_{1b} = (c_{1b}^0 - c_1^\infty) \exp(-\beta D_{12} t) + c_1^\infty \quad (4-11)$$

Hence, if β is known then just one value of c_b is all that is needed to calculate the diffusivity D_{12} . Alternatively, if an accurate value of D_{12} is available, Eq.(4-11) can be used to calibrate a diffusion cell for later use in measuring diffusion coefficients of other systems.

In this study, the volume of the two bulbs is equal $V_t = V_b$ then, we can write Eqs. (4-6) and (4-10) as

$$c_i^\infty = (c_{it}^0 + c_{ib}^0)/2 \quad (4-12)$$

$$\beta = \frac{2A}{\ell V} \quad (4-13)$$

where V is the bulb volume.

4.2.2 Two-bulb apparatus end correction

When we determine the diffusion coefficient in a two bulb system connected with a tube, the concentration gradient does not terminate at the end of the connecting tube and, therefore an *end-correction* has to be made. This correction was made in the calculation of the cell constants as an end-effect by Ney and Armistead [67]. They adjust the tube length L for end effects to give an effective length ℓ_{eff} , given by

$$\ell_{eff} = \ell + 0.82d \quad (4-14)$$

where d is the tube diameter.

Rayleigh, 1945 [88], when investigating the velocity of sound in pipes, showed that one must add $0.82r$ for thick annulus flange and $0.52r$ for a thin annulus flange to each end of the tube. Here, r is the tube radius.

Wirz, 1947 showed that the end corrections for sound in tubes depend on the annulus width, w , and diameter, d . The results fit the correlation [114]

$$\alpha = 0.60 + 0.22 \exp\left(\frac{-0.125d}{w}\right) \quad (4-15)$$

where α is the end-correction factor.

Analysis of many results on diffusion both in porous media and bulk gas also showed a significant difference between diffusion coefficients measured in different cells [108]. This difference may arise through a difference in geometry affecting the diffusion (say cell effect) or, in the case of the capillary tube, the end correction factor being incorrect. More recent work indicates that the effect is due to differences in cell geometry [106]. The existence of this difference implies that all measurements of bulk gas diffusion by the two-bulb technique may contain systematic errors up to 2% [108].

Arora et al, 1977 [4] using precise binary diffusion coefficients showed that the end correction formulation is not precise enough when an accuracy of 0.1% in coefficients is required. However, they proposed to calibrate the two-bulb cells with the standard diffusion coefficients.

According to this short bibliography, calculated diffusion coefficients in a two-bulb apparatus depend on the cell geometry and end connection tubes. Then, in this study, we will use the standard values of diffusion coefficients to calibrate the two-bulb apparatus for effective tube length.

In our work concerning the determination of tortuosity, this error may be small because we have calculated a ratio of the two diffusion coefficients. However, a better understanding of this problem requires doing more experimental or numerical studies.

4.2.3 Thermal diffusion in a two-bulb cell

For calculation of the magnitude of the Soret effect we used the same setup that we have used for diffusion processes. The diameter of the tube is small enough to eliminate convection currents and the volume of the tube is negligible in comparison with the volume of the bulbs.

In the initial state, the whole setup is kept at a uniform and constant temperature T_0 and the composition of the mixture is uniform everywhere. After closing the valve in the tube, the temperature of the top bulb is increased to T_H and the temperature of bottom bulb is lowered to T_C , the two bulbs are set at the same pressure. After this intermediate state, the valve is opened. After a short time, a final stationary state is reached, in which there is a constant flux of heat from bulb t to bulb b . Measures have been taken such that T_C and T_H remain constant and, due to the Soret effect, it is observed a difference in mass fraction between the bulbs.

Thermal diffusion separation is determined by analysing the gas mixture composition in the bulbs by katharometric analysis.

At steady-state, the separation due to thermal diffusion is balanced by the mixing effect of the ordinary diffusion, there is no net motion of either 1 or 2 species, so that $J_1 = 0$. If we take the tube axis to be in the x direction, then from Eq. (4-2) we get

$$\frac{\partial c_1}{\partial x} = -\frac{k_T}{T} \frac{\partial T}{\partial x} \quad (4-16)$$

We may ignore the effect of composition on k_T and integrate this equation on temperature gradient between T_C and T_H to get the change in concentration of the heavier component at the steady state in the lower bulb [97].

$$\Delta c_1 = -k_T \ln \left(\frac{T_H}{T_C} \right) \quad (4-17)$$

then the thermal diffusion factor α_T is calculated from the following relation

$$\alpha_T = \frac{-\Delta c_1}{c_1^0 c_2^0 \ln\left(\frac{T_H}{T_C}\right)} \quad (4-18)$$

here, c_1^0 and c_2^0 are the initial mass-fractions of the heavier and lighter components respectively in the binary gas mixture, and $\Delta c_1 = c_{1b}^\infty - c_{1l}^\infty$.

α_T values thus obtained refer to an average temperature, \bar{T} , in the range T_C to T_H ([37] and [95]) and these are determined from the formula of Brown (1940) according to which [12]

$$\bar{T} = \frac{T_H T_C}{T_H - T_C} \ln\left(\frac{T_H}{T_C}\right) \quad (4-19)$$

which is based on an assumed temperature dependence for α_T of the form $\alpha_T = a - bT^{-1}$.

The relaxation time τ_t for this process can be expressed as [95]

$$\tau_t \cong \left(\frac{V\ell}{D_{12}A}\right) \left[\frac{T_C}{T_C + T_H}\right] \quad (4-20)$$

where V is the volume of one of the bulbs. The relaxation time is therefore proportional to the length of the connecting tube, and inversely proportional to its cross-sectional area. The approach to the steady state is approximately exponential, and this was confirmed by following measurements.

The variation of pressure is small in each experience. Theory and experiment agree in showing that, at least at pressure below two atmospheres, the separation is independent of the pressure; therefore in this study the thermal diffusion factor is not changed by small variation of pressure. In most gaseous mixture the thermal diffusion factor increases with increasing pressure. The temperature and concentration dependence of the thermal diffusion factor also were found to be affected by pressure [8].

4.2.4 A transient-state method for thermal diffusion processes

In this section, a transient-state method for thermal diffusion process in a two-bulb apparatus is proposed. In this case, the flux is the sum of Fick diffusion flux and thermal diffusion flux, as

$$J_1 = \rho_\beta \frac{D_{12}}{\ell} (c_{1t} - c_{1b}) - \rho_\beta \frac{D_{12} k_T}{\ell} \ln\left(\frac{T_H}{T_C}\right) \quad (4-21)$$

at thermal equilibrium and for one-dimensional case. Then the concentration variation in the bottom bulb is given by

$$\rho_\beta V_b \frac{dc_{1b}}{dt} = -\frac{\rho_\beta D_{12}}{\ell} (c_{1b} - c_{1t}) + \frac{\rho_\beta D_{12} k_T}{\ell} \ln\left(\frac{T_H}{T_C}\right) \quad (4-22)$$

The compositions at the starting of the experiment are related by

$$c_{ib}^0 = c_{it}^0 \quad (4-23)$$

and, the composition in each bulb at any time is

$$V_t c_{it} + V_b c_{ib} = (V_t + V_b) c_{ib}^0 \quad (4-24)$$

Then one can eliminate c_{1t} from Eq. (4-22) using these two component balances

$$\frac{dc_{1b}}{dt} + \beta D_{12} c_{1b} = \beta D_{12} \left(c_{1b}^0 + \frac{V_t}{V_t + V_b} k_T \ln\left(\frac{T_H}{T_C}\right) \right) \quad (4-25)$$

A similar equation for the mass fraction of component 1 in bulb t may also be derived. The integration of equation (4-25), starting from the initial condition at $t = 0$, $c_{1b} = c_{ib}^0$, gives

$$c_{1b} = c_{1b}^0 + \left[\frac{V_t}{V_t + V_b} k_T \ln\left(\frac{T_H}{T_C}\right) \right] (1 - e^{-D_{12} \beta t}) \quad (4-26)$$

If the value of D_{12} is available, then just one value of (c_{1b}, t) is all that is needed to calculate the thermal diffusion factor and then the thermal diffusion coefficient. However, when the experimental time evaluation of the concentration is available, both D_{12} and k_T (or D_T) can be evaluated. It is sufficient to adjust D_{12} and k_T until equation (4-26) fits the experimental data.

When the volume of the two vessels is equal, Eq. (4-26) simplifies to

$$c_{1b} = c_{1b}^0 + \frac{S}{2} \left(1 - e^{-\frac{2t}{t^*}} \right) \quad (4-27)$$

where, $S = k_T \ln\left(\frac{T_H}{T_C}\right)$ and $t^* = \frac{\ell V}{AD_{12}}$ are a separation rate (or Δc_1 in Eq. (4-17)) and a diffusion relaxation time respectively.

4.3 Experimental setup for porous media

In a porous medium, the effective diffusion coefficient for solute transport is significantly lower than the free diffusion coefficient because of the constricted and tortuous solute flow paths. This effective diffusion coefficient is related to the free diffusion coefficient and tortuosity coefficient.

The mono-dimensional solute transport can be write as

$$\frac{\partial c}{\partial t} = D^* \frac{\partial^2 c}{\partial x^2} \quad (4-28)$$

where D^* is the effective diffusion coefficient.

We have used the same apparatus and method explained in the last section to measure the effective coefficients except that, here, one part of the connecting tube (4 cm long, connected to bottom bulb) is filled with a synthetic porous medium made with the spheres of different physical properties.

4.4 Results

4.4.1 Katharometer calibration

To find the relative proportions of the components of a gas mixture, the instrument needs first to be calibrated. This is done by admitting mixtures of known proportions on the open cell and observing the difference resistance between reference values and analyzed readings. The precision with which the change in composition of a mixture can be measured depends, of course, on the difference of the thermal conductivities of the two components and this also depends on the difference of the molecular masses. Fig. 4-6 shows an example of katharometer calibration curve for mixtures of $He - CO_2$, which have been obtained in order to interpolate the changes in concentration as a function of katharometer readings. One can see that the katharometer calibration curve gives a very close approximation in shape to the theoretical curve of thermal conductivity against concentration.

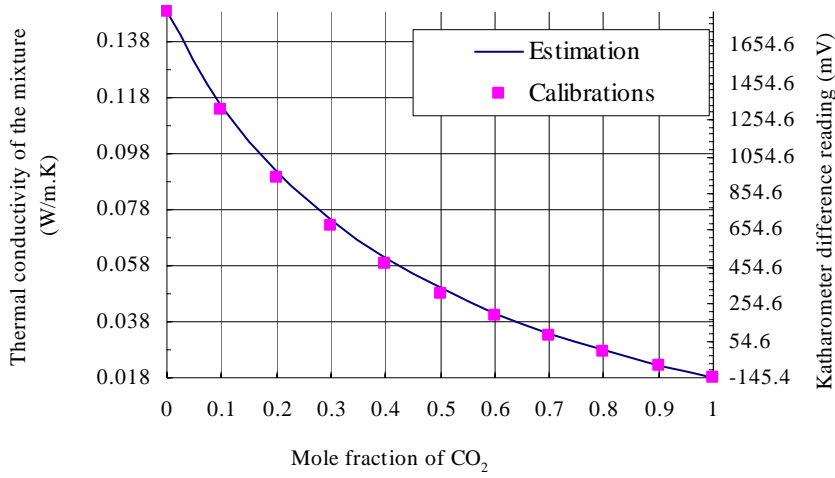


Fig. 4-6. Katharometer calibration curve with related estimation of thermal conductivity values for the system $He-CO_2$

The thermal conductivities for gas mixtures at low density have been estimated by Mason-Saxena approach [58]

$$k_{mix} = \sum_{\alpha=1}^N \frac{x_{\alpha} k_{\alpha}}{\sum_{\beta} x_{\beta} \Phi_{\alpha\beta}} \quad (4-29)$$

Here, the dimensionless quantities $\Phi_{\alpha\beta}$ are

$$\Phi_{\alpha\beta} = \frac{1}{\sqrt{8}} \left(1 + \frac{M_{\alpha}}{M_{\beta}} \right)^{-1/2} \left[1 + \left(\frac{\mu_{\alpha}}{\mu_{\beta}} \right)^{1/2} \left(\frac{M_{\beta}}{M_{\alpha}} \right)^{1/4} \right]^2 \quad (4-30)$$

where N is the number of chemical species in the mixture. For each species α , x_{α} is the mole fraction, k_{α} is the thermal conductivity, μ_{α} is the viscosity at the system temperature and pressure, and M_{α} is the molecular weight of species α .

The properties of N_2 , CO_2 and He required to calculate thermal conductivity of mixture have been listed in Table 4-2 at 300°K and 1 atm.

Table 4-2. The properties of CO_2 , N_2 and He required to calculate k_{mix} ($T=300$ °C, $P=1$ atm.)

	M_α	$\mu_\alpha \times 10^4$ (g/cm.s)	$k_\alpha \times 10^7$ cal/cm.s.K
CO_2	44.010	1.52	433
N_2	28.016	1.76	638
He	4.002	2.01	3561

4.4.2 Diffusion coefficient

Usually, five modes of gas transport can be considered in porous media [59]. As illustrated schematically in Fig. 4-7, four of them are related to concentration, temperature or partial pressure gradients (molecular diffusion, thermal diffusion, Knudsen diffusion and surface diffusion), and one to the total gas pressure gradient (viscous or bulk flow). When the gas molecular mean free path becomes of the same order as the tube dimensions, free-molecule, or Knudsen, diffusion becomes important. Due to the influence of walls, Knudsen diffusion and configurational diffusion implicitly include the effect of the porous medium.

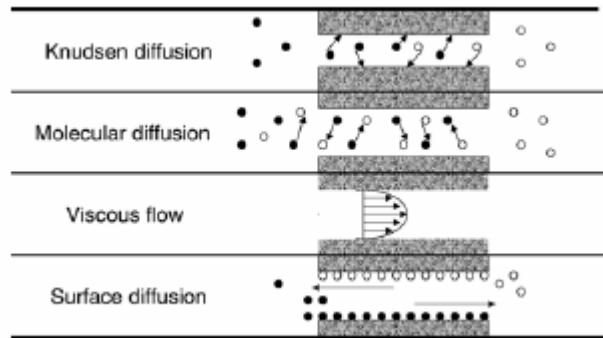


Fig. 4-7. Solute transport process in porous media

In the discussion which follows, no total pressure gradient (no bulk flow) is considered since this is the condition which prevails in the experiments presented in this study. In most of the former studies, surface diffusion was either neglected or considered only as a rapid process since its contribution to the overall transport cannot be assessed precisely. Knudsen diffusion is neglected because the pore size is larger than the length of the free path of the gas molecules. For example, in the atmospheric pressure, the mean free path of

the helium molecule at 300 °C is about 1.39×10^{-7} m. Thus, in this study, only binary molecular gas diffusion is considered.

In this type of experiment, it is assumed that the diffusion coefficient of the gas mixture is independent of composition, and the transient temperature rises due to Dufour effects are insignificant. It is also assumed that the concentration gradient is limited to the connecting tube whereas the composition within each bulb remains uniform at all times. In addition, the pressure is assumed to be uniform throughout the cell, so that viscous effects are negligible, and high enough to minimize free-molecular (Knudsen) diffusion.

For the setup described in Section 2, the cell constant β is equal to 7.16×10^{-5} , therefore we can rewrite Eq.(4-11) as

$$c_{1b} = (c_{1b}^0 - c_1^\infty) \exp(-7.16 \times 10^{-5} D_{12} t) + c_1^\infty \quad (4-31)$$

Using Eq. (4-31), only one point (c_{1r}, t) is sufficient to determine the diffusion coefficient.

The katharometer interval registration data has been set to one minute; therefore, there is sufficient data to fit Eq. (4-31) on the experimental data to obtain a more accurate coefficient, compared with a one point calculation. Then, the obtained binary diffusion coefficient is about $0.690 \text{ cm}^2/\text{s}$ for $He - N_2$ system and $0.611 \text{ cm}^2/\text{s}$ for $He - CO_2$ system. In the literature [103], binary diffusion coefficient for a $He - N_2$ system measured with two-bulb method at the condition of $p=101.325 \text{ kPa}$, and $T=299.19 \text{ °K}$, is about $0.7033 \text{ cm}^2/\text{s}$. This coefficient for a $He - CO_2$ system has been reported as $0.615 \text{ cm}^2/\text{s}$ at 300°K [28]. Using these standard coefficients a new calibrated mean cell constant has been calculated. This constant that will be used for all next experiments is equal to $\beta/1.015$.

The theoretical estimation of the diffusion coefficients also are not different from values obtained in this study which show the validity of the measuring method and apparatus (the theoretical formulation has been explained in Appendix A).

Table 4-3 shows the necessary data to estimate the diffusion coefficient for the system, $He - CO_2$ and $He - N_2$. The calculation of mixture parameters, dimensionless temperature, collision integral and diffusion coefficient from Eq. (A. 2) and for temperatures applied in this study have been listed in Table 4-4.

Table 4-3. Molecular weight and Lennard-Jones parameters necessary to estimate diffusion coefficient [10]

	M_i (g/mol)	ε/k_B (K)	σ (Å)
CO_2	44	190	3.996
N_2	28	99.8	3.667
He	4	10.2	2.576

Table 4-4. Estimation of diffusion coefficients for binary gas mixtures $He-CO_2$ and $He-N_2$ at temperatures 300, 350 and $\bar{T} = 323.7$ °K, pressure 1 bar

	$He - CO_2$			$He - N_2$		
T (K)	300	350	323.7	300	350	323.7
σ_{12} (Å)	3.286			3.121		
ε_{12}/k (K)	44.02			31.90		
T^* (-)	6.815	7.950	7.353	9.403	10.970	10.145
Ω_D (-)	0.793	0.771	0.782	0.749	0.731	0.740
D_{12} (cm^2/s)	0.596	0.772	0.677	0.715	0.925	0.812

4.4.3 Effective diffusion coefficient in porous media

A number of different theoretical and experimental models have been used to quantify *gas diffusion processes* in porous media. Most experimental models are models derived for a free fluid (no porous media) that were modified for a porous medium. Attempts have been made to define effective diffusion parameters according to the presence of the porous medium. In literature, the effective diffusion coefficients are now well established, theoretically ([60], [104], [107], [90] and [79]) and experimentally ([42], [22] and [49]). The comparison of the theoretical and experimental results for the dependence of the effective diffusion coefficient on the medium porosity shows that the results of Quintard (1993) in three dimensional arrays of spheres [79] and the curve identified by Weissberg (1963) are in excellent agreement with the experimental data [111].

Many experimental studies have been done to determine the effective diffusion coefficient for unconsolidated porous media. The diffusion of hydrogen through cylindrical samples

of porous granular materials was measured by Currie (1960) [22]. An equation having two shape factor of the form $D^*/D = \gamma \varepsilon^m$ has been proposed which fits with all granular material, m is the particle shape factor. The value of γ for glass spheres can be fixed to 0.81 [15]. The expected m value for spheres is 1.5.

For measuring effective diffusion coefficients we have used the same apparatus and method but here, one part of the connecting tube (4 cm long, connected to the bottom bulb) is filled with the porous medium made of glass spheres (Fig. 4-8). A metal screen was fixed at each end of the tube to prevent spheres fall down. The mesh size of the screen is larger than spheres diameter and smaller than the pore size. The porosity of each medium has been determined by construction of a 3D image of the sample made with an X-ray tomography device (Skyscan 1174 type, see Fig. 4-9). A section image of the different samples used in this study is shown in Fig. 4-10.

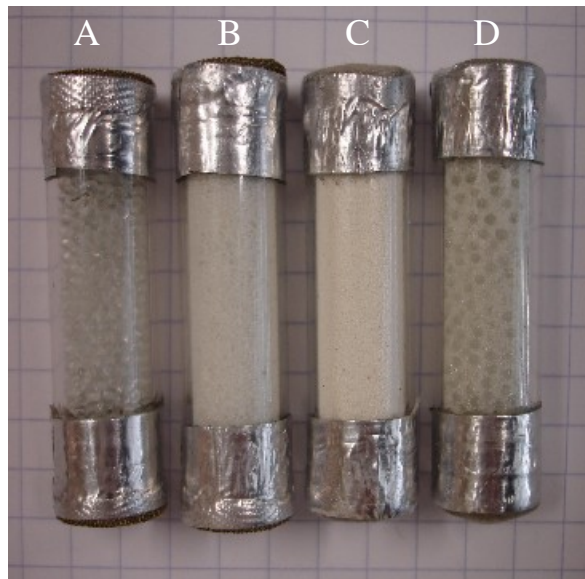


Fig. 4-8. Cylindrical samples filled with glass sphere



Fig. 4-9. X-ray tomography device (Skyscan 1174 type) used in this study

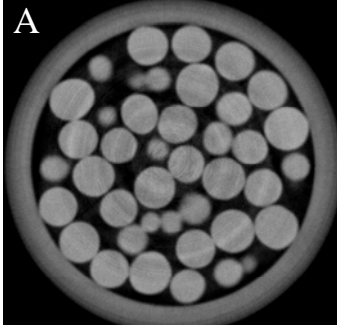
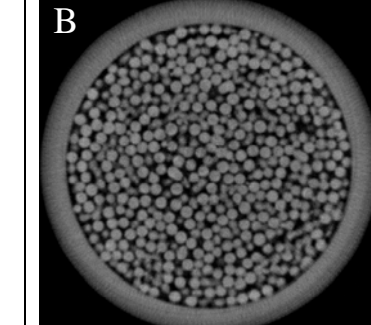
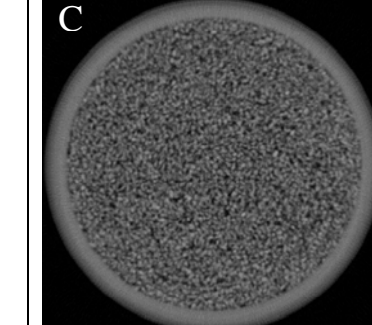
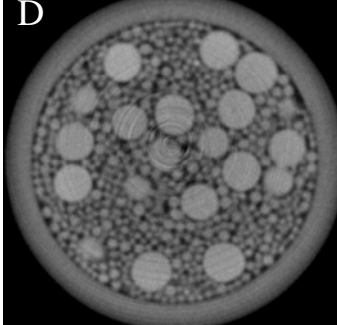
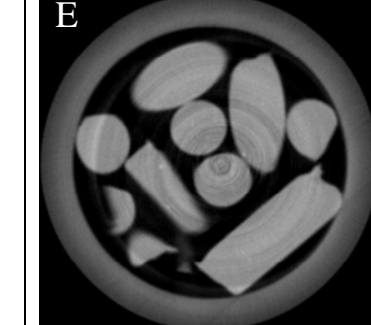
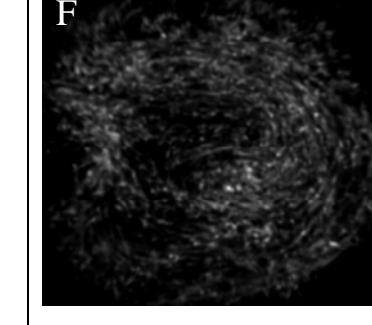
<p>A</p> 	<p>B</p> 	<p>C</p> 
<p>Glass spheres $d = 700\text{-}1000 \mu\text{m}$ $\varepsilon = 42.5 \%$</p>	<p>Glass spheres $d = 200\text{-}210 \mu\text{m}$ $\varepsilon = 40.2 \%$</p>	<p>Glass spheres $d = 100\text{-}125 \mu\text{m}$ $\varepsilon = 30.6 \%$</p>
<p>D</p> 	<p>E</p> 	<p>F</p> 
<p>Mixture of glass spheres $D = 100\text{-}1000 \mu\text{m}$ $\varepsilon = 28.5 \%$</p>	<p>Cylindrical material $d = 1500 \mu\text{m}$ $\varepsilon = 66 \%$</p>	<p>Glass wool Mean fiber diameter = $6 \mu\text{m}$ $\varepsilon \cong 66 \%$</p>

Fig. 4-10. Section images of the tube (inner diameter $d = 0.795 \text{ cm}$) filled by different materials obtained by an X-ray tomography device (Skyscan 1174 type)

The various diffusion time evolution through a free medium and porous media made of different glass spheres (or mixture of them) are shown in Fig. 4-11 and Fig. 4-12 for $He-N_2$ and $He-CO_2$ systems, respectively. These results show clearly that the concentration time variations are very different from free medium and porous medium experiments. In the case of porous medium there is a change depending on the porosity of the medium. The values of the particle diameter, corresponding porosity, and calculated diffusion coefficients are shown in Table 4-5 and Table 4-6. Here, the stated parameters are the effective coefficients and the others are the coefficient in the free fluid.

The diffusion coefficients have been obtained by curve fitting of equation (4-31) on the experimental data. We can conclude from these results that there is not significant difference between calculated ratios of D^*/D_{12} obtained from two different gas systems.

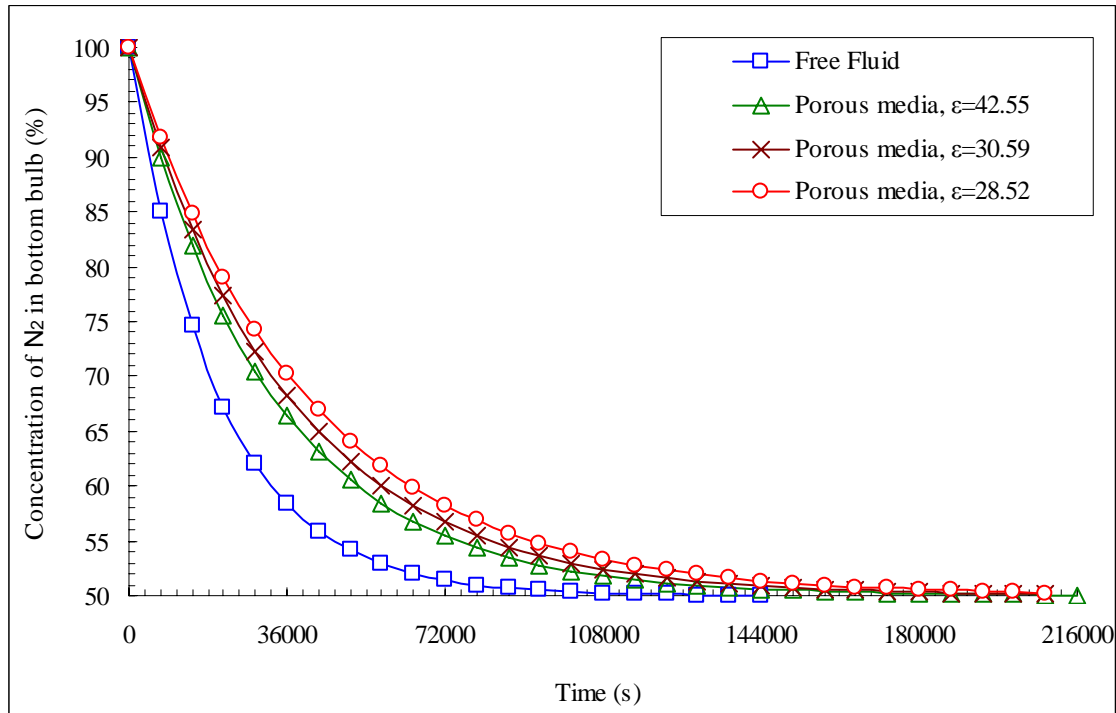


Fig. 4-11. Composition-time history in two-bulb diffusion cell for $He-N_2$ system for different medium. ($T_c = 300K$ and $c_{ib}^0 = 100\%$)

Table 4-5. Measured diffusion coefficient for $He-N_2$ and different media

particle diameter (μm)	Porosity (%)	D_{12} (cm^2/s)	D^*/D_{12} (-)
Free Fluid	100	0.70_0	1
750-1000	42.5	0.43_8	0.64
100-125	30.6	0.39_7	0.57
Mixture of spheres	28.5	0.35_5	0.51

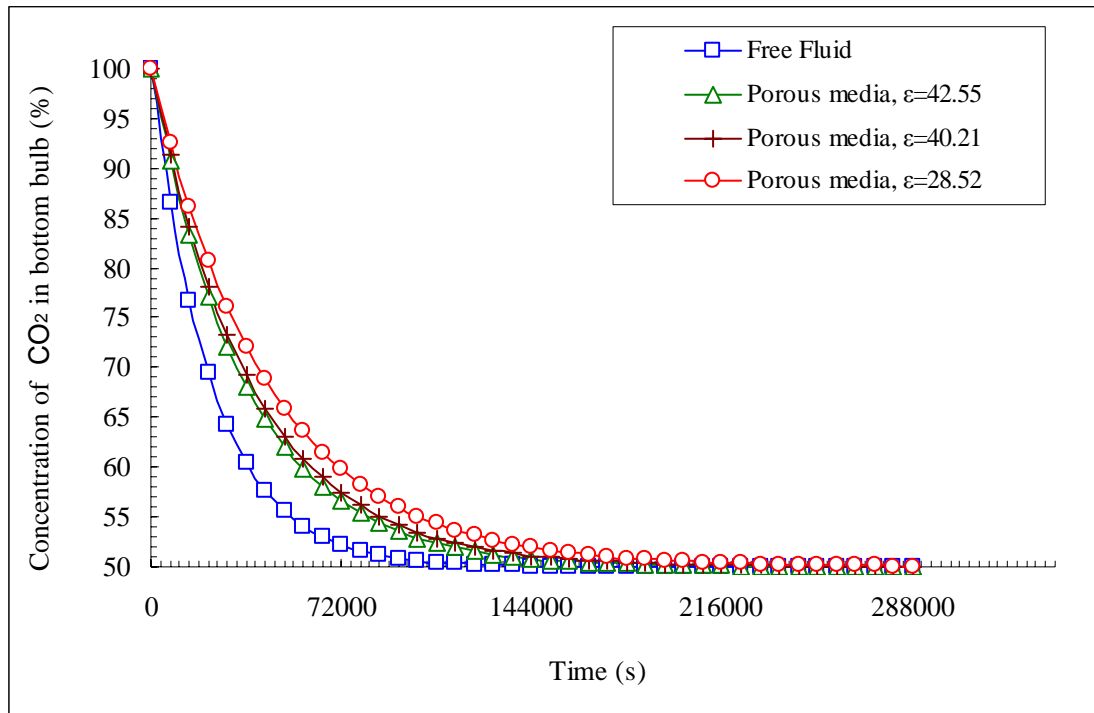


Fig. 4-12. Composition-time history in two-bulb diffusion cell for $He-CO_2$ system for different medium ($T = 300K$ and $c_{1b}^0 = 100\%$)

Table 4-6. Measured diffusion coefficient for $He-CO_2$ and different medium

particle diameter (μm)	Porosity (%)	D (cm^2/s)	D*/D (-)
Free Fluid	100	0.62_0	1
750-1000	42.5	0.40_0	0.65
200-210	40.2	0.37_5	0.61
Mixture of spheres	28.5	0.32_2	0.52

4.4.4 Free fluid and effective thermal diffusion coefficient

Experimental investigations of thermal diffusion have usually been based on the determination of the difference in composition of two parts of a given gas mixture which are at different temperatures. In this work, after obtaining the steady-state in the diffusion process, described in the section 4.4.3,(see also Fig. 4-13a), the temperature of top bulb is increased to $350^\circ K$ as shown in Fig. 4-13b. In this stage the valve between the two bulbs is closed. Increasing the temperature in this bulb will increase the pressure then, by opening a tap on the top bulb, the pressure decrease until it reaches an equilibrium value between the two bulbs.

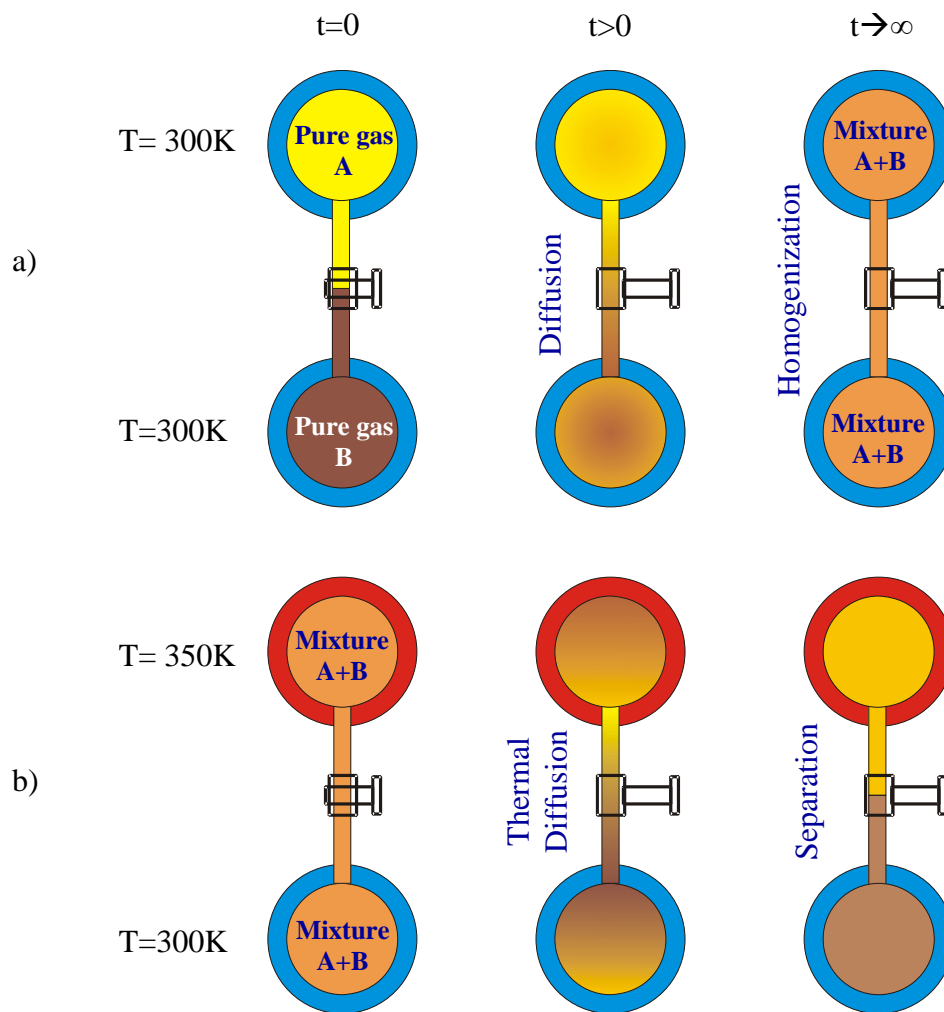


Fig. 4-13. Schematic diagram of two bulb a) diffusion and b) thermal diffusion processes

In this study, since the thermal diffusion coefficient is a complex function of concentration, temperature, pressure, and molecular masses of the components, we have tried to fix all these parameters in order to observe only the influence of porosity on the thermal diffusion process.

The separation can be found from the change in composition which occurs in one bulb during the experiment, providing that the ratio of the volumes of the two bulbs is known.

In the equation expressing the separation, the volume of the connecting tube has been neglected. Then, from equation (4-18) the thermal diffusion factor for $He-N_2$ and $He-CO_2$ binary mixtures is obtained, respectively, as about 0.31 and 0.36. In the literature, this factor, for the temperature range of 287°K -373 °K, is reported as about 0.36 for $He-N_2$ binary mixture [44]. From experimental results of composition dependence of $He-CO_2$ mixture, done with a swing separator method by Batabyal and Barua, (1968) [5] α_T

increases with increasing concentration of the lighter component. A thermal diffusion factor equal to 0.52 is obtained from the equation proposed in their paper, at $\bar{T} = 341.0$ °K [5].

A study using a two-bulb cell to determine the composition and temperature dependence of the diffusion coefficient and thermal diffusion factor of *He-CO₂* system has been done by Dunlop and Bignell, (1995) [28]. They obtain a diffusion coefficient equal to 0.615 cm²/s at 300 °K and a thermal diffusion factor of 0.415 at $\bar{T} = 300$ °K [28].

The theoretical expression for the first approximation to the thermal diffusion factor, according to the Chapman-Enskog theory may be written as follows

$$[\alpha]_1 = A(6C_{12}^* - 5) \quad (4-32)$$

where A is a function of molecular weights, temperature, relative concentration of the two components, and C_{12}^* is a ratio of collision integrals in the principal temperature dependence given by the $(6C_{12}^* - 5)$ factor [40]. We calculated the values of the thermal diffusion factors for *He-CO₂* and *He-N₂* mixtures at \bar{T} , using this theoretical approach and according to the Lennard-Jones (12:6) potential model. We obtained a thermal diffusion factor for *He-N₂* mixture about 0.32 and for *He-CO₂* about 0.41. The detail of formulation and estimation are listed in Appendix B.

As we explained in section 4.2.4, when the experimental data concerning time evolution of the concentration exist, we can evaluate the both diffusion and thermal diffusion coefficients. Therefore in this study, by a curve fitting procedure on the experimental data, two parameters D_{12} and D_T are adjusted until equation (4-26) fits the experimental curve. In fact, adjusting D_{12} fits the slope of the experimental data curves and then, D_T is related to the final steady-state of the curves. The thermal diffusion kinetics for, respectively, free media and porous media made of different glass spheres (or mixture of them) are shown in Fig. 4-14 (*He-N₂* mixture) and Fig. 4-15 (*He-CO₂* mixture). Here also, the time history changes with the porous medium porosity. The values for porosity, particle diameter of the porous medium, calculated diffusion coefficients, thermal diffusion coefficients and related thermal diffusion factor are shown in Table 4-7 for *He-N₂* mixture and Table 4-8 for *He-CO₂* mixture.

The diffusion coefficients calculated with this method are larger than the one obtained in diffusion processes for *He-N₂* system. The theoretical approach (Table 4-4) and experimental data show that the diffusion coefficient increases with increasing the

temperature. From equation (A. 2), when the ideal-gas law approximation is valid, we can write

$$D_{12} \propto \frac{T^{3/2}}{\Omega_D(T^*)} \quad (4-33)$$

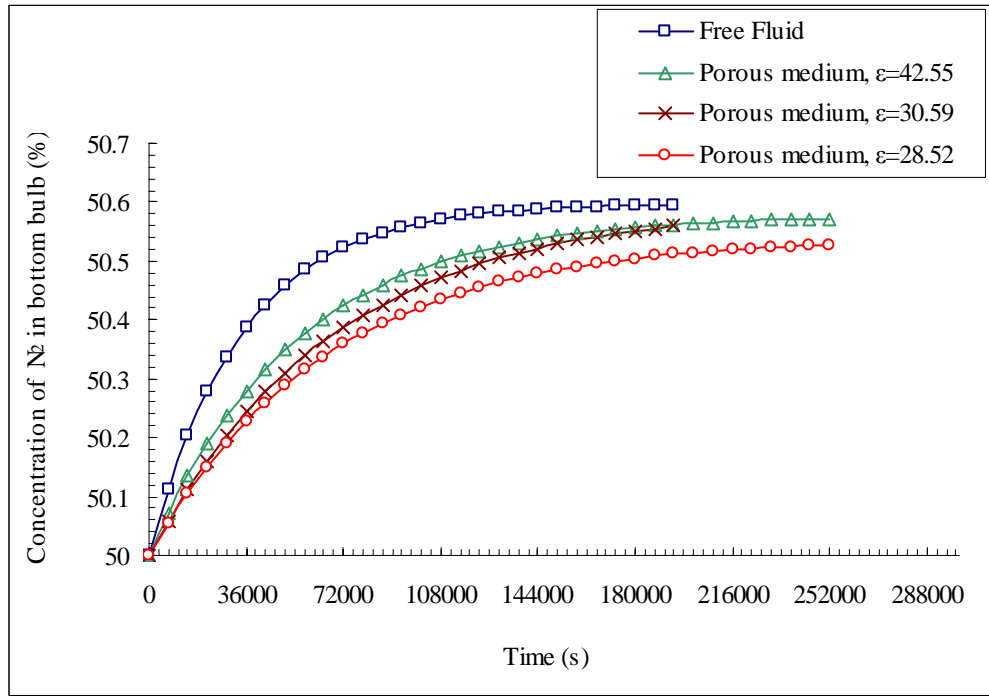


Fig. 4-14. Composition-time history in two-bulb thermal diffusion cell for $He-N_2$ binary mixture for different media ($\Delta T = 50K$, $\bar{T} = 323.7K$ and $c_{1b}^0 = 50\%$)

Table 4-7. Measured thermal diffusion and diffusion coefficient for $He-N_2$ and for different media

particle diameter (μm)	Porosity (%)	D_{12} (cm^2/s)	D^*/D_{12} (-)	α_T (-)	D_T ($cm^2/s.K$)	D_T^*/D_T (-)
Free Fluid	100	0.75 ₅	1	0.31 ₀	0.05 ₉	1
750-1000	42.5	0.45 ₇	0.60 ₅	0.31 ₂	0.03 ₅	0.61
100-125	30.6	0.40 ₆	0.53 ₈	0.30 ₈	0.03 ₁	0.53
Mixture of spheres	28.5	0.36 ₉	0.48 ₉	0.30 ₄	0.02 ₈	0.48

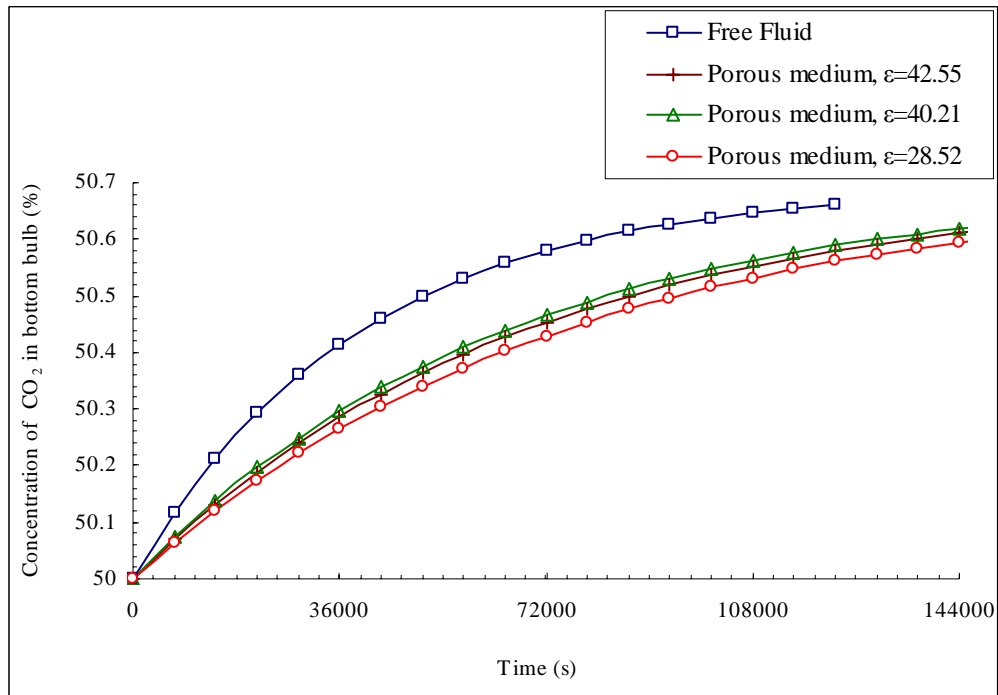


Fig. 4-15. Composition-time history in two-bulb thermal diffusion cell for $He-CO_2$ binary mixture for different media .($\Delta T = 50K$, $\bar{T} = 323.7K$ and $c_{1b}^0 = 50\%$)

Table 4-8. Measured diffusion coefficient and thermal diffusion coefficient for $He-CO_2$ and for different media

particle diameter (μm)	Porosity (%)	D_{12} (cm^2/s)	D^*/D_{12} (-)	α_T (-)	D_T ($cm^2/s.K$)	D_T^*/D_T (-)
Free Fluid	100	0.52_8	1	0.35_8	0.04_7	1
750-1000	42.5	0.30_4	0.62_7	0.36_2	0.02_8	0.61
200-210	40.2	0.32_0	0.56_7	0.36_4	0.02_7	0.59
Mixture of spheres	28.5	0.27_3	0.50_8	0.36_3	0.02_4	0.52

In a second set of thermal diffusion experiments, we eliminate the valve between the two bulbs in order to have a shorter relaxation time. In this case, the tube length is equal to 4 cm only (calibrated cell constant= $2.44 \times 10^{-4} cm^{-2}$) and we filled the system cells with a binary gas mixture ($c_{N_2}^0 = 61.25\%$). At the initial state, the whole setup is kept at a uniform and constant temperature about 325 °K and the composition of the mixture is uniform everywhere. Then, the temperature of the *top* bulb is increased to $T_H = 350$ °K

and the temperature of the *bottom* bulb is lowered to $T_C = 300$ °K. At the end of this process, when the temperature of each bulb remains constant, the pressure of the two bulbs is equal to the beginning of the experience. The thermal diffusion separation in this period is very small because of the forced convection. The katharometer reading data have been recorded with one minute interval. Concentration in bottom bulb has been determined using the katharometer calibration curve. Then, with a curve fitting procedure on the experimental data, as in the last section, the two coefficients D_{12} and D_T are adjusted until equation (4-26) fits the experimental curve. The adjusted curves for a free medium and different porous media are shown in Fig. 4-17. The values obtained for porosity, particle diameter of the porous media, calculated diffusion and thermal diffusion coefficients and thermal diffusion factor are listed in Table 4-9.

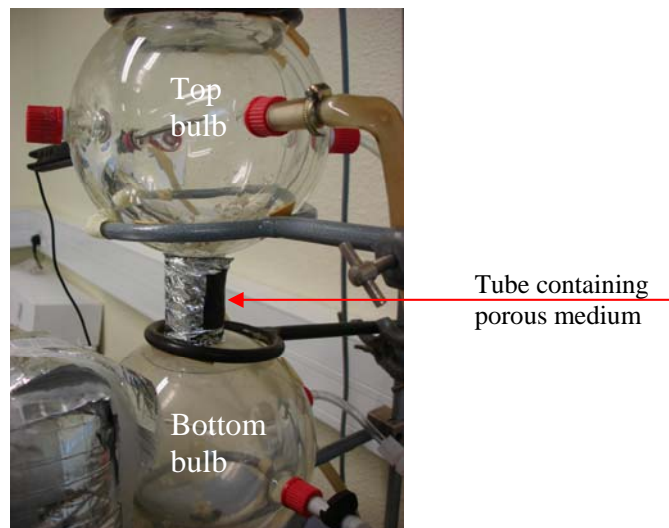


Fig. 4-16. New experimental thermal diffusion setup without the valve between the two bulbs

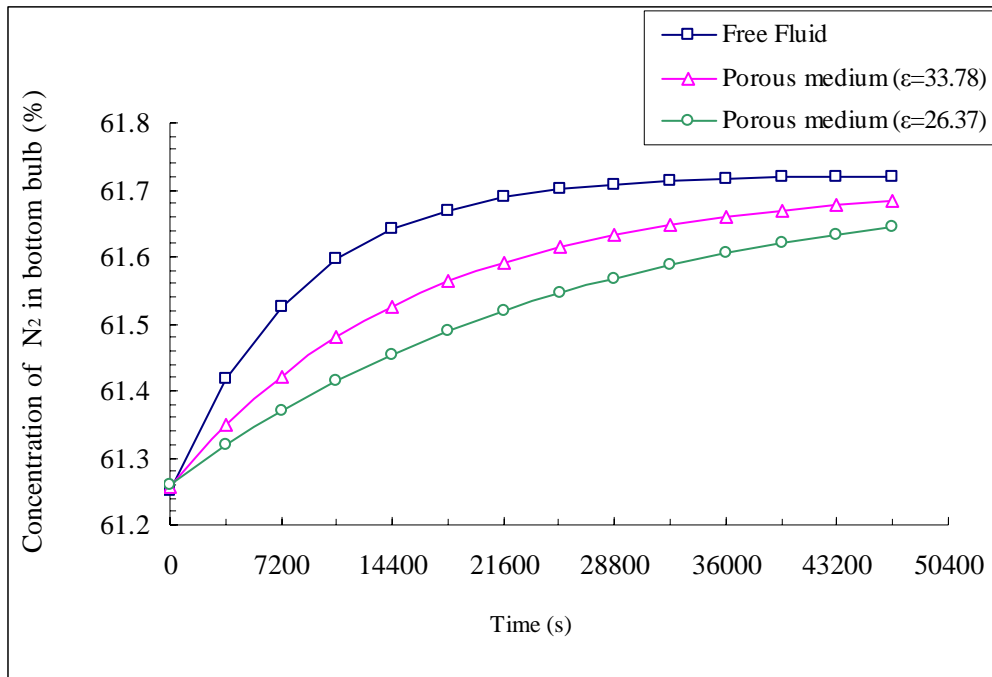


Fig. 4-17. Composition-time history in two-bulb thermal diffusion cell for $He-N_2$ binary mixture for different media ($\Delta T = 50K$, $\bar{T} = 323.7K$ and $c_{1b}^0 = 61.25\%$)

Table 4-9. Measured diffusion coefficient and thermal diffusion coefficient for $He-N_2$ and different media

particle diameter (μm)	Porosity (%)	D (cm^2/s)	D^*/D (-)	α_T (-)	D_T ($cm^2/s.K$)	D_T^*/D_T (-)
Free Fluid	-	0.48_0	1	0.25_6	0.02_9	1
315-325	33.8	0.25_7	0.53_0	0.24_8	0.01_5	0.52
5-50	26.4	0.16_5	0.34_4	0.25_2	0.01_0	0.34

4.4.5 Effect of solid thermal conductivity on thermal diffusion

In section 2.7.2, the theoretical model revealed that, for pure diffusion, the effective thermal diffusion coefficients are independent of the thermal conductivity ratio. To validate this result we have conducted some experiments with two different materials shown in Fig. 4-18. Stainless steel and glass spheres are used in these experiments which their physical properties are listed in Table 4-10.



Fig. 4-18. Cylindrical samples filled with different materials (H: stainless steel, G: glass spheres and $\varepsilon=42.5$)

Table 4-10. The solid (spheres) and fluid mixture physical properties ($T=300$ K) [48]

Material of particles	Diameter (mm)	k_{σ} (sphere) (W/m.K)	k_{β} (gases) (W/m.K)	$(\rho c_p)_{\sigma}$ (kg/m ³ × J./kg.K)	$(\rho c_p)_{\beta}$ (kg/m ³ × J./kg.K)	$\frac{k_{\sigma}}{k_{\beta}}$	$\frac{(\rho c_p)_{\sigma}}{(\rho c_p)_{\beta}}$
Stainless Steel	1	15	He=0.149	7900×477	He=0.1624×5200	301	3202
Glass	1	1.1	CO ₂ =0.0181 Mix=0.0499	2500×750	CO ₂ =1.788×844 Mix=1177	22	1593

The gas mixture used for this study is a *He* (50%)-*CO*₂ (50%) mixture. Like in the section 4.4.4, first the sample (tube of 4 cm length filled by spheres produced a void fraction about $\varepsilon=42.5$) is placed between two bulbs carefully. Next step is to vacuum the air from the system using the vacuum pump. Then, the system, which is kept at a uniform temperature of 325 K, is filled by the gas mixture at atmospheric pressure. To start the thermal diffusion process, the temperature of the top bulb is increased to 350 K and at the same time, the temperature of the bottom bulb is decreased to 300 K. The advantage of this method is that, at the end of this step, when the temperature of each bulb is constant, the pressure of the closed system will be the same as at the starting of the experiment. During this intermediate period, the thermal diffusion process is negligible because of the forced

convection between the two bulbs through the tube. Then, continuous measurements by katharometer, barometers, and thermometers are started in the two bulbs.

It is important to note that, during the tube packing, even if the spheres diameter is the same in both cases, it may result in slightly different porosity. This could be due to different spheres arrangement (because of packing and shaking degree). To avoid this error, we made three samples of each type therefore the experiment is repeated for each sample.

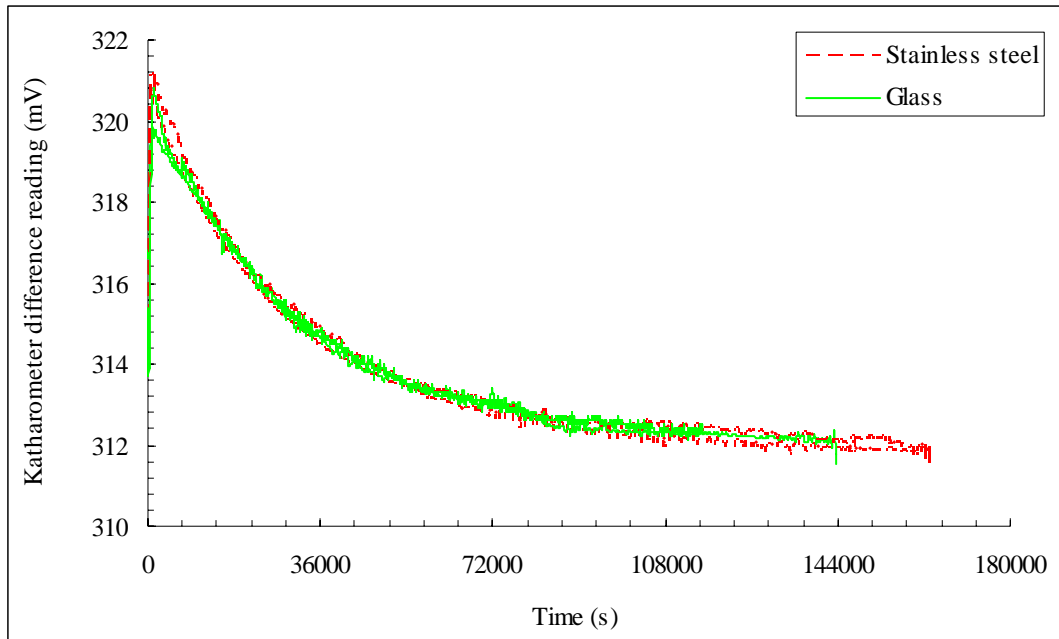


Fig. 4-19. Katharometer reading time history in two-bulb thermal diffusion cell for $He-CO_2$ binary mixture for porous media having different thermal conductivity (3 samples of stainless steel and 3 samples of glass spheres) ($\Delta T = 50K$, $\bar{T} = 323.7K$ and $c_{1b}^0 = 50\%$)

Katharometer reading time histories for porous media made of different thermal conductivity (stainless steel and glass spheres) is plotted in Fig. 4-19.

As it is shown in this plot, thermal diffusion curves for the two different materials can be superimposed and we can conclude that, in this case, the thermal conductivity ratio has no significant influence on the thermal diffusion process.

4.4.6 Effect of solid thermal connectivity on thermal diffusion

It is known that heat conduction at the contact points plays a dominant role in determining the effective heat conduction in porous media [79, 92]. To determine the effect of solid phase connectivity, one must use a higher thermal conductor than stainless steel. Because theoretical results show that the influence of this phenomenon is considerable when the thermal conductivity ratio is more than 100 as shown in Fig. 2-15. Therefore, it is better to test more conductive material. We have chosen aluminum and glass spheres with a diameter of 6mm shown in Fig. 4-20. The sample preparation is different from the last section. Here, the sample is made of one array of spheres, in which we can neglect the problem that we had concerning spheres arrangement in the tube. Here, inner diameter of insulated rigid glass tube is chosen to be $d = 0.75$ cm and length of $\ell = 5.8$ cm. The number of spheres forming the porous medium is ten, which produced a void fraction about $\varepsilon = 0.56$.

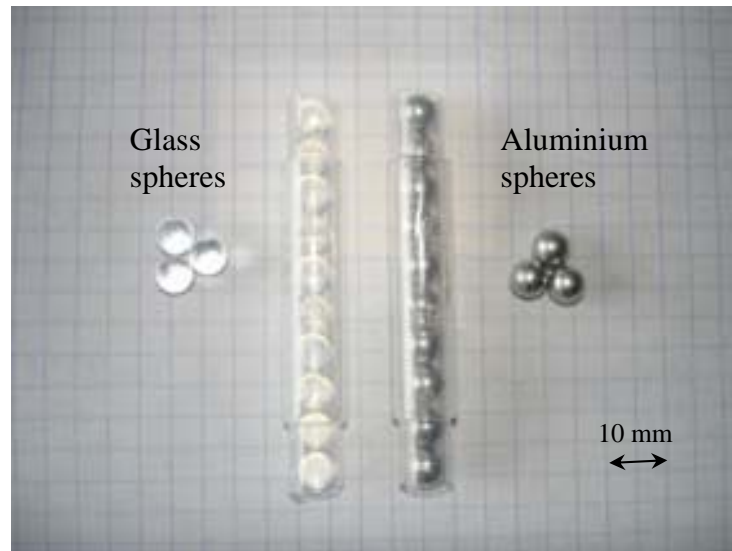


Fig. 4-20. Cylindrical samples filled with different materials (A: glass spheres, B: aluminium spheres and $\varepsilon=0.56$)

The physical properties of two materials used in this experiment are listed in Table 4-11. As we can see, the thermal conductivity ratio for aluminum and the mixture of helium and carbon dioxide is about 4749. At this value, the connectivity of the solid phase has a high influence on the effective thermal conductivity coefficients as shown in Fig. 2-15.

Table 4-11. The solid (spheres) and fluid mixture physical properties (T=300 K) [48]

Material of particles	Diameter (mm)	k_{σ} (sphere) (W/m.K)	k_{β} (gases) (W/m.K)	$(\rho c_p)_{\sigma}$ (kg/m ³ × J./kg.K)	$(\rho c_p)_{\beta}$ (kg/m ³ × J./kg.K)	$\frac{k_{\sigma}}{k_{\beta}}$	$\frac{(\rho c_p)_{\sigma}}{(\rho c_p)_{\beta}}$
Aluminum	6	237	He=0.149 CO ₂ =0.0181 Mix=0.0499	2702×903	He=	4749	2073
Glass	6	1.1		2500×750	0.1624×5200 CO ₂ = 1.788×844 Mix=1177	22	1593

Katharometer reading time histories for porous media made of aluminum and glass spheres have been plotted in Fig. 4-21.

This figure shows that, the thermal diffusion curves for two different materials are superimposed. That means that, the particle-particle contact does not show a considerable influence on the thermal diffusion process.

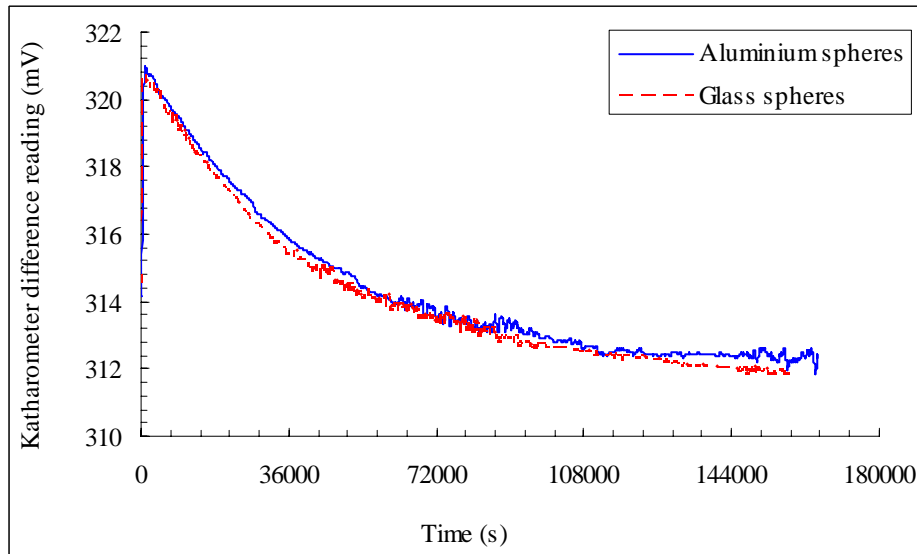


Fig. 4-21. Katharometer time history in two-bulb thermal diffusion cell for $He-CO_2$ binary mixture for porous media made of different thermal conductivity (aluminum and glass spheres) ($\Delta T = 50K$, $\bar{T} = 323.7K$ and $c_{1b}^0 = 50\%$)

4.4.7 Effect of tortuosity on diffusion and thermal diffusion coefficients

Mathematically, the tortuosity factor, τ , defined as the ratio of the length of the “tortuous” path in a porous media divided by a straight line value shown in Fig. 4-22.

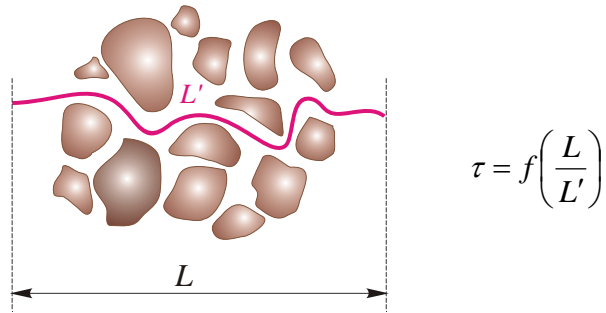


Fig. 4-22. Definition of tortuosity coefficient in porous media, L = straight line and L' = real path length

There are several definitions of this factor. The most widely used correlation for gaseous diffusion is the one of Millington and Quirk (1961) for saturated unconsolidated system [63, 62]

$$\tau = 1/\varepsilon^{1/3} \quad (4-34)$$

Tortuosity is also an auxiliary quantity related to the ratio of the effective and free diffusion coefficients. τ in many application for homogenous and isotropic environment is also defined as [69, 68]

$$\tau = \sqrt{\frac{D_{12}}{D^*}} \quad (4-35)$$

In this study, we define the tortuosity as a ratio of the effective to free diffusion coefficients as we mentioned also in chapter 2

$$\frac{D^*}{D_{12}} = \frac{1}{\tau} \text{ or, } \frac{D_r^*}{D_r} = \frac{1}{\tau}, \text{ which are } f\left(\frac{L}{L'}\right) \quad (4-36)$$

Table 4-12 presents the tortuosity factors calculated from values measured in this work (for non-consolidate spheres and the tortuosity definition with Eq. (4-36))

Table 4-12. Porous medium tortuosity coefficients

Particle diameter (μm)	Porosity (%)	$\tau = \frac{D_{12}}{D^*}$ (From diffusion experiments)	$\tau = \frac{D_{12}}{D^*}$ (From thermal diffusion experiments)	$\tau = \frac{D_T}{D_T^*}$ (From thermal diffusion experiments)	$\bar{\tau}$
750-1000	42.5	1.57	1.62	1.63	1.61
200-210	40.2	1.65	1.76	1.71	1.71
315-325	33.8	-	1.89	1.92	1.90
100-125	30.6	1.76	1.86	1.87	1.83
Mixture of spheres	28.5	1.95	2.00	1.99	1.98
5-50	26.4	-	2.91	2.90	2.90

We showed that porosity has an important influence on both effective isothermal diffusion and thermal diffusion coefficients. Another question is what may happen when there are two media with the same porosity but not the same tortuosity.

In this section we tried to construct two media with such properties as shown in Fig. 4-23.



Fig. 4-23. Cylindrical samples filled with different materials producing different tortuosity but the same porosity $\varepsilon=66\%$ (E: cylindrical material and F: glass wool)

The section image of the tubes filled by these materials obtained by the tomograph device (Skyscan 1174 type) is shown in Fig. 4-10 E and F.

The results of concentration-time histories for porous medium made with cylindrical samples and glass wool are plotted in Fig. 4-24. As we can see, the concentration-time curves for two cases are not superimposed and are completely separated. The calculated

tortuosity factor in porous medium made of cylindrical materials is $\tau = 2.37$ and for glass wool it is relatively two times less than one for cylindrical materials $\tau = 1.04$. These results indicate that the effective coefficients are not only the function of porosity but also the geometry. Thus, tortuosity prediction using only the porosity may not be enough and the permeability of the medium should be considered also.

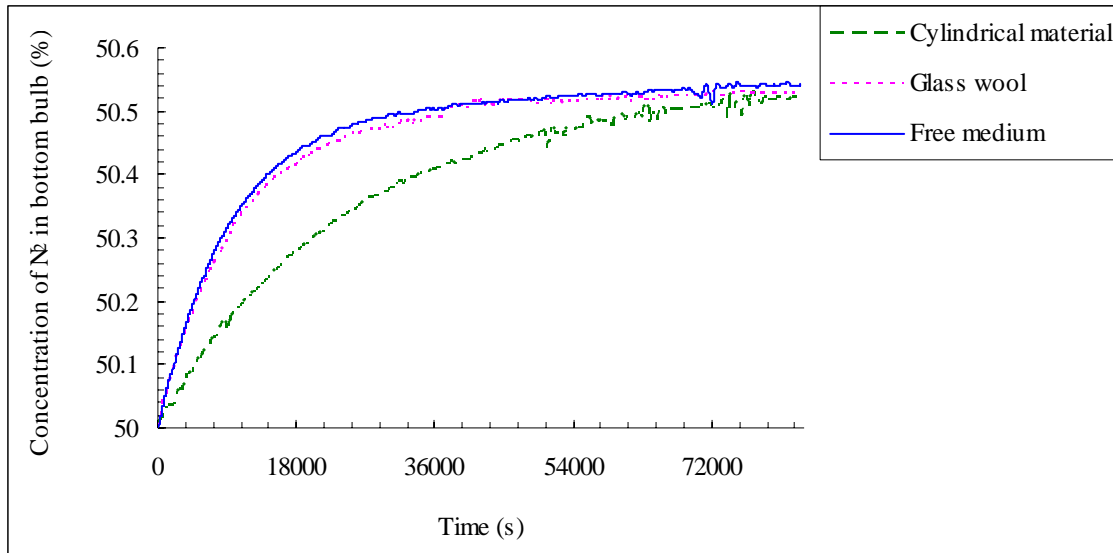


Fig. 4-24. Composition time history in two-bulb thermal diffusion cell for $He-CO_2$ binary mixture in porous media made of the same porosity ($\epsilon=66\%$) but different tortuosity (cylindrical materials and glass wool) ($\Delta T = 50K$, $\bar{T} = 323.7K$ and $c_{1b}^0 = 50\%$)

4.5 Discussion and comparison with theory

In the theoretical part of this study, chapter 2, we have presented the volume averaging method to obtain the macro-scale equations that describe diffusion and thermal diffusion processes in a homogeneous porous medium. The results of this model showed that the effective thermal diffusion coefficient at diffusive regime can be estimated with the single tortuosity, results fully discussed in the literature [79, 80]. Here, we rewrite the basic theoretical results for a pure diffusion and binary system as

$$\frac{D^*}{D_{12}} = \frac{D_T^*}{D_T} = \frac{1}{\tau}, \text{ for pure diffusion} \quad (4-37)$$

Fig. 4-25 and Fig. 4-26 show respectively a comparison of effective diffusion and thermal diffusion coefficients measured in this study and the theoretical results from the volume averaging technique for different porosity of the medium. We note that, the volume averaging process, have carried out using a model unit cell such as the one shown

in Fig. 2-6. In this system, the effective diffusion and thermal diffusion coefficients for different fractional void space is plotted as the continuous lines. These figures show that the experimental, effective coefficient results for the non-consolidated porous media made of spheres are in excellent agreement with volume averaging theoretical estimation.

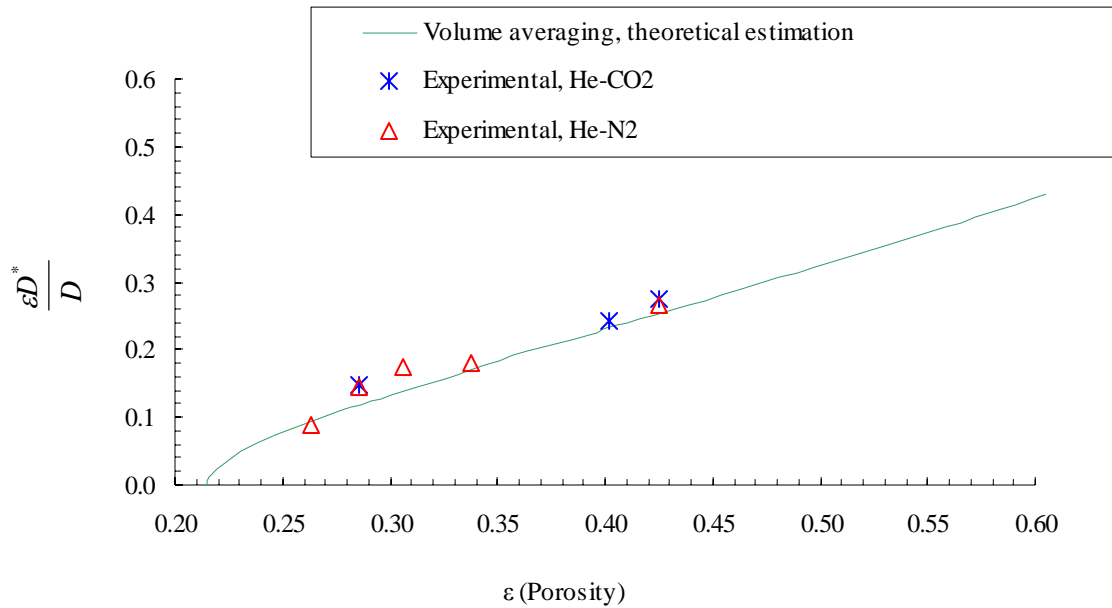


Fig. 4-25. Comparison of experimental effective diffusion coefficient data with the theoretical one obtained from volume averaging technique for different porosity and a specific unit cell

In Fig. 4-27 the ratio of k_T^*/k_T has been plotted against porosity, where, the effective thermal diffusion ratio, k_T^* , has been defined as $k_T^* = TD_T^*/D^*$. The experimental results for both mixtures are fitted with the volume averaging theoretical estimation. These results also validate the theoretical results and reinforce the fact that for pure diffusion the Soret number is the same in the free medium and porous media.

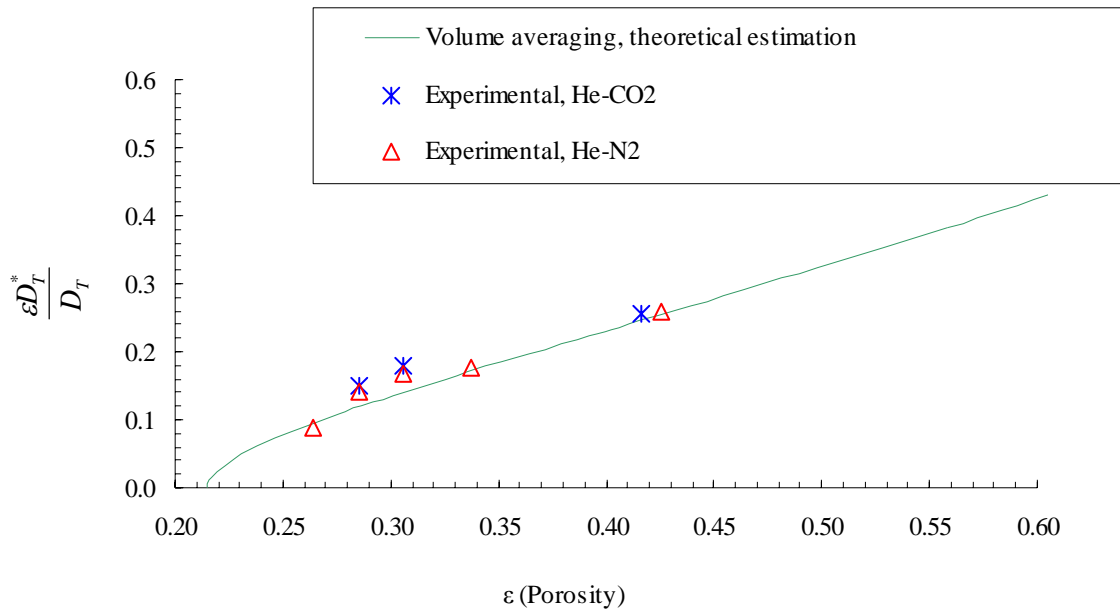


Fig. 4-26. Comparison of experimental effective thermal diffusion coefficient data with theoretical one obtained from volume averaging technique for different porosity and a specific unit cell

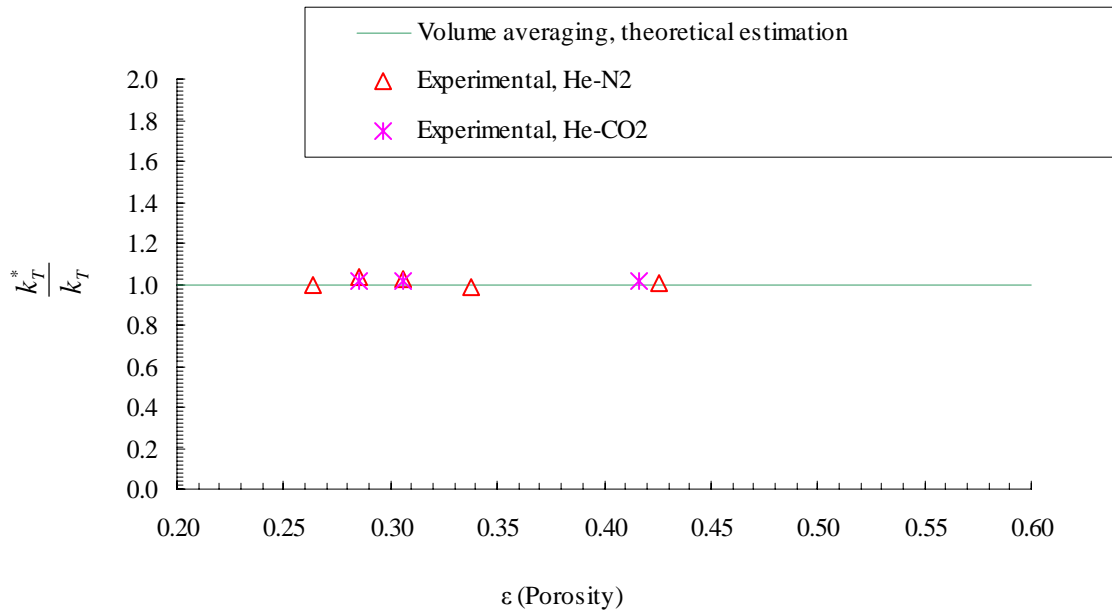


Fig. 4-27. Comparison of the experimental thermal diffusion ratio data with theoretical one obtained from volume averaging technique for different porosity and a specific unit cell

4.6 Conclusion

In this chapter, we used a “two-bulb apparatus” for measuring the diffusion and thermal diffusion coefficient in free medium and non-consolidated porous medium having different porosity and thermal conductivity, separately. The results show that for *He-N₂* and *He-CO₂* mixtures, the porosity of the medium has a great influence on the thermal diffusion process. On the opposite, thermal conductivity and particle-particle contact of the solid phase have no significant influence on thermal diffusion in porous media. The comparison of the ratio of effective coefficients in the porous medium to the one in the free medium shows that the behavior of tortuosity is the same for the thermal diffusion coefficient and diffusion coefficient. Therefore, the thermal diffusion factor is the same for a free medium and porous media. For non-consolidated porous media made of the spheres these results agree with the model obtained by upscaling technique for effective thermal diffusion coefficient proposed in the theoretical chapter 2. The tortuosity of the medium calculated using both effective diffusion and effective thermal diffusion coefficients are not different to the measurement accuracy.

Chapter 5

General conclusions and perspectives

5. General conclusions and perspectives

In this study, the effective Darcy-scale coefficients for coupled via Soret effect heat and mass transfer in porous media have been determined theoretically and experimentally. A theoretical model has been developed using the volume averaging technique. We determined from the microscopic equations new transport equations for averaged fields with some effective coefficients. The associated quasi-steady closure problems related to the pore-scale physics have been solved over periodic unit cells representative of the porous structure. Particularly, we have studied the influence of the void volume fraction (porosity), Péclet number and thermal conductivity on the effective thermal diffusion coefficients. The obtained results show that

- the values of the effective coefficients in porous media are completely different from the ones of the free medium (without the porous medium),
- in all cases, the porosity of the medium has a great influence on the effective thermal diffusion coefficients,
- for a diffusive regime, this influence is the same for the effective diffusion coefficient and thermal diffusion coefficient. As a result, for low Péclet numbers, the effective Soret number in porous media is the same as the one in the free fluid. At this regime, the effective thermal diffusion coefficient does not depend on the solid to fluid conductivity ratio,
- for a convective regime, the effective Soret number decreases and then changes its sign. In this case, a change of conductivity ratio will change the effective thermal diffusion coefficient as well as the effective thermal conductivity coefficient,
- theoretical results also showed that for pure diffusion, even if the effective thermal conductivity depends on the particle-particle contact, the effective thermal diffusion coefficient is always constant and independent on the connectivity of the solid phase.

As a validation, the initial pore-scale problem was solved numerically over an array of cylinders, and the resulting averaged temperature and concentration fields were compared to macro-scale theoretical predictions using the effective coefficients resulting from the previous theoretical study. The results showed that

- a good agreement has been found between macro-scale resolutions and micro-scale, direct simulations, which validates the proposed theoretical model,
- thermal diffusion modifies the local concentration and this modification depends locally on the porosity, thermal conductivity ratio and fluid velocity. Therefore, we cannot ignore this effect.

A new experimental setup has been designed and made-up to determine directly the effective diffusion and thermal diffusion coefficients for binary mixtures. This setup is a closed system, which helped carry out the experiments for the case of pure diffusion only. The experiments have been performed with special all-glass two-bulb apparatus, containing two double-spherical layers. The diffusion and thermal diffusion of helium-nitrogen and helium-carbon dioxide systems through cylindrical samples first without porous media and then filled with spheres of different diameters and thermal conductivities were measured at the atmospheric pressure. Concentrations were determined by analysing the gas mixture composition in the bulbs with a katharometer device. A transient-state method for coupled evaluation of thermal diffusion and Fick coefficient in two bulbs systems has been proposed. Here, with a simple thermal diffusion experiment, this model is able to determine both diffusion and thermal diffusion coefficients. The determination of diffusion and thermal diffusion coefficients is done by a curve fitting of the temporal experimental results with the transient-state solution describing the mass balance between the two bulbs. The results showed

- a dependency of the thermal diffusion and diffusion coefficients on the porosity,
- a good agreement with theoretical results, which confirm the validity of the theoretical results for pure diffusion,
- the tortuosity of the medium calculated using both effective diffusion and effective thermal diffusion coefficients were not different to the measurement accuracy,
- the experimental results also showed that the particle-particle touching has not a significant influence on the effective thermal diffusion coefficients.

There is still much work to be done concerning thermal diffusion in porous media. Several perspectives can be proposed. The following ones present especial interest

- in the theoretical part of this study we developed a coupled heat and mass transfer macro-scale equation with a non-thermal equilibrium case (using a two-equation temperature problem). One may use this model when the assumption of thermal equilibrium is not valid. However, the closure problems have not been solved for

this model. Therefore, the next step may be to solve numerically these closure problems and then compare with the one-equation results,

- the model proposed in this study is able to predict the effective coefficients in a binary mixture of gas (or liquid) phase, the future works may be to focus on more real and complex problems, i.e. multi-component and multi-phase systems.
- the effect of solid phase connectivity on the effective thermal conductivity and thermal diffusion coefficients has been investigated on a two dimensional closure problem. In the case of thermal diffusion, we eliminated the particle touching in the y -direction to calculate the longitudinal thermal diffusion coefficient. In future work, one can resolve this problem using a three dimensional model, keeping the x , y and z touching parts as shown in Fig. 5-1. The three dimensional model may be also interesting for calculating effective thermal conductivity for purpose of comparison with earlier two dimensional results,

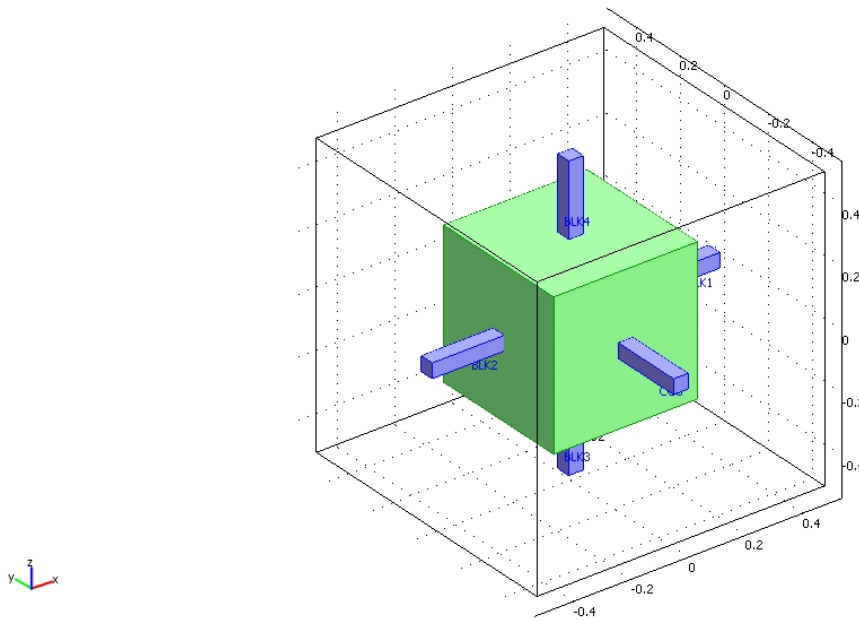


Fig. 5-1. 3D geometry of the closure problem with particle-particle touching made with COMSOL Multiphysics

- by now, there is no qualitative agreement between numerical and experimental results concerning separation in packed thermogravitational cell as shown in Fig. 5-2 [31]. We showed that the ratio of thermal conductivity is very important for the convective regime. Therefore, this should change the separation rate in a packed thermogravitational cell. Therefore, it is very interesting to find the relation

between separation and thermal conductivity ratio. This may be achieved by simple micro-scale modelling or by the design of an experimental setup for a packed thermogravitational cell filled with different materials. The results may reveal the reason of discrepancy which exists between theoretical and experiment results in a packed thermogravitational cell,

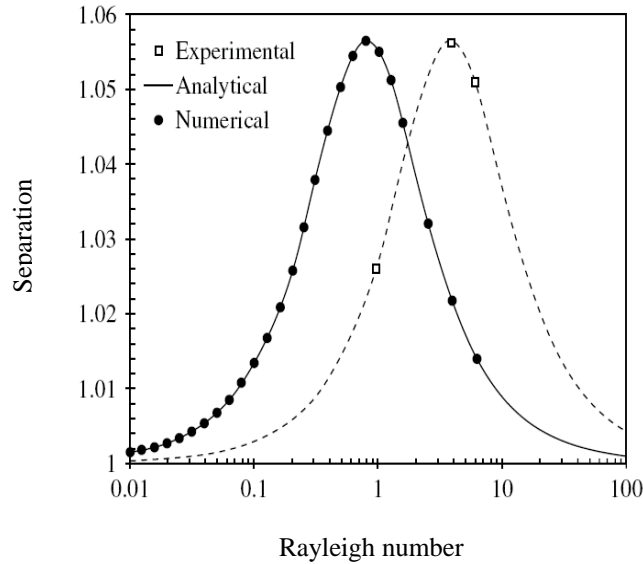


Fig. 5-2. Discrepancy between numerical results and experimental measurements in a packed thermogravitational cell [31]

- in our work the experiments have been done for a non-consolidated material. The next experiments can be done using consolidated porous media. One will be able to produce two porous media of different materials with exactly same porosity.
- in this study using a katharometer device, the experiments have been limited to binary systems. However, it is also important to measure directly the effective thermal diffusion coefficients in ternary mixtures or beyond. In future work, using, for example, a gas chromatography device, the results will be extended to more than two components,
- the experiments were performed for pure diffusion cases, which allowed us to validate the corresponding theoretical results only at pure diffusion. Designing another setup capable to measure the impact of dispersion on thermal diffusion (see Fig. 5-3) can be helpful to validate the theoretical results when the Péclet number is not zero, as well as for practical reasons.

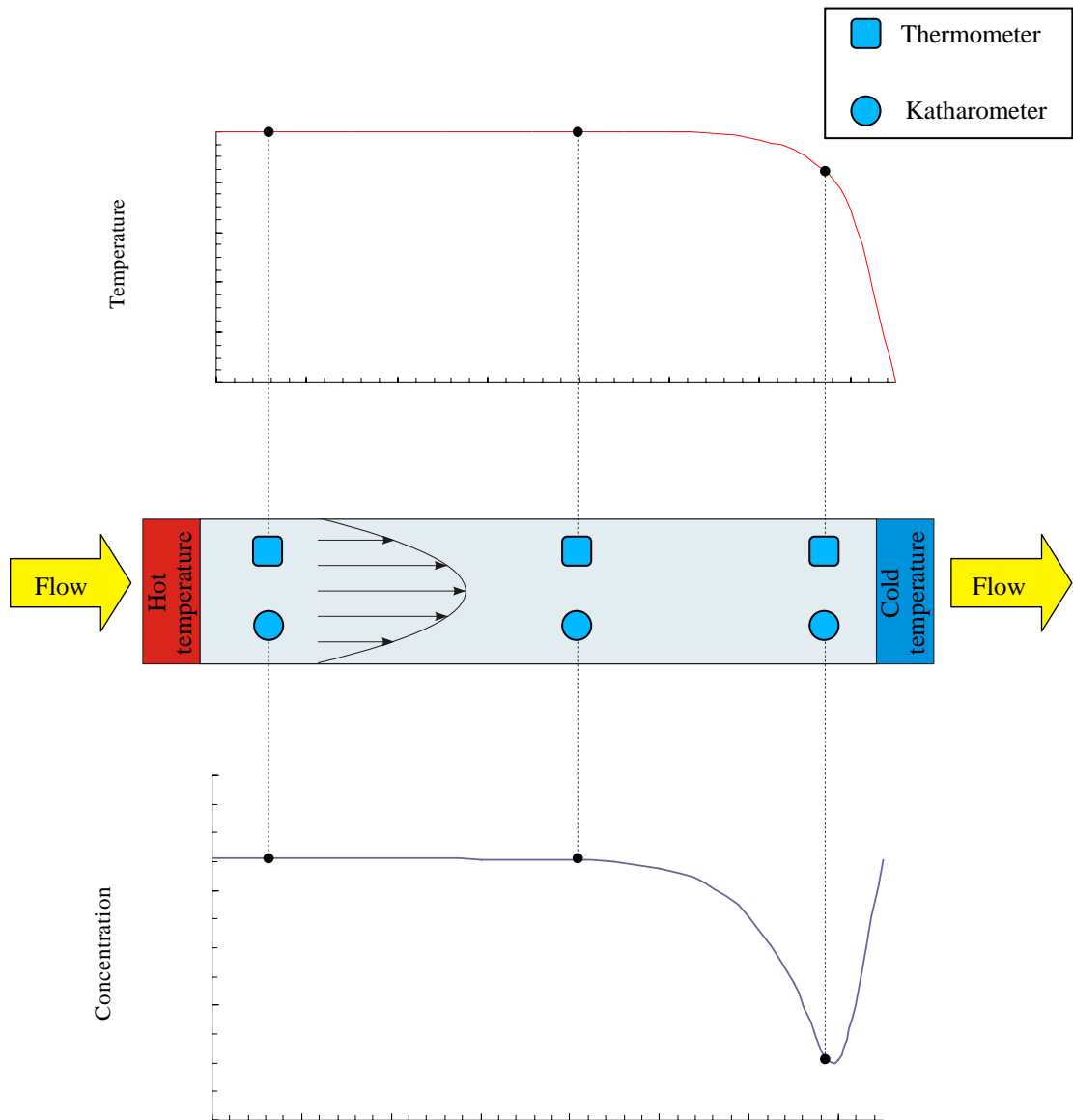


Fig. 5-3. Proposition of experimental setup for convective regime

- Finally, it could be interesting to apply the new results obtained in this work to practical situations.

Conclusions générales et perspectives en français

Dans cette étude, les coefficients effectifs à l'échelle de Darcy pour le transfert couplé de la chaleur et de la matière dans le milieu poreux ont été déterminés expérimentalement et théoriquement. Un modèle théorique a été développé en utilisant la méthode de prise de moyenne volumique. L'application du théorème de prise de moyenne volumique sur les équations microscopiques décrivant les transports à l'échelle du pore permet d'obtenir les nouvelles équations de transport pour les champs moyens avec les coefficients effectifs. Les problèmes de fermetures liées à la physique de l'échelle des pores ont été résolus sur une cellule unitaire périodique représentative de la structure poreuse. En particulier, nous avons étudié l'influence de la fraction volumique du pore (porosité), nombre de Péclet et de la conductivité thermique sur les coefficients de thermodiffusion effectifs. Les résultats obtenus montrent que :

- les valeurs des coefficients effectifs en milieu poreux sont complètement différents de celles du milieu libre (sans milieu poreux),
- dans tous les cas, la porosité du milieu a une grande influence sur les coefficients de thermodiffusion effectifs en milieu poreux,
- pour un régime diffusif ($Pe = 0$), cette influence est la même pour le coefficient de diffusion isotherme effectif et le coefficient de thermodiffusion effectif. En conséquence, pour les faibles nombres de Péclet, le nombre de Soret effectif dans le milieu poreux est le même que celui en milieu libre. Pour ce régime, le coefficient de thermodiffusion effectif ne dépend pas du ratio des conductivités thermiques,
- pour le régime convectif ($Pe \neq 0$), le nombre de Soret effectif diminue et change même de signe pour les régimes fortement convectifs. Dans ce cas, un changement du rapport de la conductivité thermique changera le coefficient thermodiffusion effectif ainsi que le coefficient conductivité thermique effective,
- en diffusion pure, même si la conductivité thermique effective dépend de la connectivité de phase solide, le coefficient thermodiffusion effective est toujours constant et indépendant de la connectivité de la phase solide,

Afin de valider les résultats théoriques précédents, le problème d'échelle du pore a été résolu numériquement sur une série de cylindres. Les températures et concentrations

moyennes sont comparées avec les prédictions macroscopiques en utilisant les coefficients effectifs obtenus avec le modèle proposé. Les résultats montrent que :

- il y a un très bon accord entre les résultats issus des résolutions à l'échelle macroscopique (avec coefficients effectifs) et microscopiques (simulations directes), ce qui valide le modèle théorique proposé,
- la thermodiffusion modifie la concentration locale et cette modification dépend localement de la porosité, du ratio de conductivité thermique et de la vitesse du fluide. Par conséquent, cet effet ne peut pas être négligé dans la plupart des cas.

Un nouveau dispositif expérimental a été conçu et mis en place afin de déterminer directement les coefficients de diffusion et thermodiffusion effectif pour des mélanges binaires. Le dispositif réalisé est un système fermé, ce qui a permis d'effectuer des expériences pour les cas de diffusion pure. Les expériences ont été réalisées avec un dispositif de type « deux bulbes » spécifique, tout en verre, contenant une double couche sphérique permettant de contrôler les températures de chaque réservoir. La diffusion et la thermodiffusion de mélanges binaires hélium-azote, et d'hélium-dioxyde de carbone, à travers des échantillons cylindriques d'abord sans milieux poreux, puis rempli avec des sphères de différents diamètres et de différentes conductivités thermiques est mesurée à pression atmosphérique. Les concentrations sont déterminées en analysant la composition du mélange de gaz dans les ampoules à l'aide d'un catharomètre qui est solidarisé à une partie de l'ampoule. Une méthode transitoire pour l'évaluation couplée du coefficient de thermodiffusion et de diffusion de Fick dans le système de deux ampoules a été proposée. Ici, avec une expérience simple de thermodiffusion, ce modèle est capable de déterminer à la fois les coefficients de diffusion et de thermodiffusion. La détermination de ces coefficients est réalisé par ajustement (« fitting ») de la courbe expérimentale de l'évolution temporelle des concentrations avec une solution analytique décrivant le bilan transitoire de matière entre les deux ampoules. Cela permet d'ajuster les coefficients jusqu'à ce que les équations se superposent avec les résultats expérimentaux. Les résultats ont montré :

- une dépendance des coefficients de thermodiffusion et de diffusion effectifs avec la porosité,
- un bon accord avec les résultats théoriques, ce qui confirme la validité des résultats théoriques en diffusion pure,

- une valeur de la tortuosité du milieu identique lorsqu'elle est calculée à partir des coefficients de diffusion effectifs ou à l'aide des coefficients de thermodiffusion effectifs, ce qui permet de proposer une valeur moyenne du coefficient de tortuosité du milieu,
- le contact particule-particule n'a pas d'influence significative sur les coefficients de thermodiffusion effectifs.

Il reste encore beaucoup des recherches et de développements à faire concernant la thermodiffusion en milieux poreux. Plusieurs perspectives peuvent être proposées; celles qui suivent présentent un intérêt particulier en prolongement du travail réalisé :

- dans la partie théorique de cette étude, nous avons développé un modèle macroscopique décrivant de transfert de chaleur et matière avec une équation de non-équilibre locale thermique (avec un problème à deux équation pour température), qu'il peut être utiliser lorsque l'hypothèse de l'équilibre thermique n'est pas valide. Toutefois, pour ce modèle les problèmes de fermeture n'ont pas été résolus. Une prochaine étape consisterait à résoudre numériquement ces problèmes des fermetures et comparer ensuite avec les résultats à une équation,
- l'effet de la connectivité de la phase solide sur les coefficients de thermodiffusion et la conductivité thermique a été traité avec un problème de fermeture à deux dimensions. Dans le cas de la thermodiffusion, nous avons éliminé la connectivité de particules dans la direction y pour ne pas « bloquer » le transfert de matière et calculer le coefficient de thermodiffusion effective longitudinal. En utilisant un modèle à trois dimensions, on pourra résoudre ce problème en gardant la connectivité de la phase solide dans les trois directions x , y et z (Fig. 5-1). Ce modèle en trois dimensions pourrait d'ailleurs être également intéressant pour la détermination de la conductivité thermique effective,
- jusqu'à présent, il n'y a pas d'accord entre les résultats numériques et expérimentaux concernant la séparation dans un cellule thermogravitationnelle [31] comme indiqué dans la Fig. 5 2. Nous avons montré que l'influence du rapport des conductivités thermiques est très importante pour le régime convectif. Ceci doit avoir des conséquences sur la séparation des espèces obtenue dans les cellules de thermogravitation. Par conséquent, il serait intéressant de trouver cette influence par modélisation numérique en l'échelle du pore ou par la réalisation d'un autre

dispositif expérimental avec une cellule thermogravitationnelle remplie de matériaux différents. Ceci pourrait peut être montrer la raison des divergences qui existent entre les résultats théoriques et expérimentaux dans la cellule thermogravitationnelle,

- dans ce travail les expériences ont été réalisées pour des matériaux non-consolidés. Les expériences suivante peut-être faite en utilisant les milieux poreux consolidés. Certaines expériences pourraient être réalisé pour déterminer par exemple l'impact de la conductivité thermique sur les coefficients de thermodiffusion en milieu poreux avec différentes propriétés thermo-physiques,
- dans cette étude, l'utilisation d'un catharomètre, a limité les expériences à des systèmes binaires. Il serait également important de pouvoir mesurer directement les coefficients de thermodiffusion effectifs dans des mélanges ternaires. Dans les travaux futurs, l'utilisation par exemple d'un dispositif de chromatographie seront permettrait d'obtenir des résultats pour des mélanges à plus de deux composants,
- le dispositif expérimental réalisé ici a permis de traiter le cas de la diffusion pure, et de valider les résultats théoriques correspondant à ce cas. La validation expérimentale des résultats théoriques lorsque le nombre de Péclet n'est pas nul (validés par ailleurs par les simulations à l'échelle du pore) nécessiterait la réalisation d'un nouveau dispositif (voir Fig. 5-3), en système ouvert, permettant de mesurer l'impact de la dispersion sur la thermodiffusion.
- Enfin, il pourrait être intéressant d'appliquer les nouveaux résultats obtenus dans ce travail à des situations pratiques.

Appendix A. Estimation of the diffusion coefficient with gas kinetic theory

The diffusion coefficient D_{12} for the isothermal diffusion of species 1 through constant-pressure binary mixture of species 1 and 2 is defined by the relation

$$J_1 = -D_{12}\nabla c_1 \quad (\text{A. 1})$$

where J_1 is the flux of species 1 and c_1 is the concentration of the diffusing species. Mutual-diffusion, defined by the coefficient D_{12} , can be viewed as diffusion of species 1 at infinite dilution through species 2, or equivalently, diffusion of species 2 at infinite dilution through species 1.

Self-diffusion, defined by the coefficient D_{11} , is the diffusion of a substance through itself. There are different theoretical models for computing the mutual and self diffusion coefficient of gases. For non-polar molecules, Lennard-Jones potentials provide a basis for computing diffusion coefficients of binary gas mixtures [76]. The mutual diffusion coefficient, in units of cm^2/s is defined as

$$D_{12} = 0.00188T^{3/2} \sqrt{\frac{M_1 + M_2}{M_1 M_2}} \frac{1}{p\sigma_{12}^2\Omega_D} \quad (\text{A. 2})$$

where T is the gas temperature in unit of Kelvin, M_1 and M_2 are molecular weights of species 1 and 2, p is the total pressure of the binary mixture in unit of bar, σ_{12} is the Lennard-Jones characteristic length, defined by $\sigma_{12} = 1/2(\sigma_1 + \sigma_2)$, Ω_D is the collision integral for diffusion, is a function of temperature, it depends upon the choice of the intermolecular force law between colliding molecules. Ω_D is tabulated as a function of the dimensionless temperature $T^* = k_B T / \varepsilon_{12}$ for the 12-6 Lennard-Jones potential, k_B is the Boltzman gas constant and $\varepsilon_{12} = \sqrt{\varepsilon_1 \varepsilon_2}$ is the maximum attractive energy between two molecules. The accurate relation of Neufield et al. (1972) is

$$\Omega_D = \frac{1.06036}{(T^*)^{0.15610}} + \frac{0.19300}{\exp(0.47635T^*)} + \frac{1.03587}{\exp(1.52996T^*)} + \frac{1.76474}{\exp(3.89411T^*)} \quad (\text{A. 3})$$

Values of the parameters σ and ε are known for many substances [76].

The self-diffusion coefficient of a gas can be obtained from Eq. (A. 2), by observing that for a one-gas system: $M_1 = M_2 = M$, $\varepsilon_1 = \varepsilon_2$ and $\sigma_1 = \sigma_2$. Thus,

$$D_{12} = 0.00188T^{3/2} \sqrt{\frac{2}{M}} \frac{1}{p\sigma_{11}^2\Omega_D} \quad (\text{A. 4})$$

Appendix B. Estimation of the thermal diffusion factor with gas kinetic theory

From the kinetic theory of gases, the thermal diffusion factor, α_T for a binary gas mixture is very complex, as described by Chapman and Cowling, 1939. Three different theoretical expressions for α_T are available, depending on the approximation procedures employed: the first approximation and second one of Chapman and Cowling and the first approximation of Kihara, 1949. The most accurate of these is probably Chapman and Cowling's second approximation, but this is rather complicated, and the numerical computation involved is quite annoying. A few sample calculations indicated that Kihara's expression is more accurate than Chapman and Cowling's first approximation (Mason and Rice, 1954; Mason, 1954), and usually differs from their second approximation by less than the scatter in different experimental determination of α_T . It therefore seemed satisfactory for the present purpose to use Kihara's approximation written in the form

$$[\alpha_T]_I = \left(\frac{S_1 x_1 - S_2 x_2}{Q_1 x_1^2 + Q_2 x_2^2 + Q_{12} x_1 x_2} \right) (6C_{12}^* - 5) \quad (\text{B. 1})$$

The principal contribution to the temperature dependence of α_T comes from the factor $(6C_{12}^* - 5)$, which involves only the unlike (1, 2) molecular interaction. The concentration dependence is given by $S_1 x_1 - S_2 x_2$ term. The main dependence on the masses of the molecules is given by S_1 and S_2 . A positive value of α_T means that component 1 tends to move into the cooler region and 2 towards the warmer region. The temperature at which the thermal diffusion factor undergoes a change of sign is referred to as the inversion temperature.

These quantities calculated as

$$S_1 = \frac{M_1}{M_2} \sqrt{\frac{2M_2}{M_1 + M_2}} \left[\frac{\Omega_{11}^{(2,2)*}}{\Omega_{12}^{(1,1)*}} \right] \left(\frac{\sigma_{11}}{\sigma_{12}} \right)^2 - \frac{4M_1 M_2 A_{12}^*}{(M_1 + M_2)^2} - \frac{15}{2} \frac{M_2 (M_2 - M_1)}{(M_1 + M_2)^2} \quad (\text{B. 2})$$

$$Q_1 = \frac{2}{M_2 (M_1 + M_2)} \sqrt{\frac{2M_2}{M_1 + M_2}} \left[\frac{\Omega_{11}^{(2,2)*}}{\Omega_{12}^{(1,1)*}} \right] \left(\frac{\sigma_{11}}{\sigma_{12}} \right)^2 \times \left[\left(\frac{5}{2} - \frac{6}{5} B_{12}^* \right) M_1^2 + 3M_2^2 + \frac{8}{5} M_1 M_2 A_{12}^* \right] \quad (\text{B. 3})$$

$$Q_{12} = 15 \left(\frac{M_1 - M_2}{M_1 + M_2} \right)^2 \left(\frac{5}{2} - \frac{6}{5} B_{12}^* \right) + \frac{4M_1 M_2 A_{12}^*}{(M_1 + M_2)^2} \quad (\text{B. 4})$$

$$\times \left(11 - \frac{12}{5} B_{12}^* \right) + \frac{8(M_1 + M_2)}{5\sqrt{M_2 M_1}} \left[\frac{\Omega_{11}^{(2,2)*}}{\Omega_{12}^{(1,1)*}} \right] \left[\frac{\Omega_{22}^{(2,2)*}}{\Omega_{12}^{(1,1)*}} \right] \left(\frac{\sigma_{11} \sigma_{22}}{\sigma_{12}^2} \right)^2$$

with relations for S_2 , Q_2 derived from S_1 , Q_1 by interchange of subscripts. The transport properties for gaseous mixtures can also be expressed in terms of the same collision integral. A_{12}^* , B_{12}^* and C_{12}^* are function of $T_{12}^* = kT/\varepsilon_{12}$ defined as

$A_{12}^* = \frac{\Omega^{(2,2)*}}{\Omega^{(1,1)*}}$	(B. 5)
$B_{12}^* = \frac{5\Omega^{(1,2)*} - 4\Omega^{(1,3)*}}{\Omega^{(1,1)*}}$	(B. 6)
$C_{12}^* = \frac{\Omega^{(1,2)*}}{\Omega^{(1,1)*}}$	(B. 7)

The subscripts on the $\Omega^{(l,s)*}$ refer to the three different binary molecular interactions which may occur in a *binary gas mixture*. By convention, the subscript 1 refers to the heavier gas. To this investigation, Lennard-Jones (12-6) model is applied, which has been the best intermolecular potential used to date for the study of transport phenomena and is expressed by a repulsion term varying as the inverse twelfth power of the distance of separation between the centers of two molecules and an attraction term varying as the sixth power of the separation distance. The force constants of pure components σ and ε obtained from viscosity data are used as Table 4-3 and Table 4-4.

References

- [1] A. Ahmadi, A. Aigueperse, and M. Quintard. Calculation of the effective properties describing active dispersion in porous media: from simple to complex unit cells. *Advances in Water Resources*, 24 (3-4):423–438, 2000.
- [2] A. Ahmadi, M. Quintard, and S. Whitaker. Transport in chemically and mechanically heterogeneous porous media V. Two-equation model for solute transport with adsorption. *Advances in water resources*, 22:59–58, 1998.
- [3] A. Amiri and K. Vafai. Analysis of dispersion effects and non-thermal equilibrium, non-darcian, variable porosity incompressible flow through porous media. *International journal of heat and mass transfer*, 37(6):939–954, 1994.
- [4] P. S. Arora, I. R. Shankland, T. N. Bell, M. A. Yabsley, and P. J. Dunlop. Use of precise binary diffusion coefficients to calibrate two-bulb cells instead of using the standard end correction for the connecting tube. *Review of Scientific Instrument*, 48 (6):673–674, 1977.
- [5] A. K. Batabyal and A. K. Barua. Composition dependence of the thermal-diffusion factors in He-CO₂ Ne-CO₂, and Xe-CO₂ mixtures. *Journal of Chemical Physics*, 48:2557–2560, 1968.
- [6] J.C. Batsale, C. Gobbé, and M. Quintard. Local non-equilibrium heat transfer in porous media, in recent research developments in heat, mass & momentum transfer. *Research Signpost, India* 1:1–24, 1996.
- [7] J. Bear. *Hydraulics of Groundwater*. McGraw-Hill Book Company, New York, 1979.
- [8] E. W. Becker. The thermal de-mixing of gases at high pressures. *Die Naturwissenschaften*, 37 (7):165–166, 1950.
- [9] A. Bejan and D. A. Nield. *Convection in Porous Media*. Springer Verlag, 1998.
- [10] R.B. Bird, W.E. Stewart, and E.N. Lightfoot. *Transport Phenomena*. 2nd Ed. New York: J. Wiley and Sons, 2002.
- [11] H. Brenner. Dispersion resulting from flow through spatially periodic porous media. *Philosophical Transactions of the Royal Society of London. Series A, Mathematical and Physical Sciences*, 297 (1430):81–133, 1980.
- [12] H. Brown. On the temperature assignments of experimental thermal diffusion coefficients. *Physical Review*, 58:661 – 662, 1940.

- [13] D. R. Caldwell. Thermal and Fickian diffusion of sodium chloride in a solution of oceanic concentration. *Deep-Sea Research and Oceanographic Abstracts*, 20 (11):1029–1039, 1973.
- [14] R. G. Carbonell and S. Whitaker. Heat and mass transfer in porous media. *Fundamentals of Transport Phenomena in Porous Media*, Martinus Nijhoff, Dordrecht, 1984.
- [15] P. C. Carman. *Flow of gases through porous media*. Academic Press Inc., New York, 1956.
- [16] M. Chandesris and D. Jamet. Jump conditions and surface-excess quantities at a fluid/porous interface: A multi-scale approach. *Transport in Porous Media*, 78:419–438, 2009.
- [17] S. Chapman and T. G. Cowling. *Thermal Combustion and Diffusion in Gases, An Account of the Kinetic Theory of Viscosity, Thermal Conduction and Diffusion in Gases*. Cambridge Mathematical Library, third Ed., 1970.
- [18] M. C. Charrier-Mojtabi, K. Maliwan, Y. Pedramrazi, G. Bardan, and A. Mojtabi. Control of thermoconvective flows by vibration. *Mecanique and Industries*, 4 (5):545–549, 2003.
- [19] F. Cherblanc, A. Ahmadi, and M. Quintard. Two-domain description of solute transport in heterogeneous porous media: Comparison between theoretical predictions and numerical experiments. *Advances in Water Resources*, 30 (5):1127–1143, 2007.
- [20] P. Costeseque, T. Pollak, J. K. Platten, and M. Marcoux. Transient-state method for coupled evaluation of Soret and Fick coefficients, and related tortuosity factors, using free and porous packed thermodiffusion cells. *European Physical Journal E, Soft matter*, 15 (3):249–253, 2004.
- [21] P. Costeseque, D. Fargue, and Ph. Jamet. Thermodiffusion in porous media and its consequences. *Thermal Nonequilibrium Phenomena in Fluid Mixtures. Lecture Notes in Physics*, Springer, Berlin, 584:389–427, 2002.
- [22] J. A. Currie. Gaseous diffusion in porous media. I. A non-steady state method. *British Journal of Applied Physics*, 11 (8):314–317, 1960.
- [23] J. H. Cushman, L. S. Bennethum, and B. X. Hu. A primer on upscaling tools for porous media. *Advances In Water Resources*, 25(8-12):1043–1067, AUG-DEC 2002.
- [24] H. Davarzani, J. Chastanet, M. Marcoux, and M. Quintard. Theoretical determination of effective thermodiffusion coefficients, application to the description of mass transfer in

- porous media. *Lecture Notes of the 8th International Meeting on Thermodiffusion (IMT8), Thermal Nonequilibrium*, 3, Forschungszentrum jülich GmbH, Bonn, Germany:181–187, 2008.
- [25] H. Davarzani, M. Marcoux, and M. Quintard. Theoretical predictions of the effective thermodiffusion coefficients in porous media. *International journal of heat and mass transfer*, 53: 1514-1528, 2010.
- [26] H. A. Daynes. Gas analysis by measurement of thermal conductivity. *Cambridge University Press, Cambridge, UK*, pages 1–302, 1933.
- [27] H. A. Daynes and G. A. Shakespear. The theory of the katharometer. *Proceedings of the Royal Society of London. Series A, Containing Papers of a Mathematical and Physical Character*, 97, Issue 685:273–286, 1920.
- [28] P. J. Dunlop and C. M. Bignell. Diffusion coefficients and thermal diffusion factors for He-CO₂, He-N₂O and He-COS. *Berichte der Bunsen-Gesellschaft*, 99:77–79, 1995.
- [29] R. E. Ewing. Aspects of upscaling in simulation of flow in porous media. *Advances in Water Resources*, 20 (5-6):349–358, 1997.
- [30] D. Fargue, P. Costeseque, P. Ph. Jamet, and S. Girard-Gaillard. Separation in vertical temperature gradient packed thermodiffusion cells: an unexpected physical explanation to a controversial experimental problem. *Chemical Engineering Science*, 59 (24):5847–5852, 2004.
- [31] D. Fargue, P. Costeseque, P. Ph. Jamet, and S. Girard-Gaillard. Separation in vertical temperature gradient packed thermodiffusion cells: an unexpected physical explanation to a controversial experimental problem. *Chemical Engineering Science*, 59 (24):5847–5852, 2004.
- [32] A. Firoozabadi. *Thermodynamics of Hydrocarbon Reservoirs*. McGraw-Hill, New York City, 1991.
- [33] E.N. Fuller, K. Ensley, and J.C. Giddings. Diffusion of halogenated hydrocarbons in helium: the effect of structure on collision cross sections. *Journal of Physical Chemistry*, 73:3679, 1969.
- [34] G. Galliéro, J. Colombani, P. A. Bopp, B. Duguay, J. P. Caltagirone, and F. Montel. Thermal diffusion in micropores by molecular dynamics computer simulations. *Physica A: Statistical Mechanics and its Applications*, 361 (2):494–510, 2006.

- [35] Ph. Georis, F. Montel, S. Van Vaerenbergh, Y. Decroly, and J. C. Legros. Measurement of the Soret coefficient in crude oil. In *Proceedings of the European Petroleum Conference*, 1998.
- [36] M. Giglio and A. Vendramini. Thermal lens effect in a binary liquid mixture: a new effect. *Applied Physics Letters*, 25 (10):555–557, 1974.
- [37] K.E. Grew and T.L. Ibbs. *Thermal diffusion in gases*. Cambridge University Press, 1952.
- [38] S.R. De Groot. *Non-Equilibrium Thermodynamics*. Dover Publication Inc., New York, 1984.
- [39] S.R. De Groot and P. Mazur. *Non-Equilibrium Thermodynamics*. Dover, New York, 1984.
- [40] J. O. Hirschfelder, C.F. Curtiss, and R. B. Bird. *Molecular Theory of Gases and Liquids*. Johns Wiley & Sons, Inc., New York, 1964.
- [41] Clifford K. Ho and S.W. Webb (Eds). *Gas transport in porous media*. Springer (Online service), 2006.
- [42] J. Hoogschagen. Diffusion in porous catalysts and adsorbents. *Industrial and Engineering Chemistry*, 47 (5):906–912, 1955.
- [43] W. Hort, S. J. Linz, and M. Lücke. Onset of convection in binary gas mixtures: role of the dufour effect. *Physical review. A*, 45(6):3737–3748, 1992.
- [44] T. L. Ibbs and K. E. Grew. Influence of low temperatures on the thermal diffusion effect. *Proceedings of the Physical Society*, 43:142–156, 1931.
- [45] I. Ryzhkov Ilya. On double diffusive convection with Soret effect in a vertical layer between co-axial cylinders. *Physica D 215*, 215 (2):191–200, 2006.
- [46] G. Jessop. Katharometers. *Journal of Scientific Instruments*, 43 (11):777–782, 1966.
- [47] M. Kaviany. *Principles of Heat Transfer in Porous Media*. Second Edition, (Second Printing), Springer-Verlag, New York, 1999.
- [48] M. Kaviany. *Principles of Heat Transfer*. John Wiley & Sons, Inc., New York, 2002.
- [49] J. H. Kim, J. A. Ochoa, and S. Whitaker. Diffusion In Anisotropic Porous-Media. *Transport In Porous Media*, 2:327–356, 1987.
- [50] L. S. Kotousov and A. V. Panyushkin. Apparatus for determining thermal-diffusion coefficients in gas mixtures. *Journal of Engineering Physics and Thermophysics*, 9 (5):390–393, 1965.

- [51] B. Lacabanne, S. Blancher, R. Creff, and F. Montel. Soret effect in multicomponent flow through porous media: local study and upscaling process. *Lecture notes in physics*, Springer, 584:448–465, 2002.
- [52] L. D. Landau and E. M. Lifschitz. *Fluid Mechanics*. 2nd Ed. Oxford, England: Pergamon Press, 1982.
- [53] D. Lasseux, A. Ahmadi, and A. A. Abbasian Arani. Two-phase inertial flow in homogeneous porous media: A theoretical derivation of a macroscopic model. *Transport in Porous Media*, 75 (3):371–400, 2008.
- [54] M. Lorenz and A.H. Emery. The packed thermodiffusion column. *Chemical Engineering Science*, 11:16–23, 1959.
- [55] C. Ludwig. *Sitzungsber. K. Preuss, Akad. Wiss.*, 20:539, 1856.
- [56] M. Marcoux and M. C. Charrier-Mojtabi. Etude paramétrique de la thermogravitation en milieu poreux. *Comptes Rendus de l'Académie des Sciences*, 326:539–546, 1998.
- [57] M. Marcoux and P. Costeseque. Study of transversal dimension influence on species separation in thermogravitational diffusion columns. *Journal of Non-Equilibrium Thermodynamics*, 32 (3):289–298, 2007.
- [58] E. A. Mason and S. C. Saxena. Approximate formula for the thermal conductivity of gas mixtures. *Physics of Fluids*, 1:361–369, 1958.
- [59] E.A. Mason and A.P. Malinauskas. *Gas Transport in Porous Media: The Dusty Gas Model*. Elsevier, Amsterdam, 1983.
- [60] J. C. Maxwell. A treatise on electricity and magnetism. *Clarendon Press, Oxford*, I, 2nd edition, 1881.
- [61] C. C. Mei. Method of homogenization applied to dispersion in porous media. *Transport in porous media*, 9(3):261–274, 1991.
- [62] R. J. Millington. Gas diffusion in porous media. *Science*, 130 (3367):100–102, 1959.
- [63] R. J. Millington. Permeability of porous solids. *Transactions of the Faraday Society*, 57:1200–1207, 1961.
- [64] C. Moyne. Two-equation model for a diffusive process in porous media using the volume averaging method with an unsteady-state closure. *Advances in Water Resources*, 20, Issues 2-3:63–76, 1997.
- [65] C. Moyne, S. Didierjean, H.P.A. Souto, and O.T. da Silveira Filho. Thermal dispersion in porous media: One-equation model. *International Journal of Heat and Mass Transfer*, 43 (20):3853–3867, 2000.

- [66] H. Nasrabadi, H. Hoteit, and A. Firoozabadi. An analysis of species separation in thermogravitational column filled with porous media. *Transport in Porous Media*, 67 (3):473–486, 2007.
- [67] E. P. Ney and F. C. Armistead. The self-diffusion coefficient of uranium hexafluoride. *Physical Review*, 71(1):14–19, 1947.
- [68] C. Nicholson. Diffusion and related transport mechanisms in brain tissue. *Reports on Progress in Physics*, 64:815–884, 2001.
- [69] C. Nicholson and J. M. Phillips. Ion diffusion modified by tortuosity and volume fraction in the extracellular microenvironment of the rat cerebellum. *Journal of Physiology (Cambridge)*, 321:225–258, 1981.
- [70] D. A. Nield and A. Bejan. *Convection in Porous Media*. Second Edition, Springer-Verlag New York, Inc., New York, 1999.
- [71] J. Ochoa-Tapia and S. Whitaker. Heat transfer at the boundary between a porous medium and a homogeneous fluid. *International Journal of Heat and Mass Transfer*, 40 (11):2691–2707, 1997.
- [72] J. K. Platten. Enhanced molecular separation in inclined thermogravitational columns. *The Journal of Physical Chemistry B*, 107 (42):11763–11767, 2003.
- [73] J. K. Platten. The Soret effect: A review of recent experimental results. *Journal of applied mechanics*, 73(1):5–15, 2006.
- [74] J. K. Platten and P. Costeseque. The Soret coefficient in porous media. *Journal of Porous Media*, 7 (4):329–42, 2004.
- [75] J.K. Platten and J.C. Legros. Convection in liquids. *Springer, Berlin*, Chap. 9, 1984.
- [76] B. E. Poling, J. M. Rausnitz, and J. P. Connell. *The Properties of Gases and Liquids*. McGraw-Hill, New York, 5th edition, 2000.
- [77] N. Puiroux, M. Prat, and M. Quintard. Non-equilibrium theories for macroscale heat transfer: ablative composite layer systems. *International Journal of Thermal Sciences*, 43(6):541–554, 2004.
- [78] M. Quintard, and S. Whitaker. Transport in ordered and disordered porous media III: Closure and comparison between theory and experiment. *Transport in Porous Media*, 15(1):31–49, 1994.
- [79] M. Quintard. Diffusion in isotropic and anisotropic porous systems: Three-dimensional calculations. *Transport in Porous Media*, Volume 11, Number 2:187–199, 1993.

- [80] M. Quintard, L. Bletzaker, D. Chenu, and S. Whitaker. Nonlinear, multicomponent, mass transport in porous media. *Chemical Engineering Science*, 61:2643–2696, 2006.
- [81] M. Quintard, F. Cherblanc, and S. Whitaker. Dispersion in heterogeneous porous media: One-equation non-equilibrium model. *Transport in Porous Media*, 44(1):181–203, 2001.
- [82] M. Quintard, M. Kaviany, and S. Whitaker. Two-medium treatment of heat transfer in porous media: numerical results for effective properties. *Advances in Water Resources*, 20(2-3):77–94, 1997.
- [83] M. Quintard and S. Whitaker. Transport in ordered and disordered porous media: volume-averaged equations, closure problems and comparison with experiment. *Chemical Engineering Science*, 14:2534–2537, 1993.
- [84] M. Quintard and S. Whitaker. Local thermal equilibrium for transient heat conduction: theory and comparison with numerical experiments. *International Journal of Heat and Mass Transfer*, 38(15):2779–2796, 1995.
- [85] M. Quintard and S. Whitaker. Theoretical analysis of transport in porous media. *Handbook of Heat Transfer in Porous Media*, edited by H. Hadim and K. Vafai, Marcel Decker, Inc., New York, Ch. 1:1–52, 2000.
- [86] G. D. Rabinovich, R. Y. Gurevich, and G. N. Bobrova. Thermodiffusion separation of liquid mixtures. [*in Russian*], *Nauka i Tekhnika, Minsk*, 1971.
- [87] G.D. Rabinovich. Separation of isotopes and other mixtures by thermal diffusion. *Atomizdat, Moscow*, 1981.
- [88] J. W. S. Rayleigh. *Theory of Sound*, (2nd Ed.). Dover, New-York, 1945.
- [89] D. Reith and F. Mueller-Plathe. On the nature of thermal diffusion in binary lennard-jones liquids. *Journal of Chemical Physics*, 112:2436–2443, 2000.
- [90] D. Ryan, R. G. Carbonell, and S. A. Whitaker. Theory of diffusion and reaction in porous media. *A.I.Ch.E. Symposium Series*, 77, No. 202:46–62, 1981.
- [91] M.Z. Saghir, C.G. Jiang, M. Chacha, Y. Yan, M. Khawaja, and S. Pan. Thermodiffusion in porous media. In *Transport Phenomena in Porous Media III*, (Eds. D. B. Ingham and I. Pop, Elsevier, Oxford, page 227–260, 2005.
- [92] M. Sahraoui and M. Kaviany. Slip and no-slip temperature boundary conditions at interface of porous, plain media: Conduction. *International Journal of Heat and Mass Transfer*, 36:1019–1033, 1993.

- [93] M. Sahraoui and M. Kaviany. Direct simulation vs volume-averaged treatment of adiabatic, premixed flame in a porous medium. *International Journal of Heat and Mass Transfer*, 37(18):2817–2834, 1994.
- [94] E. Sanchez-Palencia. On the asymptotics of the fluid flow past an array of fixed obstacles. *International Journal of Engineering Science*, 20 (12):1291–1301, 1982.
- [95] S. C. Saxena and E. A. Mason. Thermal diffusion and the approach to the steady state in gases II. *Molecular Physics*, 2 (4):379–396, 1959.
- [96] M. E. Schimpf. Studies in thermodiffusion by thermal field-flow fractionation. *Proceedings of the Third International Symposium on Thermodiffusion*, pages 58–63, 1998.
- [97] A. G. Shashkov, A. F. Zolotukhina, T N. Abramenko, and B. P. Mathur. Thermal diffusion factors for binary gas systems: Ar-N₂, Ar-CO₂, He-H₂, He-N₂O, Kr-N₂O and He-NH₃. *Journal of physics B- Atomic molecular and optical physics*, 12(21):3619–3630, 1979.
- [98] C. Soret. Influence de la temperature sur la distribution des sels dans leurs solutions. *Compte-Rendu de l'Academie des Sciences, Paris*, 91:289, 1880.
- [99] C. Tropea and J. F. Foss (Eds.) A. L. Yarin. *Springer Handbook of Experimental Fluid Mechanics*. Springer, 2007.
- [100] S. Van Vaerenbergh, J. C. Legros, J. L. Daridon, T. Karapantsios, M. Kostoglou, and Z. M. Saghir. Multicomponent transport studies of crude oils and asphaltenes in DSC program. *Microgravity Science and Technology*, 18 (3-4):150–154, 2006.
- [101] A. van Itterbeek and O. van Paemel. Measurements on the viscosity of hydrogen- and deuterium gas between 293°k and 14°k. *Physica*, 5 (10):938–944, 1938.
- [102] A. van Itterbeek and O. van Paemel. Measurements on the viscosity of neon, hydrogen, deuterium and helium as a function of the temperature, between room temperature and liquid hydrogen temperatures. *Physica.*, 7 (3):265–272, 1940.
- [103] A. S. M. Wahby and J. Los. Diffusion in lorentzian and quasi-lorentzian N₂-light noble gas mixtures. *Physica, B + C*, 145 (1):69–77, 1987.
- [104] N. Wakao and J. M. Smith. Diffusion in catalyst pellets. *Chemical Engineering Science*, 17 (11):825–834, 1962.
- [105] L. Wang and M. Quintard. Nanofluids of the future. *Advances in Transport Phenomena*, chap. 4:179–243, 2009.

- [106] H. Watts. Diffusion of krypton-85 in multicomponent mixtures of krypton with helium, neon, argon and xenon. *Transactions of the Faraday Society*, 60 (10):1745–1751, 1964.
- [107] H. L. Weissberg. Effective diffusion coefficient in porous media. *Journal of Applied Physics*, 34 (9):2636–2639, 1963.
- [108] K. R. Weller, N. S. Stenhouse, and H. Watts. Diffusion of gases in porous solids. II. theoretical background and experimental method. *Canadian Journal of Chemistry*, 52 (15):2684–2691, 1974.
- [109] S. Whitaker. Diffusion and dispersion in porous media. *AIChE J*, 13:420–427, 1967.
- [110] S. Whitaker. The forchheimer equation: A theoretical development. *Transport in Porous Media*, 25 (1):27–61, 1996.
- [111] S. Whitaker. *The method of Volume Averaging*. Kluwer Academic Publishers, Dordrecht, The Netherlands, 1999.
- [112] S. Wiegand. Thermal diffusion in liquid mixtures and polymer solutions. *Journal of Physics: Condensed Matter*, 16 (10):357–379, 2004.
- [113] S. Wiegand and W. Köhler. Measurement of transport coefficients by an optical grating technique. *Thermal Nonequilibrium Phenomena in Fluid Mixtures Lecture Notes in Physics*, Springer-Verlag, 584:189–210, 2002.
- [114] M. A. Yabsley and P. J. Dunlop. A study of the two-bulb method for measuring diffusion coefficients of binary gas mixtures. *Physica A*, 85 (1):160–174, 1976.
- [115] F. Zanotti and R. G. Carbonell. Development of transport equations for multiphase system-I. General development for two phase system. *Chemical Engineering Science*, 39, Issue 2:263–278, 1984.
- [116] F. Zanotti and R. G. Carbonell. Development of transport equations for multiphase systems-II. Application to one-dimensional axi-symmetric flows of two phases. *Chemical Engineering Science*, 39, Issue 2:279–297, 1984.

